STUDY OF FLOW AND NOISE GENERATION FROM CAR A-PILLARS

by

B.C. POPAT

Thesis submitted for the degree of

Doctor of Philosophy

of the

University of London

and for the

Diploma of Imperial College

Department of Aeronautics

Imperial College of Science Technology and Medicine

Prince Consort Road

London

SW7 2BY

February 1991

ABSTRACT

An experimental investigation has been performed to study the flow around three road vehicle models and in particular the flow around the A-Pillar region. Mean and fluctuating pressure surveys were conducted in the A-Pillar region for several A-Pillar angles (0^{o}-60^{o}) and Reynolds Numbers ($5.672x10^{5}$-$9.580x10^{5}$), these surveys were also conducted on a blunt swept plate model (Reynolds No. $5.270x10^{4}$-$1.166x10^{5}$).

Wind tunnel and water tunnel flow visualization techniques were used on the three road vehicle models as a means of investigating the structure of the A-Pillar flow.

Wind tunnel flow visualization results for the road vehicle models indicate the presence of three distinctive flow regimes within the A-Pillar region, depending upon A-Pillar angle. The three flow regimes observed are :-

TYPE I Three-dimensional bubble

TYPE II Vortex bubble (mixed flow)

TYPE III Fully developed vortex

Water tunnel flow visualization results clearly show the difference between the 40^{o} and 60^{o} road vehicle model flow structures. The 40^{o} models generate a complex flow structure within the A-Pillar region with several vortices present at any one time. But the 60^{o} models generate a classical vortex type structure within the A-Pillar region.

Measurements of time-mean surface pressures indicate that all three regimes are Reynolds number dependent. Mean pressure coefficient results show that the A-Pillar angle at which the lowest Cp values are generated on the road vehicle models is 40^{o} and that for the Swept plate model the angle is 30^{o}.

A plot of the vortex core angle versus A-Pillar angle for the road vehicle models combined with published data on vortex angles for delta wings produces a

single curve.

Measurements of fluctuating pressure are presented for a range of A-Pillar angles for the road vehicle models and the largest levels of Cp_{rms} are found to occur for an A-Pillar angle of 40^{o}.

A simple potential flow model shows that oscillations of the A-Pillar vortex normal to the model surface are much more effective at generating pressure fluctuations then oscillations parallel to the model surface.

CONTENTS

	Page No.
Abstract	2
Contents	4
Acknowledgements	7
Nomenclature	8
List of figures	10
List of Photographs	18
Chapter 1 Introduction	20
1.1 General	20
1.2 Review of Research	22
1.3 Comparisons with Swept and Delta Wings	31
1.4 Comparisons with Flat Roof, Low-Rise Buildings	35
1.5 Purpose of Study	37
Chapter 2 Equipment and Procedure	39
2.1 Wind Tunnel	39
2.1.1 Ground Simulation	39
2.1.2 Wind Tunnel Calibration	41
2.2 Instrumentation	42
2.2.1 Static Pressure	42
2.2.2 Fluctuating Pressure	42
2.2.3 Other Electronic Equipment	45
2.2.3.1 PC/AT Computer	45
2.2.3.2 Labmaster Tecmar Card	45
2.2.3.3 Power Supply	46
2.2.3.4 Amplifier	46
2.2.3.5 Oscilloscope	46

2.2.3.6 Plotter 46

2.2.3.7 Filter 46

2.3 Flow Visualization 47

2.4 Data Reduction 49

2.4.1 Blockage Correction 49

2.4.2 Mean Pressure 51

2.4.3 Fluctuating Pressure 52

2.4.4 Pressure Spectra 53

2.5 Mean Static Pressure Set-up 54

2.6 Fluctuating Pressure Set-up 55

2.7 Model Details 56

2.7.1 Road Vehicle Model 56

2.7.2 Swept Edge Model 57

2.8 Experimental Errors 58

Chapter 3 Results 60

3.1 Flow Visualization (Wind Tunnel) 61

3.1.1 Whole Model 61

3.1.2 Top Half 64

3.1.3 Whole Model + Plate 66

3.2 Flow Visualization (Water Tunnel) 67

3.2.1 A-Pillar Angle = 40^{o} 68

3.2.2 A-Pillar Angle = 60^{o} 68

3.3 Mean Static Pressure 69

3.3.1 Whole Model 70

3.3.2 Top Half 73

3.3.3 Whole Model + Plate 76

3.3.4 Swept Plate 77
3.4 R.M.S Fluctuating Pressure 79
3.4.1 Whole Model 79
3.4.2 Top Half 82
3.4.3 Whole Model + Plate 83
3.4.4 Swept Plate 84
3.5 Power Spectra 85

Chapter 4 Discussion 88
4.1 Three-Dimensional Bubble 89
4.2 Vortex Bubble Structure (Mixed Flow) 94
4.3 Fully Developed Vortex 98
4.4 Power Spectra 103
4.5 General Discussion 105

Chapter 5 Conclusions 112
5.1 Flow Visualization 112
5.2 Mean Pressure 114
5.3 Fluctuating Pressure 115

Chapter 6 Suggestions for Further Work 117

References 118

Appendices 125

Figures 137

Acknowledgements

I would like to express my sincere thanks to my supervisor, Professor P.W. Bearman for his Guidance and help through the three years of this work.

Financial support was provided by the Science and Engineering Research Council during this period.

I would also like to thank members of the Aeronautics Department workshop who constructed the models and provided invaluable advice, in particular messers John Coles, Jack Beazley and Ian James. My thanks to John O'Leary who took and produced the photographs.

Above all I wish to thank my parents for their help and encouragement.

Nomenclature

Cp	Mean Pressure Coefficient
P	Measured Pressure
U	Free Stream Velocity
K1, K2	Wind Tunnel correction Constants
L	Tube Length (when measuring fluctuating pressure)
V	Volume
C_s	Speed of Sound
Q	Mass flow rate through a control Volume
A	Control volume cross-sectional area
C	Wind Tunnel cross-sectional area
S	Model cross-sectional area
d_t	Tubing diameter
N	Number of data samples
h	Sampling interval
T_r	Record length
F_c	Nyquist frequency
Be	Desired resolution bandwidth
BV	Base vortex
HV	Horseshoe vortex
VB	Vortex breakdown
n	frequency
F{x(n)}	Power Spectral density of x
n_n	Non-dimensionalized frequency

Greek

ρ	Fluid density
γ	A-Pillar Angle (Windscreen Angle)
ε_r	Normalised standard error
μ	Viscosity of Air
ζ	Damping parameter
ω_n	Natural frequency Parameter

Subscripts

m	Measured value in Wind Tunnel working section
s	Static value in Wind Tunnel working section
s1	Static value at the beginning of Wind Tunnel working section
t	Pitot value in Wind Tunnel working section
t1	Pitot value in the Wind Tunnel expansion chamber
c	Corrected value
rms	Root mean square
a	Atmospheric
min	minimum
n	non-dimensional
1,2,3	different areas or volumes
f	fluctuating

List of Figures

Fig.1.1.1 Flow around a passenger car (schematic), from Hucho (1987).

Fig.1.2.1 Critical areas in development of wind noise, from Thompson (1964).

Fig.1.2.2 Comparisons of noise levels due to different sources as a function of speed for a typical production car, from Buchiem et al (1983).

Fig.1.2.3 Range of flow induced interior noise of present-day production cars at 110 Km/h and 180 km/h, from Buchiem et al (1983).

Fig.1.2.4 Correlation of flow-induced interior noise with transmission loss for production cars at 110 Km/h, from Buchiem et al (1983).

Fig.1.2.5 Correlation of flow-induced interior noise with drag coefficient for production cars at 110 Km/h, from Buchiem et al (1983).

Fig.1.2.6a,b Types of air flow generated on a cuboid in order to measure sound levels, from Stapleford et al (1971).

Fig.1.2.7 Flow visulation of three types of flow generated on the cuboid using oil film technique, from Stapleford et al (1971).

Fig.1.2.8 Surface sound pressure levels in the frequency range 500 Hz to 1500 Hz for (a) Attached flow; (b) Two-dimensional separation; (c) Vortex region, from Stapleford et al (1971).

Fig.1.2.9 Mean noise spectra for different types of flow, from Stapleford et al (1971).

Fig.1.2.10 Effect of Tunnel wind speed on typical noise spectrum on square-edged box at zero yaw angle, from Stapleford et al (1971).

Fig.1.2.11 Pressure distribution on side window glass (from Watanabe et al (1978)).

Fig.1.2.12 Schematic representation of the fluctuating pressure intensity distrubation on a car-body surface, from Dobrzynski (1983).

Fig.1.2.13 Unsteady surface pressure spectrums in the side-window area, from Dobrzynski (1983).

Fig.1.2.14 Comparisons of surface pressure fluctuations for a production car and a low-drag car, from Buchiem et al (1983).

Fig.1.2.15 Sound pressure levels originating from different car body areas, from Buchiem et al (1983).

Fig.1.2.16 Comparisons of predicted and measured interior noise spectra, from Buchiem et al (1983).

Fig.1.2.17 A typical example of the variation of each noise component with car road and air speed, from Romberg et al (1977).

Fig.1.2.18 A spectral comparison of each noise component, from Romberg et al (1977).

Fig.1.2.19 Comparison of car aspiration noise: road and wind tunnel data, from Romberg et al (1977).

Fig.1.2.20 Microphone and pressure gauge positions on full scale car model, from Watanabe et al (1978).

Fig.1.2.21 Different A-Pillar shapes tested on full scale model, from Watanabe et al (1978).

Fig.1.2.22 Effect of rain gutter height on wind noise (100 Km/h: front seat), from Watanabe et al (1978).

Fig.1.2.23 Three-dimensional model used to investigate airflow in the A-Pillar region, from Watanabe et al (1978).

Fig.1.2.24 Schematic representation of flow-field around A-Pillar, from Watanabe et al (1978).

Fig.1.2.25 Flow pattern on front side window of full scale model, from Watanabe et al (1978).

Fig.1.2.26 Surface pressure distribution on 1/3 scale model at zero yaw angle, from Bearman et al (1989).

Fig.1.2.27 Surface pressure distribution on 1/3 scale model at ten degrees yaw angle, from Bearman et al (1989).

Fig.1.2.28 Surface pressure distribution on 1/3 scale model at twenty degrees yaw angle, from Bearman et al (1989).

Table 1.2 Relation between character of flow, maximum sound pressure level and frequency range, from Hucho (1987).

Fig.1.3.1 Details of Sutton's Swept edge model, from Sutton (1983).

Fig.1.3.2 Features of the surface oilflow pattern at forty five degrees sweep with wind speed 30 m/s, from Sutton (1983).

Fig.1.3.3 Surface oil-flow pattern and pressure distribution for sharp edged swept wing, from Poll (1980).

Fig.1.3.4 Surface oil-flow pattern and pressure distribution for RAE 101 leading edge swept wing, from Poll (1980).

Fig.1.3.5 Surface oil-flow pattern for a blunt edged swept wing at Reynolds No. 1.7E06, from Poll (1980).

Fig.1.3.6 Surface oil-flow pattern for a blunt edged swept wing at Reynolds No. 0.9E06, from Poll (1980).

Fig.1.3.7 Delta wing at fixed angle of attack $\alpha = 10^{o}$, from Gad-el-Hak et al (1985).

Fig.1.4.1 Contour plot of mean pressure coefficient for flat roof low-rise building, flow yaw angle being forty five degrees, from Kind (1986).

Fig.1.5.1 Flow separation on the bonnet and reattachement on the windscreen as a function of windscreen rake angle γ, from Scibor-Rylski (1984).

Table 1.2 Relation between character of flow, maximum sound pressure level and frequency range, from Hucho (1987).

Fig.2.1.3.1 A general sketch of the Wind Tunnel working section and contraction nozzle.

Fig.2.1.3.2 Wind Tunnel static pressure calibration curve (K1).

Fig.2.1.3.3 Wind Tunnel calibration curve (K2).

Fig.2.2.1.1 Setra Transducer calibration curve.

Fig.2.2.1.2 Diagrams of Setra Transducer and cap design.

Fig.2.2.2.1 Druck Transducer calibration curve.

Fig.2.2.2.2 Diagrams of Druck Transducer and cap design.

Fig.2.2.2.3 Druck transducer dynamic responce testing setup.

Fig.2.2.2.4 A typical frequency responce curve for Druck transducer.

Fig.2.2.2.5 Transducer system versus tube length.

Fig.2.5.1 Mean static pressure setup diagram.

Fig.2.6.1 Fluctuating pressure setup diagram.

Fig.2.7.2.1 Diagram of Swept Plate model.

Fig.3.3.1.1 Mean Cp Distribution in A-Pillar region for 0° Whole Model at Reynolds No.5.672×10^5.

Fig.3.3.1.2 Mean Cp Distribution in A-Pillar region for 10° Whole Model at Reynolds No.5.672×10^5.

Fig.3.3.1.3 Mean Cp Distribution in A-Pillar region for 20° Whole Model at Reynolds No.5.672×10^5.

Fig.3.3.1.4 Mean Cp Distribution in A-Pillar region for 30° Whole Model at Reynolds No.5.672×10^5.

Fig.3.3.1.5 Mean Cp Distribution in A-Pillar region for 30° Whole Model at Reynolds No.7.65×10^5.

Fig.3.3.1.6 Mean Cp Distribution in A-Pillar region for 30° Whole Model at Reynolds No.9.58×10^5.

Fig.3.3.1.7 Mean Cp Distribution in A-Pillar region for 40° Whole Model at Reynolds No.9.58×10^5.

Fig.3.3.1.8 Mean Cp Distribution in A-Pillar region for 50° Whole Model at Reynolds No.$9.58x10^5$.

Fig.3.3.1.9 Mean Cp Distribution in A-Pillar region for 60° Whole Model at Reynolds No.$5.672x10^5$.

Fig.3.3.2.1 Mean Cp Distribution in A-Pillar region for 0° Top Half at Reynolds No.$7.65x10^5$.

Fig.3.3.2.2 Mean Cp Distribution in A-Pillar region for 20° Top Half at Reynolds No.$9.58x10^5$.

Fig.3.3.2.3 Mean Cp Distribution in A-Pillar region for 40° Top Half at Reynolds No.$5.672x10^5$.

Fig.3.3.2.4 Mean Cp Distribution in A-Pillar region for 60° Top Half at Reynolds No.$9.58x10^5$.

Fig.3.3.3.1 Mean Cp Distribution in A-Pillar region for 0° Whole Model + Plate at Reynolds No.$9.58x10^5$.

Fig.3.3.3.2 Mean Cp Distribution in A-Pillar region for 20° Whole Model + Plate at Reynolds No.$7.65x10^5$.

Fig.3.3.3.3 Mean Cp Distribution in A-Pillar region for 40° Whole Model + Plate at Reynolds No.$5.672x10^5$.

Fig.3.3.3.4 Mean Cp Distribution in A-Pillar region for 60° Whole Model + Plate at Reynolds No.$9.58x10^5$.

Fig.3.3.4.1 Mean Cp Distribution in Root region for 0° Swept Plate at Reynolds No.$1.166x10^5$.

Fig.3.3.4.2 Mean Cp Distribution in Root region for 20° Swept Plate at Reynolds No.$8.652x10^4$.

Fig.3.3.4.3 Mean Cp Distribution in Root region for 40° Swept Plate at Reynolds No.$8.652x10^4$.

Fig.3.3.4.4 Mean Cp Distribution in Root region for 60° Swept Plate at Reynolds No.$8.652x10^4$.

Fig.3.4.1.1 R.M.S Cp Distribution in A-Pillar region for 0° Whole Model at Reynolds No.9.58x10^5.

Fig.3.4.1.2 R.M.S Cp Distribution in A-Pillar region for 10° Whole Model at Reynolds No.9.58x10^5.

Fig.3.4.1.3 R.M.S Cp Distribution in A-Pillar region for 20° Whole Model at Reynolds No.7.65x10^5.

Fig.3.4.1.4 R.M.S Cp Distribution in A-Pillar region for 30° Whole Model at Reynolds No.9.58x10^5.

Fig.3.4.1.5 R.M.S Cp Distribution in A-Pillar region for 40° Whole Model at Reynolds No.7.65x10^5.

Fig.3.4.1.6 R.M.S Cp Distribution in A-Pillar region for 50° Whole Model at Reynolds No.7.65x10^5.

Fig.3.4.1.7 R.M.S Cp Distribution in A-Pillar region for 60° Whole Model at Reynolds No.9.58x10^5.

Fig.3.4.2.1 R.M.S Cp Distribution in A-Pillar region for 0° Top Half at Reynolds No.5.672x10^5.

Fig.3.4.2.2 R.M.S Cp Distribution in A-Pillar region for 40° Top Half at Reynolds No.7.65x10^5.

Fig.3.4.2.3 R.M.S Cp Distribution in A-Pillar region for 60° Top Half at Reynolds No.5.672x10^5.

Fig.3.4.3.1 R.M.S Cp Distribution in A-Pillar region for 0° Whole Model + Plate at Reynolds No.7.65x10^5.

Fig.3.4.3.2 R.M.S Cp Distribution in A-Pillar region for 40° Whole Model + Plate at Reynolds No.5.672x10^5.

Fig.3.4.3.3 R.M.S Cp Distribution in A-Pillar region for 60° Whole Model + Plate at Reynolds No.9.58x10^5.

Fig.3.4.4.1 R.M.S Cp Distribution in Root region for 0° Swept Plate at Reynolds No.8.652×10^4.

Fig.3.4.4.2 R.M.S Cp Distribution in Root for 40° Swept Plate at Reynolds No.1.166×10^5.

Fig.3.4.4.3 R.M.S Cp Distribution in Root region for 60° Swept Plate at Reynolds No.5.270×10^4.

Fig.3.5.1 Power Spectra plot of peak Cp_{rms} Tapping for 40° Whole Model at three speeds (25.9, 35.0, 43.8m/s).

Fig.3.5.2 Power Spectra plot of peak Cp_{rms} Tapping for 60° Whole Model at three speeds (25.9, 35.0, 43.8m/s).

Fig.3.5.3 Comparisons of the Power Spectra curves for the 40° and 60° Whole models (peak Cp_{rms} Tappings) at 43.8m/s.

Fig.3.5.4 Power Spectra plot of peak Cp_{rms} Tapping for the three 40° models at 43.8m/s.

Fig.3.5.5 Power Spectra plot of 4 pressure tappings on the 40° Whole Model at 35.0m/s.

Fig.3.5.6 Power Spectra plot of 3 pressure tappings on the 60° Whole Model at 35.0m/s.

Fig.4.1 Diagram of TYPE I flow - The bubble.

Fig.4.2 Diagram of TYPE II flow - Vortex bubble (mixed flow).

Fig.4.3 Diagram of TYPE III flow - Free vortex layer.

Fig.4.5.1 Cp_{min} versus A-Pillar angle for whole model.

Fig.4.5.2 Cp_{min} versus sweep angle for Swept Plate Model.

Fig.4.5.3 Cp_{min} versus A-Pillar angle for three Road Vehicle Models at Reynolds No.7.65×10^5.

Fig.4.5.4 Cp_{min} versus Reynolds No. for 0^o A-Pillar Angle. for three Road Vehicle Models.

Fig.4.5.5 Cp_{min} versus Reynolds No. for 40^{o} A-Pillar Angle. for three Road Vehicle Models.

Fig.4.5.6 Cp_{min} versus Reynolds No. for 60^{o} A-Pillar Angle. for three Road Vehicle Models.

Fig.4.5.7 Vortex Core Angle versus A-Pillar Angle for all four Models and Elle's Data.

Fig.4.5.8 Mean Cp distribution on Swept Plate Model for AR=6.0 at Reynolds No.8.652×10^{4}.

Fig.4.5.9 Peak R.M.S Cp versus Reynolds No. for 0^{o} A-Pillar Angle for all three Road Vehicle Models.

Fig.4.5.10 Peak R.M.S Cp versus Reynolds No. for 40^{o} A-Pillar Angle for all three Road Vehicle Models.

Fig.4.5.11 Peak R.M.S Cp versus Reynolds No. for 60^{o} A-Pillar Angle for all three Road Vehicle Models.

Fig.4.5.12 Power Spectra plot of peak Cp_{rms} Tapping for the three 60° models at 35.0m/s.

Fig.A.1.1 Diagram of Mark to Space scaling for the A/d timing clocks.

Fig.A.4.1 Sample of 40^{o} whole model raw fluctuating data for Re No.9.58×10^{5}.

Table A.4 Experimental mean pressure data (volts) for 40^{o} whole model, Re No.9.58×10^{5}.

Fig.A.5.1 Diagrams of Idealised Potential flow model for Road Vehicle models.

Fig.A.5.2 Comparison between averaged experimental and potential Cp_{min} data for whole model, three A-Pillar angles.

Table A.5 Comparison between averaged experimental and potential Cp_{rms} data for whole model, three A-Pillar angles.

List of Photographs

Pl.2.7.1.1,2 Photographs of the Road Vehicle models.

Pl.2.7.2.1 Photograph of the Tapping grids used on the Swept Plate model.

Pl.3.1.1 Typical wind tunnel flow visualization results.

Pl.3.1.1.1a-d Wind Tunnel Flow Visualization of 0° Whole Model at three Reynolds Nos.

Pl.3.1.1.2a-d Wind Tunnel Flow Visualization of 10° Whole Model at three Reynolds Nos.

Pl.3.1.1.3a-d Wind Tunnel Flow Visualization of 20° Whole Model at three Reynolds Nos.

Pl.3.1.1.4a-d Wind Tunnel Flow Visualization of 30° Whole Model at three Reynolds Nos.

Pl.3.1.1.5a-d Wind Tunnel Flow Visualization of 40° Whole Model at three Reynolds Nos.

Pl.3.1.1.6a-d Wind Tunnel Flow Visualization of 50° Whole Model at three Reynolds Nos.

Pl.3.1.1.7a-d Wind Tunnel Flow Visualization of 60° Whole Model at three Reynolds Nos.

Pl.3.1.2.1a Wind Tunnel Flow Visualization of 0° Top Half at Reynolds No.7.65×10^5.

Pl.3.1.2.1b Wind Tunnel Flow Visualization of 20° Top Half at Reynolds No.7.65×10^5.

Pl.3.1.2.1c Wind Tunnel Flow Visualization of 40° Top Half at Reynolds No.7.65×10^5.

Pl.3.1.2.1d Wind Tunnel Flow Visualization of 60° Top Half at Reynolds No.5.672×10^5.

Pl.3.1.3.1a Wind Tunnel Flow Visualization of 0° Whole Model + Plate at Reynolds No.7.65×10^5.

Pl.3.1.3.1b Wind Tunnel Flow Visualization of 20° Whole Model + Plate at Reynolds No.7.65×10^5.

Pl.3.1.3.1c Wind Tunnel Flow Visualization of 40° Whole Model + Plate at Reynolds No.3.457×10^5.

Pl.3.1.3.1d Wind Tunnel Flow Visualization of 60° Whole Model + Plate at Reynolds No.5.672×10^5.

Pl.3.2.1.1 Water Tunnel Flow Visualization of 40° Whole Model at Reynolds No.10^3.

Pl.3.2.1.2 Water Tunnel Flow Visualization of 40° Whole Model + Plate at Reynolds No.10^3.

Pl.3.2.2.1 Water Tunnel Flow Visualization of 60° Whole Model at Reynolds No.10^3.

Pl.3.2.2.2 Water Tunnel Flow Visualization of 60° Whole Model + Plate at Reynolds No.10^3.

1.INTRODUCTION

1.1 GENERAL

Aerodynamics only became the dominating design criterion for road vehicles after the oil crisis in the early 1970's. This increased importance of aerodynamics in the road vehicle design process is clearly illustrated by the increase in the number of Wind tunnels that have been built in recent years by the vehicle manufacturers. Previously models were designed by the styling department and aerodynamic development was based on fine tuning of the model. But in the post oil crisis years road vehicle aerodynamics was concerned almost exclusively with vehicle performance and directional stability, and has only recently focused on other factors such as :- accumulated rain water; wind noise; engine cooling; efficient brakes (clean and cool); keeping windows and lights dirt free; etc.

Road vehicles are considered to be bluff bodies in terms of fluid mechanics, thus the flow around a road vehicle cannot be treated in the same way as the flow around an aircraft. But parallels do exist between the aerodynamics of road vehicles and aircraft in terms of the primary objectives :- low aerodynamic drag; directional stability: and good driving or flying characteristics. The flow past road vehicles is strongly governed by separation unlike that for an aircraft (fig.1.1.1), thus the flow field has to be treated as a whole rather than several more or less independent flow fields or flow modules. The drag of road vehicles is dominated by the pressure drag contribution, thus areas of flow separation are important. The major areas of flow separation on road vehicles are :-

i) Engine bonnet separation (cowl)

ii) Roof separation

iii) A-pillar separation

iv) C-pillar separation

v) Wheels and Wheel arches

vi) Features beneath vehicle

These separation regions may or may not interact with each other, but these areas play an important part in the formation of the vehicle wake.

As motor vehicle manufacturers have been forced to reduce design times due to increased competition and wind tunnels costs have escalated, other methods have been developed to study the flow field around road vehicles. Trends similar to those in the aerospace industry are being followed in the development of numerical techniques for vehicle flow field simulation. Several approaches have been adopted, but at present considerable effort is being devoted to numerical solution of the time-averaged Navier-Stokes equations. However, progress is hindered by the lack of reliable methods for predicting flow separation and the formation of the near wake region. Some of these difficulties can be attributed to the inadequacies of the model used for representing turbulence in the Navier-Stokes equations. But a better numerical model may be obtained if we can provide an improved physical model of the flow field.

One major effect not mentioned is that of the difference between the flow environment in a wind tunnel and that experienced by a car on the road. In a wind tunnel the flow is usually smooth and uniform, whereas in real life it is often gusty and the mean flow is sheared. In general the approaching flow is yawed relative to the direction of the vehicle. In addition, it is found that drag increases with yaw angle, due to the presence of additional vortices and the fact that some vortices will be strengthened and some vortices will be weakened depending upon the yaw angle. The vehicle handling is also dependent upon the yaw angle, and the stability of the vehicle is just as important criterion as that of low drag, especially since modern road vehicles have been found to be susceptible to cross winds (Hucho {1987}), due to the reduction in weight and the effects caused by low drag designs. The characteristic cause of vehicle instability is the concentration of negative pressure on the leeward side, at the front of the vehicle. This produces a yawing

moment causing an angular deviation (increase in yaw angle), this tends to increase the yawing moment. As the drag of a vehicle is reduced, its susceptibility to cross winds increases because areas of flow separation have been removed. Thus large negative pressures are generated on the leeward side, producing large yawing moments. The conflicting goals between drag optimization and reduction of side forces are overcome by optimizing for separation-free flow at the front of the vehicle for yaw angle smaller than 10 degrees, but permitting flow separation at larger angles, where side winds cause more concern. These large yaw angles occur only briefly, thus subsequent increases in drag at these large angles can be tolerated.

1.2 REVIEW OF RESEARCH

In recent years low interior noise has become an important criterion in the development of road vehicles. The main sources of interior noise come from the engine, the tyres, and aerodynamic effects. Initial studies were based on reducing engine and tyre noise and aerodynamic noise was considered to be relatively unimportant.

The above mentioned studies concluded that wind noise was mainly generated by air leakage, and aerodynamic shape is a minor factor (Thompson {1964}). The critical areas in order of importance are (fig.1.2.1) :-

i) Vent windows, doors and A-pillar sealing from roof rail to about 1 ft below the belt line,

ii) C-post area at belt line,

iii) Upper rear of front door area,

iv) All other areas from roof rail to 1 ft below the belt line.

The second type of wind noise was wind throb, this occurs when one window is left open and the passenger compartment acts as a Helmholtz resonator. Edge tones are caused by vortices which are shed periodically from the region of the A-pillar

impinging on the rear of the window opening. The peak amplitude occurs when the vortex shedding frequency matches the natural frequency of the Helmholtz resonator. As the natural Helmholtz frequency is fixed by the body shape and styling, wind throb can be reduced by modifying the shedding frequency of the vortices.

A detailed study conducted by Chanaud at el (1975) concluded that there were two primary sources of aerodynamic noise, the engine-cooling fan and the interaction of either the entire vehicle or some of its components with the air stream created by vehicle movement. The primary contributors to the vehicle-air interaction sound were assumed to be the turbulent boundary-layer pressure fluctuations and air buffeting at higher speeds (window open). The highest mean velocities were found to occur near the front of the hood and around the windscreen, thus higher pressure fluctuations will be generated due to local regions of flow separations generating noise.

Figure 1.2.2 shows the interior noise levels caused by different noise sources for a typical production car. We can conclude that engine noise is the main problem, except at the highest speeds. But with the advancements of modern noise-control measures for engine enclosures and low-noise tyres, interior noise caused by the air flow around road vehicles will become a problem even at speeds of 100 Km/h.

Consequently, several studies (5,16,17) were conducted based on wind tunnel tests to isolate the level and sources of interior noise related to external aerodynamics, The interior noise of fifteen different production cars was analyzed in a wind tunnel study (5). Figure 1.2.3 shows the range of noise levels at different frequencies at two speeds (110 Km/h and 180 Km/h). Interior wind noise levels were found to be independent of vehicle transmission loss, thus it was concluded that differences in the interior noise levels can be attributed to the external flow

around each road vehicle. The transmission loss was determined by measuring the noise level inside the car compared to the noise level at the same position in the wind tunnel without the car. The transmission losses (effective noise reduction achieved due to the insulating properties of the vehicle shell) were found for these test conditions to range from 23.5 dB to 26.5 dB. Figure 1.2.4 shows that there is no correlation between interior wind noise level and vehicle transmission loss. The interior noise level of each car was correlated to its measured drag coefficient (fig.1.2.5). It was concluded that a low drag coefficient does not necessarily mean a low interior noise level, but a reduction in drag produced a reduction in the interior noise level. Thus interior noise levels may be reduced by reducing the drag, but the noise level also depends upon other parameters.

There are differences in the way wind noise is generated and in the generated frequencies. A low frequency (10-50 Hz) wind throb occurs when side windows or sliding roofs are open and high frequency (above 1KHz) noise is generated due to inefficient door and window seals. One method of reducing wind noise is by limiting the frequency spectrum, with efforts being made to achieve so-called "uniform" noise. "Uniform" noise is achieved by producing as far as possible a speed independent noise frequency spectrum, so total noise rises continuously without generating discrete frequencies. This "uniform" noise spectrum is achieved by removing areas of flow separation from the vehicle design. The interior noise levels are a function not only of sound pressure levels, but also the conduction characteristics of the road vehicle. The second method is to eliminate the noise source by means of design optimization.

The air flow around a body can be divided into several categories :-

i) Attached flow

ii) Quasi-two-dimensional separation

iii) Reattached flow

iv) Three-dimensional vortex separation

These various types of flow are illustrated in fig.1.2.6.a and fig.1.2.6.b.

Figure 1.2.6.a shows flow separation occurring at A, owing to the sharp radius on the leading edge which attempts to generate a large adverse pressure gradient that the flow can not support. The flow reattaches near point B and remains attached up to the trailing edge, it then forms a thick wake downstream. A slow circulating flow adjacent to the body surface is produced between points A and B. A strong spiral vortex develops if the leading edge is yawed relative to the incident flow (type iv). Attached flow along the entire length of the body can be achieved by rounding the edges of the body, thus reducing the adverse pressure gradient.

Stapleford and Carr (1971) conducted an investigation which covered the relationship between the character of the noise and the nature of the air flow around the vehicle. Initially a simple rectangular model was used to generate several distinct types of flow, the noise induced at the surface was measured using flush mounted microphones. The locations of the microphones were based on surface flow patterns, the flow patterns were obtained for a square edged box at zero yaw angle and at 30 degrees yaw angle (fig.1.2.7). Several microphones were placed in each region of a specific type of flow obtained on the two angles tested. Similar measurements were also made on a scaled model of a typical saloon car to show the validity of the rectangular model results.

Figure 1.2.8 shows the peak sound pressure level values obtained in the 500-1500 Hz frequency band, and they show clearly the effect of each flow regime upon the surface pressure levels. Sound pressure levels in the vortex region are 15-20 dB higher than those in areas of attached flow, thus the areas containing 3-dimensional separations are the most noise intensive. Using the oil flow patterns (fig.1.2.7) and the noise spectra plots (fig.1.2.9), we can conclude that the critical frequency range is approximately 400-900 Hz for the vortex flow field. The frequency spectra were found to be independent of Reynolds number (fig.1.2.10) for the rectangular box tested. Comparing these plots with those obtained for the

saloon car model at zero yaw angle, we find that in the region of the A-pillar the pattern is similar to that for the vortical flow region on the rectangular model. The respective flow pattern on the car model indicates that the flow separates at the A-pillar and reattaches along an inclined line as sketched on the photograph (fig.1.2.11). A spiral vortex is present with its origin at the apex of the bonnet, windshield and side panel intersection.

The measured maximum sound pressure levels and the frequency range over which they were measured are given in table.1.2, these values should be viewed as a guide, and not anything more. Stapleford and Carr drew the following conclusions :-

i) High aerodynamic noise levels are a consequence of various forms of flow separation, in particular noise attributable to vortical flows is especially loud. Other regimes of flow separation become noise intensive at lower frequencies relative to attached flow noise levels.

ii) Aerodynamic shape is an important factor, which affects wind noise levels, thus minimizing flow separations (elimination of sharp edges and abrupt contour changes) will help to reduce wind noise levels.

Dobrzynski et al (18) conducted a study using 1/4 in. diameter condenser microphones installed at 42 select locations on a typical mid-range full scale road vehicle at wind speeds up to 53 m/s (190 Km/h). Interior noise levels and surface pressure levels were recorded simultaneously. A schematic representation of the fluctuating pressure intensity distribution on the car-body surface was obtained (fig.1.2.12). Thus from this we can conclude that the highest fluctuating pressure levels were found downstream of the A-pillar, where the flow separates generating vortices shed from the A-pillar. They travel along the side windows towards the roof where the flow area expands significantly. Pressure intensities are highest in the A-pillar vortex region and close to protruding door/window frames, where

localized flow separation occurs, but intensities past the A-pillar vortex reattachment-line are low. Typical surface pressure spectra on a side window are shown in figure 1.2.13. The reference pressure levels were obtained on the front bonnet and major portions of the roof, these levels correspond to levels obtained on the surface of a flat plate with an attached boundary layer. Comparisons between positions 1 and 2 (fig.1.2.13) indicate that pressure intensities in the vortical flow region are significantly higher than those produced by the localized flow separation behind the protruding door/window frame.

A second study was conducted (5) to compare the wind noise sources of a production vehicle (Cd=0.42) with those of an experimental vehicle of similar size and shape, but low drag (Cd=0.25). Fluctuating pressures were measured at five positions and comparisons made, the highest levels were again found in the A-pillar region. The experimental vehicle's results were surprisingly similar (fig.1.2.14) although there was no A-pillar vortex present on this vehicle. But the experimental vehicle's side windows are recessed by 5mm compared to the outer contour of the A-pillar producing a local separation region, which obviously has a similar effect to that produced by a vortex. The A-pillar region was modified by eliminating the window recess and decreasing the A-pillar curvature. These changes reduce the fluctuating pressure levels down to the level produced underneath an undisturbed boundary layer. But the above changes only marginally improved the drag coefficient of the research vehicle. Thus substantial noise reductions can be achieved by avoiding flow separations, even if these measures do not reduce the aerodynamic drag. The A-pillar vortex region is the most critical in terms of noise generation, thus flow separation of any form such as :- A-pillar vortices; and localized quasi two-dimensional flow separations should be avoided.

A prediction model was developed which relates the exterior flow properties (fluctuating surface pressure intensity and pressure field correlation dimensions) to interior sound pressures. The model replaces the turbulent surface pressure field

with a distribution of point forces. These forces excite bending waves in the car panels causing a radiation of acoustic energy. The equation (Cremer et al {1967}) shows that sound power is proportional to the mean square value of the fluctuating forces. This relationship, however is only valid for frequencies below the coincidence frequency Fa of the particular panel. Fa is typically below 3 KHz for car window panels and below 14 KHz for sheet metal panels. The total sound pressure intensity is obtained by the addition of all sound pressure components originating from the various vehicle body panels which contribute substantially to the overall noise level.

The location of the drivers left ear (left hand drive vehicle) is usually taken as a convenient noise reference location, for the fast-back vehicle used in this particular test. All window areas as well as the roof were found to be the prime contributors to aerodynamically induced interior noise (fig.1.2.15). Comparisons between predicted and measured interior noise spectra for two wind speeds indicate excellent agreement at higher wind speeds, but at lower speeds large deviations are observed. As the measured data was obtained in a wind tunnel the difference at lower speeds is likely to be a result of excessive tunnel background noise levels (fig.1.2.16).

Romberg et al (1977) assumed that the interior noise level of a given car is a function of three major factors :-

i) Road speed,

ii) Air speed,

iii) Car acoustic sealing effectiveness.

These tests were conducted on an oval track at the following speeds 45, 60, 70, 80 and 90 m.p.h. The microphone recording the interior noise levels was located in the proximity of the front passengers head. The analysis of the data is based on the method used by Harris (1957), this method allows the total car noise to be resolved into three components ; aerodynamic noise, residual noise (frequencies below 250

Hz i.e engine, exhaust, tyre noise and any rotating machinery), and aspirating noise (frequencies above 4200 Hz i.e noise due to air leaks). One method used to analyze the data was to identify the magnitude each component contributes to the total noise level as a function of vehicle road and/or air velocity (fig.1.2.17). These magnitudes are a function of vehicle type. Usually the total noise level is evaluated according to its sources as a function of frequency, as shown in figure 1.2.18. Spectral analysis provides the possibility of assessing the nature of the total noise at each frequency level. The accuracy of the method used and the data obtained on the road was verified using the Lockheed-Georgia 16'x 23' wind tunnel. As the wind tunnel results would be free from residual noise, correlation between the aerodynamic and aspirating noise components as a function of speed or frequency is possible. The data correlates well, with the exception of the first three octave band levels (fig.1.2.19), as these bands are dominated by residual noise (on the road). The aerodynamic portion of the road data is considered to be less accurate than the tunnel data. The data was found to be repeatable within about +/- 0.5 dB with the exception of the highest components (repeatable within +/- 2 dB).

Production requirements, water accumulation, drag and wind noise are all taken into account when designing the A-pillar. Several studies have been conducted, showing the effects of A-pillar design upon aerodynamic drag (6,7,8), but all these are based on different production models. Thus only general conclusions which are applicable to all production vehicles can be obtained from these results :-

i) Drag is reduced by rounding off the A-pillar,

ii) Flow around an A-pillar is improved if the side window is recessed as little as possible, windows flush with the A-pillar being the best solution. Such solutions have been used by Audi and V.W. for their latest production models.

Watanabe et al (1978) conducted a detailed study of the A-pillar region of a

specific road vehicle. From the aforementioned study it became clear that wind noise was influenced by flow separation. Thus fundamental tests were also conducted based on a simplified three-dimensional model and a 1/5 scale model of a road vehicle. The initial tests were conducted on a full scale model in a wind tunnel and on the road. Comparisons between these tests showed that the frequency characteristics were similar for the on-road and wind tunnel sound pressure results. The interior noise levels were measured at two microphone positions as shown in figure 1.2.20. The effect of body shape upon interior noise levels was studied by testing five body modifications to the original shape. This study was based on drag coefficient and wind noise results. The standard lateral curvature windshield was replaced with a flat windshield which produced the largest increase in interior noise level. The drag coefficient also increased but only marginally. The other modifications (to the B-pillar and the C-pillar) increased the interior noise level and the drag, but these increases were less significant. These results once more indicate that the A-pillar region has the largest influence on wind noise. Thus additional tests were conducted to study the influence of A-pillar shape upon wind noise. Four A-pillar cross-sections were tested (fig.1.2.21), and sound pressure levels were recorded at the 'first corner' (microphone 1). A-pillar shape 2 with a smooth transition from the windshield to the side window was found to be the best shape. The effect of rain gutter height was also studied, the noise level increased as the height was increased, but above a specific level the noise level decreased with increasing rain gutter height (fig.1.2.22). This effect is discussed later (see section 1.4). As stated earlier, a simplified model was made (fig.1.2.23) to investigate the flow separation behind the A-pillar based on flow visualization tests conducted in a wind tunnel. A comprehensive sketch was obtained from these tests (fig.1.2.24). It shows that two vortices are present, one recirculating in almost the whole region, and the other in a smaller scale just behind the A-pillar. These results were confirmed by mean pressure coefficient results and flow visualization obtained on

the full scale model (fig.1.2.25).

Bearman et al (1989) conducted tests on 1/3 scale models to study the effects of vortices upon the vehicle wake and the surface pressure distribution. As we are concerned with wind noise, only the surface pressure distribution results are discussed. The model was based on a Honda Accord and the effect of yaw angle on the surface pressure distribution was studied. Figure 1.2.26 shows the surface pressure distribution at zero yaw, low pressures with minimum Cp values between -1.4 and -1.5 were found behind the A-pillars and the C-pillars. As the model is yawed the lowest pressures were found near the leeward C-pillar and behind the leeward A-pillar, where the region of low pressure increased as the yaw angle was increased. But the effect caused by the vortex becomes less localized with increasing yaw angle. This may be caused by the vortex bursting or unsteady movements of the vortex core. As the yaw angle was increased to 20 degrees the A-pillar region extends along the A-pillar towards the roof. It appears that the A-pillar vortex also travels horizontally downstream along the leeward side of the car (figs.1.2.27 & 1.2.28).

1.3 COMPARISONS WITH SWEPT AND DELTA WINGS

The flow patterns obtained for the simplified road vehicle models around the A-pillar region are very similar to the flow around swept and delta wings at incidence.

Sutton (1982) made mainly qualitative observations of flows with boundary layer separation from blunt swept edges (fig.1.3.1), with the separation fixed at the leading edge. The flat sides of the plate he used were always aligned with the free-stream direction, and the angle of sweep of the edges was varied from 30 to 60 degrees. The experiment consisted mainly of surface oil flow observations, it was found that there was very little variation in the observed characteristics of the flow in the speed range tested (25-50 m/s).

In a region adjacent to the floor of the tunnel, the flow was similar to that found near the leading edges of thin delta wings at incidence. Further away the separation is less vigorous, with the oil flow pattern showing a narrow reattachment region rather than a reattachment line. This suggests that the flow changes to a swept two-dimensional type with a length scale determined by the plate cross-section dimensions (fig.1.3.2). Sutton also found that the Quasi-two-dimensional flow was extremely sensitive to small disturbances.

Poll (1980) conducted an experimental investigation to study the formation and development of spiral vortex flows over Swept back wings. The principal method was surface oil flow visualization supplemented by surface pressure measurements. Spiral vortex flows were not observed for sweep angles less than 15 degrees, at higher sweep angles the flow visualization indicated that there are three different mechanisms for the formation of spiral vortices. The mechanism and the critical incidence angle for the onset of vortex flow were found to depend upon the leading edge radius, sweep angle and Reynolds Number. The dependence upon Reynolds number increased with increasing leading edge radius, but comparisons with other work {Black (1958) and Dickmann (1976)} suggests that other factors, apart from those stated above, are important in determining the type of vortical flow occurring on a given wing. Poll also found that the flow in the wing root apex region is similar to that obtained on thin delta wings at incidence, the combination of sweep and incidence to produce this type of conical flow are presented. The 'critical' value for the stream wise incidence for the formation of conical type flows decreases with increasing sweep angle and is also strongly dependent upon leading edge radius. The sharp leading edge model exhibits spiral vortex flow at the lowest incidence (less than 4 degrees) for all sweep angles. Results obtained for the sharp leading edge model are similar to those obtained by Sutton and Watanabe et al in the A-pillar region of the simplified model (fig.1.2.24). The combination of sweep

angle and incidence necessary for the formation of conical type of spiral vortex flows is shown in figure.1.3.3. Comparing this with a similar plot (fig.1.3.4) for a wing with a larger leading radius indicates that Reynolds number dependency increases with increasing leading radius. This dependency for large leading edge radii wings can be seen clearly in figures. 1.3.5 & 1.3.6. This investigation revealed that for sweep angles in excess of 15 degrees there are at least three different ways in which a spiral vortex is generated over a swept-back wing :-

i) A full span vortex formed by the flow separating at the primary separation line, this type of vortex flow is similar to that generated on thin delta wings at incidence.

ii) A part-span vortex formed when the primary separation reattaches to form a bubble near the root of the wing, but fails to reattach on the outboard sections. The portion which does not reattach rolls up to form a vortex.

iii) A part-span vortex can be formed when the boundary layer leaves the surface along a line of secondary separation downstream of a short separation bubble. The secondary separation line forms first in the vicinity of the tip, the resulting free shear layer rolls up to form the vortex.

Elle (1958) conducted a series of flow visualization tests on delta wings at low speeds. These tests were used to determine the location of the vortex centre line as a function of the apex angle and wing incidence. Elle found that variations in the position of the vortex centre line was negligible as the incidence was varied, Lee (1953) found that vortex centre line position was independent of Reynolds number. But the secondary separation line moved outwards considerably with increasing Reynolds number (0.5×10^6 to 5.0×10^6). Thus it was concluded that the movement of the secondary separation line is dependent upon the thickness of the boundary layer, but independent of the position of the vortex centre line. These observations were confirmed by Elle. The position of the vortex centre line is found to be a function of the sweep angle, as the incidence of the delta wing is increased the

spiral vortex breaks down. The angle at which breakdown occurs is dependent upon the sweep angle. This breakdown first occurs far downstream of the wing and moves rapidly towards the wing apex with increasing incidence, with breakdown angle increasing as sweep angle increases. Thus the wing sweep angle is the dominating parameter and the other flow features are less significant. This was demonstrated by using a series of yawed delta wings. The breakdown position was almost identical for edges of equal sweep, whether this was with an unyawed or a yawed wing of a smaller apex angle.

Zohar et al (1987) also studied the phenomenon of vortex breakdown (VB), but this study was based on surface pressure measurements of four wings having aspect ratios 1.07-2.80 (55-75 degrees sweep angle). Direct comparisons between the 60 degree swept wing and the 75 degree wing at incidence ($a=20^{o}$) indicates that suction peaks are induced by the vortices on both wings and these peaks are largest near the apex and decrease in the downstream direction. These figures also indicate that the highly swept wing (75 degrees) has a larger non-dimensional vortex suction region (fraction of the wing area), but the 60 degrees wing has a higher negative pressure coefficient on its upper surface. These suction peaks continue to increase with incidence as long as they are not affected by vortex breakdown. But the effects of vortex breakdown on each wing are different, for the 60 degree delta wing the minimum Cp value continues to increase with incidence regardless of VB position as long as it has not reached the apex ($a<32$ degrees). Above this incidence the suction peak disappears indicating the loss of the vortex system. For the 75 degree delta wing the suction peak increases with incidence until VB reaches the trailing edge ($a=35$ degrees). After this point, vortex breakdown travels along the wing towards the apex with increasing incidence and the peak suction continues to decrease with a complete loss in the suction peak when VB reaches the apex in a similar manner to the other wing. The classical view of the flow over a delta wing at

incidence is that the flow is dominated by two large attached vortices generated by the flow separation at the leading edges. The flow separates along the entire leading edge forming a strong shear layer and this wraps up in a spiral fashion resulting in a vortex. Gad-el-Hak et al (1985) studied this generation process, the flow was visualized by injecting dye from slots in the leading edge. A cross-sectional view of the flowfield observed is shown in figure.1.3.7. This shows that the geometry of the shear layer is more complex than expected. The flow rolls up into regions of concentrated vortices (discrete) separated by a thin braid of dye. These discrete vortices seem to be parallel to the leading edge and the trajectory of these vortices follow the general outline of the main large vortex. As they follow this course, two vortices begin to roll around each other and merge forming a single larger vortex. This experiment did not indicate whether the primary vortex is formed as a result of repeated merging of the secondary vortices or that the secondary vortices set up the initial shear layer which results in the formation of the primary vortex. The shedding rate for the secondary vortices was found to be independent of the wing sweep angle and leading edge shape, but dependent upon the Reyonlds number.

1.4 COMPARISONS WITH FLAT ROOF ,LOW-RISE BUILDINGS

Several studies have been conducted to study the worst suctions near edges on flat roof, low rise buildings. But inconsistencies have been noted between the suction data published by different authors. The effects of parapet height upon these high suction regions was also studied, the highest values are found where there are oblique wind directions (α=40-50 degrees). Initial studies conducted by Slathopoulos et al (1980) reported worst mean and peak suction pressure coefficients of -1 and -5 respectively, but Kind et al (1986) reported much higher mean and peak suction values of approximately -3 and -7 respectively. They also reported that worst suctions decreased with increasing parapet height, while other investigators (Kramer et al (1979) and Lythe et al (1983)) found worst suctions at

specific parapet heights. Kind et al repeated their experiments on much larger models and found their results to be consistent with those previously obtained, thus they concluded that there were two possible hypotheses to explain the inconsistencies in the suction results :-

i) Large scale-effects caused by the distorted scaling of the atmospheric boundary layer thickness to building height ratio.

ii) A lack or scarcity of pressure taps sufficiently close to the roof edge to sense the true suction peaks.

As Kind et al obtained reasonably good agreement between the data obtained using different scale models we can conclude that the evidence supports the second hypothesis.

This hypothesis also accounts for the inconsistencies in the results of the variation in suction values due to variations in parapet height. Initially without a parapet the vortex flow is very close to the edge of the model in a very narrow region (fig.1.4.1). As the parapet height is increased the vortex strength decreases and the region widens and at the same time it moves inwards from the roof edges. The inconsistencies are due to the scarcity of pressure tappings near the roof edge and can be explained by the movement of the vortex away from the roof edges. Initially the pressure at the edge of the vortex is recorded, as the parapet height is increased the vortex core moves over the tappings resulting in a peak pressure. With a further increase in parapet height the vortex core moves away from the pressure tappings resulting in a lower suction value. This type of movement was also observed on the road vehicle model tested by Watanabe et al (1978), where he reports a relationship between rain gutter height and side window recess (similar to a parapet). The effect is similar as again there are a limited number of pressure tappings and as the rain gutter height is increased the vortex core migrates away from the A-pillar edge.

1.5 PURPOSE.OF.STUDY

Lay (1933) found that as windshields angles became flatter the aerodynamic drag decreased. Thus in recent years with drag reduction being an important factor, windshield inclination angles have increased dramatically.

Scribor-Rylski (1984) investigated the flow over the bonnet and windshield regions of a road vehicle model. The windshield used was a flat windshield and not a lateral curvature windshield of the type used on production vehicles. The results show that the flow remains attached across the front edge of the hood with separation occurring at the cowl (hood-windshield intersection). The flow must reattach somewhere on the windshield, and as the windshield becomes steeper, separation moves towards the hood and the reattachment R moves towards the rear (fig.1.5.1). Production vehicles have lateral curvature windshields, thus the separation bubbles are smaller than those for a flat windshield. The location and shape of the three-dimensional separation bubble is highly dependent upon the lateral curvature of the windshield. Several authors (6,7,8) have confirmed Lay's (1933) investigation that the aerodynamic drag decreases as the windshield inclination angle is increased, but windshield angles of more than 60 degrees are not practical because of light diffusion (internal reflection) and a rapid increase in temperature of the passenger compartment due to solar heating. The reduction in drag due to highly inclined windshields is only moderate, but the excessive speeds around the A-pillar are reduced, resulting in a lower momentum loss. A lower pressure peak occurs in the transition region between the windshield and the roof, reducing the momentum loss in the boundary layer, thus allowing a greater pressure recovery and a lower drag.

The aim of this project is to study the effects of the windshield angle on the A-pillar vortex for a simplified model (section 2.7.1). The study is based on static and dynamic pressure measurements in the A-pillar region, later flow visualization

techniques will be used to supplement the pressure data. The windshield angle is varied from 0 to 60 degrees. The model is made up of two sections, the top section representing the windshield and the A-pillar region, is similar to Watanabe's model (fig.1.2.23). The other section (base) represents the main body of a road vehicle and this type of model is considered to be a better representation of a road vehicle than that used by Watanabe et al. A second model was also used (swept plate) as a comparative study and a detailed description is given in section 2.7.

2.EQUIPMENT AND PROCEDURE

2.1.1 WIND TUNNEL

The tests were conducted in the 3'x3' wind tunnel in the department of Aeronautics at Imperial College. This wind tunnel is a low speed closed-return type tunnel; details of the tunnel can be found in the work of Clements and Unwin (1973). This wind tunnel was chosen because of its low turbulence level (less than 0.04%). The quality of the air stream is dependent upon the contraction ratio (K), the nozzle contour, and the screens, the fan power required is also dependent upon these three factors. A lower turbulence level and an increase in the uniformity of the air flow will be obtained across the wind tunnel working section (cross section) by using a larger value of K, provided a suitable nozzle contour is used. Bradshaw and Pankhurst (1964) recommended that K should be between 10 and 12 for low turbulence wind tunnels. The contraction ratio of this wind tunnel is 9.

2.1.2 GROUND SIMULATION

Simulation of the ground is a major problem in road vehicle simulation, early tests were conducted with the model in the middle of the wind tunnel. This method was found to be inadequate and several ground simulation methods were developed, these include :-

i) A mirror image model

ii) Using the wind tunnel floor

iii) Testing on a separate ground plane.

iv) Using a moving ground plane

Heald (1934) conducted comparative tests of ground simulation techniques, he found that the mirror image and the ground plane techniques give similar results if the boundary layer on the ground plane was kept thin by carefully shaping the leading edge of the ground board. Hucho et al (1975) have shown that the velocity

profile underneath the vehicle is only influenced by the ground plane boundary layer in the immediate vicinity of the model. Assuming the ground plane to be a smooth flat plate, we can calculate the maximum ratio of displacement thickness to underbody height for the boundary layer. A one-seventh power-law profile gives a value of 0.125, but the work of Dobereny (1976), Mason (1973) and Hucho (1975) suggests that a thickness ratio of less than 0.1 is desirable.

The most commonly used ground simulation methods at present are :-

i) The best solution at first sight seems to be a moving ground plane. The upstream boundary layer is removed by suction upstream of the moving ground belt. This generates the correct boundary condition on the moving floor, i.e the velocity at the floor is equal to the free stream velocity. The main disadvantages are that model mounting becomes difficult and the installation of the moving floor is expensive and complicated.

ii) Mounting on the existing fixed floor, but this often requires the reduction of the floor boundary layer thickness. The boundary layer can be removed either by suction through a slot upstream of the model or a forward facing slot. A major disadvantage is the cost of the suction system and its installation.

iii) A ground board is commonly used for scale model testing, Cooper (1984) states that the ground board should start no less than two body widths upstream of the vehicle model and extend no less than four to six body widths downstream. The disadvantages are that:- the wind tunnel cross-section area is reduced, finite downstream extent of the ground board results in a dual flow path which may produce flow uncertainties; its advantages are that its easy to manufacture and install and a thin boundary layer is produced.

All these methods have their advantages and disadvantages (Hucho {1987}), but it is expected that the effects of the type of ground simulation used will be negligible in the A-pillar region. Thus the basic method of using a fixed ground board is used in this research. The main reason for using the fixed ground

board was that its easy to manufacture and install.

2.1.3 WIND TUNNEL CALIBRATION

All wind tunnels are calibrated after their construction and the main reason for calibrating the wind tunnel is that the pitot-static measurements are not usually made in the tunnel working section. The static pressure reading is taken at the entrance to the tunnel working section and the pitot reading is made in the settling chamber, where the air velocity is very small (~1/9xU). The static reading in the working section will be different to that recorded at the entrance, partly due to the growth of the boundary layer along the wind tunnel walls and flow acceleration due to curvature at the end of the nozzle contraction. A pressure gradient is often present along the working section length. Clements and Unwin (1973) reported these observations and obtained the calibration factors and turbulence levels for the 3'x3' wind tunnel. In order to simulate road conditions, a ground board was installed in the wind tunnel, thus the wind tunnel flow properties are modified and the tunnel had to be recalibrated with the ground board installed.

The calibration factors are calculated using a pitot-static tube placed in the same position as the model and recording the pressure at this position and the reference position over the wind tunnel speed range. Consider a general sketch of the wind tunnel working section and contraction nozzle (fig.2.1.3.1).

Calculating the pressure coefficient we get :-

$$C_p = \frac{2(P_m - P_s)}{\rho U_\infty^2} \qquad 2.1$$

$$C_p = \left[\frac{P_m - P_{s1}}{P_{t1} - P_{s1}} + \frac{P_{s1} - P_s}{P_{t1} - P_{s1}} \right] * \frac{2(P_{t1} - P_{s1})}{\rho U_\infty^2} \qquad 2.2$$

Let $\quad K_1 = \frac{P_{s1} - P_s}{P_{t1} - P_{s1}} \qquad K_2 = \frac{2(P_{t1} - P_{s1})}{\rho U_\infty^2}$

$$C_p = \left[\frac{P_m - P_{s1}}{P_{t1} - P_{s1}} + K_1 \right] * K_2 \qquad 2.3$$

This analysis is identical that used by Obasaju (1982), it was found that K1 had a range of values (fig.2.1.3.2) about a mean value of 0.015 (see section 2.7). The variation of K2 with wind tunnel speed is obtained by calibrating the wind tunnel with the ground board installed (fig.2.1.3.3).

2.2. INSTRUMENTATION

2.2.1 STATIC PRESSURE

A 1/2" Setra pressure transducer was used to measure the mean pressures and pressure coefficients were calculated. The range of this transducer is +/- 0.1 psi, but the pressures obtained were found to be as low as -0.7 psi. Thus the transducer had to be calibrated over a range which exceeded its nominal range, but the transducer was found to be linear over this large range of values (fig.2.2.1.1). This Setra transducer was found to be almost drift free.

The transducer was too large to be flush mounted to the model surface. As a result a cap manufactured in the department which terminates with a short tube was used. The diagrams of the transducer and cap are reproduced from Obasaju's thesis (1982) (fig.2.2.1.2). An 'O' ring is used to obtain a seal such that pressure can only be applied to the diaphragm either through the cap or the equalization tube at the rear of the transducer.

2.2.2 FLUCTUATING PRESSURE

A Druck PD42 pressure transducer was used for collecting the fluctuating pressure data (range +/- 1.09 psi, calibration curve shown in figure 2.2.2.1). The main reason for using this transducer rather than the Setra transducer is because the

Druck transducer is much smaller, so it can be mounted very close to the model surface. A new cap was designed to fit the Druck transducer diaphragm, its design is very similar to that used for the Setra transducer (fig.2.2.2.2). A cap is required because the transducer is again not small enough to be flush mounted. The natural frequency of this transducer is 5 KHz, but this frequency is reduced as a result of the cap and tubing system used with this transducer. Several methods have been developed to calculate the response characteristics of these systems :-

i) Doebelin (1966) treats the cap/tubing system as a second order mechanical system. The equations developed using this method for the cap/tubing system were used to obtain an estimate for the length of tubing required for a given frequency range. He represents the damping and equivalent natural frequency parameters of the cap/tubing system as :-

$$\omega_n = \frac{C_s}{(L_1+L_2)\sqrt{\frac{1}{2}+\frac{V_1}{(V_2+V_3)}}} \qquad 2.4$$

$$\zeta = \frac{64\mu(L_1+L_2)}{\pi d_t^4 C_s}\sqrt{\frac{1}{2}+\frac{V_1}{(V_2+V_3)}} \qquad 2.5$$

The above equations only hold if the tubing volume is approximately the same order of magnitude as the cap volume (p.401).

Damping can be reduced by increasing dt, but to increase the resonant frequency above the maximum frequency of interest we have to reduce the tubing length.

ii) Gumley (1983) devised a step by step design method based on analysis, numerical studies, experimental work and existing literature.

iii) Irwin et al (1979) devised a new method for reducing and correcting the distortion effects based on a digital correction technique using the known tubing/cap

transfer function. This technique allows considerably longer tubes and higher frequency responses to be obtained. A simpler technique of inserting restrictions in the tubing system is also evaluated in this paper.

The method used in the present experiments to obtain the optimum cap/tubing system is partly based on the method recommended by Gumley. The effects of the cap/tubing system were estimated by measuring the output relative to an identical flush mounted transducer. The experimental setup used to compare the dynamic response of each system with varying tube length is shown in figure 2.2.2.3. The variation in frequency response with tubing length is obtained using the following procedure :-

i) A tubing length is chosen and attached to the cap.

ii) The frequency response of the cap/tubing transducer and the flush mounted transducer is estimated by varying the loudspeaker output frequency using a signal generator.

iii) Steps i and ii are repeated for different tube lengths

T_{r2}/T_{r1} is the ratio of cap/tubing transducer output to that of the flush mounted transducer output. Several dynamic response curves were obtained, a typical curve is shown in figure 2.2.2.4. These curves were used to obtain an overall graph of resonant frequency versus tubing length and more importantly the frequency at which the system starts to amplify the pressure signal for each tube length. A significant difference was found between the values predicted by Doebelin's model and those obtained experimentally for the system resonant frequency (fig.2.2.2.5) for tube lengths below 30mm. This is assumed to be due to errors in the assumptions used in developing the mechanical system theory.

2.2.3 OTHER ELECTRONIC EQUIPMENT

2.2.3.1 PC/AT COMPUTER

The mean and fluctuating data was collected using an A/D conversion board. The data was then transferred to the computer and stored on its hard disc. The A/D board is controlled by the computer and the data is then backed up on floppy discs. The computer was also used for post processing the data, and to produce the final contour plots.

2.2.3.2 LABMASTER TECMAR CARD

A Tecmar card is a programmable A/D conversion kit. It is made up of 2 main sections :-

i) The Mother board, which can be plugged into an available slot in the P.C. or Expansion Chassis. This board contains all the A/D control circuitry, the timer, the D/A converters and the interrupt control.

ii) The Daughter board, this board performs the actual A/D conversion. This board also contains the jumpers, which are used to control the user selectable options for each module. This board can be used to collect signals from a single channel or multiple channels (8 differential or 16 single ended). The board can also be used to sample sequentially using up to eight channels. The maximum sampling rate is 30KHz for a single channel, but 27.5 KHz for multi channel sampling. But this speed is significantly reduced if the A/D card is programmed in Fortran or Basic.

The conversion kit has a 12 bit resolution, but it contains an 8 bit data bus and the P.C. is a 16 bit machine. This problem is overcome by reading the data in two parts, first the lower 8 bits are read and then the higher 8 bits. The highest 4 bits are ignored when the data is stored on the hard disc.

2.2.3.3 POWER SUPPLY

The power supply used to drive the pressure transducers is a compact Constant LM 50/30 power pack.

2.2.3.4 AMPLIFIER

The amplifiers used are all made by the electrical section, in the Department of Aeronautics, Imperial College. Their maximum gain is 500, but the gain has to be reduced for high voltages as they saturate at approximately 10V.

2.2.3.5 OSCILLOSCOPE

A Tektronix oscilloscope was used in the experimental set-up to check the signals generated by the transducers. The scope was used as a check on all the equipment to make sure it was all working correctly (amplifier, filter, transducer, etc). As the A/D card has a +/- 10 v limit, the scope was used to keep the transducer signal below this critical value.

2.2.3.6 PLOTTER

The contour plots and the spectra plots were obtained using a Hewlett-Packard HP7470A plotter. The plotter can be programmed using HP-GL (Hewlett-Packard Graphics Language), but as all the programs were written in Fortran a subroutine developed by Mackwood was used. This subroutine converts the Fortran commands into HP-GL basic commands.

2.2.3.7 FILTER

A Kemo V8F8 filter was used as a low frequency pass filter with a cut-off frequency of 1000 Hz. This filter was used because it has a very low background noise level over its operating range (0.01-100KHz).

2.3 FLOW VISUALIZATION

Visualization of the flow field is a useful tool as it clarifies the physical values such as pressures, air speeds and aerodynamic forces to verify the feasibility of our solutions. Flow visualization produces a qualitative analysis which enables us to visualize the flow field which is inherently invisible and it is very effective in detecting areas of flow separation. The most widely used method is the smoke generator, where the smoke is usually generated by heating a mineral oil derivative (Shell Ondina G17) which is then injected into the air flow using a long thin stem. Smoke is also used to study wake zones and separation bubbles, illustrating their form and size by injecting the smoke directly into the bubble or wake. Surface oil film and wool tufts are the other methods that are used for flow visualization in road vehicle flows, each of these methods has its advantages and disadvantages.

When wool tufts are used, the costs are low. The problems are that it takes a long time to attach the tufts, and the movement of the tufts does not necessarily correspond to the flow direction under all conditions.

The other method is to use surface oil film, where the model is coated with oil mixed with a pigment. This mixture can be applied to any model at all subsonic speeds, the ratio of oil to pigment depends upon several factors such as wind tunnel speed, model shape, skin friction and viscosity of the material used for the oil flow mixture. The main disadvantages of this method are :-

i) It usually takes a long time to obtain the correct mixture for each model used and each Reynolds number.

ii) It is very messy; models and the wind tunnel need a through clean out afterwards.

Initial tests were conducted using the oil film method to obtain the best ratio of oil to pigment for each Reynolds number. But it was found that a large pigment content was required, producing errors due to gravity because the mixture was applied to a vertical surface. Initial tests were conducted with the model mounted on

the side wall of the tunnel. Gravitational effects were removed by attaching the model to the floor of the tunnel. Another method which is less widely used, but is very similar to the oil film method, is based on a simple mixture of white spirit and French chalk. The main advantages of this method are that only two variables are involved and the final results are clearer then those produced using the oil film method. A second series of tests were conducted using this method and it was found that the time required for each visualization was significantly shorter, results were more "accurate" and details of the flow field were clearer. Thus this mixture of French chalk and white spirit was used for all further surface flow visualizations.

A second series of flow visualization experiments were conducted in a water tunnel. A closed return water tunnel was used for these experiments. Water is a very convenient medium to use, as moderate Reynolds numbers can be achieved at very low speeds because of its low kinematic viscosity. Furthermore, a wide range of dyes and markers are available, some of which are neutrally buoyant.

There are several disadvantages :-

i) Usually a new model is made specifically for testing in water, thus costs increase.

ii) The settling times can be long, especially if the speed is changed.

A road vehicle model was tested in the water tunnel with the windscreen angle set at 40 and 60 degrees. The effect of splitting the flow at the base of the A-pillar of the vehicle model using a plate was also photographed. These water visualization experiments were conducted at a Reynolds number of approximately 10^3 (based on 2x model width).

2.4 DATA REDUCTION

2.4.1 BLOCKAGE CORRECTION

A critical factor affecting the design of a scale model is the size of the wind tunnel working section (cross-sectional area). The ratio of the frontal area of the model to that of the working section of the wind tunnel is called the Blockage ratio. This ratio should be kept as small as possible. For economic reasons attempts are made to construct wind tunnels as small as possible, but the presence of the tunnel walls changes the flow field around models because :-

i) The growth of the boundary layer along the walls of the working section produce a pressure gradient along the wind tunnel working section. This can be accounted for by diverging the walls of the working section.

ii) The streamline curvature is altered by the walls and the effects produced by this change in the flow field are not well understood.

iii) The air velocity in the vicinity of the model will be increased compared to the calibrated value, obtained with the wind tunnel empty.

The velocity will increase in the vicinity of the model and its wake, then reducing asymptotically downstream. The increase due to the wake is termed 'Wake Blockage' and that due to the model 'Solid Blockage'. The two main methods used to overcome these problems are either to use an Open section wind tunnel or to modify the working section of a closed-return wind tunnel by streamlining the walls, or using slotted walls (Hucho{1987}). If these options are not available then a correction method can be used to obtain the required data. Several correction methods have been developed, but if the model is yawed at large angles then the flow may separate from the working section walls and it is no longer possible to make a sensible correction.

Carr and Stapleford (1982) conducted a series of tests to compare several blockage correction methods and several wind tunnels. The correction methods they compared were :- the area ratio method based on continuity, the Hackett and

Wilsden (1979) pressure-signature method and the method developed by Mercker (1985). They concluded that allowing for the limitations of the experimental data, for blockage ratio's in the range 3.5 to 10%, the area ratio method provides the best overall correction of the three methods tested.

Applying the continuity equation for incompressible flow (assuming 1-D flow).

$$\frac{U_1}{U_0} = \frac{A_0}{A_1} \qquad 2.6$$

$$\frac{U_c}{U_m} = \frac{U_1}{U_0} = \frac{A_0}{A_1} = \frac{1}{(C/(C-S))} \qquad 2.7$$

Considering the dynamic pressures :-

$$\frac{Q_m}{Q_c} = \left\{ \frac{U_c}{U_m} \right\}^2 = \frac{1}{(1-(S/C))^2} \qquad 2.8$$

$$\frac{Q_m}{Q_c} = \left\{ 1 + \frac{2S}{C} \right\} \qquad 2.9$$

Thus if the blockage ratio of the model used is 5% :-

$$Qc = 0.909\ Qm \qquad 2.10$$

Blockage also effects the mean static pressure distribution, we can correct for this blockage effect using the formula {Maskell(1965)} :-

$$\frac{Q_c}{Q_m} = \left\{ \frac{1-C_{Pc}}{1-C_{Pm}} \right\} \qquad 2.11$$

$$C_{Pc} = 1 - \frac{Q_c}{Q_m}(1 - C_{Pm}) \qquad 2.12$$

2.4.2 MEAN PRESSURE

The mean pressures were obtained using the 1/2" Setra pressure transducer, this transducer was found to be very stable after a short warm up period. The reference port of the transducer was connected to the wind tunnel static pressure tapping, which is at the entrance to the tunnel working section. The differential pressure between the model surface and the tunnel static pressure is converted to a voltage by the transducer; this data is then collected by the Tecmar card and the average value for a 25 second sample (approx.25,000 data points) is calculated and stored on the computer hard disc. The tunnel pitot-static value is recorded four times during each tunnel run and the average value is used to obtain the pressure coefficient at each position on a model.

$$C_p = \frac{P_m - P_s}{P_t - P_s} \qquad 2.13$$

The pressure coefficient has to be corrected using the wind tunnel calibration and the blockage correction to obtain the correct pressure coefficient.

2.4.3 FLUCTUATING PRESSURE

The fluctuating pressures were obtained using the Druck PDCR42 pressure transducer; the main reasons for using this transducer were, that it is very small so by fitting a cap to the transducer it can be used in small enclosed spaces like those encountered near the apex of the top model (the corner of the side window, windshield, and bonnet), the second reason is that the operating range of this transducer is higher than that of the Setra transducer.

The cut-off frequency on the filter was set at 1KHz, the sampling frequency was set at 3.5KHz for the Tecmar card and the number of samples per pressure tapping was 35000. This number of data points were required to obtain accurate pressure spectra plots (see section 2.4.4). The filter cut-off frequency was set at 1.0KHz as a result of the work conducted by Carr et al (see section 2.2.2). Based on a tubing length of approximately 22mm, signal amplification can be avoided if the cut-off frequency is set at 1.0KHz (fig.2.2.2.5). Initial tests were conducted with the reference port of the transducer connected to the wind tunnel static pressure, but this set up resulted in errors in the pressure spectra plots as a result of small fluctuations in the tunnel static pressure. During the main fluctuating pressure experiments the reference port of the transducer was left open to atmospheric pressure. The transducer was used to record the differential pressure (difference between the tapping and atmospheric) for each tapping point. The data is initially stored on the Tecmar card and once all the data has been collected for each tapping it is transferred to the hard disc and then backed up on to floppy discs. This data is used to obtain the pressure spectra plots and the root mean square pressure coefficient defined as :-

$$C_{Prms} = \frac{2}{\rho U_{\infty}^2} \sqrt{\overline{(P_m - P_s)^2}} \qquad 2.14$$

2.4.4 PRESSURE SPECTRA

Spectra were generated for certain tappings using the fluctuating pressure data. The spectra are obtained using computer software based on the Fast Fourier Transform method (FFT). The various parameters involved in the computation of Power Spectra were obtained by following the criteria stated by Bendat et al (1971). If we assume a normalised standard error (ε_r) of approximately 0.1, we can calculate the required record length time and number of samples (N) provided we specify a desired resolution bandwith (B_e) for the resulting power spectra.

As the FFT routine is based on the Cooley-Tukey procedure, the number of samples has to be a power of two, namely,

$$N = 2^P \qquad 2.15$$

Thus assuming a maximum value of 5Hz for B_e, we can calculate the number of data points required from the FFT routine. As the Nyquist frequency (f_c) is 1.75KHz, the maximum number of data points (N) required is 350. But as this value has to be a power of 2, it is increased to 512. Thus the number of data points required per FFT is 2N (where N=512).

The relevant equations are :-

$$h = \frac{1}{2f_c}, \qquad m = \frac{1}{B_e h} \qquad 2.16$$

$$N = \frac{m}{\varepsilon_r^2}, \qquad T_r = Nh \qquad 2.17$$

Where h is the sampling interval and T_r is the record length.

Using the equations shown above we can calculate the sample size. This gives a value of approximately 50k, but this was considered to be accessive and reducing it to 2^{15} resulted in the value of ε_r increasing to 0.125 which was

considered to be acceptable.

As 2^{10} samples were used per FFT and 2^{15} samples were available, 32 spectra were generated for each data file and an average power spectra was produced. The program used was a modified version of a program written by Mackwood at Imperial College.

2.5. MEAN STATIC PRESSURE SET-UP

The apparatus was set-up as shown in figure 2.5.1. The models contain at least fifty fine brass pressure tappings (1mm diameter), this requires the use of two scanivalves and a scanivalve controller. The first connection on each scanivalve is attached to the wind tunnel pitot pressure, thus at the beginning and the end of each scanivalve head run the pitot-static pressure is recorded. A software package was developed (appendix 1) to control the data acquisition, using the Tecmar A/D card, and to store the data on the hard disc. An amplifier was used to improve the accuracy of the results by increasing the signal size to nearly fill the range of the A/D unit. A voltmeter, accurate to three decimal places, showed that the pressure transducer drift was almost negligible. A voltage off-set was used if required to zero the transducer output at the beginning of each run. The scanivalve controller was operated manually to switch to the next pressure tapping. As all the pressures on the side of the model were lower than ambient static pressure (-ve Cp) the pressure transducer was connected the "wrong" way around. The pressure tappings were connected to the reference tube via the scanivalve and the tunnel static pressure was connected to the front diaphragm via the cap/tubing system. The maximum overload for the Setra transducer is thirty times full range in the positive direction and only five times in the negative direction, thus if the transducer had been used in the "correct" format it would have overloaded because of the very low pressures recorded (-0.7 psi). The transducer calibration was still found to be linear down to these low pressures. The data is initially stored as a voltage and its then converted

directly to pressure coefficients using another software package (appendix 2).

2.6 FLUCTUATING PRESSURE SET-UP

This set-up is shown in figure 2.6.1, it is different from the mean pressure set-up in that a scanivalve is not used. Instead the pressure transducer (Druck PDCR42) is connected directly to the larger pressure tappings (2mm dia.). This set-up incorporates an oscilloscope and a filter, the oscilloscope is used to study the trace of the transducer output. The noise ratio (i.e. ratio of background noise to signal strength levels) was found to be below 5% for all fluctuating pressures recorded. As the maximum output of the Druck transducer is only +/- 15mv for a range of +/- 0.75psi, the signal has to be amplified to improve the accuracy of the A/D conversion as its range is +/- 10v for a 12-bit integer. Thus using two amplifiers, the transducer output (A/C) was amplified using a gain of 5,000. The quality of the signal was improved by using separate inputs (to the first filter and amplifier) for the negative and positive output lines from the transducer. Thus the amplifier removes the common background noise from the transducer output before the signal is passed to the second amplifier and then the filter. The filter generated a small amount of noise, but the level was very small compared to the amplified noise level produced by the amplifiers, the transducer and other electrical equipment. Another software package (appendix 1) was developed to control the data collection and storage on the hard disc. The background noise levels were found to be very sensitive to the precise set-up used and the type of equipment used. The transducer power supply, the amplifier and filter all affected significantly the background noise levels, noise ratio's as high as 50% could be obtained depending upon the set-up used. The effect of the wind tunnel motor was found to be minimal when a steady speed had been reached, but its effects became noticeable when the tunnel fan was accelerating. Several software packages (appendices 2,3) have been developed for data reduction, contour plotting of mean Cp, r.m.s Cp and pressure

power spectra.

2.7 MODEL DETAILS

2.7.1 ROAD VEHICLE MODEL

The aim of this project was to study the A-pillar vortex for a simplified model (Pl.2.7.1.1,2). The windshield on the model is flat and does not have lateral curvature as often used on production vehicles. Also the A-pillar in not inclined inwards to approximately 15 degrees to the vertical plane as on most production vehicles. The reason for using a flat windshield was to reduce the number of variables (reduced to two for these experiments), one variable being the Reynolds number (tunnel speed) and the other being the windshield inclination angle. This angle was varied from 0 degrees relative to the vertical to 60 degrees inclination. The method used to obtain a large A-pillar region was to build a half model and to mount the model on the tunnel side wall. Thus the model size is twice that of a whole model, for the same wind tunnel blockage ratio. Carr et al (1986) state that for a car in a closed wind tunnel the largest blockage ratio that should be used is 5%. Using this value and the typical dimensions for a car given by Hucho (1987), a 1/5 scale model was found to be the largest size that could be used in the 3'x 3' wind tunnel. The model is made up of two sections, a base section to represent the main body of a road vehicle which is common to most of the tests conducted. The other part is the top section which represents the windshield region. Seven top sections were made each with a different windshield angle (0-60 in steps of 10 degrees). The curvature of the A-pillar is another critical factor, as the curvature is increased the flow can remain attached further around the A-Pillar. It is thought that the strength of the A-pillar vortex can be reduced by increasing the curvature of this A-pillar. In this series of experiments the edge of the A-pillar was a sharp corner to ensure that a vortex would be formed and to fix the separation point. It is likely that

the flow will be less Reynolds number dependent with a sharp A-Pillar.

Each top section contained pressure tappings on the side window adjacent to the A-pillar. They contained two types of pressure tappings, small diameter (1mm) tappings which were used to obtain the mean pressures, and larger diameter (2mm) brass tappings for the fluctuating pressures. The pressure tapping array was set out on 5 degree radii from the apex. This arrangement was chosen so that comparisons could be made easily between each model and also because it was thought that the critical length scale for vortical type flows is the distance from the apex and not the width of the model as in 2-D separated flows (Cherry et al {1982}).

The model was kept as simple as possible without the added complication of wheels, wheel arches, engine compartment flow, side mirrors or fore body details.

2.7.2 SWEPT EDGE

The flow field on delta wings and that near the root and tip of swept wings is thought to be similar to that generated at the A-pillar. A second model consisting of a swept, blunt plate, was made to investigate the vortical type flow found at swept edges in more detail (Sutton{1983}). The aim was then to compare the vortical type flow fields between the A-Pillar and the swept plate models, and verify if the relevant length scale in the two cases is the distance from the apex for vortical type flows.

The plate has a uniform cross section as shown in figure 2.7.2.1 and it was mounted horizontally in the centre of the wind tunnel working section. The plate has a flat nose and separation is fixed at the sharp edges, the sides are at first flat and than taper to a thin trailing edge. The plate passes through both sides of the tunnel where it is sealed and clamped at the required angle. To reduce the boundary layer on the side wall, adjacent to the upstream edge of the model, an end plate is used. Mean and fluctuating pressure data was obtained at the same angles as for the road vehicle model. The end plate is used to simulate the windshield-bonnet

junction, the swept plate model passes through the end plate where it is then sealed. The end plate has a flap at its trailing edge, which is used to ensure zero circulation around it.

The tappings grid for mean pressure is identical to that used on the road vehicle model, except that the tappings extend further from the apex on the swept plate model. The larger brass tappings used for measuring the fluctuating pressure are also set up in a grid to cover the expected three-dimensional separation flow field (Pl.2.7.2.1). Some smaller copper tappings are also attached further along the plate to try and locate the position where the flow changes from a three-dimensional separation to that expected on an infinite swept plate model.

2.8 EXPERIMENTAL ERRORS

Errors are present in most experiments, but they can be reduced significantly if it is known where these errors are likely to occur. Systematic errors were found to be present in the following cases :-

i) Converting the pressure data from analog to digital form. The A/D unit is a 12-bit unit and its limits were set at +/- 10v, this gives us a resolution of +/- 0.005v.

ii) The wind tunnel Betz reading. The range of Betz readings for this series of experiments was 11-94mm. The Betz manometer can be read accurately to +/- 0.1mm, thus the resolution varies from +/-0.01 to +/- 0.001.

iii) Temperature changes of up to five degrees were found to occur during long runs when collecting the mean pressure data. The thermometer could be read to an accuracy of +/-0.1 of a degree. The wind tunnel temperature at the beginning of the experiment was found to be between 20-25 degrees, thus the operating temperature range is 20-30 degrees. The errors likely are +/- 0.05, -0.03.

iv) The tunnel static pressure correction K_1. K_1 varies with tunnel speed, thus as the speed increases so the value of K_1 increases. K_1 was found to vary between

0.010-0.020 over the tunnel operating range. Thus if the average Cp value is assumed to be -2.0, the likely error is +1.0% if K_1 is removed from the analysis.

3 RESULTS

The initial study was based on only three A-Pillar angles (40^{o},50^{o},60^{o}), but this was later increased to include the lower angles (0-30 degrees). These lower angles were included to produce a comprehensive study, but the relevant A-Pillar angles as far as road vehicles are concerned, are usually 40-60 degrees.

Each model setup was tested at three speeds (25.9,35,43.8m/s) to study Reynolds Number (Re) effects. Several different Model setups were tested. The road vehicle and swept plate model Reynolds numbers are based on their respective widths (0.328m & 0.050m), for the road vehicle model the 'whole' model width is used (twice model width). The series of tests conducted during this project is summarized in the table below.

FLOW VISUALIZATION (WIND TUNNEL)

WHOLE MODEL	7 ANGLES	3 SPEEDS
TOP HALF	4 ANGLES	3 SPEEDS
WHOLE MODEL + PLATE	4 ANGLES	3 SPEEDS

FLOW VISUALIZATION (WATER TUNNEL)

WHOLE MODEL	2 ANGLES	1 SPEEDS
WHOLE MODEL + PLATE	2 ANGLES	1 SPEEDS

MEAN STATIC PRESSURE DATA

WHOLE MODEL	7 ANGLES	3 SPEEDS
TOP HALF	4 ANGLES	3 SPEEDS
WHOLE MODEL + PLATE	4 ANGLES	3 SPEEDS
SWEPT PLATE	4 ANGLES	3 SPEEDS

FLUCTUATING PRESSURE DATA

WHOLE MODEL	7 ANGLES	3 SPEEDS
TOP HALF	3 ANGLES	3 SPEEDS
WHOLE MODEL + PLATE	3 ANGLES	3 SPEEDS
SWEPT PLATE	3 ANGLES	3 SPEEDS

The four angles used when the top half of the model, whole model +plate and the swept plate were tested were 0,20,40 and 60 degrees.

3.1 FLOW VISUALIZATION (WIND TUNNEL)

Flow visualization results were obtained for the three road vehicle models. The base model was painted black, but as each top section contains pressure tappings, these were covered with black Fablon (self adhesive plastic). The model was mounted on the wind tunnel floor for visualization of the side window flow and on the tunnel side window for visualization of the top surface of the model.

Using a French chalk + white spirit mixture, the results were obtained for the two lower Re used for the pressure results and an even lower Re (3.457×10^5). The white spirit evaporates too fast for the high Re case resulting in a partly developed flow structure on the model. This is because the tunnel has to be stopped before the dry french chalk is blown away. Flow visualization is used as a qualitative guide to the type of flow generated and also as a comparison with the mean Cp contour plots. Typical flow visualization results are shown in Pl.3.1.1.

3.1.1 WHOLE MODEL

A-PILLAR ANGLE = 0^o (Pl.3.1.1.1a-d)

The photographs show a large separation bubble for all three Re. The size of the core of the spiral flow decreases as Re increases and it becomes unstable (instability is shown by the radial splashes surrounding the spiral core). The overall

size of the spiral separation remains constant and it extends on to the roof of the vehicle model. The spiral flow is being fed by the horseshoe vortex sitting on the bonnet of the vehicle and by the separated flow from the front edge of bonnet wing.

The horseshoe vortex feeds the core of the spiral flow, whereas the bonnet separation feeds the outer region of the spiral flow. This is observed by following the secondary separation lines of the horseshoe vortex and the bonnet-wing separation. The wing separation starts at the front of the bonnet and is continually fed along its length as indicated by the primary and secondary separation lines. As a result of the spiral flow, a large region of the flow on the side of the base model is entrained onto the top half of the vehicle model. The flow separating from the A-Pillar reattaches downstream forming a large separation bubble, with the spiral flow contained within this bubble.

A-PILLAR ANGLE = 10^{o} (Pl.3.1.1.2a-d)

The photographs show similar trends to those obtained for the 0^{o} model, the core size decreases and instability (similar to the previous case) increases as Re increases. The feeding mechanism is identical to the previous case. The spiral flow area is smaller and its closer to the A-Pillar-bonnet intersection (apex). But the flow along the top edge of the model is different from the previous case.

A-PILLAR ANGLE = 20^{o} (Pl.3.1.1.3a-d)

The photographs show a separation bubble containing a spiral flow, the overall size of the spiral flow increases as Re increases. But the spiral core decreases in size and moves towards the apex as Re increases. The spiral core in closer to the apex than for the previous case. The feeding mechanism is identical to that for the 0^{o} and 10^{o} cases. The separation bubble is smaller compared to the 10^{o} case and its shape has changed.

A-PILLAR ANGLE = 30^{o} (Pl.3.1.1.4a-d)

A narrow almost parallel separation region is obtained. The spiral core has moved towards the A-Pillar and away from the apex compared to the 20^{o} case. The spiral core reduces in size and moves towards the apex as Re increases. The horseshoe vortex still feeds the spiral flow, but the size of the horseshoe vortex has reduced significantly and it is almost parallel to the freestream direction on the side of the base model. The bonnet wing vortex is also entrained into the spiral flow, but the bubble region containing the spiral flow separates and forms a vortex adjacent and downstream of the bubble (bubble vortex). The bubble vortex continues onto the roof of the model as it moves downstream.

A-PILLAR ANGLE = 40^{o} (Pl.3.1.1.5a-d)

A large bubble vortex is obtained on the side window, the vortex does not originate from the A-Pillar apex, but from the separation at the front on the vehicle. As the Re increases so the secondary separation line along the bonnet-wing gets closer to the primary separation line. The flow separating from the A-Pillar is entrained by the base model separation. The spiral flow is confined to the secondary separation region adjacent to the A-Pillar. As Re increases the spiral core moves towards the apex. A kink in the vortex is observed near the apex for the higher Re.

The top view of the model shows a horseshoe vortex on the bonnet, but it is not seen on the side views. The top view also shows that the vortex moves onto the roof before moving downstream into the vehicle wake.

A-PILLAR ANGLE = 50^{o} (Pl.3.1.1.6a-d)

The separation region is dominated by a vortex, which covers almost the entire length of the roof along the side window. The secondary separation is a continuous line from the separation at the front of the bonnet to the roof of the

model. Kinks in the secondary separation line near the A-Pillar apex indicate the mixing of two vortices. No spiral type separation is observed in the secondary separation region. The secondary separation line adjacent to the A-Pillar is initially straight (near apex), but then curves towards the A-Pillar-roof intersection. The relative curvature of the secondary separation line increases as Re increases. The sharpness of this separation line reduces as Re increases and the area covered by the vortex is noticeably smaller than for the 40^{o} model.

A-PILLAR ANGLE = 60^{o} (Pl.3.1.1.7a-d)

For the low Re case, a continuous clear secondary separation line is observed from the front of the bonnet wing to the roof of the model. The vortex appears as a single vortex emanating at the front of the bonnet wing. The area of the vortex in much smaller then for the 50^{o} model, but the vortex reattachment line is almost straight.

A large secondary separation region is obtained adjacent to the A-Pillar, but this region decreases as Re increases. This is due to the secondary separation line increasing in curvature near the roof (moving closer to the roof-A-Pillar intersection). A kink appears in the secondary separation line near the apex, this kink becomes more marked as Re increases. The overall shape and size of the vortex remains constant, but the separation region at the front of the bonnet wing decreases in size as Re increases. This was also found for all the other model angles.

3.1.2 TOP HALF

A-PILLAR ANGLE = 0^{o} (Pl.3.1.2.1a)

A large separation bubble is observed for all three Re, this region can be subdivided into two further sections. The top half contains a large recirculation region and a clearly defined secondary separation line where the French chalk has

built up. The lower section contains a spiral flow, with the core sitting near the apex. The spiral core is the same distance downstream of the A-Pillar as the secondary separation line for the low Re. But this line moves nearer the apex as Re increases. The reattachment length remains constant with the lower recirculation feeding the spiral core.

A-PILLAR ANGLE = 20^{o} (Pl.3.1.2.1b)

The length of the 2-dimensional separation bubble has reduced compared to the previous case. Thus a smaller secondary separation region is generated. The flow still contains the spiral flow, but its smaller and just above the apex. As Re increases the area of the spiral flow increases, capturing a larger area of the 2-dimensional separation bubble. At the same time the spiral core area reduces and moves nearer the apex.

A-PILLAR ANGLE = 40^{o} (Pl.3.1.2.1c)

The main bubble vortex is not well defined for the low Re case, but the secondary separation region is clearly visible and its a straight line emanating from the apex to the roof. The vortex originates from the apex for all three Re's (identical to delta wings). The low Re photograph shows a secondary vortex in the secondary separation region. As Re increases the secondary separation line becomes less well defined near the roof and this effect moves upstream as Re increase. At the same time the separation line moves towards the A-pillar-roof intersection. The shape and size of the primary vortex remains constant.

A-PILLAR ANGLE = 60^{o} (Pl.3.1.2.1d)

All three photographs show a fully developed vortex flow. The secondary separation line is clearly visible and is a straight line from the apex to the model

roof. The vortex originates from the apex for all three Re (identical to a Delta wing). The lower Re photograph also shows a vortex in the secondary separation region. As Re increased the secondary separation line became less well defined near the model roof and this effect increased with Re. The secondary separation line also curves towards the roof-A-Pillar intersection at the same time, but the shape and size of the primary vortex remained constant.

3.1.3 WHOLE MODEL + PLATE

A-PILLAR ANGLE = 0^{o} (Pl.3.1.3.1a)

The plate acts as a boundary between the A-Pillar and the bonnet flow regimes. The horseshoe vortex passes below the plate, thus the plate forces the bonnet-wing separation further down the side of the base model. This is shown by the shape of the secondary separation lines. Further downstream the plate wake acts as a barrier keeping the two flow regimes apart.

Above the plate, a very large 2-dimensional type separation region is formed, this region covers almost 2/3 of the top half of the model. For the low Re case the secondary separation region is not clear, but this region becomes clearer as Re increases. The top view along with the three side views show a separation bubble on the plate, with its centre at the same position downstream as the secondary separation line. The large primary separation bubble continues on to the roof of the model.

A-PILLAR ANGLE = 20^{o} (Pl.3.1.3.1b)

The general structure of the flow field below the plate is similar to the previous case. The main difference is that the horseshoe vortex is smaller, thus the bonnet-wing separation is closer to the primary separation line (dark line).

Above the plate a large separation bubble is generated, but it only covers half the top half of the model. The definition of the secondary separation is clearer

in the photographs at the higher Re. A spiral flow is observed for the high Re case, with the core near the A-Pillar-roof intersection. This spiral flow is in the primary separation region. The visualization results show a separation bubble on the plate.

A-PILLAR ANGLE = 40^{o} (Pl.3.1.3.1c)

Below the plate the flow remains unchanged, with the horseshoe vortex and the bonnet-wing separation adjacent to each other. Above the plate a large bubble vortex forms which starts at the A-Pillar apex. A large secondary separation region is obtained for the low Re case, but this region decreases in size as the secondary separation line moves towards the A-Pillar as Re increases. The overall size of the bubble vortex increases with Re.

A-PILLAR ANGLE = 60^{o} (Pl.3.1.3.1d)

The horseshoe vortex is smaller and closer to the bonnet edge compared to the previous models. Thus the bonnet-wing separation is nearer the primary separation line. Above the plate a fully developed vortex is present originating at the apex. The general shape and size remains constant, but the area occupied by the vortex is significantly smaller than for the 40^{o} model. The secondary separation line is straight for the low Re case, but starts to curve towards the A-Pillar-roof intersection near the roof as Re increases.

3.2 FLOW VISUALIZATION (WATER TUNNEL)

On the base model the dye is injected into the separation region, whereas on the top model the dye is injected on to the windscreen adjacent to the A-Pillar. The angle of dye injection should be as close to the local velocity direction as possible to minimize disturbance of the local flow.

3.2.1 A-PILLAR ANGLE = 40°

WHOLE MODEL (Pl.3.2.1.1a-d)

The separation from the base model is stable upstream of the apex. This flow is then entrained into the separation from the A-Pillar, at the same time the flow from the base separation becomes unstable. The side views show that the flow in the A-Pillar region in not completely random, but that the flow has a very complex structure and starts to break down near the roof.

The top view shows that the bonnet-wing separation is similar to that obtained on a body of revolution at incidence. But in the A-Pillar region the flow is on the surface, its very similar to a turbulent boundary layer. These photographs give a clearer view of the complex flow structure, where several vortices are present within the A-Pillar region at any one time.

WHOLE MODEL + PLATE (Pl.3.2.1.2a-d)

The flow below the plate is identical to that obtained for the previous case on the side of the bonnet, which is forced below the plate and runs parallel to the plate. But as it reaches a point directly below the apex, it becomes unstable.

Above the plate a complex flow field is obtained. The initial structure is similar to a delta wing, but within a short distance the flow changes. The A-Pillar region contains several vortices at different stages of formation and growth.

3.2.2 A-PILLAR ANGLE = 60°

WHOLE MODEL (Pl.3.2.2.1a-d)

A very stable vortex is obtained in the A-Pillar region. The structure is identical to that obtained on delta wings, with breakdown near the roof. Two separation regions formed on the base body interact, forming a single separation region. This separation region is then entrained into the A-Pillar region. The shear layer separating from the A-Pillar wraps itself around the base separation forming a

single vortex. This vortex is very stable almost to the roof were it seems to burst.

The top view shows a stable vortex with subsequent flow separating from the A-Pillar rapping itself around the base vortex without much diffusion of the dye. The vortex core migrates away from the model surface as we move downstream.

WHOLE MODEL + PLATE (Pl.3.2.2.2a-d)

The separation from the base is forced below the plate and the bonnet vortices remains parallel to the plate as they move downstream. Downstream of a point directly below the apex the two vortices interact and move towards the plate.

Above the plate a strong vortex is generated, this vortex starts at the apex and grows as it moves downstream. As it grows, its core moves away from the body surface. The two dyes wrap themselves around each other without mixing, except when the vortex bursts near the roof. For this particular setup some of the dye was entrained into the secondary vortex region adjacent and parallel to the A-Pillar.

3.3 MEAN STATIC PRESSURE

A typical mean static pressure coefficient contour plot is shown in fig.3.3.1.1. The mean pressure is recorded on the side of the model, it is then converted to a pressure coefficient and these values are used to generate the contour plot shown. The colour change in the contour plots is used to indicate regions of low pressure (Cp below -1.5 are shown in red). For models containing a vortex type structure a core line is also shown. This core line is obtained using the lowest Cp values collected on each arc moving downstream from the apex. The aim is to show the position of the centre of the vortex, assuming that the lowest Cp will be below the vortex core (based on potential theory).

3.3.1 WHOLE VEHICLE MODEL

A-PILLAR ANGLE = 0^{o} (fig.3.3.1.1)

The contour plots show a large 3-dimensional separation region near the apex. The contours indicate a large circular region of low pressure on the side of the model with its centre close to the apex. Further along the model the contours are parallel to each other and the pressure rises indicating a probable reattachment region. The exact position of the reattachment is not clear from these plots. As the wind tunnel speed was increased, the region where the pressure coefficient was below -1.5 contracted significantly. But the reduction in the peak suction magnitude was small (-1.741 to -1.553). As the tunnel speed increased the low pressure region moves towards the apex, at the same time the area of the low pressure region decreases. The overall size of the large circular region decreases as tunnel speed increases.

A-PILLAR ANGLE = 10^{o} (fig.3.3.1.2)

A 3-dimensional separation region is present near the apex, but this region is smaller then that for the 0^{o} case. The overall shape of the separation region is similar to the previous case. The peak suction pressure and the low pressure region were found to decrease with increasing Re. The overall size of the primary separation region is approximately 2/3 that for the 0^{o} case and the core is noticeably closer to the apex. The peak suction pressure coefficient values were found to decrease with increasing Re. Comparisons with the previous case shows that the peak suction values are lower for this case than for the equivalent values for the previous case.

A-PILLAR ANGLE = 20^{o} (fig.3.3.1.3)

Between 10^{o} and 20^{o} the flow structure changes noticeably, the separation bubble is no longer contained in a 3-dimensional separation bubble (spiral flow). As the flow structure changes it rotates until finally it is parallel to the A-Pillar. This is seen clearly from the curvature of the reattachment region contours. The peak suction pressure coefficients reduce as Re increases and the magnitude of each peak value was higher than the equivalent value for the 0^{o} case. A large low pressure region is present for the lowest Re, but this region reduces significantly as Re increases. The reattachment region is smaller than for the 0^{o} and 10^{o} cases. The overall size and shape of the low pressure region was found to be independent of Re. The core region (red) is closer to the apex than for the previous cases.

A-PILLAR ANGLE = 30^{o} (figs.3.3.1.4-3.3.1.6)

The minimum Cp value decreased significantly between this case and the 20^{o} case. This indicates the presence of a vortex type flow in the A-Pillar region. But the contour plots show a double separation region. This is seen clearly for the high Re case where the lower separation is entrained into to the A-Pillar separation bubble, indicating that the A-Pillar separation is stronger. The red line indicates the position of the peak suction values (core). The contour plots do not indicate the presence of a vortex as observed on delta wings, but a hybrid case i.e a mixture of a bubble separation and a vortex. As Re reduces, the A-Pillar separation becomes weaker and the lower separation becomes more dominant. This change in strength is indicated by the bubble vortex core line, which moves away from the A-Pillar as Re decreases. As the A-Pillar separation gets weaker so the angle of the lower separation changes and its core line rotates towards the A-Pillar. The size and shape of the bubble vortex is independent of Re, but the minimum Cp value and the area of the low pressure region decreases with increasing Re.

A-PILLAR ANGLE = 40^{o} (fig.3.3.1.7)

The contour plots indicate the presence of a single bubble vortex, producing a very low pressure coefficient value at the apex. The overall size and shape of the vortex has changed compared to the 30^{o} case. The plots show that the position and size of the bubble is independent of Re, but the peak negative pressure coefficient decreases with increasing Re.

The area of the low pressure region is dependent upon Re, but the position of the vortex core line is independent of Re. The angle of the bubble vortex core line changes near the apex. The core line is a straight line after this change in angle and is independent of Re.

A-PILLAR ANGLE = 50^{o} (fig.3.3.1.8)

A vortex emanating from the apex is present in the A-Pillar region. The vortex size has reduced compared to the previous case, but the vortex angle and the low pressure region have increased relative to the previous case. The vortex core angle remains constant as Re increases, but the low pressure area decreases and the peak negative pressure coefficient increases as Re increases. The peak negative pressure coefficient increased noticeably as the A-Pillar angle increased from 40^{o} to 50^{o} (-4.88 to -3.637).

Initially the contour plots indicated the presence of a single vortex with a small area near the apex without any contour due to an error in the contour plotting package. But when the vortex core line was added it indicated the presence of a second vortex just below the A-Pillar vortex. As we move downstream the second vortex becomes entrained into the stronger A-Pillar vortex. The entrainment position was found to be independent of Re.

A-PILLAR ANGLE = 60^{o} (fig.3.3.1.9)

As the A-Pillar angle is increased the area of the fully developed vortex region decreases. The overall shape and size of the vortex region is independent of Re, but the low pressure region increases as Re increases. This increase occur only in the downstream direction. The vortex core extends further downstream compared to the previous angle.

When the contour plots were generated it was assumed that a single vortex was present and the odd contouring near the apex was due to one of the pressure tappings being blocked. But with the addition of the vortex core line, its clear that a second vortex is present near the apex. Initially the second vortex is dominant, but further downstream the A-Pillar vortex becomes dominant entraining the second vortex. The entrainment of the second vortex occurs further downstream for this angle then for the 50^{o} case, but the position of entrainment is independent of Re.

The contour plots indicate the presence of a strong concentrated vortex, it occupies a small area with a low pressure region almost all the way along the centre of the vortex to the roof. But the peak negative pressure coefficients are significantly higher than the equivalent values for the 50^{o} case.

3.3.2 TOP HALF

Watanabe et al (1978) indicated that similar results to those obtained for a road vehicle in the A-Pillar region could be obtained by using a simplified model. The simplified model of Watanabe is very similar to the top halves of the vehicle models used in this research.

The top halves with four A-Pillar angles (0^{o},20^{o},40^{o},60^{o}) were tested. The aim of these experiments was to study the effect of the base model on the flow in the A-Pillar region. Each model was mounted on a ground board at the same position in the wind tunnel as the whole model.

A-PILLAR ANGLE = 0^{o} (fig.3.3.2.1)

A large low pressure region is obtained near the A-Pillar, followed by a long pressure recovery region. The position of the separation remains constant as Re increases, but the size of the low pressure region increased for the highest Re case. The peak negative pressure coefficient (Cp_{min}) decreased with increasing Re. The contour plots indicate the presence of a second pressure recovery region adjacent to the A-Pillar. This becomes clearer for the high Re case, where this region has moved closer to the primary separation region.

The large low pressure region starts near the apex, it rotates as it moves downstream until its almost parallel to the A-Pillar near the roof of the model. The formation of the low pressure region moves closer to the apex as Re increases.

A-PILLAR ANGLE = 20^{o} (fig.3.3.2.2)

A complex 3-dimensional separation region is observed, which spans 2/3 of the side of the model adjacent to the A-Pillar. Generally the shape of the separation region remains fixed in position, but there is a small reduction in the size of the separation region with increasing Re. The contour plots also indicate the presence of a secondary separation region adjacent to the A-Pillar for the high Re case. A pressure recovery region is observed downstream of the primary separation region, this region is small near the apex but expands rapidly downstream becoming parallel to the A-Pillar and then perpendicular to the freestream direction near the roof. This indicates the presence of a vortex type flow near the apex, but a bubble type flow as we move towards the roof of the model. The angle of the separation core changes in the spanwise direction from 53^{o} at the apex to 20^{o} (parallel to the A-Pillar) at the edge of the separation region.

The peak negative Cp has increased compared to the 0^{o} case. The peak negative Cp value reduces by a small amount as Re increases from the low to medium Re, but reduces significantly for the high Re case.

A-PILLAR ANGLE = 40^{o} (fig.3.3.2.3)

The contour plots for the lower two Re show a vortex type flow near the apex, which then changes to a bubble vortex (hybrid). But the high Re case shows a fully developed vortex flow. The main difference between the two flow regimes is the vortex core line angle, the angle increases as the vortex develops fully (core angle changes from 60^{o} to 65^{o}). For the lower two Re the angle for the vortex core line near the apex is identical to the high Re case. The low Re case contains a second low Cp region adjacent to the A-Pillar, but is not seem in the contour plots for the two higher Re cases. The previous trend of peak negative pressure coefficient decreasing with increasing Re continues for this model case. The low pressure region decreased as Re increased, except when the flow regime changed, then the low pressure region increased to a level where it was larger then for the low Re case.

A-PILLAR ANGLE = 60^{o} (fig.3.3.2.4)

A fully developed vortex flow is observed for all three Re. The vortex core angle is identical and the position of the low pressure region is almost identical. The only difference in the low pressure region appears near the apex, where the low pressure region decreases as Re increases.

The peak negative pressure coefficient initially increased as Re increased (-2.078 to -2.235), but then decreased as Re increased (-2.107).

3.3.3 WHOLE MODEL + PLATE

The plate was added to the whole model to try and isolate the top half of the model.

A-PILLAR ANGLE = 0^{o} (fig.3.3.3.1)

A large 2-dimensional separation region is generated on the side window. The contour plots also show a large reattachment region. The plots show a short secondary separation region adjacent to the A-Pillar. A second narrow low pressure region is obtained adjacent and parallel to the A-Pillar. The low Re case shows a third low pressure region on the plate near the A-Pillar, this region grows as Re increases, significantly affecting the primary separation region. The high Re plot does not show the plate low pressure region. The primary and secondary separation regions positions remain constant as Re increases.

A small increase in the peak negative Cp is obtained for the two lower Re (-0.968 to -0.974), but a larger increase for the high Re case.

A-PILLAR ANGLE = 20^{o} (fig.3.3.3.2)

For the low Re, the plot shows a large 2-dimensional separation region of the same size as for the 0^{o} case. As Re increases the plate separation disappears and the primary separation bubble spans the whole top section. A small reduction in the bubble length is observed as Re increases. The peak negative Cp reduces as Re increased.

A significant change in the flow field is observed as Re increased. The primary separation bubble moves in a spanwise direction forming a smaller bubble and a second low pressure region is formed in the top half of the model adjacent to the A-Pillar. A very complex flow structure is obtained for the high Re case.

A-PILLAR ANGLE = 40^{o} (fig.3.3.3.3)

The overall shape and size of the bubble vortex remains constant, but as Re increases the initial vortex region near the apex reduces in size. The vortex core region decreases as Re increases, with a noticeably larger decrease for the high Re case.The position of the vortex core line remains constant for all three Re (50^{o}). The peak negative Cp increases from -1.03 to -3.48 as the A-Pillar angle increases from 20^{o} to 40^{o}. The peak negative Cp decreases as Re increases.

A-PILLAR ANGLE = 60^{o} (fig.3.3.3.4)

A fully developed vortex flow is obtained for all three Re. The vortex core line remains constant (70^{o}) as Re increases. The only change occurs in the size of the low pressure region, this region increases in size as Re increases, But a further increase in Re resulted in a decrease in the size of the low pressure region.

A similar trend is observed for the peak negative Cp values, it increases from -2.078 to -2.235 as Re increases and then down to -2.107 with a further increase in Re.

3.3.4 SWEPT PLATE

Sutton's (1982) qualitative results on a flat swept plate indicated that flows similar to those obtained on the vehicle model (40^{o} to 60^{o} degrees) were generated on the swept plate. But the mean Cp contour plots show large differences between the swept plate and road vehicle model results. The contour plots for the swept plate were generated in the region shown in Fig.2.7.2.1.

SWEEP ANGLE = 0^{o} (fig.3.3.4.1)

A double separation region is present for the low Re case. The primary separation bubble is a large 3-dimensional bubble near the apex (plate-side board

intersection), which then becomes a 2-dimensional bubble as we move in the spanwise direction. The secondary separation bubble seems to be a bubble which is formed as a result of flow separation from the side board. A large reattachment region is shown by the contour plots. The secondary separation bubble disappears as Re increases and the primary separation bubble remains constant for the two lower Re cases.

The high Re case shows a smaller separation bubble, a small 3-dimensional bubble is present at the apex with the axis of the vortex rotating until it is parallel to the leading edge as we move in a spanwise direction. The flow changes to a 2-dimensional bubble away from the wall junction. The peak negative Cp is very similar for all three Re.

SWEEP ANGLE = 20^{o} (fig.3.3.4.2)

A fully developed vortex is present on the model. The shape and size of the vortex remains constant as Re increases, but a small increase was obtained in the peak negative Cp as Re increased.

The vortex remains very close to the leading edge of the model, but it is closer to the leading edge compared to the 0^{o} case. As a result of the fully developed vortex structure the peak negative Cp increases sharply as the sweep angle increased from 0^{o} to 20^{o}. As we move in a spanwise direction the vortex rotates to align itself with the leading edge of the model. The peak negative Cp increases with increasing Re.

SWEEP ANGLE = 40^{o} (fig.3.3.4.3)

A fully developed vortex is obtained on the model. The low pressure region beneath the vortex is narrower and does not align itself with the leading edge within the contour plot region. The low suction region increased markedly as Re increased, but a further increase in Re reduced the low pressure region to its initial

level (low Re level). The vortex is closer to the leading edge for this sweep angle than for the 20^{o} case. The peak negative Cp increases with Re, but the initial increase in Cp for the low to medium Re is significantly larger than that for the medium to high Re case. The peak negative Cp were found to be noticeably higher than for the 20^{o} case.

SWEEP ANGLE = 60^{o} (fig.3.3.4.4)

The three contour plots show a reattachment region, thus a separation bubble is present but its probably adjacent to the leading edge where it could not be detected (not enough tapping adjacent to the leading edge). The middle Re plot shows a small section of a vortex near the apex, this produced a high peak negative Cp value. But this peak Cp value is lower than that obtained for the 40^{o} case.

3.4 R.M.S FLUCTUATING PRESSURE

The fluctuating pressure is obtained using a different pressure tapping grid to that used for the mean pressures. The position of these larger tappings is based on the mean Cp contour plots. Several tappings were placed in each different flow regime (low pressure region, pressure recovery region, near the apex, etc). The fluctuating pressure signal was processed to generate root mean square (r.m.s) pressure coefficients at each pressure tap. These coefficients were used to generate the contour plots. The colour change on the contour plots occurs at a Cp_{rms} value of 0.15.

3.4.1 WHOLE MODEL

A-PILLAR ANGLE = 0^{o} (fig.3.4.1.1)

The contour plots show a separation region adjacent to the A-Pillar. For the low Re case the contours indicate a spiral type flow centered near the apex. The

high r.m.s pressure region increases in the upstream direction until it covers the whole separation region as Re increases from the low to the medium case. The general structure remains fixed for these two Re cases. A further increase in Re results in a change in shape of the separation region, it also moves closer to the apex. The peak Cp_{rms} value is effectively constant for lower two Re, but reduces as Re increases.

A-PILLAR ANGLE = 10^{o} (fig.3.4.1.2)

A 3-dimensional bubble is situated near the apex. This bubble is similar to the 0^{o} model, except it is smaller. Moving downstream a large reattachment is found adjacent to the separation bubble. The contour plots indicate the position of a the reattachment line, with the highest Cp_{rms} values found along this reattachment line. As Re increases the high r.m.s region expands either side of the reattachment line, but the position of the line remains the same. A further increase in Re reduces the extent of the high r.m.s region (both sides of the reattachment line) to a level were its smaller than for the low Re case. The peak Cp_{rms} value follows a similar trend to the high r.m.s pressure region.

A-PILLAR ANGLE = 20^{o} (fig.3.4.1.3)

Trends similar to the two previous models are obtained for this model. A three-dimensional bubble adjacent to the A-Pillar followed by a reattachment region. The high r.m.s pressure region is found either side of the reattachment line. The low Re case shows a second high r.m.s region below the primary separation bubble. As Re increases the bubble migrates away from the A-Pillar and the high r.m.s pressure region expands. A further increase in Re produces a contour plot almost identical to the low Re case. The reattachment line position is independent of Re. The variation in peak Cp_{rms} value is similar to that for the high r.m.s pressure

region.

A-PILLAR ANGLE = 30^{o} (fig.3.4.1.4)

The contour plots show a very different form to that for the previous models indicating a change in the flow field. The flow separates from the A-Pillar and reattaches along a line emanating from the apex. This reattachment line is a straight line, which remains the same as Re increases. The high r.m.s pressure region is located around this line, as Re increases this region expands in the upstream direction into the separation region. A further increase in Re produces a decrease in the high r.m.s region except near the roof. The peak Cp_{rms} value decreases as Re increases.

A-PILLAR ANGLE = 40^{o} (fig.3.4.1.5)

The high r.m.s pressure region is around a straight line emanating from the apex for all Re. The only changes that occur to the contour plots as Re increases are:-

i) The high r.m.s pressure region initially increases, then it decreases.

ii) The peak Cp_{rms} value follows a similar trend as the high r.m.s pressure region.

The area of the bubble vortex has reduced compared to the previous case i.e the reattachment line is closer to the A-Pillar.

A-PILLAR ANGLE = 50^{o} (fig.3.4.1.6)

The flow structure is very similar to the mean Cp contour plots obtained for a fully developed vortex, a strong core section surrounded by a weaker region. The contour plots show large r.m.s pressure gradients near the apex. The high r.m.s pressure region, initially quite large reduces in area then expands rapidly in the downstream direction, this trend is obtained for all three Re. The overall area

occupied by the parallel contour lines remains constant, but the high r.m.s pressure region initially expands then contracts as Re increases. The low Re case produced two areas of high r.m.s pressure, whereas for the higher Re only a single area was obtained.

The overall size of the separated region is noticeably smaller and closer to the A-Pillar than for the 40^{o} model. The peak Cp_{rms} is almost identical for the higher Re, but lower for the low Re (0.250 to 0.279).

A-PILLAR ANGLE = 60^{o} (fig.3.4.1.7)

The Cp_{rms} contour plots are similar to the mean Cp plots. The plots show a narrow concentrated region near the apex with a reduction in the r.m.s pressure level as we move downstream. The angle of the r.m.s pressure region remains constant as Re increases. As Re increases the high r.m.s pressure region initially expands downstream, but then contracts. The contour plots show two regions of high r.m.s pressure near the apex, both regions expand rapidly then contract as Re increases. The peak Cp_{rms} value increases noticeably (low to medium Re), but then decreases (medium to high Re).

3.4.2 TOP HALF

A-PILLAR ANGLE = 0^{o} (fig.3.4.2.1)

Re has a negligible effect on the shape and size of the r.m.s contour plots. The highest values of Cp_{rms} occur in the reattachment region. The peak Cp_{rms} value decreases as Re increases.

A-PILLAR ANGLE = 40^{o} (fig.3.4.2.2)

The contour plots show a high r.m.s pressure region surrounded by a low pressure region. This flow regime is located either side of a straight line emanating

at the apex, with the peak Cp_{rms} value adjacent to the apex.

A-PILLAR ANGLE = 60^{o} (fig.3.4.2.3)

A long narrow r.m.s pressure region is obtained, this region is located around a straight line. The general shape and size of the region is independent of Re, but the following effects are observed as Re increases:-

i) The high r.m.s pressure region is confined to a small region near the apex, this region becomes smaller until it finally disappears.

ii) The peak Cp_{rms} value decreases markedly.

3.4.3 WHOLE MODEL + PLATE

A-PILLAR ANGLE = 0^{o} (fig.3.4.3.1)

All three contour plots show a large separation bubble, with the core at the apex. The size of the bubble remains constant for the lower two Re, but increases in size for the higher Re. The Cp_{rms} values are below 0.15 for all three plots. The peak Cp_{rms} value is identical for the lower two Re, but lower for the high Re case.

A-PILLAR ANGLE = 40^{o} (fig.3.4.3.2)

The contour plots show a central core of high Cp_{rms} surrounded by a region of low Cp_{rms} for all three Re.The size of the core region (high Cp_{rms}) initially increases then decreases as Re increases. The final core size is larger than for the low Re case. The contours are centred around a straight line emanating from the apex and the angle of this line is independent of Re. For the medium and high Re cases, a small region of low Cp_{rms} appears near the apex. The peak Cp_{rms} values decreased as Re increased.

A-PILLAR ANGLE = 60^{o} (fig.3.4.3.3)

The contour plots for all three Re are identical in all respects, except for the contour directions in the high Cp_{rms} region. The angle, shape and size are identical. The contours adjacent to the A-Pillar change as Re increases until they are normal to the A-Pillar for the medium Re and the contour angle increases with Re. The peak Cp_{rms} increases with Re.

3.4.4 SWEPT PLATE

The mean and fluctuating pressure tapping grids are coarser than those used for the vehicle models. But the contour plots cover the same areas as those for the road vehicle models.

SWEEP ANGLE = 0^{o} (fig.3.4.4.1)

The overall shape of the pressure contours is identical for all three Re. The peak Cp_{rms} decreases as Re increases. The flow is a 3-dimensional bubble formed near the apex, this bubble starts to rotate as we move in a spanwise direction until its almost parallel to the leading edge. The large number of contours parallel and adjacent to the leading edge indicate the presence of a second pressure recovery region.

SWEEP ANGLE = 40^{o} (fig.3.4.4.2)

The contour plots are similar to the mean Cp plots for the same model. The r.m.s pressure core line is a straight line emanating from the apex, its angle remains constant as Re increases. A large Cp_{rms} region is obtained for the low Re case, this region initially expands in the downstream direction, but a further increase in Re has no effect on this region. The peak Cp_{rms} value increases significantly as Re increases.

SWEEP ANGLE = 60^{o} (fig.3.4.4.3)

All three contour plots are identical. They show a large region of parallel contour lines very close together near the apex, then expanding as the flow moves downstream. The peak Cp_{rms} value decreases as Re increases. The peak Cp_{rms} value was measured near the apex.

3.5 POWER SPECTRA

The fluctuating pressure is also used to generate the Power Spectra density plots, but as the Power Spectral density is a function of the frequency (n). It can be non-dimensionalized by multiplying it by U/L, where U is the freestream velocity and L is a characteristic length. A non-dimensional frequency (n_n) is obtained by multiplying the frequency by L/U. In these experiments it was not clear what was the most appropriate length scale to use, so the data is plotted using L=1.0m. Thus the Power Spectral density plots are plotted as $\log_{10}[F\{Cp'(n)\}xU/L]$ versus nL/U (n_n).

Figure 3.5.1 is a plot of the Power Spectral density of the fluctuating pressure measured on the 40^{o} road vehicle model (whole model). The plot shows the effect of Re on fluctuating pressure, the data used was collected at the tapping point on the model where the peak Cp_{rms} was measured. All three plots collapse on to a single broadband spectrum, with the curves containing two broad peaks, one at n_n=11 and the second at 20.

The 60^{o} whole model also produced a broadband spectrum (Fig.3.5.2), with all three plots following a single curve up to n_n=14. Between n_n=14 and 28 the plots (U=35.0 and 43.8m/s) produced a higher spectra level before plot B dropped back to the same level as plot C. The peak values for the two higher speed plots occurred at approximately n_n=20.

A comparison between spectra for the two model angles (40^{o} and 60^{o})

using fluctuating pressure data collected at the peak Cp_{rms} tapping point and for the highest Re (Fig.3.5.3), shows good agreement for the low n_n range (0-7) and for the high range (15-25). But for the intermediate range (7-15) the 40^o model produced a noticeably higher fluctuating pressure level with a peak at 11. The highest peak value for both angles was at n_n value of 19.

The effect of different road vehicle model configurations (i.e whole model, top half and whole model with plate) on the fluctuating pressure was studied using the 40^o model data {high Re case (fig.3.5.4)}. All three spectra are very similar, almost collapsing onto a single curve. The largest difference occurs at low n_n. The peak value for all three plots was about the same (n_n=19).

Figure 3.5.5 shows four spectral plots obtained for the 40^o model (high Re case). Three of the plots are from tappings within the A-Pillar bubble vortex and one is from a tapping in the attached flow region. Tapping A is the peak Cp_{rms} tapping, with tapping B being on the same radial (angle) as tapping A, but one position downstream. The third tapping is on the same arc (same distance from the apex as tapping B), but on a different radial (see model figures). For the 60^o model only two tappings were used for a comparison between different positions within the Vortex flow region (fig.3.5.6).

The four spectral plots for the 40^o model show that the spectra for tapping B and C follow a single curve, but with a constant difference between them over the whole n_n range plotted. But the plot for tapping A is different, but it is contained within the limits of the other two spectra plots. Below an n_n value of 3.0 the level of the spectra for the attached flow region is similar to the vortex flow region levels, but above n_n=3.0 the spectra levels are significantly lower than those obtained for the vortex region. But one sharp spike was obtained at n_n=6.0 for the attached flow region.

The two spectra plots obtained within the vortex region for the 60^o model (Fig.3.5.6) were obtained on the same radial (same angle), where tapping A (peak

Cp_{rms} tapping) was one position upstream of tapping B.

The general difference observed between the vortex and attached flow region are similar for both angles. But for the 60^{o} model the spectra plots within the vortex region are almost identical up to n_n=12.5, above this value they start to diverge. The peak spectra value for tapping B occurs at a lower n_n value (19.0) compared to tapping A (20.0).

4.DISCUSSION

The region under study for all four models is dominated by flow separation. The type of separation is a function of the A-Pillar or model sweep angle. In general the separation region is very complex with a combination of 3-dimensional separation bubbles and vortices. At present, our understanding of 3-dimensional flow separation rests principally on observations drawn from experimental studies utilizing flow visualization techniques. Several authors (refs.9,19,21,37,51) including Maskell (1955) have based their analysis on the patterns of skin-friction lines obtained on model surfaces using oil-flow techniques.

Maskell's (1955) analysis of 3-dimensional separated flows is based on limiting streamlines. A streamline is defined by the condition that its direction at any point is the direction of motion of the fluid element at that point. The limiting streamline is a line which represents the motion of fluid particles that pass infinitely close to a solid surface. Separation is defined such that it occurs at a point only when two distinct limiting streamlines, lying in the solid surface, converge and meet at that point. They then combine and depart from the surface in the form of a single 'separation streamline'.

Based on the principles of limiting streamlines, Maskell initially studied the conditions required for flows to separate from different types of surfaces (curved surfaces and salient edges). He then went on to consider complex 3-dimensional separation regions, these regions were subdivided into three types:-

TYPE I	Three-Dimensional Bubble	(fig.4.1)
TYPE II	Vortex bubble (mixed flow)	(fig.4.2)
TYPE III	Free vortex layer	(fig.4.3)

As a result of the distinctive nature of the limiting streamlines on each type of flow

field stated above Maskell concluded that :- 'Ideas of the physical nature of any three-dimensional flow are greatly clarified by the present generalized definition of separation and the subsequent classification of the components of the viscous region into :-

i) free vortex layer

ii) bubbles.

The fact that both these components result from the same universal type of separation is particularly important, for it is then easy to understand how bubbles and free vortex layers exist together, and how one type of flow might develop gradually into another'.

Lighthill (1963) extended the concept of limiting streamlines just above the surface by pointing out that they approximate to skin friction lines on the surface. Hence the ideas of Maskell can be applied to the flow features indicated by surface oil-flow patterns.

Considering each of the three types of 3-dimensional separation regions proposed by Maskell in more detail :-

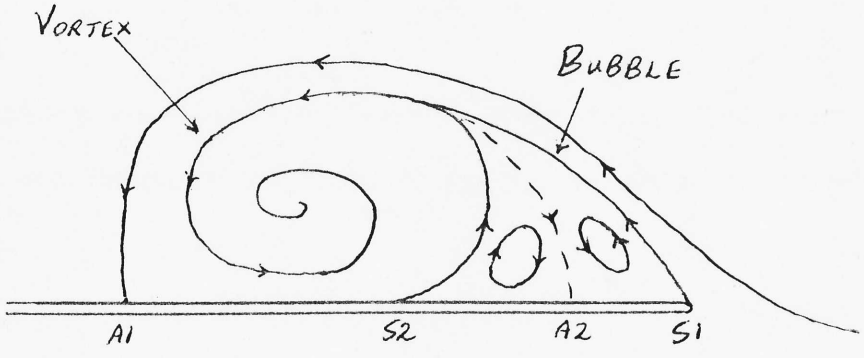
TYPE I - THE BUBBLE

Figure 4.1 shows the average separation surface in a 2-dimensional flow with separation occurring at or near a leading edge. At small yaw angles, the flow can be expected to be nearly 2-dimensional due to the cross flow velocities being small. The flow may reattach to a surface downstream forming a bubble. This bubble contains a slowly recirculating flow, which is distinct from the mainstream flow. Often this recirculating flow is not steady and the reattachment point may

oscillate in the streamwise direction. Alternatively the bubble may close downstream of the body by meeting a separation surface from a second separation point. This bubble contains a double recirculation region and is likely to be more unsteady than the bubble reattaching onto a surface. In the case of the A-Pillar flows investigated in this study it is shown that the flow reattaches on to the vehicle body.

TYPE II - VORTEX BUBBLE (MIXED FLOW)

Figure 4.2 shows the averaged flow structure obtained on a moderately swept wing with separation occurring at the leading edge. In this case the flow is markedly more 3-dimensional. Considering the flow in a plane normal to the freestream direction (see below). It is observed that a bubble is formed by the primary separation (S1) meeting a secondary separation surface from a second separation point (S2) downstream, these two separation surfaces form a bubble adjacent to the leading edge. This bubble contains a double recirculating flow with a second reattachment point (A2) between the two recirculating flows. The shear layers from S1 and S2 combine and roll up to form a vortex adjacent and downstream of the bubble.



TYPE III

Figure 4.3 shows the structure and surface flow patterns generated by the flow separation from a highly swept leading edge. The flow is very strongly 3-dimensional, with the shear layer separating from the leading edge rolling up to form the primary vortex. An adverse pressure gradient is generated along the surface below the primary vortex core position and the leading edge of the model surface. This pressure gradient may cause the flow in this region to separate, forming a small secondary vortex close to the leading edge.

Although the above descriptions of the three flow types are based on flow patterns observed over aircraft wings, similar flows are generated around bluff bodes. Type I and Type III flows have been observed on rectangular boxes, buildings and road vehicles by several authors (Stapleford et al (1971), Kind (1986), Surry et al (1983), etc). Although a car is a complex 3-dimensional shape, it is possible to find flow separation patterns in the vicinity of the A-Pillar that approximate to the types mentioned above.

In this investigation the different types of flow pattern were identified primarily from surface oil flow patterns around and downstream of the A-Pillar area. The specific surface features associated with each flow type are :-

TYPE I

i) Surface streamlines showing flow reversal upstream of the reattachment line (region), with the reattachment region approximately normal to the main flow direction.

ii) A secondary separation line and separation region adjacent and parallel to the leading edge. A build up of French chalk adjacent to the secondary separation line.

The features stated above are observed on Pl.3.1.2.1a, Pl.3.1.3.1a, and

Pl.3.1.3.1b.

TYPE II

i) Adjacent to the leading edge, a build up of French chalk is observed, adjacent to the secondary separation line. This line of French chalk is almost parallel to the leading edge.

ii) Downstream of the secondary separation line,the classic S shaped surface streamlines are observed, indicating the presence of a vortex.

The features stated above are observed on Pl.3.1.2.1c and Pl.3.1.3.1c.

TYPE III

i) A straight secondary separation line at a specific angle, but not parallel to the leading edge. As this type of flow is an open flow, we do not get a build up of chalk adjacent to this line.

ii) The classic S shaped streamlines observed downstream of the secondary separation line. This region is narrow near the apex, but then expands as we move downstream as more fluid is entrained by the vortex (see fig.4.3).

iii) A straight line of inflexion can be drawn through the centre of the S shaped streamlines.

The features stated above are observed on Pl.3.1.2.1d, Pl.3.1.3.1d and Pl.3.1.1.7a-d.

The selection of the various angles as being Type I, II, or III was based on the flow features stated above. However it should be realized that for the whole model and some of the top half models tested, the flow was more complex than that observed over swept wings. This is due to the influence of the base model on the whole model (especially for the lower angles 0^{o}-40^{o}) and the ground board on the

top half models (0°,20°). The influence of the base model and the ground board on the flow in the A-Pillar region is discussed later (see sections 4.1-4.3). Hence the classification into the flow types suggested by Maskell can only be considered as approximate, but it does aid understanding of the complex 3-dimensional flows fields generated.

Certain features of the mean and r.m.s C_p contour plots can be used to interpret which type of flow separation regime is present. The features that indicate a particular flow type are :-

TYPE I

A flow is likely to be of type I if the mean C_p plots show a low pressure region downstream of the leading edge, followed by a pressure recovery region as we move downstream.From the separation point the C_p value decreases, with the peak close to the centre of the primary recirculation region and then the C_p value increases up to the reattachment line, with the C_p contours roughly parallel to each other and normal to the freestream direction. The peak negative C_p values are generally above -1.0 for this type of flow.

In this regime the r.m.s C_p plots indicate that the highest fluctuations lie well downstream near the flow reattachment line. Observations of the highest fluctuations occurring in the reattachment region have been reported by Cherry et al (1983) on an infinite blunt flat plate and by Watanabe et al (1978) on a backward facing step (both 2-dimensional).

Typical examples of a bubble are fig.3.3.3.1 and fig.3.4.3.1.

TYPE II

Considering the mean C_p plots for the 30^o and 40^o road vehicle models, the plots show a contour structure which is neither clearly a bubble or a vortex (see below). But the pressure contours show a mixture e.g peak value close to the apex and some contours almost normal to the freestream direction well downstream of the leading edge.

The r.m.s C_p contour plots show that the highest fluctuations are generated away from the apex, either side of a straight line emanating from the apex. The contours are in general parallel to this peak line. Thus again we have a mixture of features from type I and type III flows.

Typical examples are figs.3.3.1.6, 3.3.1.7, 3.4.1.4, and 3.4.1.5.

TYPE III

In this type of flow the mean C_p plots show a narrow suction region which expands as we move downstream. The peak suction value will reduce as we move downstream because the vortex moves away from the model surface. The peak suction values lie along a line emanating from the apex. The C_p contours will be parallel to the peak suction line and very close together indicating a very large pressure gradient.. Due to the high flow velocities induced by the vortex below the vortex, the peak suction values will be noticeably lower than -1.0.

The r.m.s C_p plots should be similar to the mean C_p plots, with the largest fluctuations being generated beneath the vortex core. The most intense fluctuations occurring near the apex because the vortex is nearest to the model surface in this region.

Typical examples of a vortex are fig.3.3.3.4 and fig.3.4.1.7.

The A-Pillar separation regions on the road vehicle models are very complex, each containing several vortices and a bubble separation or just several vortices.The type of flow generated on each model is dependent upon the A-Pillar or sweep angle and is related to the flow type generated as follows :-

MODEL TYPE	MODEL ANGLE	FLOW TYPE
ROAD	0,10,20	I
VEHICLE	30,40	II
MODELS	50,60	III

MODEL TYPE	MODEL ANGLE	FLOW TYPE
SWEPT	0,10	I
PLATE	20-60	III

The above table is based on wind tunnel flow visualization results. The mean Cp contour plots indicate a mixed structure only for the 30^{o} model (whole model only) and a vortex structure for the 40^{o} model. Each flow type obtained on the various models is discussed in detail in the following sections.

4.1 THREE-DIMENSIONAL SEPARATION BUBBLE

The flow visualization results show a very complex flow structure in the A-Pillar region for all three models (whole models- 0^{o},10^{o},20^{o}). The general nature of flow separation is identical, but the size and shape is a function of Re and A-Pillar angle.

Consider the 0^{o} whole model, the flow visualization results (Pl.3.1.1.1a-d) show a large spiral flow in the A-Pillar region. The nature of the streamlines

downstream of the spiral flow indicate a reattachment region, the mean Cp contour plot (fig.3.3.1.1) shows a pressure recovery region in the same region. The Cp_{rms} plot (fig.3.4.1.1) shows that the highest fluctuations were obtained within this reattachment region. Thus all three sets of results indicate a reattachment region, with the flow separating from the A-Pillar and reattaching downstream. The mean Cp plots show that the low pressure spiral flow region (red contours) near the A-Pillar decreases in size and moves towards the A-Pillar as Re increases. The cause of the spiral flow is not indicated by the pressure (mean and r.m.s) contour plots, but the flow visualization results indicate the probable cause. They show a three-dimensional separation bubble at the front of the base model, moving downstream the separation continues along the side of the base model (thick white line is separation line). The results also show a parallel flow region between the A-Pillar and the spiral core (parallel to A-Pillar), which is probably a secondary separation region.

This separation rolls up forming a vortex along the side, which is continually being fed by the base separation. Half way between the A-Pillar and the front of the vehicle model, a second vortex appears along the side of the base model. This is due to the horseshoe vortex sitting on the bonnet which rolls around the bonnet into the side flow. The position where this horseshoe vortex (HV) appears on the side of the base model is indicated by the abrupt change in direction for the primary separation line of the base vortex.

As the two vortices move downstream, they seem to interact forming a single vortex. The position where the two vortices mix moves downstream as Re increases, but these vortices are rotating in opposite directions. As the combined vortex moves downstream it is entrained into the A-Pillar bubble region, forming a spiral flow which entrains the trapped fluid in the A-Pillar bubble, resulting in a large spiral flow covering the whole separation bubble. The spiral flow seems to

entrains some fluid from the secondary separation bubble near the apex. The direction of rotation of the spiral flow indicates that the HV is the dominant vortex. As Re increases the base vortex (BV) and HV decrease in size, this may be due to the flow becoming turbulent, resulting some how in a smaller mixed vortex and a smaller spiral core. Thus the spiral core moves towards the apex.

The overall size of the A-Pillar bubble region remains constant as Re increases. The reduction in Cp_{min} and mean Cp core region with Re could be due to several factors :- a weaker spiral core, movement of the core away from a set of pressure tappings and increased instability of the spiral flow, resulting in high mean Cp_{min} values.

The highest pressure fluctuations were obtained downstream of the spiral flow region, with the position of the highest fluctuations remaining approximately constant as Re increased, indicating that reattachment position remains fixed. Cherry et al (1983) found that the highest fluctuations occurred just upstream of reattachment.

Similar trends were obtained for the 10^{o} and 20^{o} whole models. The main differences between the models are :-

i) The flow visualization results (Pls.3.1.1.2,3a-d) show that reattachment moves towards the A-Pillar as model angle increases, with a resultant decrease in the secondary separation bubble size. Thus the spiral core moves towards the apex. The mean Cp plots (figs.3.3.1.2,3) show that the pressure recovery region becomes shorter and moves towards the A-Pillar as model angle increases. But the Cp_{rms} plots (fig.3.4.1.2,3) show that the core region does not move as A-Pillar angle increases.

ii) The mean Cp and flow visualization results show that the spiral flow region only covers 3/4 of the side window height for the 10^{o} model, but expands and covers the whole region as the angle increases to 20^{o}.

iii) Pls.3.1.1.2,3a-d show that the spiral core region migrates towards the roof

as A-Pillar angle increases.

iv) The separation bubble at the bonnet-windscreen intersection decreases in size as the angle increases, thus fluid downstream of the HV near the bonnet wing separates at the bonnet edge forming a third separation region.

The mean Cp plot for the 0^{o} top half model (fig.3.3.2.1) shows a flow similar to that obtained on the 0^{o} swept plate root region (fig.3.3.4.1). The plot indicates a three-dimensional bubble in the bottom half of the side window, which rotates until it is parallel to the A-Pillar (2-d bubble). Downstream, a reattachment region is indicated by the large pressure recovery region. The Cp_{rms} plot (fig.3.4.2.1) shows that the highest fluctuations occur within the pressure recovery region.

But the flow visualization results (Pl.3.2.1.1a) show a different flow structure. The bottom half of the side window contains a spiral flow, with the top half containing a separation bubble (2-d). Thus the flow separates from the A-Pillar, reattaches downstream on the side window, with the top half of the side window producing a secondary separation region adjacent to the A-Pillar. The exact cause of the spiral flow is not clear from the results, but one possible cause could be that the A-Pillar bubble adjacent to the groundboard causes the groundboard BL within the A-Pillar bubble region to separate. The spiral core is situated directly below the secondary separation line. The flow either side of the secondary separation line forces the separated BL to follow the local flow direction resulting in a localized spiral flow. But this spiral flow is only strong enough to entrain half the A-Pillar bubble region. Re had a negligible effect on the position of the spiral core.

The flow development is identical for the 20^{o} model except in the following respects (Pl.3.2.1.1b, fig.3.3.2.2) :-

i) The spiral core is closer to the apex, with a subsequent change in the spiral core shape.

ii) The primary and secondary separation lengths have reduced.

iii) The spiral core decreases in size and moves towards the apex as Re increases, with a subsequent increase in the size of the secondary separation bubble.

The flow visualization result for the 0^{o} whole model with plate (Pl.3.1.3.1a) shows a very complex flow structure for the A-Pillar region. The base separations (BV and HV) are forced below the plate and so do not influence the flow within the A-Pillar region. Beyond the plate, the flows above and below the plate are separated by the plate wake. The surface streamlines indicate a very large A-Pillar bubble, with reattachment occurring downstream of the back of the plate. A large secondary separation region is also generated adjacent to the A-Pillar (thick white line is secondary separation line).

The mean Cp plot (fig.3.3.3.1) shows a large low pressure region followed by a large pressure recovery region. The nature of the low pressure region indicates that its probably a large two-dimensional separation bubble.

As the A-Pillar angle increases the two-dimensional bubble gets shorter (Pl.3.1.3.1b), but it contains a spiral type region with the core near the roof (fig.3.3.3.2). This region moves towards the roof and becomes very complex as Re increases.

The discussion of the 0^{o} swept plate model is based on the mean Cp (figs.3.3.4.1,2) and Cp_{rms} (fig.3.4.4.1) contour plots. The low Re case shows a 3-dimensional bubble which rotates as we move in a spanwise direction until its parallel to the leading edge (two-dimensional bubble). But this case contains a separation region on the side wall adjacent and downstream of the 3-dimensional separation bubble. As Re increases the side wall BL stays attached and a separation bubble similar to the top half model is generated, with the bubble length decreasing with increasing Re. The Cp_{rms} contour plot shows that the swept plate model did not contain a region of high pressure fluctuations, with the position of the mean

reattachment line remaining approximately fixed. This has to be considered an approximation due to the coarse nature of the large pressure tapping grid used for the four models.

4.2 VORTEX BUBBLE STRUCTURE

The mean Cp contour plots for the 30^{o} model (figs.3.3.1.4-6) indicate a large rapidly expanding 3-dimensional bubble or a vortex. As Re increases the angle of the core line migrates towards the A-Pillar, with the high Re case showing clearly the possibility of a double vortex type structure merging to form a single structure. Thus based on these plots we would probably conclude that the vortex or bubble in the A-Pillar region is generated by the two vortex type structures amalgamating, i.e the A-Pillar vortex being entrained by the BV. As Re increases the merging position moves downstream and the BV strength alters producing the change in the vortex core line angle with a double high Cp region near the apex. If the low pressure region was due to a fully developed vortex then the mean Cp contour lines within the reattachment region would be expected to be parallel to each other along a line emanating from the apex (these types of contour are obtained downstream of the mean Cp core region for all three plots).

The Cp_{rms} plot (fig.3.4.1.4) only shows a single reattachment type region for all three Re, with the highest fluctuations adjacent to the reattachment line. But the position of this line has changed from being approximately perpendicular to the freestream direction to a line emanating from the apex (similar to a vortex core line) as A-Pillar angle increases from 20^{o} to 30^{o}.

The flow visualization results (Pl.3.1.1.4a-d) show a significantly more complex structure than that stated above. The structure generated is a mixed structure (Maskell(1955)), a bubble adjacent and almost parallel to the A-Pillar

with a vortex adjacent and downstream of the bubble, but emanating from the bubble. The vortex expands rapidly near the roof, indicating that it has probably burst (observed for all three Re). The flow within the bubble is very complex, producing a spiral flow (similar to that produced for the lower model angles).

The presence of the vortex type structure near the apex (mean Cp contour plot) is due to the movement of the spiral core towards the A-Pillar and at the same time away from the apex, as A-Pillar angle has increased to 30^{o}. Thus within a short region near the apex the vortex flow is parallel to the side window, but then rotates due to the primary recirculation region to form the spiral flow (perpendicular to side window). The kink in the core line angle occurs adjacent to the spiral core and it then follows the vortex core region. The change in the core line angle is probably due to the vortex breakdown point moving towards the apex as Re increases. As Re increases the base separation (BV) moves towards the primary separation line, thus the vortex has to rotate through a larger angle because the BV is almost parallel to the freestream upstream of the apex for the high Re case.

The position of the high Cp_{rms} region is within the vortex core region and the expansion of the Cp_{rms} core region as Re increases could be due partly to increased instability of the BV and partly due to the A-Pillar vortex tripping the model BL, producing a turbulent BL below the vortex region. For the 30^{o} model, half the A-Pillar region is dominated by a bubble and half by a vortex type flow.

As the A-Pillar angle is increased to 40^{o}, the separation region adjacent to the windscreen becomes very small (Pl.3.1.1.5a-d). The horseshoe vortex is still sitting on the model, just downstream of the 0^{o} whole model HV position, but the side views do not show the presence of a horseshoe vortex. The HV seems to act as a boundary, splitting the base separation into two distinct separation regions, both producing vortices which interact. The second BV is

entrained by the primary BV downstream of the HV position. The A-Pillar region is dominated by a rapidly expanding vortex type flow with a narrow bubble adjacent to the A-Pillar, which is dominated by a spiral flow (core adjacent to the roof-A-Pillar intersection). As Re increases the spiral core moves towards the apex. Two kinks are obtained in the flow visualization results indicating two mixing points. One is due to the two BV's mixing and the second is due to the entrainment of the A-Pillar vortex by the mixed BV's.

Based on the flow visualization and Cp results obtained by Poll (1980) for a sharp leading edge swept wing, Poll states that the position of the spiral core ('oil blob') indicates the vortex burst point.

The flows generated on the top half (Pl.3.1.2.1c) and whole model with plate (Pl.3.1.3.1c) are very similar, but less well defined with the vortex emanating from the apex. The above plots are less well defined, probably due to the vortex being 'weaker' or further from the side window surface producing higher Cpmin values, but almost similar mean Cp contour plots (fig3.1.1.7, fig.3.1.2.5, fig.3.1.3.5). The appearance of a spiral flow within the secondary separation region adjacent to the A-Pillar for the whole model indicates the presence of a recirculation bubble and not a secondary vortex. A similar structure is obtained for the other two vehicle models tested.

The mean Cp contour plots are almost identical for all three models i.e. a large vortex in the A-Pillar region which expands rapidly, then bursts near the roof. Vortex breakdown is indicated by the rapid expansion of the contour lines normal to the core line and downstream, with the flow turning near the roof to align itself with the freestream. The vortex core line angle is identical for all three models. The main differences between the three models are :-

i) The vortex core region ($Cp<-1.5$) is noticeably larger for the whole model compared to the other two models, but the region is almost identical on the other

two models. The difference is especially noticeable near the apex.

ii) The vortex core region for the low Re whole model is larger than the vortex core region for the high Re case for the other two models.

iii) The vortex core region area reduces more significantly for the whole model with plate than for the top half model as Re increases.

The reduction in the vortex core region as Re increases is due to the movement of the vortex breakdown point towards the apex in a similar manner to the flow over delta wings (Thompson (1985)). But the core region is significantly larger for the whole model due to the BV contribution which enhances the A-Pillar vortex.

The angle of the Cp_{rms} core region is identical for all three models (fig.3.4.1.5, fig.3.4.2.2, fig.3.4.3.2) and Re. The overall area of the Cp_{rms} core region is very similar for all the cases except for the whole model, where a major portion of the vortex region is covered by the Cp_{rms} core region. But the mechanism generating the large Cp_{rms} core region for all three models could not be ascertained from the mean Cp, Cp_{rms} or flow visualization results. But the fluctuations could be due to the vortex oscillating in the A-Pillar region and/or due to a turbulent BL underneath the vortex.

The water tunnel flow visualization results were obtained at a Re of approximately 10^3. As Wortmann (1984) and Thompson (1985) have found that vortex flows are Re dependent, its not possible to make quantitative comparisons, but as stated by Thompson 'some of the basic mechanisms of the vortex interactions will be qualitatively similar, irrespective of Re'.

The 40^o whole model results (Pl.3.2.1.1) show a very complex separation region with the flow very close to the body surface, if not interacting with the surface. The flow is very unstable, but does have a complex structure and it is not completely random. The two base separation regions interact forming an unstable vortex, which entrains the A-Pillar separation forming a

complex unstable vortex region. As the base separation regions interact, they become unstable and move closer to the body surface. The complex structure breaks down 2/3 of the way to the roof.

The flow generated on the whole model with plate (Pl.3.2.1.2) is identical below the plate to the previous model, with the two BV's interacting and becoming unstable at a point just downstream of the apex. Above the plate, a vortex generated at the apex, initially stable, then becomes unstable and moves towards the body surface continually entraining fluid separating from the A-Pillar. But half way along the A-Pillar the flow breaks down completely. Even before breakdown the structure is very complex, containing several vortices within the region at any one time for both road vehicle models.

4.3 FULLY DEVELOPED VORTEX

The flow structure obtained for the 50^{o} and 60^{o} models is identical to that of the classical fully developed vortex obtained on delta wings (top half and whole model with plate) and similar to that on a double delta wing for the whole model.

For the 50^{o} case (fig.3.3.1.8) the overall size and shape of the vortex region is identical for all three Re's, but subtle differences are observed even though the core line angle remains the same. Initially the vortex core region decreases by a small amount as Re increases, but a further increase in Re produces a noticeable decrease in the core region, partly due to the vortex breakdown point moving towards the apex. As stated above for the whole model at least two vortices are involved, with the BV being entrained into the A-Pillar region. The BV moves towards the primary separation line as Re increases, but its core angle adjacent to the apex remains constant.

The flow visualization results (Pl.3.1.1.6a-d) show a classical vortex

emanating from the 3-dimensional separation at the front of the base model, with two kinks, one just upstream of the apex and the second just downstream of the apex i.e two entrainment points. The strength and stability of the BV is affected by the reduction of the 3-dimensional bubble as Re increases. The presence of a burst vortex near the roof is indicated by the rapid expansion of the vortex region and the curvature of the secondary separation line.

The Cp_{rms} contour plot (fig.3.4.1.6) show a large core region (Cp_{rms}>0.15) either side of a line emanating from the apex. The angle of the mean and r.m.s Cp core regions is identical, thus the highest pressure fluctuations are generated under the vortex with the core region initially expanding and then contracting as Re increases. The large Cp_{rms} core region near the apex is due to the presence of a double vortex system, as the vortices interact the high core region contracts and then expands as we move downstream. The expansion is due to the growth of the vortex as more fluid is fed to the vortex from the A-Pillar. The initial increase and then decrease in the Cp_{rms} core region is probably due to changes in the BV stability and size as Re increases.

A concentrated slender vortex is obtained when the model angle is increased to 60^{o} (fig.3.3.1.9). Vortex stability has increased and the core line is nearer the A-Pillar compared to the 50^{o} model. The increased stability is inferred from the fact that the core region is narrower, but noticeably longer then for the previous angles. The change in the vortex core length or the core angle as Re increases is negligible, but the BV moves nearer the primary separation line as Re increases (Pl.3.1.1.7a-d). The entrainment position has moved downstream compared to the 50^{o} model. The entrainment position is indicated by the change in the vortex core line angle, this change is smaller for the 60^{o} model compared to the 50^{o} model.

The top half (fig.3.3.2.4) and the whole model with plate (fig.3.3.3.4)

also generates a narrow concentrated vortex, but both these regions are narrower with a smaller core region than that generated on the whole model. The core region initially expanded then contacted as Re increased. These models only generate a single vortex, but the angle of the vortex core line is identical for all three models. The mean Cp plots show that the vortex breakdown position is dependent upon Re.

The similarities between the three models observed from the flow visualization results (Pl.3.1.1.7a-d, Pl.3.1.2.1d, Pl.3.1.3.1d) are :-

i) A narrow concentrated vortex which expands rapidly adjacent to the roof, indicating vortex breakdown in this region.

ii) The secondary separation line curvature near the roof increases with increasing Re, probably due to vortex breakdown.

iii) The large secondary separation region adjacent to the A-Pillar becomes smaller as Re increases. This effect was observed on delta wings by Wortmann (1984) and on double delta wings by Thompson (1985). This shift is attributed to boundary layer transition to a turbulent BL before it separates to generate the secondary vortex. Thus the secondary vortex is smaller, so its displacement effect is reduced allowing the primary vortex to move outboard (towards the A-Pillar) and towards the body surface.

The main differences between the whole model and the other two models are :-

i) The whole model vortex emanates from the 3-dimensional separation at the front of the base model and not the apex, as for the other two models.

ii) As a result of the above difference, the whole model vortex is more stable, so vortex breakdown is delayed to a point further downstream compared to the other models.

The structure of the Cp_{rms} contour plot for the whole model (fig.3.4.1.7) is similar to the mean Cp plot, with a core centre along the same

core angle as that for the mean Cp contours. Thus the highest fluctuations occur below the vortex core. The Cp_{rms} core region expands as Re increases from the low Re case, but then decreases for the high Re case. This is thought to be due to BL transition from a laminar to a turbulent BL below the vortex; this increases the pressure fluctuations, with the vortex moving towards the body surface. A further increase in Re reduces the Cp_{rms} core region as the vortex moves away from a line of pressure tappings (towards the A-Pillar).

The Cp_{rms} contour plots for the top half (fig.3.4.2.4) and the whole model with plate (fig.3.4.3.4) shows a narrower Cp_{rms} core region. But the core angle is identical for all three models and is aligned with the mean Cp core line. But the Cp_{rms} core region is significantly smaller for the top half compared with the whole model and it disappears as Re increases. But for the whole model with plate this region is very large and remains large as Re increases. The cause of this large core region could be due to the plate BL becoming turbulent (several tappings were very close to the plate). The general shape and size of the Cp_{rms} contour region is similar to the top half model.

The water flow visualization results for the 60^{o} models (whole model (Pl.3.2.1.1) and whole model with plate (Pl.3.2.2.1)) both show a narrow concentrated vortex, but several important differences were observed between the two models.

The whole model vortex emanates from the two separation regions on the base. These two regions interact forming a single vortex before being entrained into the A-Pillar region. But on the plate model the A-Pillar vortex emanates from the apex, with the base separation forced below the plate. The separation below the plate breaks down just downstream of the apex. Above the plate a very stable vortex is formed (identical to a delta wing flow), with a secondary vortex adjacent to the A-Pillar. The A-Pillar vortex bursts earlier on

the plate model, but the breakdown position on the whole model fluctuated along the vortex core line (observed during experiments).

The flow visualization photographs show that the whole model vortex is more complex then the vortex flow on the plate model, with the larger whole model vortex closer to the body surface. These photographs also show different types of vortex breakdown on the models. A bubble type breakdown on the plate model (above the plate). The nature of breakdown below the plate is not clear. But on the whole model, a spiral breakdown is observed. This is shown by the plan view photographs and the side view close ups. A large amount of research has been conducted on vortex breakdown mechanisms and the variables affecting the type of breakdown (bubble or spiral) (Leibovich(1983)). But only general conclusions have been drawn about the breakdown mechanisms and the variables affecting them.

Turning to the swept plate model, the transition from type I separation to type III separation occurs between 10^{o} and 20^{o} sweep angle. The flow generated on the 20^{o} model has a strong vortex (fig.3.3.4.2), close to the leading edge, but not parallel to it. A large vortex core region covering the whole vortex region was obtained for the low Re case within the pressure tapped region, the spanwise length of this region decreased as Re increased.

As the sweep angle increases to 40^{o} (fig.3.3.4.3), the vortex region becomes narrower and moves towards the leading edge, with a subsequent reduction in the core region. The core region expanded rapidly, then decreased in size as Re increased. The increase is due to the vortex moving towards the surface caused by a similar mechanism to that for the 60^{o} whole model i.e transition of BL. A subsequent increase in Re moves the vortex away from a line of pressure tappings.

A further increase in the sweep angle to 60^{o} (fig.3.3.4.4), produces a narrower vortex region, which forms closer to the leading edge. The mean Cp

contour plots show similar trends to those observed on the 40^{o} sweep angle setup within the core region. But the nature of the contours at mid-span indicate that the vortex bursts in this region. The mean C_p contour plot shows that the vortex position varies with Re, it moves downwards and outwards (towards leading edge) as Re increases.

The C_{prms} contour plots (figs.3.4.4.2-3) show that the core region is downstream of the mean C_p core line. But the highest fluctuations were generated below the vortex core region. The increase in the C_{prms} core region is due to BL transition to a turbulent BL, with the region remaining the same with a further increase in Re. The 60^{o} C_{prms} contour plot (fig.3.4.4.3) produced very low pressure fluctuations, indicating that a very weak stable vortex is generated on the model or that the tapping spacings are too large to detect the vortex.

4.4 POWER SPECTRA

By plotting the spectral data in terms of non-dimensional quantities, several interesting flow features are observed.

The 40^{o} whole model plot (fig.3.5.1) shows a spectrum with two broad peaks at n_n=11 and 20, whereas the 60^{o} whole model spectra plot (fig.3.5.2) only shows a single broad peak at n_n=20.

Considering the nature of the flows generated on the 40^{o} and 60^{o} whole models, several sources could generate the pressure fluctuations which produce the broad peaks :-

i) Primary vortex oscillating above the model surface

ii) Oscillations of the secondary separation line

iii) Turbulent eddies within the BL underneath the vortex

iv) Turbulent eddies circulating within the vortex and passing over the model surface.

v) Oscillations of the reattachment line

If the broad peaks were generated by the turbulent eddies (iii and iv), then the appropriate length scale we would use is the eddy size (assume approx. 5mm). This would mean for the flow velocities studied here that the relevant frequencies are likely to be in the range 5-10KHz. However the fluctuating pressure data was filtered at 1KHz, and thus it is not possible that the broad peaks are generated by these sources.

Thus the broad peak generated on both the whole models (40^{o}, 60^{o}) could be due to any one of the other sources. However it is not clear what the relevant length scale is likely to be.

The water flow visualization results (Pl.3.2.1.1,Pl.3.2.2.1) show a very complex flow structure, with what appears to be several vortices within the A-Pillar region for the 40^{o} whole model. But for the 60^{o} whole model the primary vortex generated in the A-Pillar region appears to be completely steady.

The r.m.s C_p plots for the 40^{o} and 60^{o} whole models also show a large difference between the two models. For the 60^{o} whole model the highest pressure fluctuations are confined to the apex region and they decrease as we move downstream. But for the 40^{o} whole model the highest pressure fluctuations are generated along a line emanating from the apex. The angle of this line is such that it lies directly under the vortex generated on this model (see Pl.3.1.1.5a-d). Thus the broad peak generated on the 60^{o} whole model spectra plot is probably due to oscillations of the primary vortex because the region of maximum r.m.s C_p coincides with the region of lowest mean C_p plots. The

wind tunnel flow visualization results show that this region lies beneath the core of the main vortex.

For the 40^{o} whole model the pressure fluctuations are possibly due to a combination of oscillations of the primary vortex and oscillations of the secondary separation line, with the combination of these oscillations producing the high pressure fluctuation region along a line emanating from the apex. It is thought that the higher broad peak (n_n=20) obtained on both models is probably due to oscillations of the vortex, and the lower broad peak (n_n=11) on the 40^{o} model is probably due to the oscillations of the secondary separation line.

Figure 3.5.2 shows that as Re increases the spectra levels of the broad peak increase noticeably. This effect could be due either to the amplitude of the vortex oscillations increasing with Re or that the primary vortex moves towards the model surface due to the BL below the vortex becoming turbulent. Transition delays secondary separation, resulting in a smaller secondary vortex, allowing the primary vortex to move closer to the model surface (Wortmann (1984)).

The plots for the three models with a 40^{o} A-Pillar angle collapse onto more or less a single curve (fig.3.5.4) except at frequencies below about n_n=4.0. As all three spectra are almost the same, we can conclude that the basic flow structure must be very similar in each case.

Figure 3.5.5 shows the results obtained at four tappings on the 40^{o} whole model, with 3 tappings within the vortex region (A,B,C) and one in the attached flow region. Tappings A and B lie directly below the vortex core with tapping A upstream of tapping B and on the same radii. Thus the shape of the spectra plots for the respective tappings and their relative positions suggests that the relevant length scale could be based on the distance from the vortex origin to the relevant tapping. Tapping C lies near the edge of the vortex, but the same distance from the apex as tapping B. Thus the similar nature of the spectra plots

with an almost constant difference between the two spectra plots (lower levels for tapping C) over the range plotted suggests that the spectra levels could be dependent upon a scaling factor based on distance from the C_{prms} core line to the relevant tapping.

A similar plot for the 60^{o} whole model (fig.3.5.6) shows that the spectral levels measured at the two tappings within the vortex region are almost identical up to n_n equal to about 12.5. According to the mean and r.m.s C_p contour plots, tapping A is just about under the vortex core area, but tapping B is outside this region. The plots suggest that the highest spectra levels are due to the primary vortex oscillating (see appendix 5) and that these levels reduce noticeably for tapping B. The highest levels for the tapping within the attached flow region were also around n_n=20.0, except for the single spike at 7.5. The the cause of the spike is not clear.

The spike was obtained for the majority of the spectral plots at approximately 7.0-8.0 and may be due to the wind tunnel or electrical equipment noise.

4.5 GENERAL DISCUSSION

All mean Cp data used for the contour plots has been corrected for the effects of wind tunnel blockage.

Figure 4.5.1 shows a plot of Cp_{min} versus A-Pillar angle for the whole model and the effect of Re on the results. The results seem to be Re dependent for all angles except 60^{o}. The nature of change in the Cp_{min} values shows the change in flow structure from a bubble separation to a fully developed vortex as A-Pillar angle increases. The dependence of the results on Re can be attributed to several factors for each flow structure, these are stated below:-

i) Three-dimensional bubble

a) The reduction in the size of the spiral core region and its movement towards the apex. The movement of the core could result in it moving away from a tapping. A reduction in its size could produce a similar effect on the pressure contour plots.

b) The increased instability of the core as Re increases will reduce the suction peak as only the mean suction pressure will be recorded i.e at a point near the core, as the instability increases the data recorded will be a function of time as the core oscillates producing a lower mean value at that point (assuming a normal type pressure distribution around the core).

c) The stability and strengths of the base separations are dependent upon Re (separation of a curved surface), they effect the spiral region.

ii) vortex bubble structure

a) For the 30^{o} model the peak negative Cp values are within the bubble region, thus the factors affecting the results are similar to those stated above i.e spiral core instability, reduction in spiral core size, core movement, etc.

b) The 40^{o} model's flow is turbulent, even for the low Re case. The vortex is unsteady, generating a broadband peak at n_n=11 (see section 4.4).

c) As the basic structure of the A-Pillar separation is a vortex, it should move outboard as Re increases, resulting in an increase in the Cp_{min} value (core moves away from a pressure tapping line). The movement of the vortex must be small since the peak Cp_{min} value was recorded at the same tapping for all three Re's.

d) Re effects on the BV strength and its movement towards the primary separation line as Re increases.

iii) fully developed vortex

As the A-Pillar angle increases above 40^{o}, the flow separating from the A-Pillar rolls up to form a fully developed vortex. This stable vortex has moved away from the surface as the angle increased, noticeably decreasing the Cp_{min} value. Other factors affecting the Cp_{min} value are :-

a) The movement of the BV as Re increases, with BV moving towards the primary separation line.

b) Movement of the vortex initially downwards and outwards as the BL becomes turbulent and then a continual outward movement as Re continues to increase.

c) The position of vortex breakdown indicate stability of the vortex, thus affecting the Cp_{min} value. For the 60^{o} whole model the breakdown position oscillated.

For the 60^{o} whole model, Re effects appear to be almost negligible (a small increase in Cp_{min} as Re increased). This is due to the vortex moving towards the surface, but at the same time moving away from a tapping producing a small increase in Cp_{min}. The worst angle as far as Cp_{min} values are concerned is 40^{o} for the whole model.

A similar curve was obtained for the swept plate model (fig.4.5.2), but the lowest Cp values were found on the 30^{o} sweep model and not 40^{o} (whole model). On the swept plate model, a bubble type structure was obtained only for 0^{o} and 10^{o} models, but a vortex structure for the other model angles. Re effects below sweep angles of 20^{o} appear to be negligible, but this is probably due to the movement of the 3-dimensional bubble region as Re increases.

The general trend observed for the fully developed vortex region on the swept plate (20^{o}-60^{o}) based on the mean and r.m.s Cp contour plots is that as the Re increases, the BL on the model becomes turbulent and the vortex moves downward and outboard towards the leading edge. This outward movement

continues as Re increases. But the Cp_{min} values for 20^{o},30^{o}, and 40^{o} sweep angle increase as Re increases. As these values were recorded adjacent to the apex, in this region the increase in Cp_{min} with Re is probably due to the vortex core moving towards a tapping line as Re increases. But for the 60^{o} model the vortex core initially moves towards a tapping line, then away with a further increase in Re.

Comparisons between the three vehicle models of Cp_{min} versus A-Pillar angle (fig.4.5.3) produces a similar Cp_{min} distribution as that for the whole model, except that only four angles were tested for the other two models. The worst angle in terms of Cp_{min} is 40^{o} for both the top half and whole model with plate. A closer examination of the variation of Cp_{min} with Re for the three models using the results for three angles (0^{o},40^{o} and 60^{o}) shows that the BV has a significant effect on pressure levels generated in the A-Pillar region. The pressure levels generated on the whole model with plate and the top half are almost identical for all three angles and Re's tested. The difference in Cp_{min} between the whole model and the other two models (fig.4.5.4) was very similar for the lower angles (0^{o}-20^{o}), except for the top half 20^{o} model where the Cp_{min} value is in between that for the other two models due to the ground board BL separation. As the A-Pillar angle increased to 40^{o} (fig.4.5.5) the difference increased significantly, but a further increase in A-Pillar angle (fig.4.5.6) reduced the difference to a level below that for the 0^{o} model.

The vortex core line angle was plotted against the A-Pillar or sweep angle (fig.4.5.7) for all four models. Similar data from Elle's report (1961) was also used as a comparison. The error band for the four models used in this research is +/- 2.5^{o}, due to the nature of the mean pressure tapping grid used. The error band for Elle's data in not known. The results show that the three vehicle model results and those from Elle's report lie along the same curve,

whereas the swept plate results generate a parallel curve for the lower angles (20^{o}-40^{o}), but then joins the vehicle data curve. The difference between the swept plate and the vehicle models can be attributed to the difference in the aspect ratios for the various models. The vehicle model's aspect ratio (AR) being 0.646 and an infinite AR for the swept plate (AR is defined as span/thickness). As swept plate AR was reduced to 6.0, the vortex core angle and the Cp_{min} value increased (fig.4.5.8).

The variation of Cp_{rms} with vehicle model type and Re is important as it has a significant effect on the noise levels generated on that model. Thus the variation of peak Cp_{rms} with model type and Re was plotted for three angles (0^{o},40^{o}, and 60^{o}). For the 0^{o} models (fig.4.5.9), the lowest fluctuations are generated on the whole model with plate. This is expected due to the nature of the flow field, the primary bubble does not contain an unstable spiral flow. The whole model produces the highest fluctuations due to the unstable BV.

For the 40^{o} models (fig.4.5.10), the highest fluctuations are generated on the whole model, again due to the BV contribution, but comparing the mean and Cp_{rms} contour plots for the other two models, their peak Cp_{rms} values should be very similar. The cause of the higher fluctuations on the whole model with plate were assumed to be due to the plate turbulent BL contribution. But this effect was not detected in the spectra plots (fig.3.5.4) as the plots for all three models collapsed onto a single curve below a n_n value of 25.0.

A similar plate turbulent BL assumption was made for the 60^{o} model (fig.4.5.11) , with the plate BL fluctuations being the dominant factor as the pressure tappings are closer to the plate compared to the 40^{o} model. But the spectral plots from the peak Cp_{rms} tapping data for the three models (fig.4.5.12), show significantly higher spectra levels for the whole model with plate over the whole spectral bandwidth compared to the other two models. The

plots for the other two models collapse onto a curve, the plate model curve shape is similar but with an almost constant difference over the whole bandwidth, except for n_n below 6.0. The highest spectra levels were generated below n_n=6.0 for the whole model with plate, but the contribution of the plate turbulent BL alone would not produce such a large increase in Cp_{rms}. Thus the similar nature of the plots can be attributed to several factors :-

i) The whole model results (peak Cp_{rms}) near the apex are different due to the presence of two vortices interacting, thus affecting the position of the A-Pillar vortex core.

ii) For the top half, the lower peak Cp_{rms} value obtained near the apex is probably due to the ground board BL affecting the flow field in this region. The large ground board BL will displace the vortex core towards the A-Pillar.

iii) But for the whole model with plate the plate BL is very thin, thus its displacement effect on the vortex and its effect on the flow field within the apex region are negligible.

The results obtained using a simple potential flow theory (appendix 5) are now compared with the mean Cp results from the road vehicle whole model. For A-Pillar angles greater than 30^{o}, where the water flow visualization results (Pl.3.2.1,2) show that the vortex core angle is close to the A-Pillar angle, the theoretical results are similar (Fig.A.5.1) to the mean Cp results for the whole model. The theoretical Cp_{rms} results generated (table.A.5) assuming that the vortex position fluctuates normal to the model surface show similar trends to the experimental results obtained in the apex region on the whole model. The theoretical Cp_{rms} results generated assuming that the vortex position fluctuates parallel to the model surface with the same displacement as that for the normal direction are an order of magnitude smaller than the experimental results.

Comparisons between the theoretical mean Cp results and those obtained experimentally on the other two road vehicle models shows a large

difference due to the vortex core angle being larger than the A-Pillar angle because the vortex emanates from the apex. The nature of the theoretical Cp_{rms} results indicate that if the vortex is oscillating within the A-Pillar region and contributing to the pressure fluctuations, then the major contribution is probably due to oscillations of the vortex normal to the model surface rather than parallel to the model surface.

5.CONCLUSIONS

An experimental investigation of the A-Pillar vortex region on idealised road vehicle models has been carried out. The investigation was aimed at examining the effect of A-Pillar angle upon the flow structure and flow-induced noise. Mean and fluctuating pressure surveys were conducted in the A-Pillar region for several A-Pillar angles (0^{o}-60^{o}) and Reynolds Numbers ($5.672x10^{5}$-$9.580x10^{5}$). The models used were a whole model, top half attached to a ground board and whole model with a small plate attached near the root of the A-Pillar (see section 2.7). These surveys were also conducted on a blunt swept plate model ($5.270x10^{4}$-$1.166x10^{5}$). Flow visualization techniques were also used on the road vehicle models as a means of investigating the structure of the A-Pillar flow.

5.1 FLOW VISUALIZATION

i) Wind Tunnel

Flow visualization results for the wind tunnel study show the presence of three distinctive flow structures within the A-Pillar region, dependent upon the A-Pillar angle. The three flow regimes generated on the models are :-

TYPE I	Three-dimensional bubble
TYPE II	Vortex bubble (mixed flow)
TYPE III	Fully developed vortex

The type of flow generated on each model and the angle at which each flow type is obtained is summarised in the table below:-

MODEL TYPE	MODEL ANGLE	FLOW TYPE
ROAD	0,10,20	I
VEHICLE	30,40	II
MODELS	50,60	III

MODEL TYPE	MODEL ANGLE	FLOW TYPE
SWEPT PLATE	0,10	I
MODEL	20-60	III

The above table is based on flow visualization results for the road vehicle models and pressure results for the swept plate model.

ii) Water Tunnel

Water tunnel flow visualization results for the 40^{o} models show an almost identical complex flow structure for the whole model and whole model with plate. But the position of vortex breakdown is affected by the base vortex which enhances the A-Pillar vortex and so moves the breakdown position downstream for the whole model. The nature of the flow on the whole model with plate within the A-Pillar vortex region indicates that the instability is due to two factors :-

i) Unstable Base vortex

ii) Partial entrainment of the A-Pillar vortex into the boundary layer.

The two 60^{o} models (whole model and whole model with plate) have a similar fully developed vortex in the A-Pillar region, but several differences were observed between the two models :-

i) The vortex on the whole model appears to be less stable due to the entrainment of the base vortex into the A-Pillar vortex.

ii) The vortex on the whole model appears to be closer to the model surface.

iii) The whole model vortex breakdown position was observed to oscillate about a mean position, not observed for the other model.

iv) The type of vortex breakdown, bubble type breakdown for the whole model with plate and spiral type for the whole model.

5.2 MEAN PRESSURE

The mean Cp contour plots only indicate the presence of TYPE I flow (0^o-30^o) and TYPE III flow (40^o-60^o) on all three Road Vehicle models. The basic flow structure for the top half and whole model with plate are very similar to that for the whole model. All three flow regimes are found to be Reynolds Number (Re) dependent for the vehicle models, but for the swept plate the mean Cp results indicated that Re dependence was confined to sweep angles greater than 20^o.

The presence of three different flow regimes can also be seen from the plot of Cp_{min} versus A-Pillar angle for the whole model. For TYPE I flows the Cp_{min} values are similar, but as the A-Pillar angle increases, TYPE II flow is generated with the Cp_{min} values decreasing significantly with a further increase in A-Pillar angle (TYPE III flow), the Cp_{min} values start to increase noticeably. Based on the four angles tested for the top half and the whole model with plate, a similar trend to that obtained for the whole model is obtained for these two models. Thus the critical A-Pillar angle defined as the angle for the lowest Cp_{min} value generated on all three road vehicle models is 40^o and for the swept plate model the critical sweep angle was found to be 30^o.

The variation of Cp_{min} with A-Pillar angle was similar for all three models, with the magnitudes almost identical for the top half and whole model with plate (except for the 20^o model). But the Cp_{min} values for the whole model are significantly lower, indicating that the model base has a large effect on the flow within the A-Pillar region for all angles.

A plot of the vortex core angle versus A-Pillar angle for all four models, with additional data obtained from Elle (1961) show that the vehicle data and the delta wing data lie along the same curve. But the swept plate data initially runs parallel to the vehicle data, but than joins the main curve at a sweep angle of 60^o. The difference between the two curves is thought to be due to the two models

having different Aspect Ratio's (AR). As the 40^{o} sweep angle model AR is reduced to 6.0, its vortex core angle moved towards the vehicle model curve and the Cp_{min} value increased significantly.

5.3 FLUCTUATING PRESSURE

The C_{prms} contour plots show that the highest levels are generated on the 40^{o} vehicle models and on the 30^{o} model for the swept plate.

For the 0^{o} A-Pillar angle models the lowest levels are obtained on the whole model with plate, due to the absence of an unsteady spiral flow region within the primary separation bubble. The highest levels were found on the whole model for both the 0^{o} and 40^{o} models. For the 60^{o} models the highest C_{prms} levels were found on the whole model with plate, these values were significantly higher than those obtained for the other two models (almost identical).

A study of the power spectral density results was carried out for the 40^{o} whole model as it generated the highest C_{prms} values. For this model, all three non-dimensional spectral plots (one for each Re tested) collapsed on to a single curve with two broad peaks at n_n=11.0 and 20.0. But the spectral plots for the 60^{o} whole model showed only one broad peak at n_n=20.0 for the two higher Re values. This increase in the spectral levels of the broad peak (n_n=20.0) for the higher Re is thought to be due to the unsteady primary vortex moving closer to the model surface because the BL below the vortex becomes turbulent, delaying secondary separation. Thus the secondary vortex is smaller reducing the influence of the secondary vortex on the primary vortex, allowing the primary vortex to move closer to the model surface (Wortmann (1984)). Thus the main cause of the pressure fluctuations for the 60^{o} model is thought to be the unsteadiness of the primary vortex. The spectral plots for the 40^{o} whole model suggest that the vortex is oscillating for all three Re and the second peak at n_n=11.0 could be due to

oscillations of the secondary separation line underneath the vortex region. The spectral study also shows that the flow structure within the A-Pillar region is similar for all three 40^{o} models.

Spectral plots for the 40^{o} and 60^{o} whole models show that the spectra levels measured in the attached flow region are noticeably lower than the levels generated within the vortex flow region, except for frequencies below about n_n=6.0. Spectra results obtained at three positions within the vortex region for the 40^{o} whole model seem to suggest that a relevant length scale could be a function of the distance from the primary vortex origin to the relevant tapping.

The spectral plots for the signal obtained at the tapping giving the peak C_{prms} tapping for the three 60^{o} models follow the same curve for n_n above 6.0, but the spectra levels generated on the 60^{o} whole model with plate are noticeably higher. The nature of the plots indicate that the difference is due to the vortex core position being a function of the type of model tested. For the whole model the vortex core position is effected by the base vortex, but for the other two models the primary factor is the displacement effect of the respective plate and ground board boundary layers.

A simple potential flow model (appendix 5) predicts mean C_p values which are similar to the whole model mean C_p results within the apex region for A-Pillar angles greater than 30^{o}. But the experimental results for the other two road vehicle models are different to the theoretical results. The theoretical C_{prms} results indicate that if the vortex is oscillating and contributing to the pressure fluctuations within the A-Pillar region, then a major contribution is probably due to the vortex oscillating normal to the model surface rather than oscillating parallel to the model surface.

6. SUGGESTIONS FOR FURTHER WORK

The flow visualization results show clearly that the base separation has a significant effect on the flow within the A-Pillar region. Thus a quantitative study, making use of mean and fluctuating pressure measurements should be carried out in the base separation region. This study should be aimed at investigating the influence of the base vortices and the horseshoe vortex on the A-Pillar region.

The fluctuating pressure grid used was rather coarse. Thus the density of the grid should be increased within the high Cp_{rms} region for each A-Pillar angle. The fluctuating pressure data was collected for a single point at any one time. By making simultaneous measurements at several points an estimate of spatial correlation could be obtained at a number of positions to determine correlation lengths. This correlation data can also be used to analyse the nature of vortex unsteadness generated on the 30^{o} and 40^{o} models.

Several variables, which were fixed for this research should be varied to study their influence on the A-Pillar region. Some of these variables are :-

i) A-Pillar curvature

ii) Windscreen curvature (single and double)

iii) On most production vehicles the A-Pillar region (side window) is inclined (approx.15^{o}) relative to vertical.

The pressure measurements show that the flow is Reynolds number dependent, thus scale effects should be studied. Larger models should be tested in a bigger wind tunnel to study Reynolds number effects.

The conditions generated in a wind tunnel may be significantly different to those encountered on the road. Thus the effects of natural wind conditions on the A-Pillar region should be studied. The important variables involved when considering natural winds are :- wind yaw angle, turbulence levels, etc.

5.REFERENCES

1. BEARMAN P.W, De BEER D, & HARVEY J.K

Experimental studies of road vehicle flow fields - AIAA-89-1887 (AIAA 20th Fluid Dynamics, Plasma Dynamics and Lasers Conference, Buffalo, New York, June 12-14, 1989).

2. BEARMAN P.W, MOREL T

Effect of free stream turbulence on the flow around bluff bodies. - Prog. Aerospace Sci. Vol.20, pp.97-123, 1983.

3. BENDAT J.S, PIERSOL A.G

RANDOM DATA: Analysis and Measurement Procedures - Wiley, 1971.

4. BRADSHAW P, PANKHURST R.C

The design of low speed Wind Tunnels. Progr. in Aeron. Sci. Vol. 5, Pergamon Press, London 1964.

5. BUCHIEM R, DOBRZYNSKI W, MANKAU H, & SCHWABE D

Vehicle interior noise related to external aerodynamics. Int. J. of Vehicle Design, Technological Advances in Vehicle Design, Series, SP3, Impact of Aerodynamics on Vehicle Design, pp.197-209.

6. BUCHIEM R, PIATEK R, & WALZER P

Contribution of aerodynamics to fuel economy improvements for future passenger cars, First International Automotive Fuel Economy Conference, Washington, October, 1979.

7. BUCHIEM R, LEIE B

The development of the new Audi 100 - a new approach in aerodynamic passenger car design, International Symposium Vehicle Aerodynamics, Wolfsburg, 1982.

8. CARR G.W

The aerodynamics of basic shapes for road vehicles, part 2, saloon car bodies, MIRA Rep. No.1968/9.

9. CARR G.W, STAPLEFORD W.R

Blockage effects in Automotive wind-tunnel testing - S.A.E 860093.

10. CHANAUD R.C, MUSTER D

Aerodynamic noise from motor vehicles - Journal of Aoust. Soc. America, Vol.58, No.1, July 1958, pp.31-38.

11. CHERRY N.J, HILLIER R, & LATOUR M.E.M.P

The unsteady structure of Two-dimensional Separated and Reattaching flows. J. of Wind Eng. and Ind. Aero. 11(1983), 95-105.

12. CLEMENTS M.P.M, UNWIN G.P

Calibration of the 3'x3' low speed Wind Tunnel of Imperial College. Third Year project 1973.

13. COOPER K.R

The wind tunnel simulation of surface vehicles, J. of Wind Eng. and Ind. Aerodynamics, Vol.17, 1984, pp.167-198.

14. DAVIS J.P

Wind Tunnel investigation of road vehicle wakes - Phd. - University of London, 1982.

15. DOBERENY M.E, SELBERY B.P

A parametric investigation of the validity of 1/25 scale automobile aerodynamic testing. S.A.E 760189 (1976).

16. DOBRZYNSKI W

Significance of unsteady surface pressure for aerodynamically induced interior noise of automobiles - DFVLR-FB-83-28, Sept 1983.

17. DOBRZYNSKI W, GEHLHAR B, HELLER H, & MANKAU

External flow induced interior noise - A problem in advanced automobile design - Proc. Inter-Noise 81, pp.723-726.

18. DOBRZYNSKI W, GEHLAR B

Aerodynamically induced internal noise in passenger cars - Sources and possibilities of reduction, International Symposium, Wolfsburg, Germany, 1982.

19. ELLE B.J

An investigation at low speed of the flow near the apex of thin Delta wings with sharp leading edges, Aeronautical Research Council, R&M 3176, Jan.1958.

20. GAD-EL-HAK M, BLACKWELDER R.F

The discrete vortices from a Delta wing, AIAA Journal, Vol.23, June 1985, pp.961-962.

21. GAD-EL-HAK M, BLACKWELDER R.F

Control of the discrete vortices from a Delta wing, AIAA Journal, Vol.25, August 1987, pp.1042-1049.

22. GUMLEY S.J

A detailed design method for pneumatic tubing systems. J. of Wind Eng. and Ind. Aero. 13(1983) 441-452.

23. HEALD R.H

Comparisons of the ground-plane and image methods for representing ground effects in tests on vehicle models. J. Res. Natl. Bur. Stand. (U.S.), 13(1934).

24. HUCHO W.H

Aerodynamics of Road Vehicles - University Press, Cambridge, 1987.

25. HUCHO W.H, JANSSEN L.J, & SCHWARZ G

The Wind Tunnel's ground plane boundary layer - its interference with the flow underneath cars. S.A.E 750066 (1975).

26. IRWIN H.P.A.H, COOPER K.R, & GIRARD R

Correction of distortion effects caused by tubing systems in measurements of fluctuating pressures. J. Indst. Aero. 5(1979), 93-107.

27. KIND R.J

Worst suctions near edges of flat rooftops on low-rise buildings, J. of Wind Eng. and Ind. Aerodynamics, Vol.25, 1986, pp.31-47.

28. KRAMER C, GREHARDT H.J, & SCHERER S

Wind pressure on block-type buildings. J. of Ind. Aerodyn. Vol.4, 1979, pp.229-242.

29. KUCHEMANN D

The Aerodynamic Design of Aircraft. - PERGAMON PRESS, 1978.

30. LAY W.E

Is 50 miles per gallon possible with correct streamlining ? S.A.E Journal, Vol.32, pp.144-156 and 177-185.

31. LEE G.H

Note on the flow around delta wings with sharp leading edges - Handley page Ltd, R & M 3070, Sept. 1953.

32. LEIBOVICH S

Vortex Stability and Breakdown, AGARD-CP-342, April 1983.

33. LIU M.J, LU Z.Y, QIU C.H, SU W.H, GAO X.K, DENG X.Y, & XIONG S.W

Flow Patterns and Aerodynamic Characteristics of a Wing-Strake Configuration. - J. of Aircraft, Vol.17, May, 1980.

34. LOREA A, CASTELLUCCIO V, COSTELLI A, & MASOERO M

A wind tunnel method for evaluating the aerodynamic noise of cars - S.A.E 860215.

35. LYTHE G, SURRY D

Wind loading of flat roofs with and without parapets. J. of Wind Eng. Ind. Aerodyn. Vol.11, 1983, pp.75-94.

36. MACKWOOD P

Private Communication - 1989.

37. MASKELL E.C

Flow Separation in Three Dimensions - R.A.E Aero.2565, Nov. 1955.

38. MASON W.T, SOVRAN G

Ground plane effects on the aerodynamic characteristics of automobile models - an examination of Wind Tunnel test technique. Adv. Road Veh. Aerodyn. Br. Hydrodyn. Res. Assoc., Fluid Eng. (1973).

39. OBASAJU

Pressure fluctuations on stationary and oscillating Square section Cylinders - PhD - University of London, 1977.

40. OSWALD L.J

Exterior radiated aerodynamic noise of vehicles at highway speeds - Proc. Inter-Noise 78, San Francisco, 1978, pp.711-714.

41. PETERKA J.A, MERONEY R.N, & KOTHARI K.M

Wind flow patterns about buildings, J. of Wind Eng. and Ind. Aerodynamics, Vol. 21, 1985, pp.21-38.

42. POLL D.I.A

On the generation and subsequent development of spiral vortex flow over a swept-back wing, AGARD CP-342.

43. POTTHOFF J

The Aerodynamic lay out of UNICAR Research vehicle - International Symposium, Wolfsburg, Germany, 1982.

44. REDINIOTIS O.K, TELIONIS D.P

Periodic vortex shedding over Delta wings - AIAA-89-1923 (AIAA 20th Fluid Dynamics, Plasma Dynamics and Lasers Conference, Buffalo, New York, June 12-14, 1989).

45. ROMBERG G.F, LAJOIE R.G

An objective method of estimating car interior aerodynamic noise - S.A.E 770393.

46. SCIBOR-RYLSKI A.J

Road Vehicle Aerodynamics, 2nd edition, Pentech Press, London, 1984.

47. SELL M

Private Communication - 1988.

48. STAPLEFORD W.R, CARR G.W

Aerodynamic noise in road vehicles - MIRA, Rep. No.1971/2.

49. STATHOPOULOS T, SURRY D, & DAVENPORT A.G

A simplified model of wind pressure coefficients for low-rise buildings. - Proc. 4th Colloq. on Industrial Aerodyn. Aachen, 1980, part1, pp.17-31.

50. SUTTON E.P

Experiments on a flow with swept separation and reattachment of a boundary layer - IUTAM Symposium on turbulent shear layers, 1983.

51. TAKAGI M, HAYASHI K, SHIMPO Y, & UEMURA S

Flow visualization techniques in automotive engineering. Impact of aerodynamics on Vehicle design. Int. J. of Vehicle Design. SP3, London, 1983, 500-517.

52. THOMPSON J.R

Wind Noise - A practical approach, S.A.E - Preprint 840B.

53. WATANABE M, HARITA M, & HAYASHI E

The effect of body shape on wind noise - S.A.E 780266.

54. WENTZ,Jr W.H, McMAHON M.C

An experimental investigation of the flow about Delta and Double-Delta wings at low speeds - NASA CR-521.

55. WORTMAN A

On Reynolds number effects in vortex flow over Aircraft wings - AIAA 22nd Aerospace Sci. Mtg., Reno, Nevada, 9-12 Jan. 1984, Paper AIAA-84-0137.

56. ZOHAR Y, Er-El J

Influence of the aspect ratio on the aerodynamics of the delta wing at high angle of attack, J. of Aircraft, Vol.25, No.3, March 1988, pp.200-205

APPENDIX:1

DATA ACQUISITION SYSTEMS

The 3'x3' wind tunnel is controlled manually, with the speed adjusted according to the reading on a Betz manometer. A computer is used to control an A/D unit and store data on a hard disc. This data is then backed up on floppy discs at a later date.

Data collection and storage on the hard disc is controlled by software. Two codes were written, one for collecting the mean pressure data and the second for collecting the fluctuating pressure data. Initially the data is stored in terms of voltages read directly from a pressure transducer and later it is processed to generate the mean and r.m.s pressure coefficient contour plots and power spectral density plots.

Both codes use the Tecmar card's internal clocks to set the sampling speed. Each sample is recorded when the mother board (see section 2.2) detects a rise in the clock from a low bit (0) to a high bit (1). The sampling speed can be adjusted by changing the mark to space ratio (fig.A.1.1).

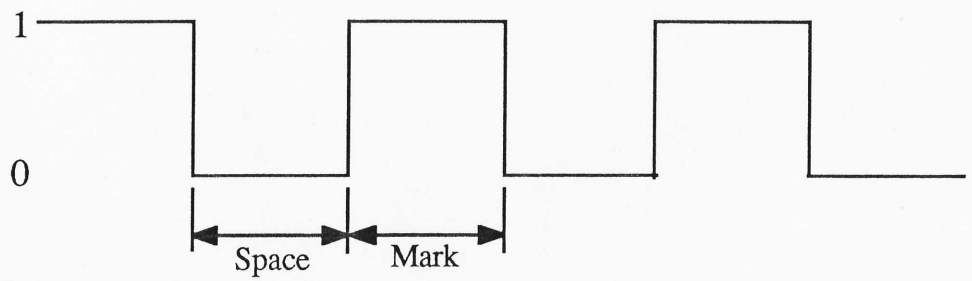


Fig.A.1.1

The only significant difference between the two codes occurs in the storage of the data on the A/D unit memory chip and in the storage format on the hard disc.

For the recording of mean pressure data (fig.2.10), using a scanivalve, the output from the transducer is zeroed and then the wind tunnel is started and the

speed set. The wind tunnel is allowed to settle before the tunnel pitot-static is recorded (first port on scanivalve). The scanivalve is then incremented manually, the voltage is allowed to settle and the sampling started again. The pitot-static value is recorded at the beginning and end of each scanivalve run.

During a scanivlave run the data recorded is the differential pressure between the model static pressure and the tunnel static pressure. For each tapping, only the mean values are recorded, and they are then stored on the hard disc. Before storage the data has to be converted from a 12-bit integer, as generated by the A/D unit to a 16-bit real number.

In the case of fluctuating pressure, the data is collected for a particular tapping and initially stored on a mother board. The data is then transferred to the hard disc. The data is stored as an integer array, so as to reduce the data file size on the hard disc. For this setup the transducer is connected as closely as possible to each tapping, via a cap/tubing system, to extend as far as possible the frequency range of the transducer-cap/tubing system.

APPENDIX 2

MEAN PRESSURE COEFFICIENT

The raw mean pressure data is processed to obtain mean pressure coefficients. The raw data is recorded in terms of a pressure differential voltage (see appendix 1). Thus for each model angle the pitot-static value is recorded several times during each run. The pressure coefficients are obtained by dividing each model tapping voltage by the mean pitot-static voltage. Having obtained the uncorrected mean pressure coefficient, the effects of wind tunnel blockage (due to the presence of the model) and tunnel calibration factor have to be considered.

Let the uncorrected mean pressure coefficient be Cpm. Then the mean pressure coefficient Cp is given by :-

$$Cp_c = (Cp_m + K_1) \qquad \text{A.2.1}$$

$$Cp = 1 - \frac{Q_c}{Q_m}\{1 - Cp_c\} \qquad \text{A.2.2}$$

But the wind tunnel calibration factor (K2) is a function of tunnel speed (fig.2.3.1.2) and the blockage ratio (Q_c/Q_m) for a wind tunnel blockage of 5% is 0.909. The variation K1 over the tunnel operating range is small (fig.2.1.3.3), thus :-

$$Cp = 1 - \frac{Q_c}{Q_m}\{1 - (Cp_m + K_1)K_2\} \qquad \text{A.2.3}$$

$$Cp = 1 - \frac{Q_c}{Q_m}\{1 - Cp_mK_2 - K_1K_2\} \qquad \text{A.2.4}$$

The corrected mean pressure coefficient values are used to generate the final contour plots.

The computer reads the raw data, calculates the mean pitot-static value and the corrected mean pressure coefficients. Then the pressure coefficients are written to a second file ready to be used to generate the contour plots.

APPENDIX 3

CONTOUR PLOTTING PROGRAM

The mean and fluctuating pressure data were collected for each model from a grid of pressure tappings (Pls.2.7.1.1,2 & 2.7.2.1) Using this data, the mean and r.m.s pressure coefficients were calculated (appendix2), and these values were then used to generate a series of contour plots.

For the array of tappings nearest to the A-Pillar/bonnet intersection only alternate mean pressure tappings were installed due to space limitations (Pl.2.7.1.1,2). Thus intermediate values were calculated using linear interpolation. Having obtained a regular grid of data points, these were used to generate the contour plots.

The contour plotting package for the mean pressure and fluctuating pressure data is identical, except that there are fewer fluctuating pressure tapping points. For the mean pressure data the contour package generates the pressure tapping grid used based on the windscreen angle, correct width/height ratio and number of tappings per arc. For the fluctuating pressure data the position of each pressure tapping has to be specified.

Once the magnitude and position of each data point is known, the maximum and minimum pressure coefficient values are obtained and used as the limits for the contour plots. The number of contours plotted can be varied depending upon the detail required and the increment in contour level is linear. It is assumed that the pressure coefficient varied linearly between data points.

Two main methods are available for plotting contours :-

i) Contour tracking method, where a particular contour is plotted through the whole region. This process is then repeated for all other contours.

ii) Cell plotting method, where a particular cell is considered and all contours

found in that cell are plotted before moving to another cell. This process is continued until the whole region is covered.

The first scheme is really a second order scheme, thus using it when the data has been linearised will not increase the accuracy of the contour plots. The algorithm required for the first scheme is also very complex, especially as a regular grid is used to obtain the original data. Thus the second scheme was used. Effectively the second scheme is a contour tracking scheme but in a single cell at a time. If three three sides of a cell contain a particular contour value then the scheme will join these three points. The main disadvantage with this scheme is that its direction dependent, it will give correct results if the cells are incremented in a particular sequence, i.e depends if the cells are incremented in the downstream direction or along a pair of arcs (Pl.2.7.2.1).

Calculation of contour magnitudes

The magnitude of the contours can be calculated using the contour increment value, the position of minimum C_p or maximum C_{prms} indicated with a cross on the contour plots and the fact that the contour colour changes (black to red) when C_p becomes less than or equal to -1.5. For the C_{prms} plots the colour changes when C_{prms} is greater than or equal to 0.15.

The magnitude of the first red contour adjacent to the black contours is given by :-

$$(\text{Min.}C_p - N_1 \times \text{Contour increment}) <= -1.5 \qquad \text{A.3.1}$$

$$(\text{Max.}C_{prms} - N_1 \times \text{Contour increment}) >= 0.15 \qquad \text{A.3.2}$$

Where N_1 = Integer value

Considering an example for each of the above cases we get :-

Using figure 3.3.1.1 for the mean C_p plots

Contour increment = -0.042 Min.C_p = -1.671

Thus using Eq.A.3.1 gives N_1 </= 4.07

thus $N_1 = 4$

Therefore the value of the first red contour adjacent to the black contours is

$$C_p = (-1.671-(4x-0.042)) = -1.503$$

Using figure 3.4.1.1 for the rms C_p plots

Contour increment = -0.004 Max.C_{prms} = 0.233

Thus using Eq.A.3.2 gives N_1 </= 20.75

thus $N_1 = 20$

Therefore the value of the first red contour adjacent to the black contours is

$$C_{prms} = (0.233-(20x0.004)) = 0.153$$

Thus having calculated the value of one contour, the others contour values can be calculated using the value of the contour increment.

If a colour change is not present on the plots, then the value of the first contour next to the position of the minimum mean C_p (x) or maximum rms C_p (x) is equal to :-

$$C_p = (\text{Min.}C_p - \text{Contour increment})$$

$$C_{prms} = (\text{Max.}C_{prms} - \text{Contour increment})$$

The magnitude of the rest of the contours can now be calculated using the value of the maximum (for C_{prms} plots) or minimum (for C_p plots) contour and the contour increment, because the contour values change linearly.

APPENDIX 4

Due to the large volume of data collected for both mean and fluctuating pressures for all four models (several Mbytes), only a sample of the raw data collected is included in this thesis. One mean pressure run (40^{o} whole model, Re No.$9.580x10^{5}$) and part of one fluctuating pressure data file collected on the same model at the same Re are included in this appendix.

The mean pressure data collected is shown in the table below followed by a plot of the fluctuating pressure data :-

Tube Number	Pressure Mean Voltage	Tube Number	Pressure Mean Voltage	Tube Number	Pressure Mean Voltage
1	1.00248	34	4.46442	66	1.53953
2	-0.92478	35	3.90013	67	1.51473
3	7.35527	36	3.51047	68	1.49026
4	5.51936	37	3.10652	69	1.45157
5	4.36149	38	2.72655	70	4.20591
6	3.73859	39	2.58458	71	3.08317
7	3.40424	40	2.41678	72	2.52476
8	3.18956	41	2.33023	73	2.00921
9	5.64639	42	5.27815	74	1.83072
10	4.60911	43	4.43702	75	1.73768
11	3.89292	44	3.72310	76	1.62683
12	3.48287	45	3.44648	77	1.42599
13	3.21218	46	3.16452	78	1.39075
14	3.01912	47	2.82018	79	1.39455
15	9.43431	48	2.57149	80	1.37899
16	6.46876	49	2.15190	81	1.35959
17	4.96692	50	-0.91601	82	5.07983
18	4.19109	51	0.99610	83	3.99785
19	3.64488	52	0.99503	84	2.70098

Tube Number	Pressure Mean Voltage	Tube Number	Pressure Mean Voltage	Tube Number	Pressure Mean Voltage
20	3.34971	53	1.91868	85	1.92930
21	3.06553	54	1.87188	86	1.80218
22	2.84686	55	1.90451	87	1.76045
23	7.00616	56	1.87667	88	1.70594
24	5.50445	57	5.52761	89	1.64933
25	4.44356	58	4.68396	90	1.58318
26	3.79427	59	3.47329	91	1.50069
27	3.52495	60	3.13785	92	1.44614
28	3.10311	61	2.68880	93	1.49341
29	2.79744	62	2.35816	94	1.46683
30	2.65439	63	2.10506	95	1.08317
31	8.53722	64	1.91283	96	1.08188
32	6.17690	65	1.68400	97	0.98947
33	5.17741				

Table A.4

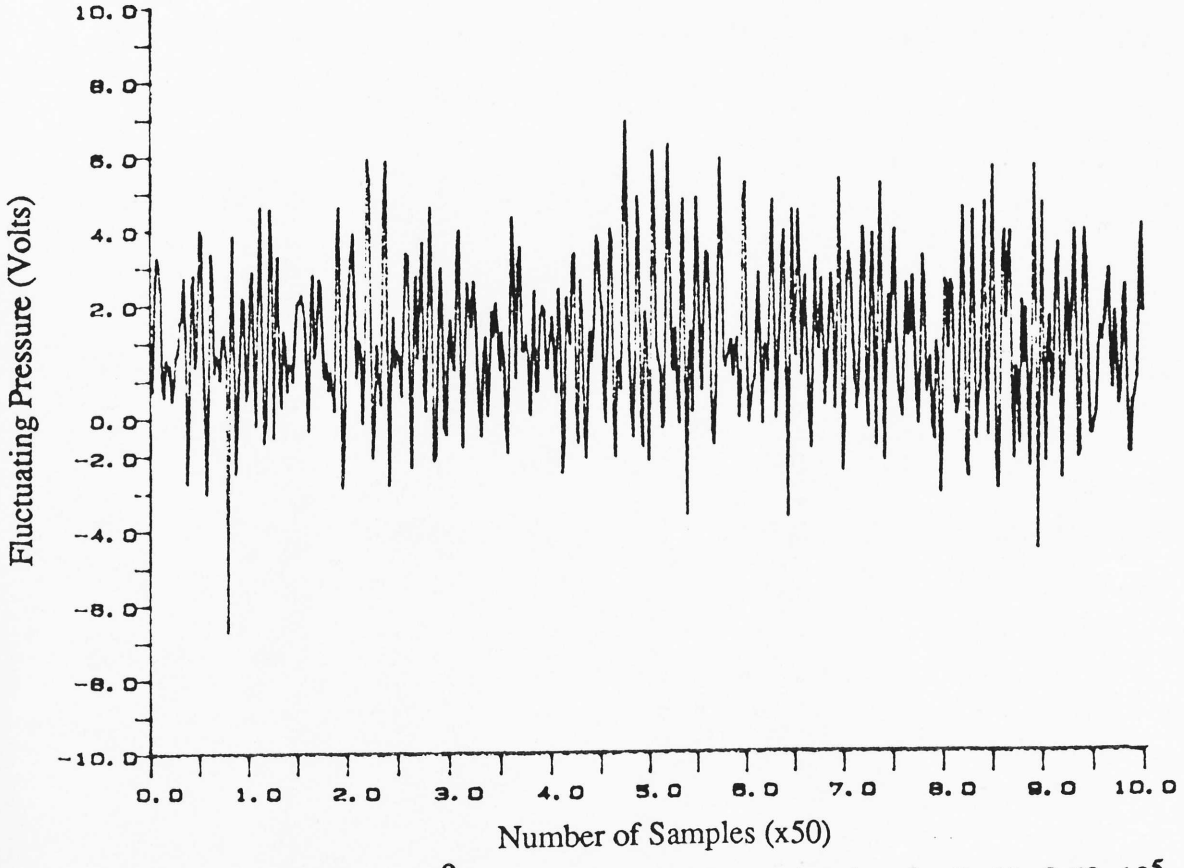


Fig.A.4.1 Sample of 40^{o} whole model raw fluctuating data for Re No.9.58×10^{5}.

APPENDIX 5

A simple potential theory has been developed to try to predict the levels of mean and fluctuating pressure generated on road vehicle models. This theory only applies when the flow within the A-Pillar region is dominated by a strong vortex. The following assumptions were made when developing the model :-

i) Potential flow.

ii) No change in the flow along the vortex axis i.e 2-d flow along the vortex.

iii) The frequency and amplitude of oscillations are small when the vortex is assumed to oscillate, thus unsteady terms in Bernoulli's equation are ignored.

iv) Vortex core angle is assumed to be the same as the A-Pillar angle.

v) Vertical and horizontal vortex oscillations are assumed to be decoupled i.e oscillates independently in either direction.

Figure A.5.1 shows the idealised model used in developing the potential flow solution. Let the average height of the vortex above the model surface be a_0, thus if the vortex is in equilibrium then :-

$$U\cos\theta = \frac{\Gamma}{4\pi a_0} \qquad \text{A.5.1}$$

$$\Gamma = 4\pi a_0 U\cos\theta \qquad \text{A.5.2}$$

Now consider a general height a for the vortex, thus the u and v velocity components at a point P are :-

$$U - \frac{2\Gamma}{2\pi r}\cos\phi\cos\theta \qquad \text{A.5.3} \qquad \frac{2\Gamma}{2\pi r}\cos\phi\sin\theta \qquad \text{A.5.4}$$

Applying Bernoulli's equation at point P and substituting for the velocity term gives

$$P_\infty + \frac{1}{2}\rho U^2 = P + \frac{1}{2}\rho\left[\left(U - \frac{2\Gamma}{2\pi r}\mathrm{Cos}\phi\mathrm{Cos}\theta\right)^2 + \left(\frac{2\Gamma}{2\pi r}\mathrm{Cos}\phi\mathrm{Sin}\theta\right)^2\right] \qquad \text{A.5.5}$$

Substituting eq.A.5.2 and Cos ϕ = a/r into eq.A.5.5 and reducing the equation into a pressure coefficient gives :-

$$C_p = -8\mathrm{Cos}^2\theta\frac{aa_o}{r^2}\left[2\frac{aa_o}{r^2} - 1\right] \qquad \text{A.5.6}$$

Minimum pressure occurs directly beneath the vortex core (x'=0),

where $r^2 = a^2+x'^2$, therefore :-

$$C_p = -8\mathrm{Cos}^2\theta\frac{a_o}{a}\left[2\frac{a_o}{a} - 1\right] \qquad \text{A.5.7}$$

Assuming that the pressure fluctuations are generated by the vortex oscillating normal to the body surface such that :-

$$a = a_o + \varepsilon a_o \,\mathrm{Sin}\omega t \qquad \text{Where } \varepsilon << 1$$

Therefore

$$C_p = -8\mathrm{Cos}^2\theta\frac{1}{1+\varepsilon\mathrm{Sin}\omega t}\left[\frac{2}{1+\varepsilon\mathrm{Sin}\omega t} - 1\right] \qquad \text{A.5.8}$$

Using a series expansion and considering only the 1st Order terms gives :-

$$C_p = -8\mathrm{Cos}^2\theta\,[1 - 3\varepsilon\mathrm{Sin}\omega t\,] \qquad \text{A.5.9}$$

Now assume that the pressure fluctuations are generated due to the vortex oscillating parallel to the body surface such that :-

$$a = a_o \qquad x' = \varepsilon a_o \,\mathrm{Sin}\omega t$$

Therefore

$$C_p = -\frac{8\cos^2\theta}{1+\varepsilon^2\sin^2\omega t}\left[\frac{2}{1+\varepsilon^2\sin^2\omega t} - 1\right] \qquad \text{A.5.10}$$

Again using a series expansion and considering only the first two terms gives :-

$$C_p = -8\cos^2\theta[1-3\varepsilon^2\sin^2\omega t] \qquad \text{A.5.11}$$

Comparing equations A.5.9 and A.5.11 gives the mean minimum pressure coefficient term :-

$$C_{pmin} = -8\cos^2\theta \qquad \text{A.5.12}$$

The r.m.s and fluctuating pressures generated by the vortex oscillating are :-

Vertical	Horizontal	
$C_{pf} = 24\varepsilon\cos^2\theta\sin\omega t$	$C_{pf} = 24\varepsilon^2\cos^2\theta\sin^2\omega t$	A.5.13
$C_{prms} = 12\sqrt{2}\varepsilon\cos^2\theta$	$C_{prms} = 12\sqrt{2}\varepsilon^2\cos^2\theta$	

Using equation A.5.12, we can compare the variation of Cp_{min} versus A-Pillar angle with the experimental results obtained for the whole model (fig.A.5.2). The table below (A.5) shows a comparison between the averaged experimental $C_{p_{rms}}$ data for the whole model using the above equations (where ε=0.05).

Model Angle	Avg. Experimental	vertical	horizontal
40	0.2746	0.4979	0.025
50	0.2694	0.3506	0.017
60	0.1991	0.2121	0.011

Table A.5

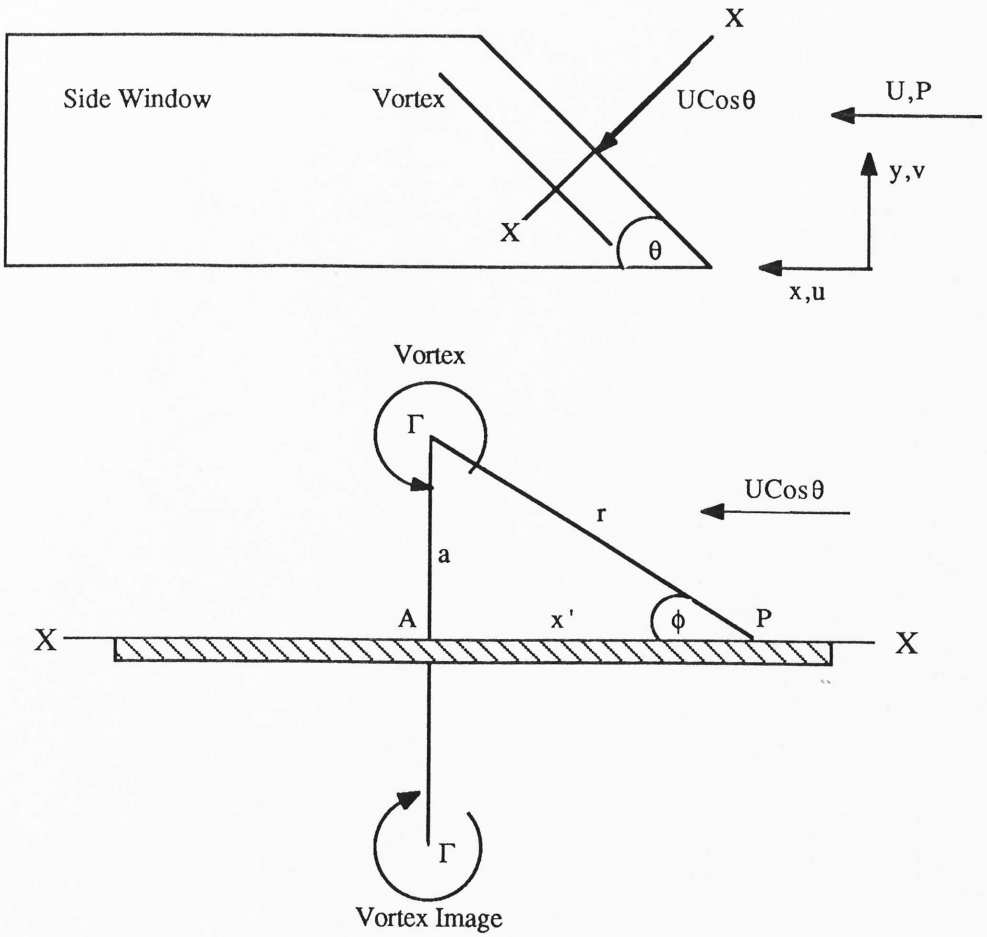


Fig.A.5.1

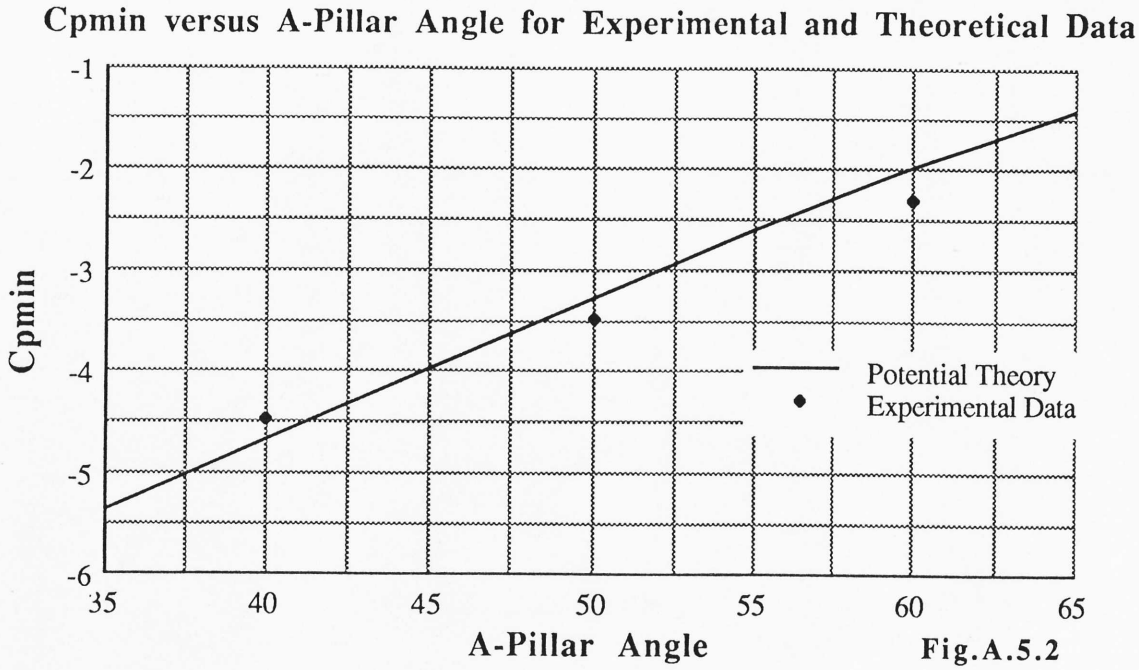


Fig.A.5.2

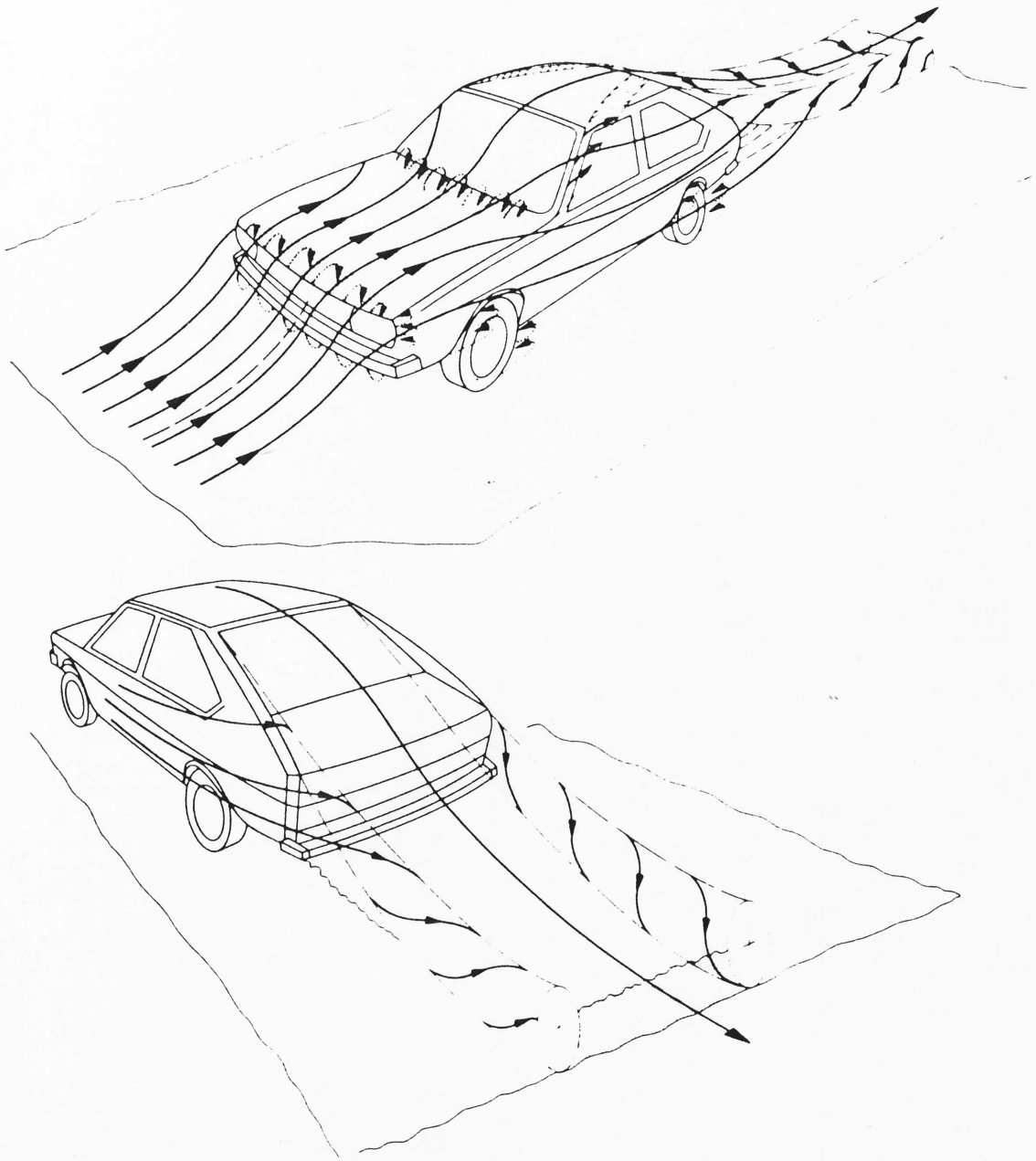


Fig.1.1.1 Flow around a passenger car (schematic), from Hucho (1987).

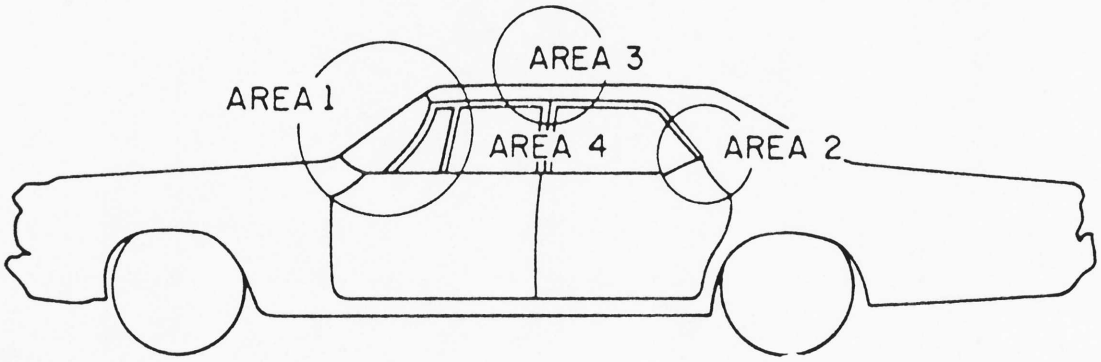


Fig.1.2.1 Critical areas in development of wind noise, from Thompson (1964).

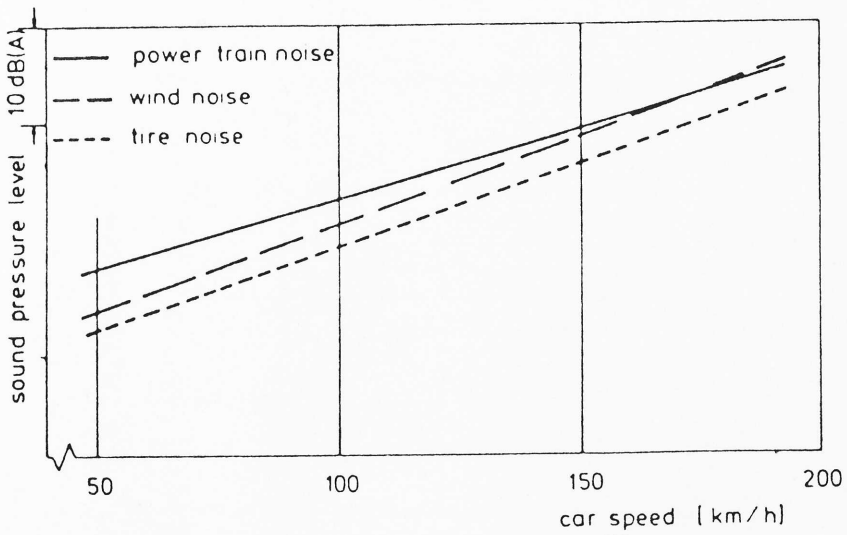


Fig.1.2.2 Comparisons of noise levels due to different sources as a function of speed for a typical production car, from Buchiem et al (1983).

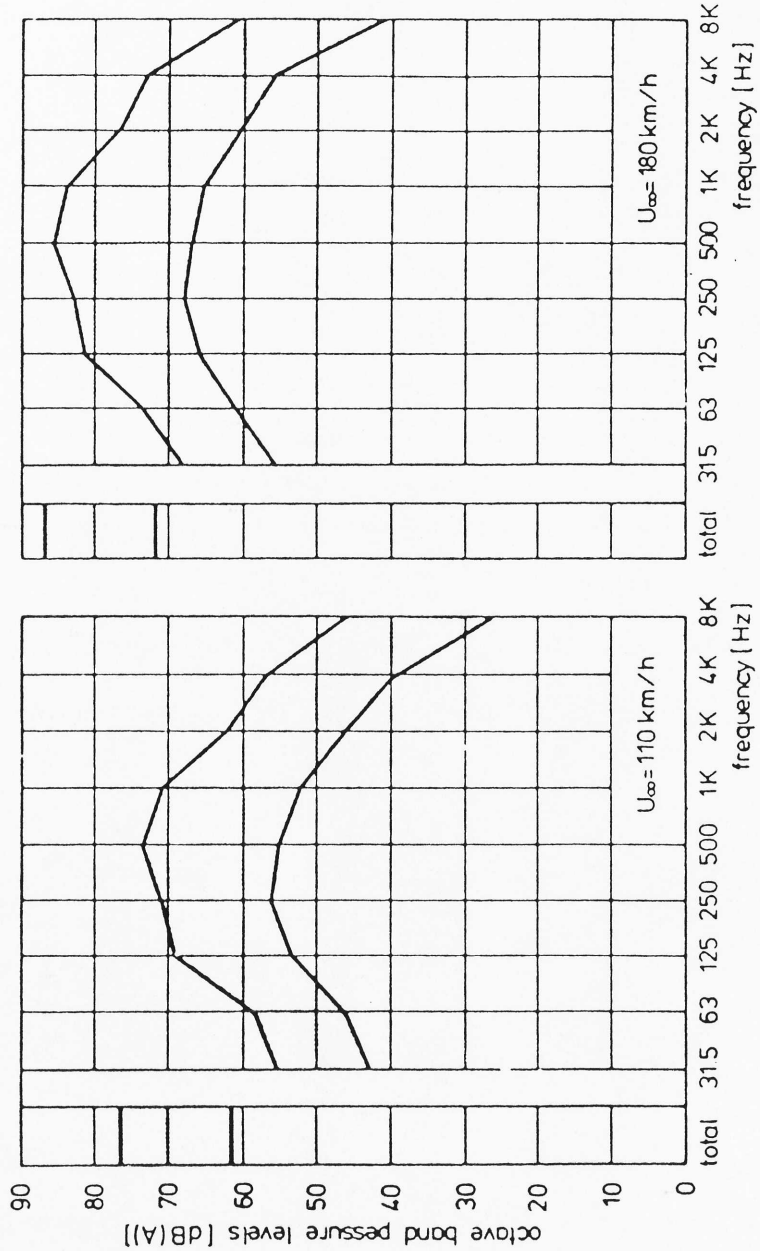


Fig.1.2.3 Range of flow induced interior noise of present-day production cars at 110 Km/h and 180 km/h, from Buchiem et al (1983).

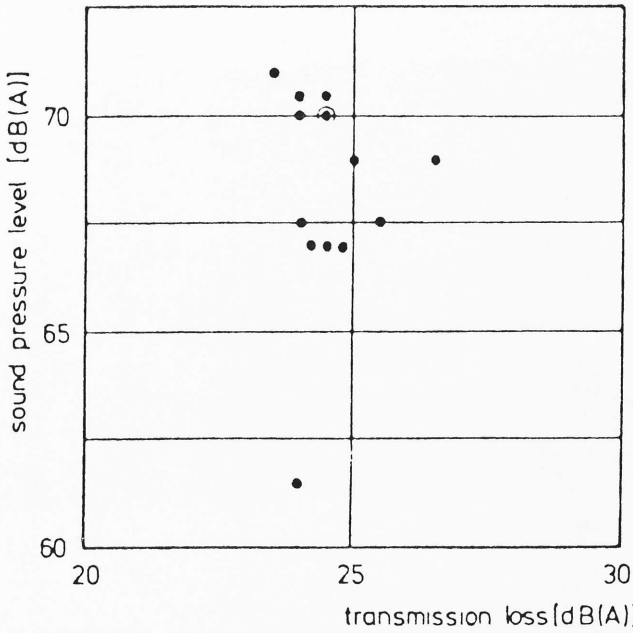


Fig.1.2.4 Correlation of flow-induced interior noise with transmission loss for production cars at 110 Km/h, from Buchiem et al (1983).

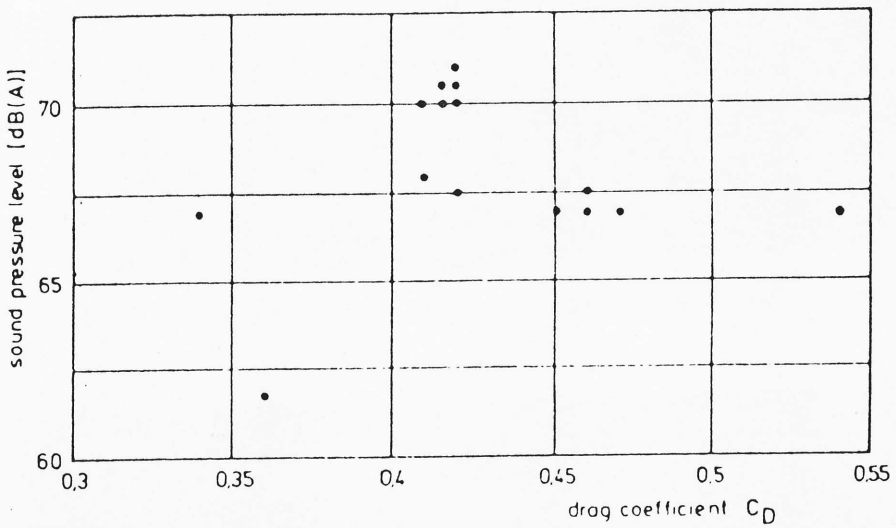


Fig.1.2.5 Correlation of flow-induced interior noise with drag coefficient for production cars at 110 Km/h, from Buchiem et al (1983).

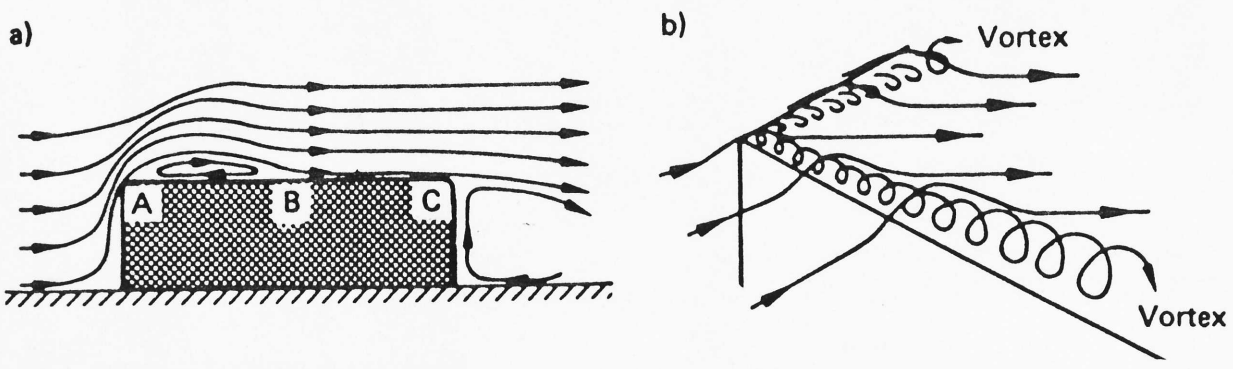
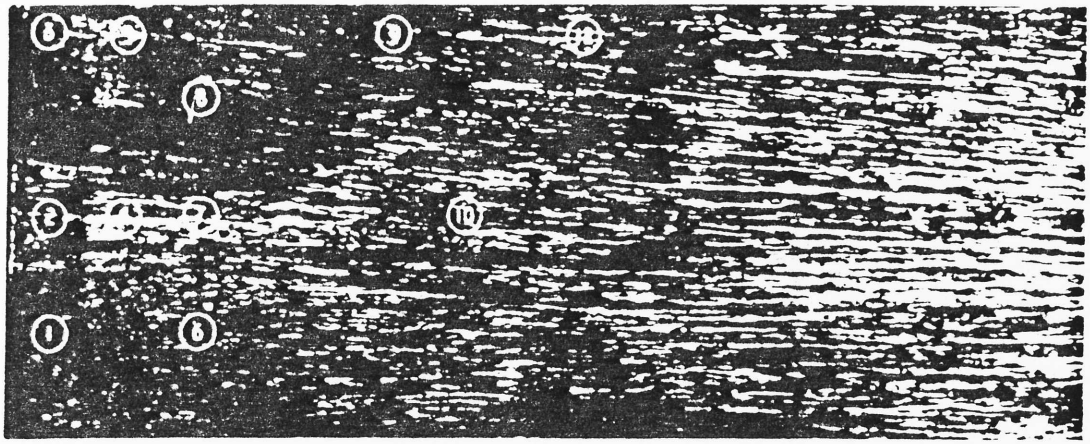
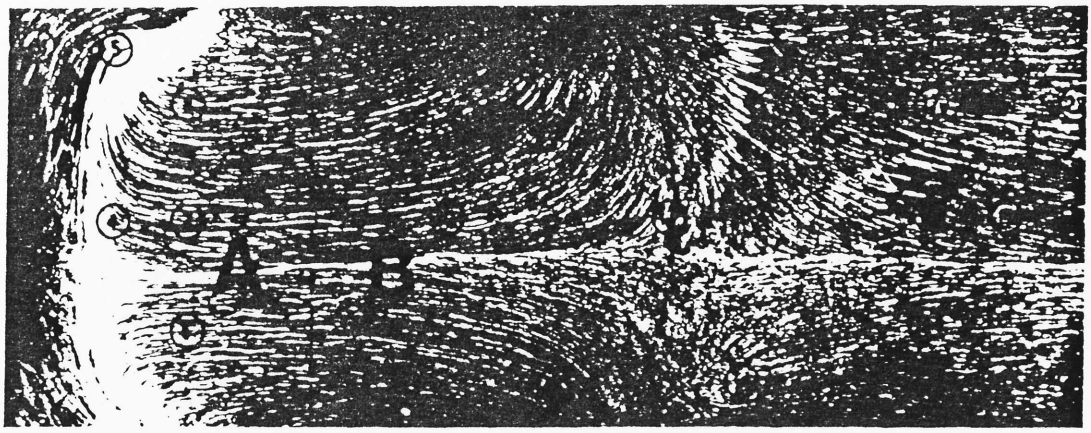


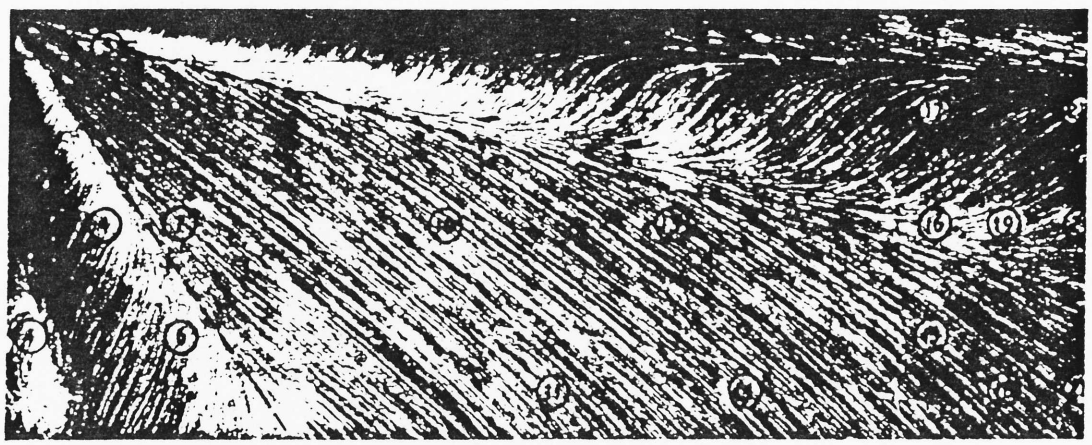
Fig.1.2.6a,b Types of air flow generated on a cuboid in order to measure sound levels, from Stapleford et al (1971).



Oil film picture of air flow in contact along entire length (front edge is rounded.



Oil film picture of the quasi-two-dimensional separation bubble with reattached air flow



Oil film picture of cuboid with air flow under 30°, with formation of two three-dimensional vortices

Fig.1.2.7 Flow visulation of three types of flow generated on the cuboid using oil film technique, from Stapleford et al (1971).

Character of flow	*Max. sound pressure level* L_{max} (dB(A))	*Frequency range of* L_{max} (Hz)
All attached	111	800 to 1200
Separation bubble A	108	400 to 500
Separation bubble B	115	200 to 500
Reattached	113	300 to 600
Vortex	130	500 to 800

Table 1.2 Relation between character of flow, maximum sound pressure level and frequency range, from Hucho (1987).

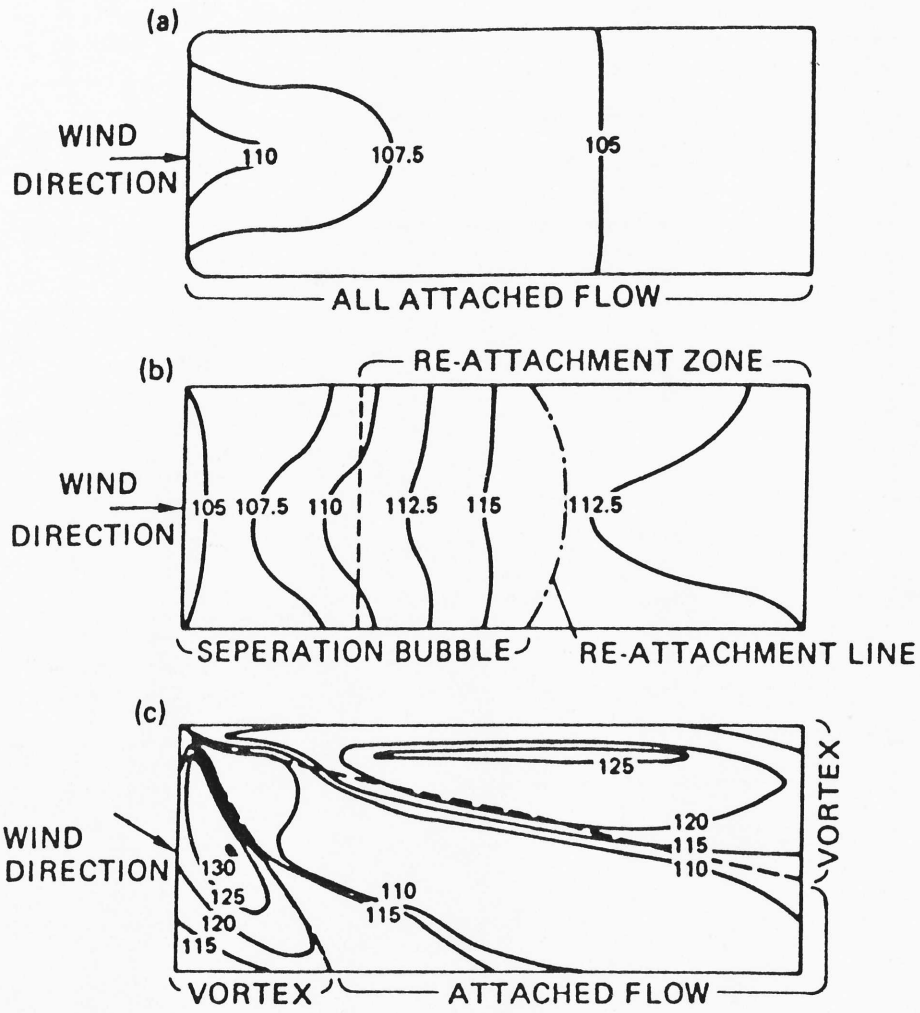


Fig.1.2.8 Surface sound pressure levels in the frequency range 500 Hz to 1500 Hz for (a) Attached flow; (b) Two-dimensional separation; (c) Vortex region, from Stapleford et al (1971).

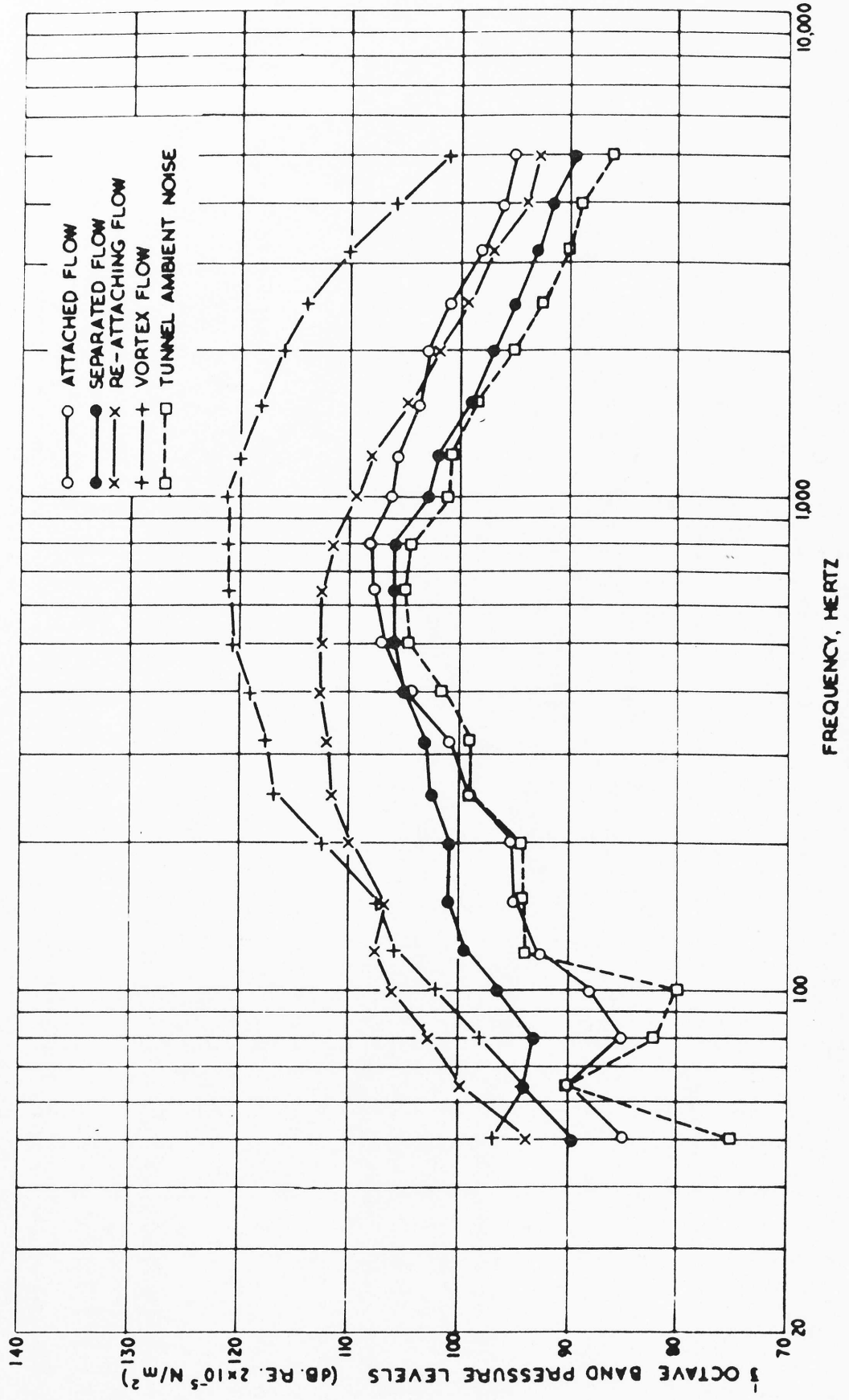


Fig.1.2.9 Mean noise spectra for different types of flow, from Stapleford et al (1971).

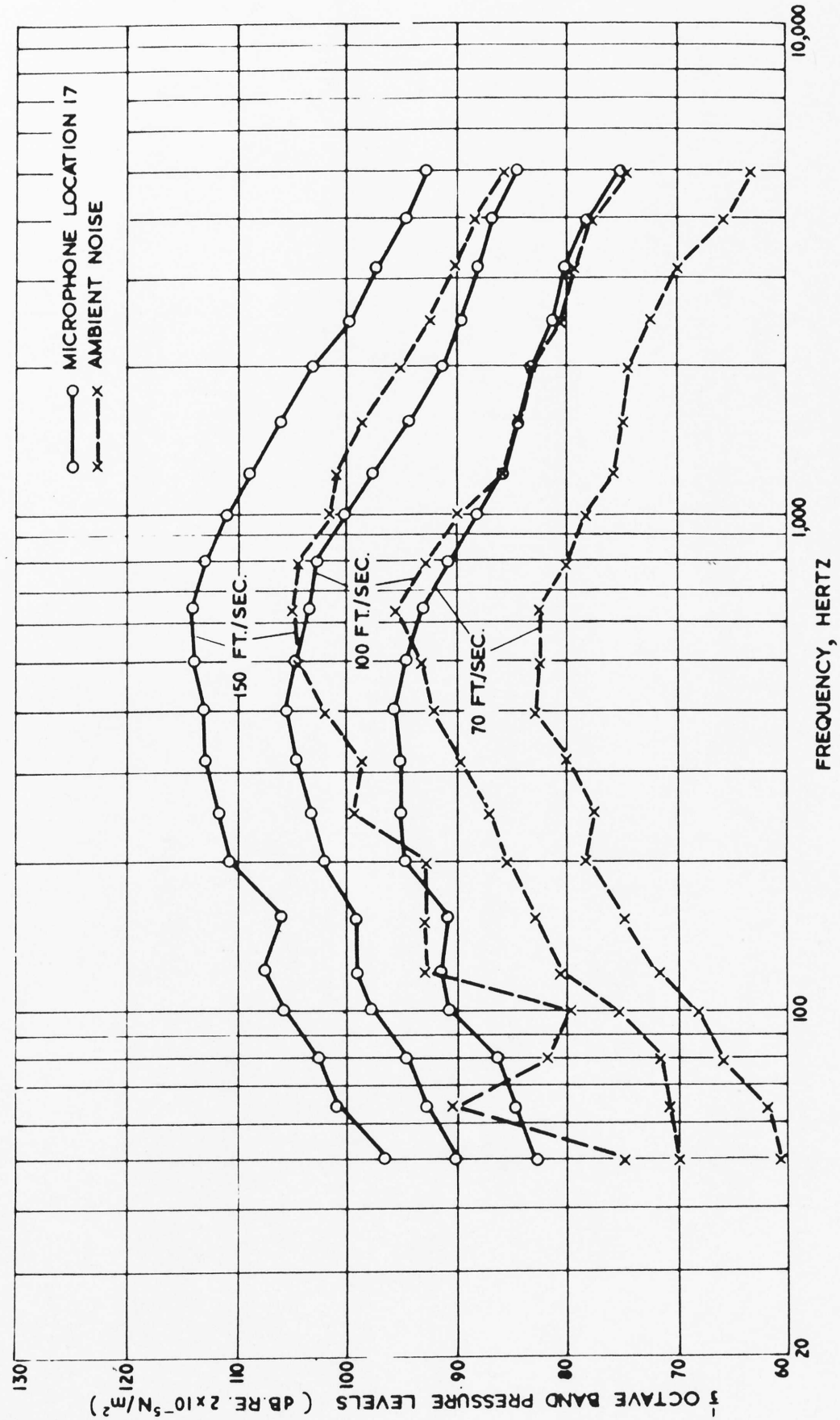


Fig.1.2.10 Effect of Tunnel wind speed on typical noise spectrum on square-edged box at zero yaw angle, from Stapleford et al (1971).

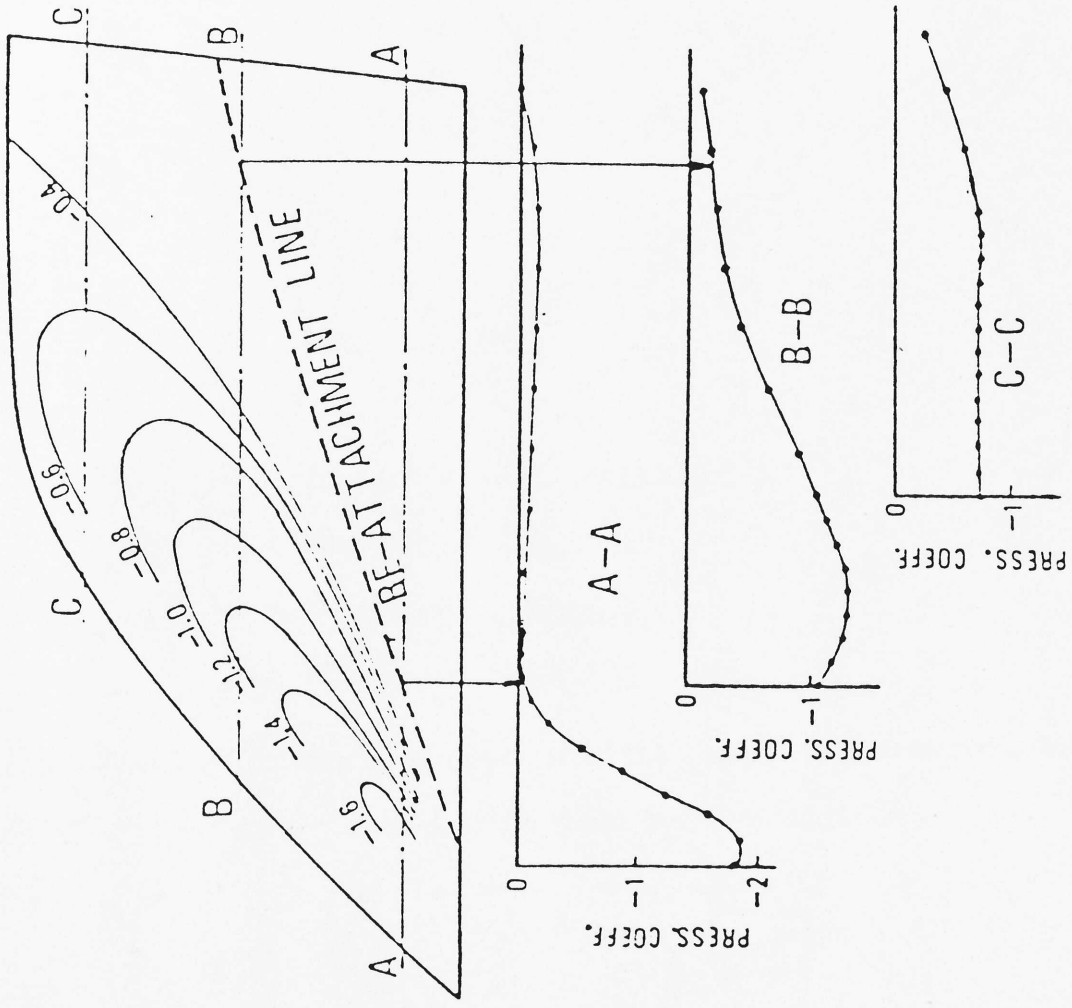


Fig.1.2.11 Pressure distribution on side window glass, from Watanabe et al (1978).

Distribution of External Fluctuating Pressure Intensity

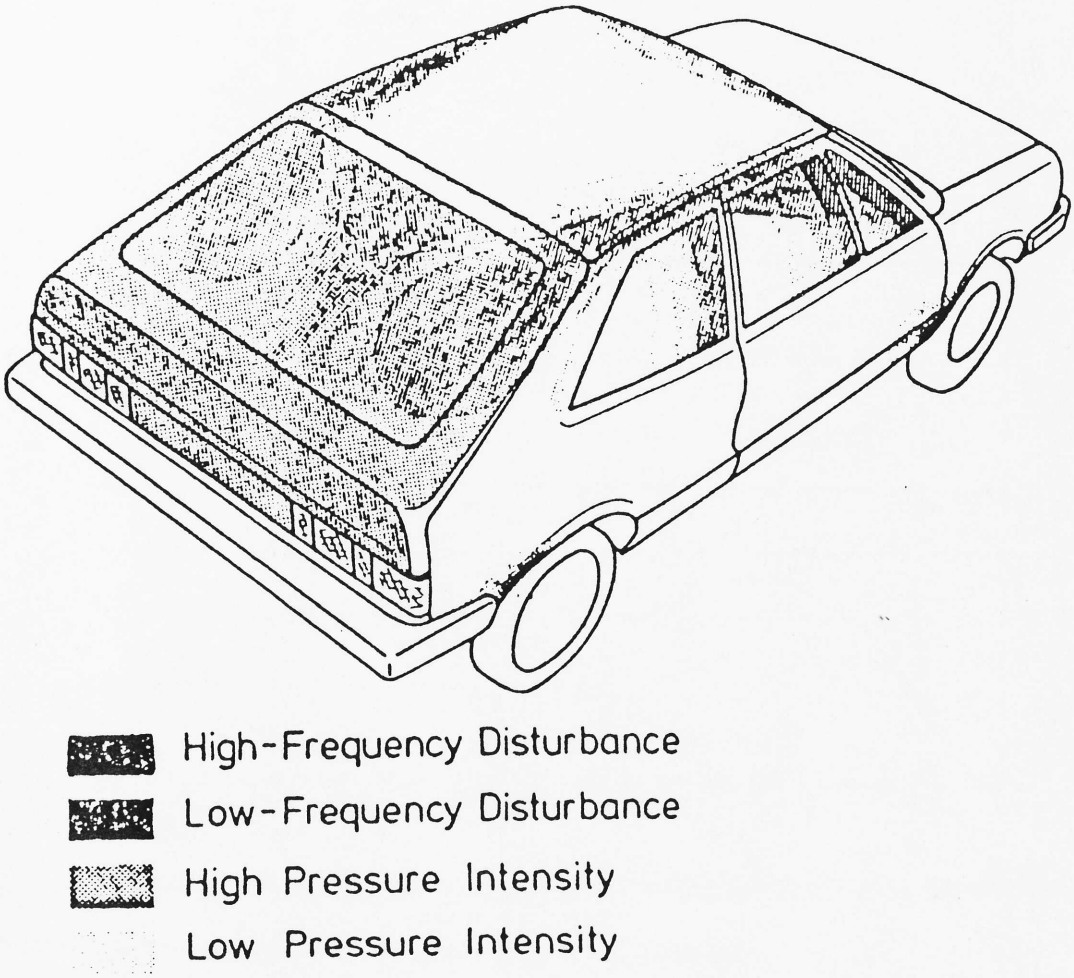


Fig.1.2.12 Schematic representation of the fluctuating pressure intensity distrubation on a car-body surface, from Dobrzynski (1983).

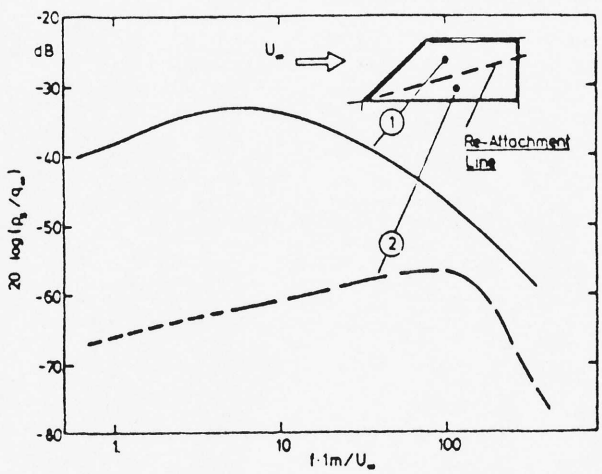


Fig.1.2.13 Unsteady surface pressure spectrums in the side-window area, from Dobrzynski (1983).

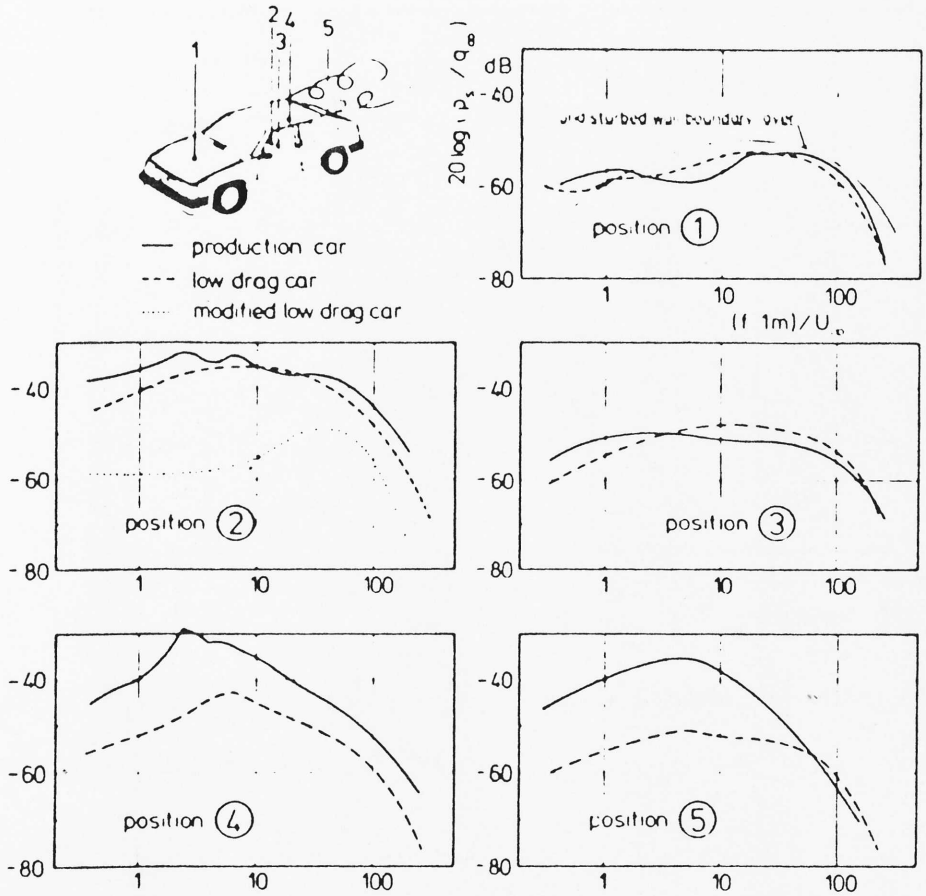


Fig.1.2.14 Comparisons of surface pressure fluctuations for a production car and a low-drag car, from Buchiem et al (1983).

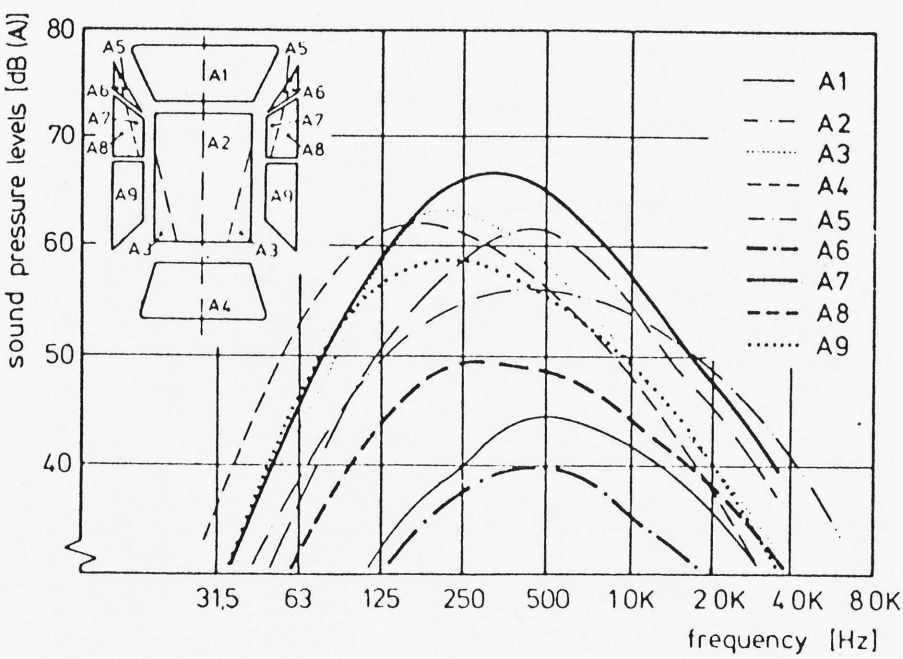


Fig.1.2.15 Sound pressure levels originating from different car body areas, from Buchiem et al (1983).

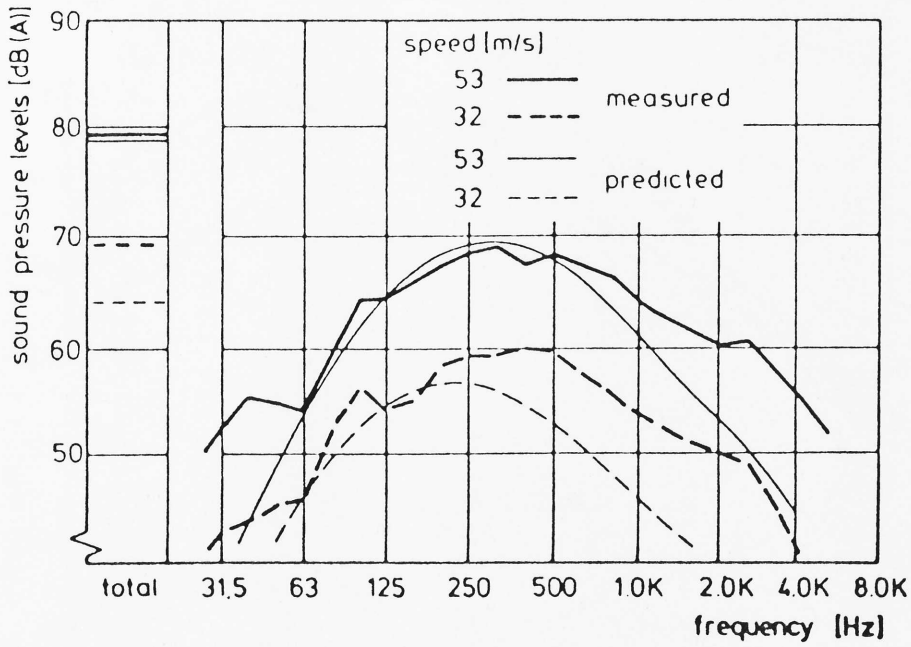


Fig.1.2.16 Comparisons of predicted and measured interior noise spectra, from Buchiem et al (1983).

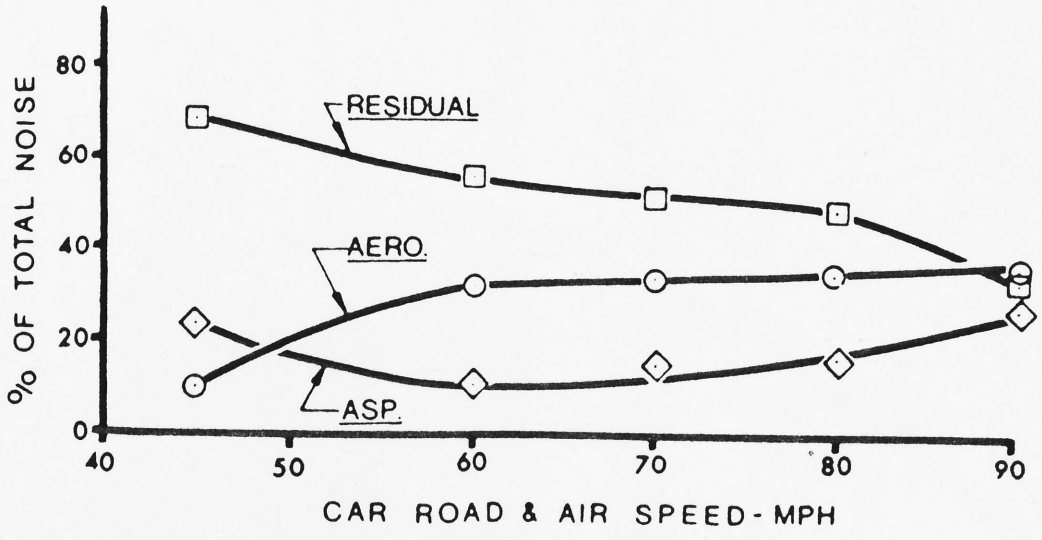


Fig.1.2.17 A typical example of the variation of each noise component with car road and air speed, from Romberg et al (1977).

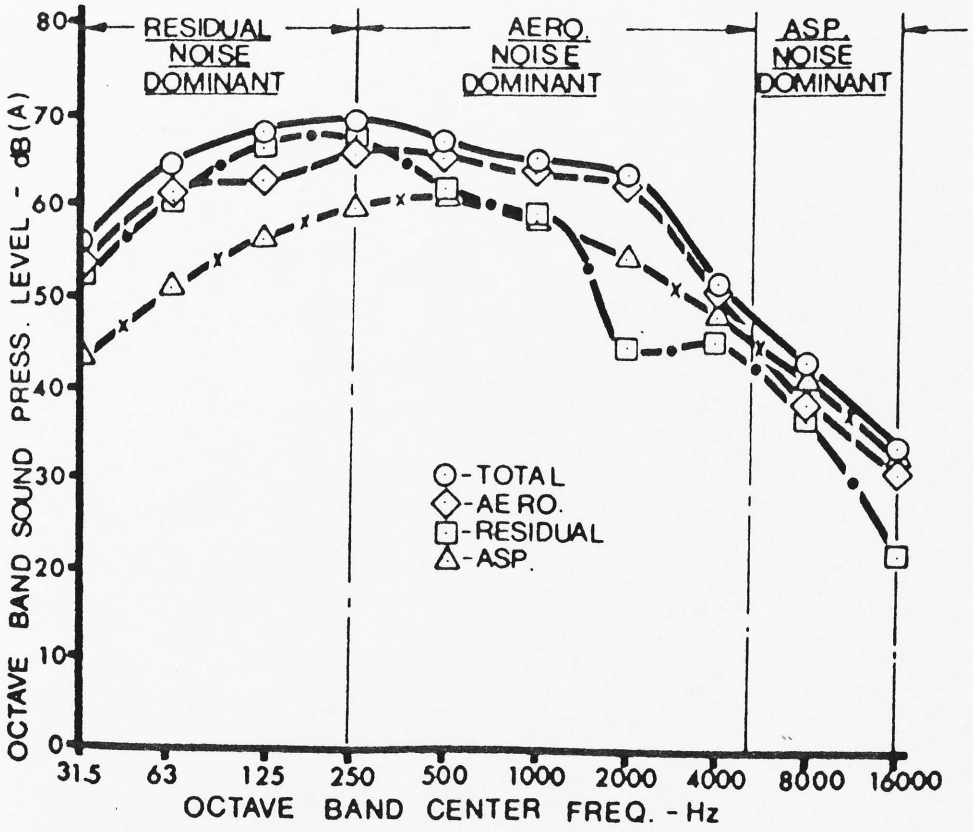


Fig.1.2.18 A spectral comparison of each noise component, from Romberg et al (1977).

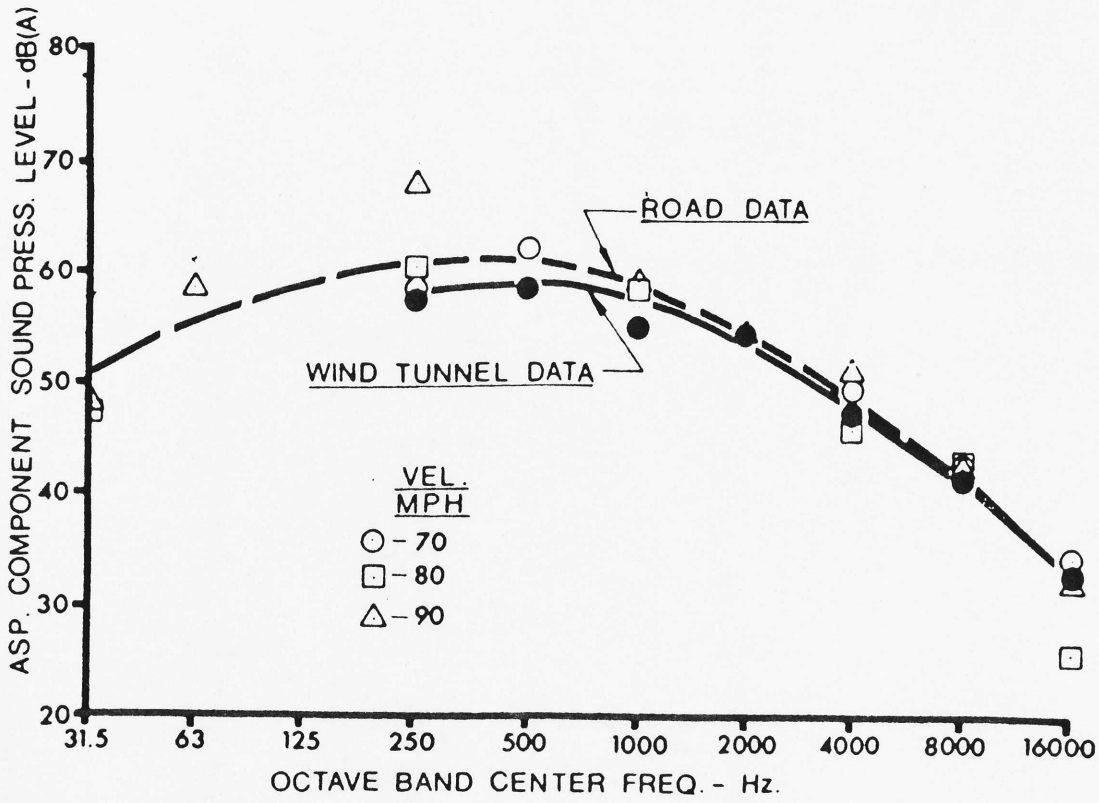


Fig.1.2.19 Comparison of car aspiration noise: road and wind tunnel data, from Romberg et al (1977).

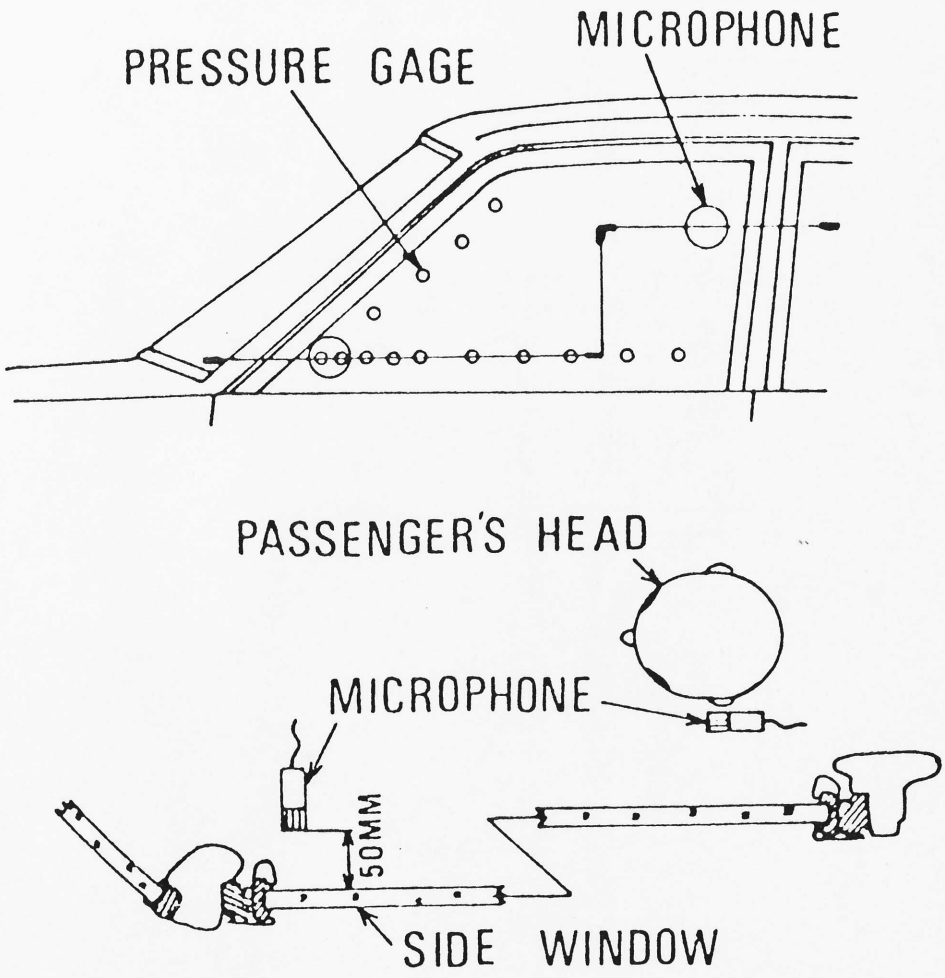


Fig.1.2.20 Microphone and pressure gauge positions on full scale car model, from Watanabe et al (1978).

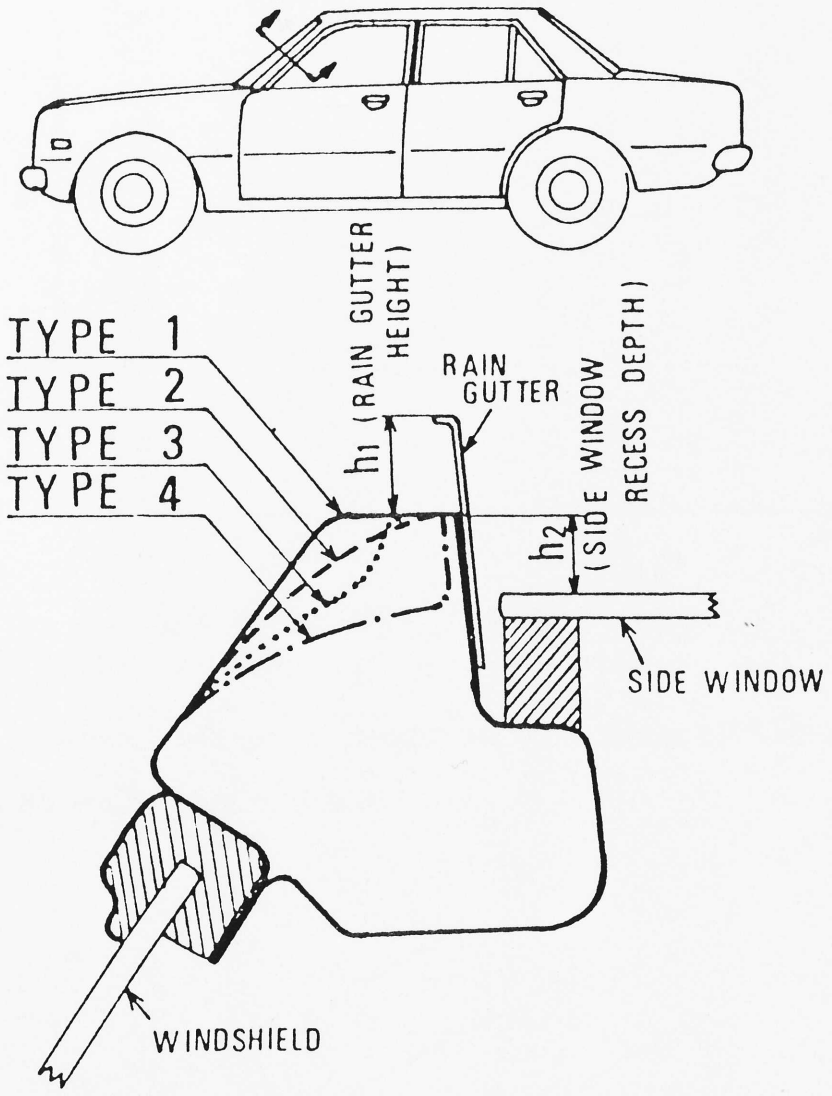


Fig.1.2.21 Different A-Pillar shapes tested on full scale model, from Watanabe et al (1978).

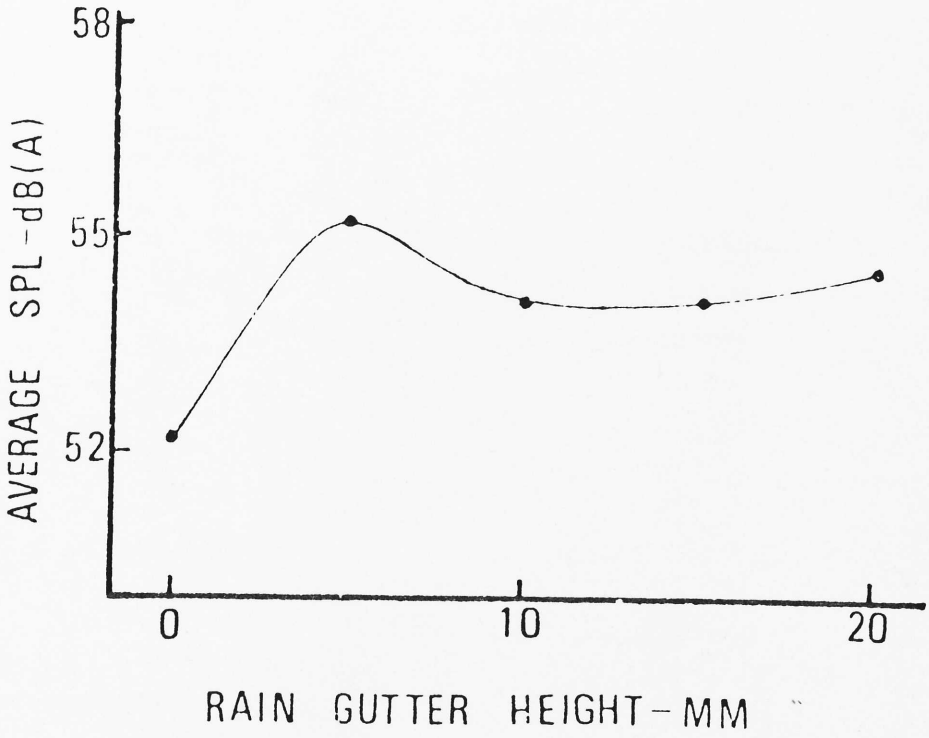


Fig.1.2.22 Effect of rain gutter height on wind noise (100 Km/h: front seat), from Watanabe et al (1978).

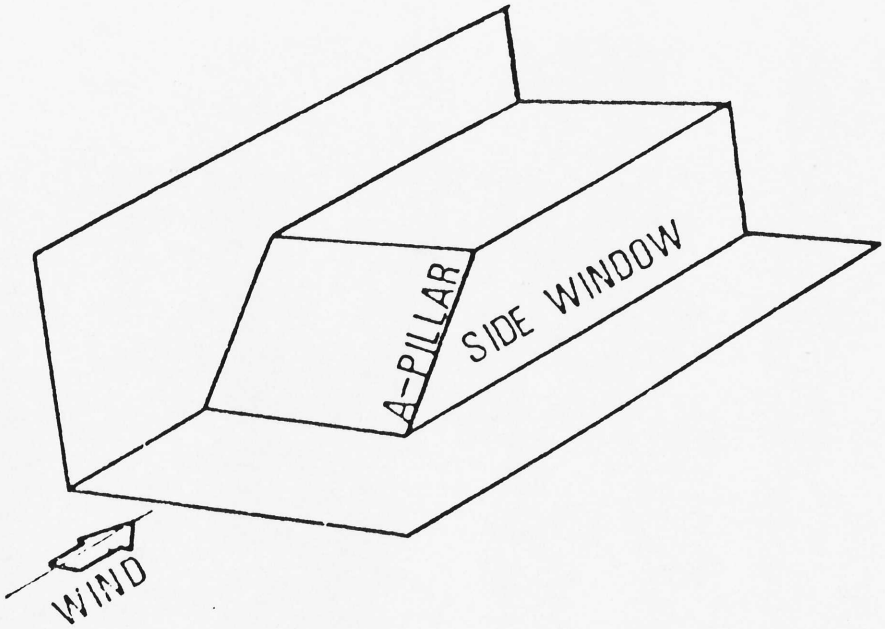


Fig.1.2.23 Three-dimensional model used to investigate airflow in the A-Pillar region, from Watanabe et al (1978).

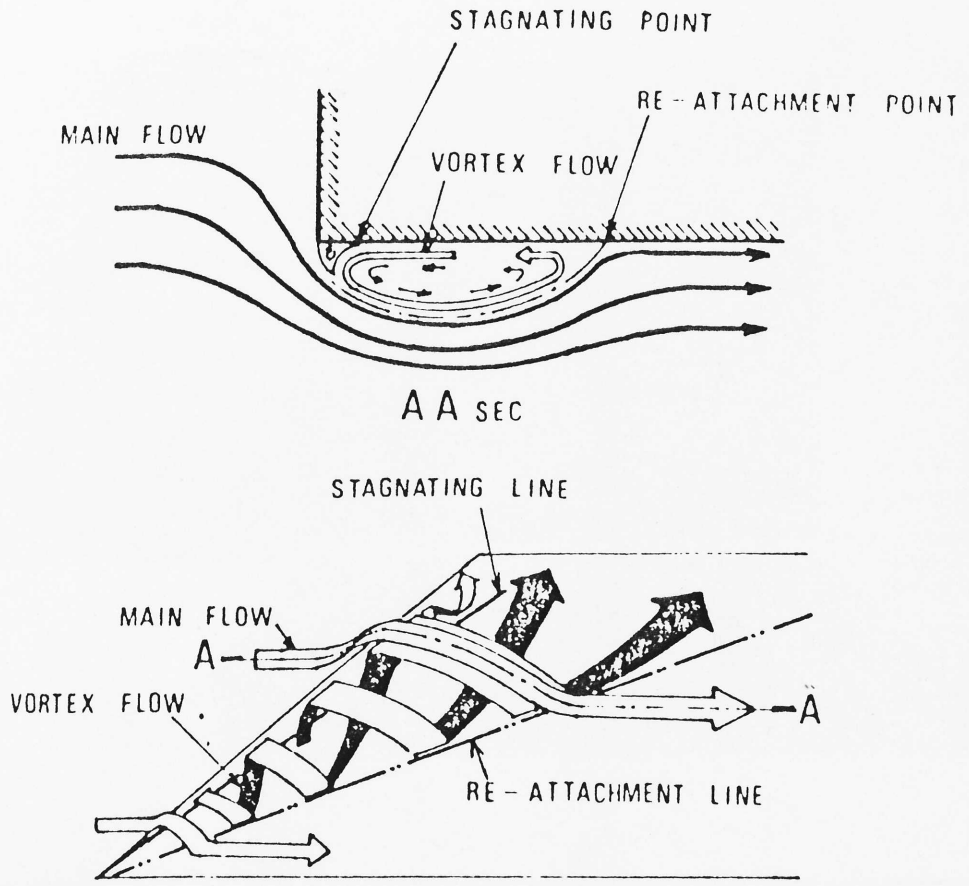


Fig.1.2.24 Schematic representation of flow-field around A-Pillar, from Watanabe et al (1978).

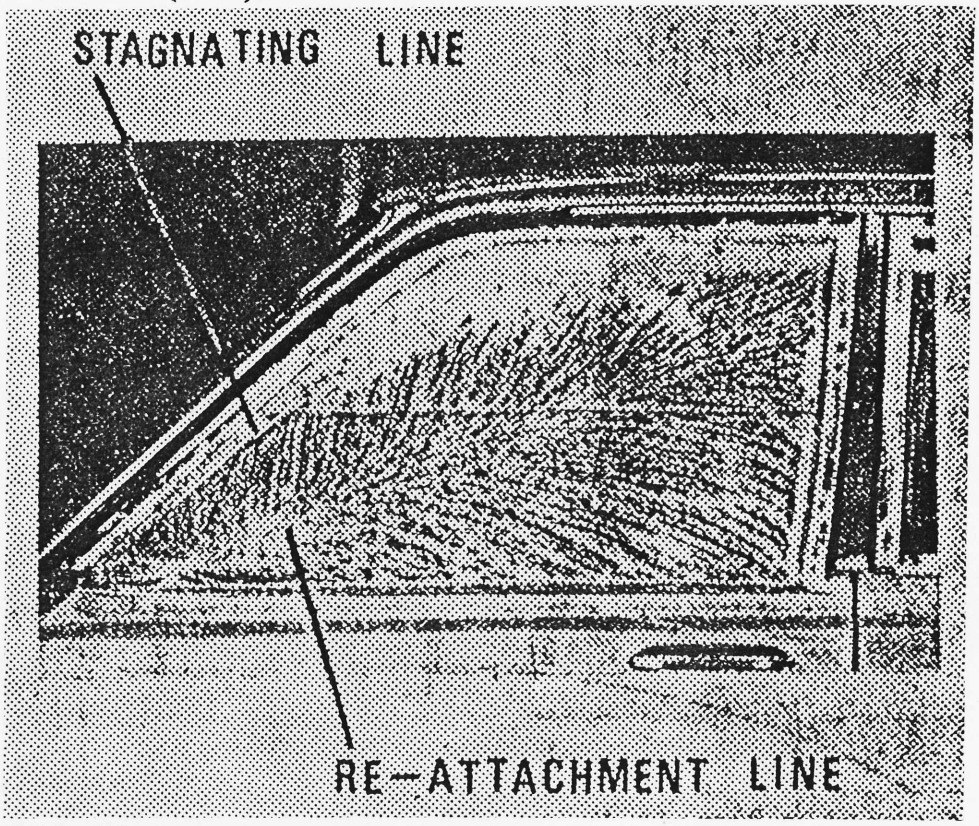


Fig.1.2.25 Flow pattern on front side window of full scale model, from Watanabe et al (1978).

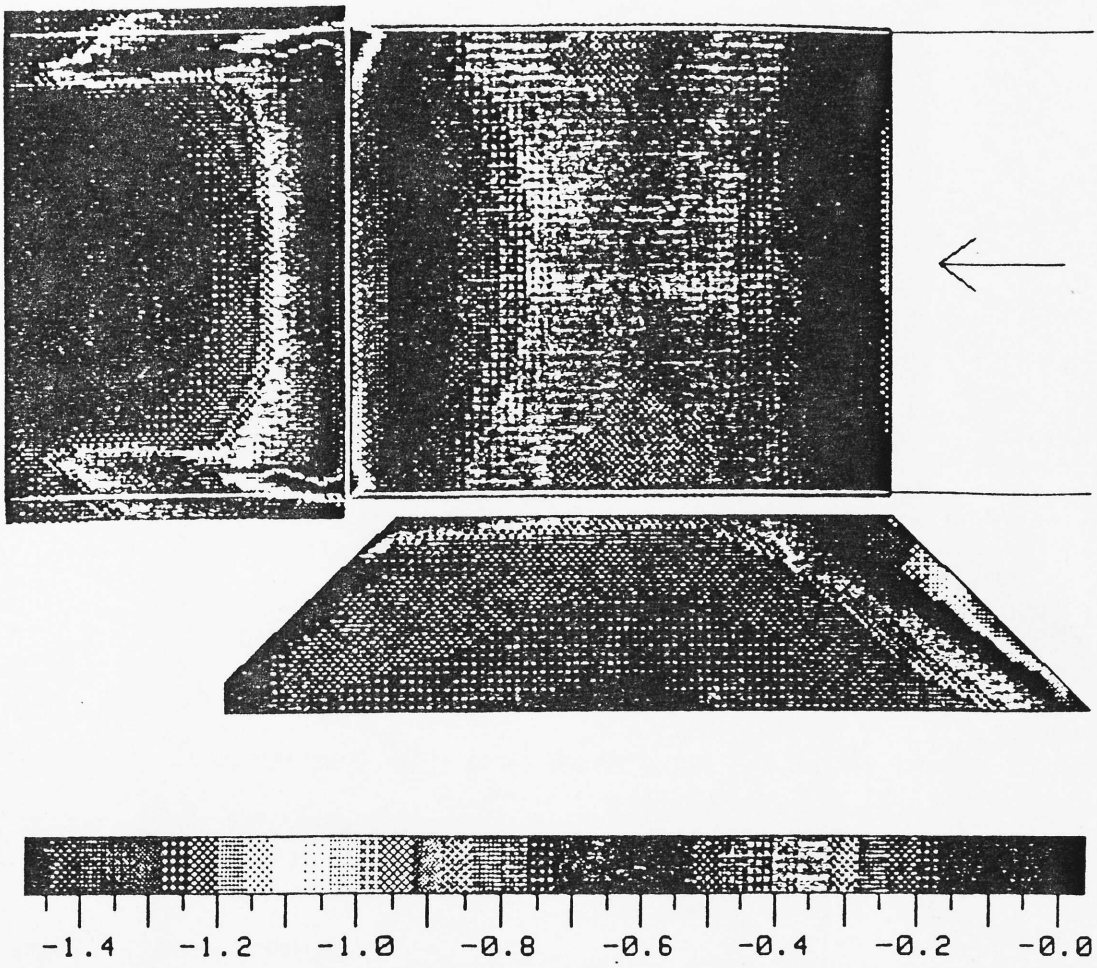


Fig.1.2.26 Surface pressure distribution on 1/3 scale model at zero yaw angle, from Bearman et al (1989).

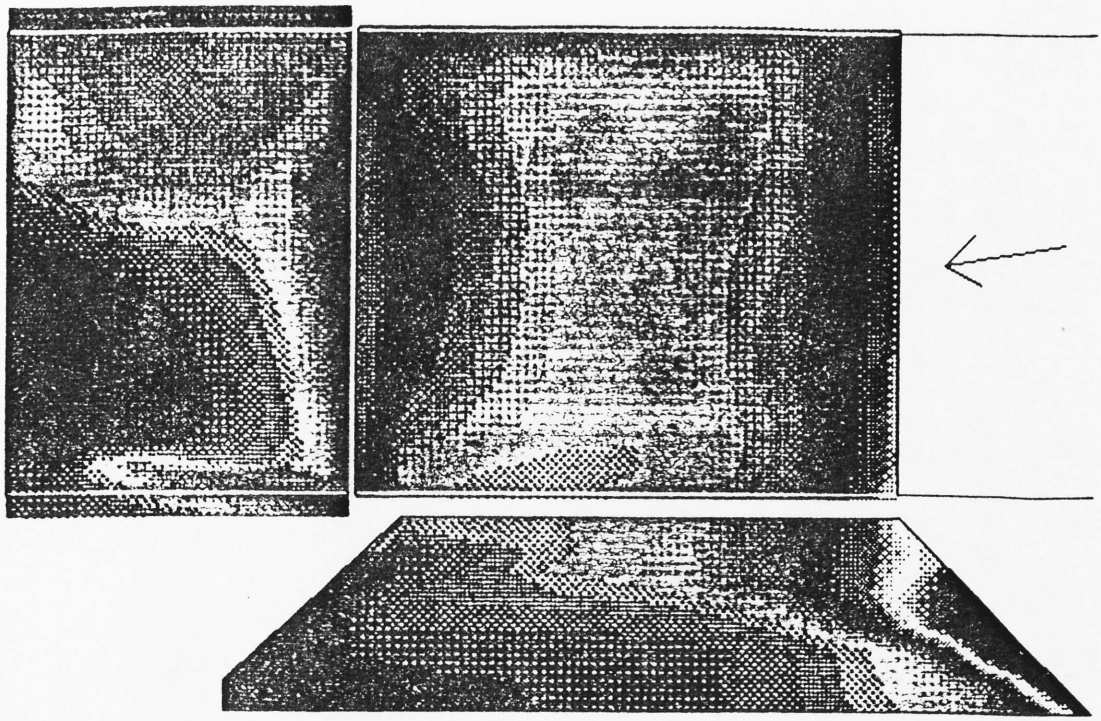


Fig.1.2.27 Surface pressure distribution on 1/3 scale model at ten degrees yaw angle, from Bearman et al (1989).

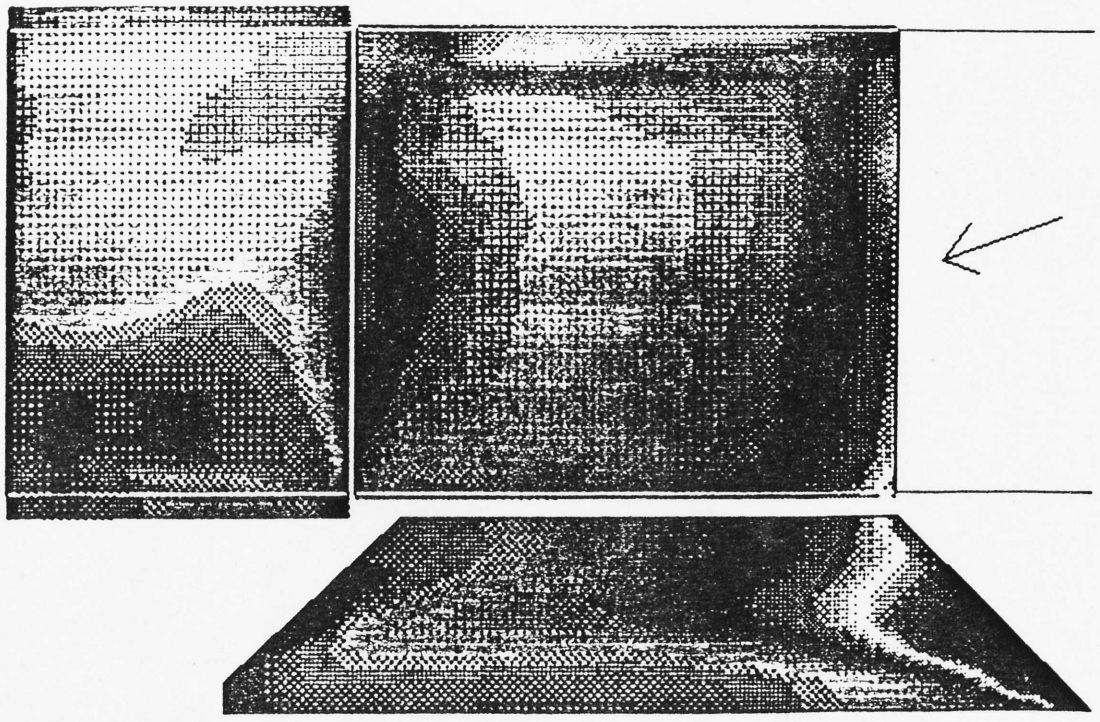


Fig.1.2.28 Surface pressure distribution on 1/3 scale model at twenty degrees yaw angle, from Bearman et al (1989).

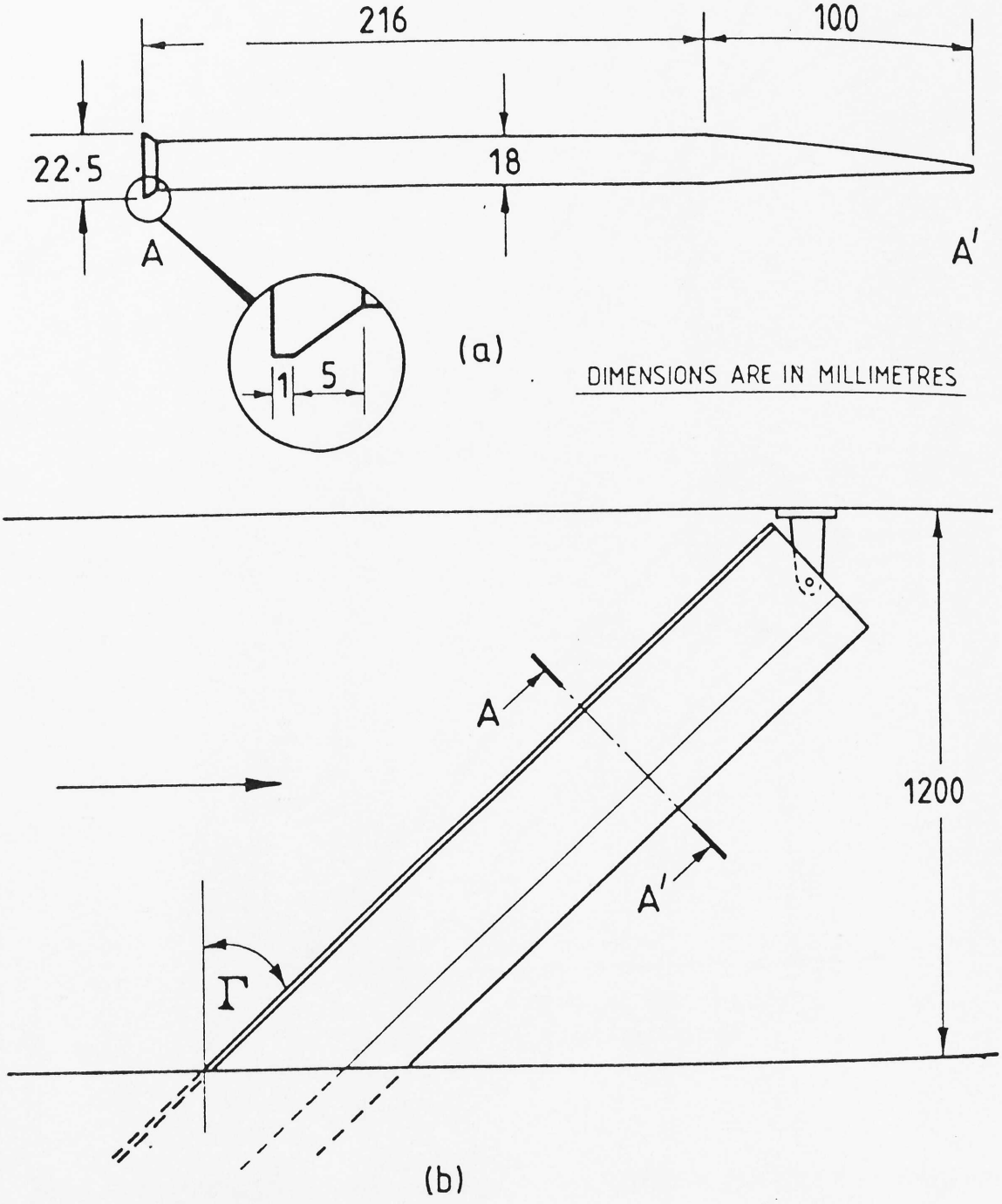
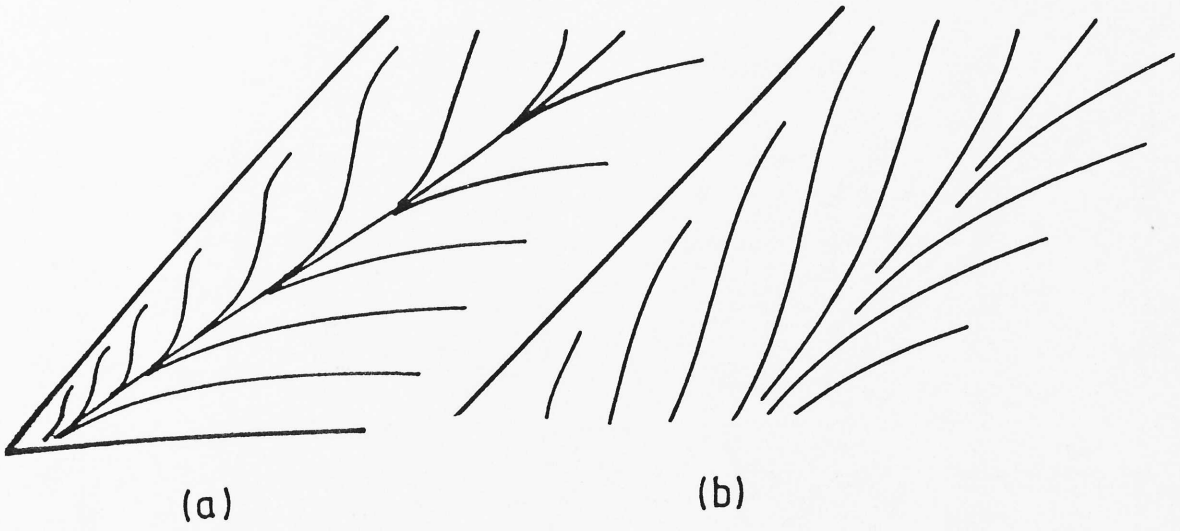
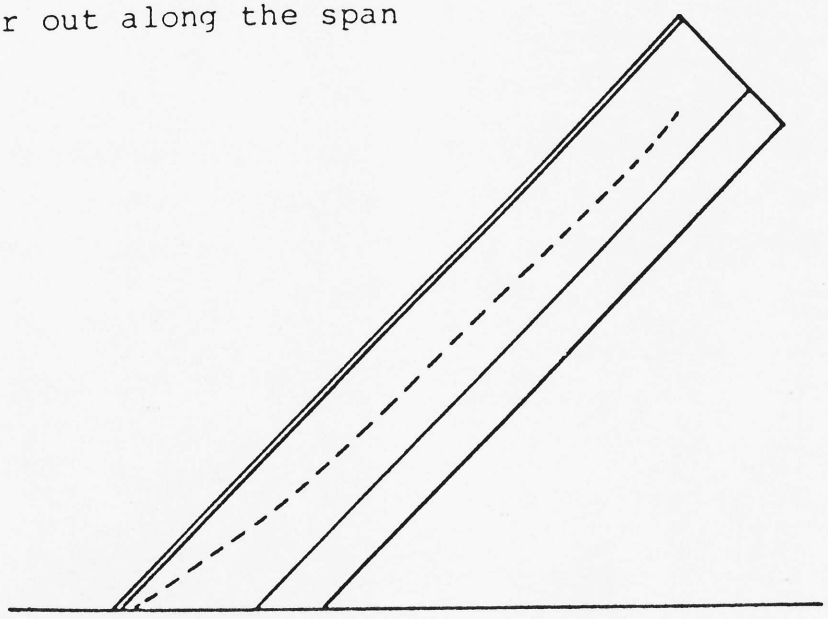


Fig.1.3.1 Details of Sutton's Swept edge model, from Sutton (1983).



Sketches of limiting streamlines
(a) close to the tunnel floor
(b) further out along the span



(c) Shape of the reattachment line

Fig.1.3.2 Features of the surface oilflow pattern at forty five degrees sweep with wind speed 30 m/s, from Sutton (1983).

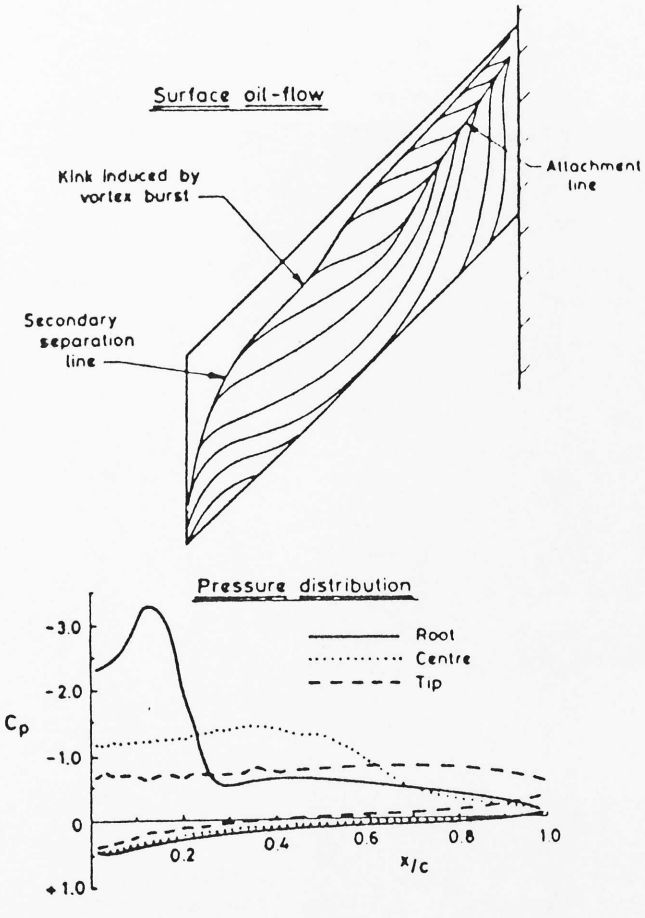


Fig.1.3.3 Surface oil-flow pattern and pressure distribution for sharp edged Swept wing.

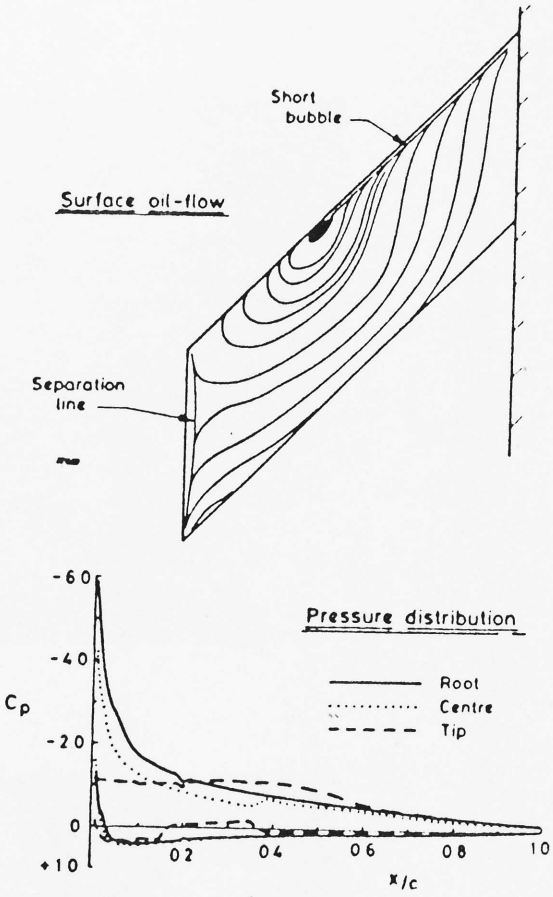


Fig.1.3.4 Surface oil-flow pattern and pressure distribution for sharp edged Swept wing

from Poll (1980)

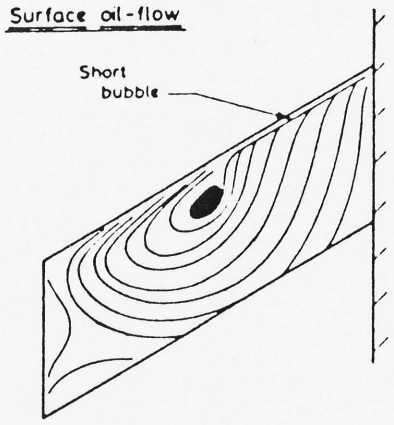


Fig.1.3.5 Surface oil-flow pattern for a blunt edged Swept wing at Reynolds No.1.7e06.

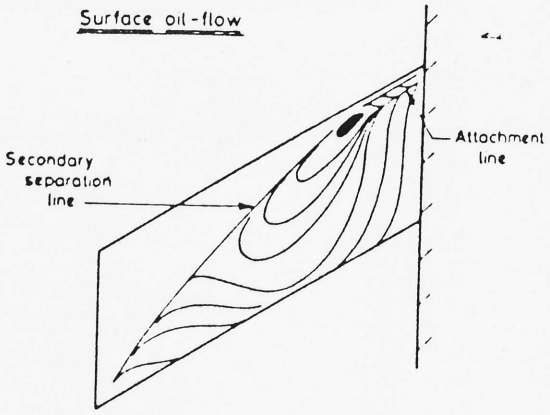


Fig.1.3.6 Surface oil-flow pattern for a blunt edged Swept wing at Reynolds No.0.9e06.

from Poll (1980)

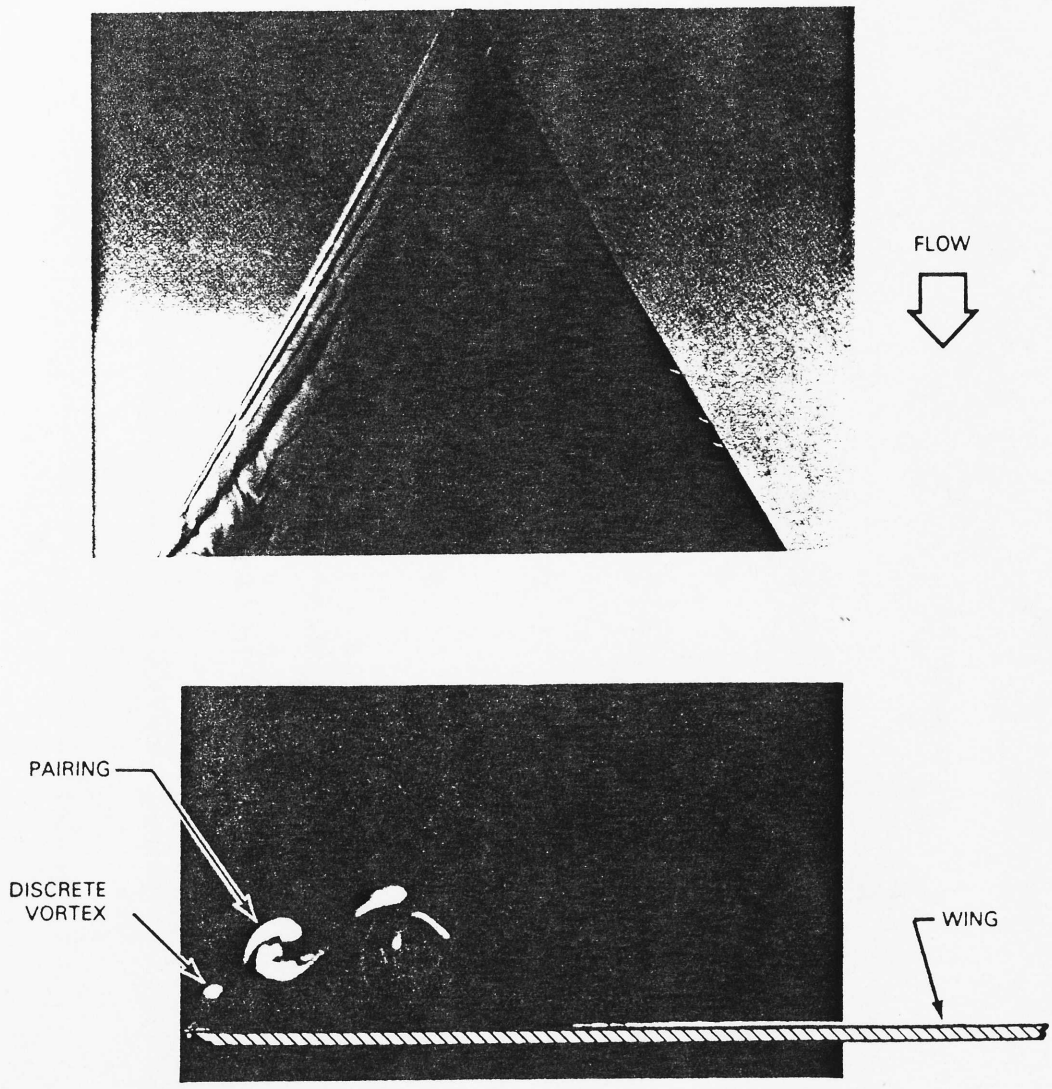


Fig.1.3.7 Delta wing at fixed angle of attack $\alpha = 10^{o}$, from Gad-el-Hak et al (1985).

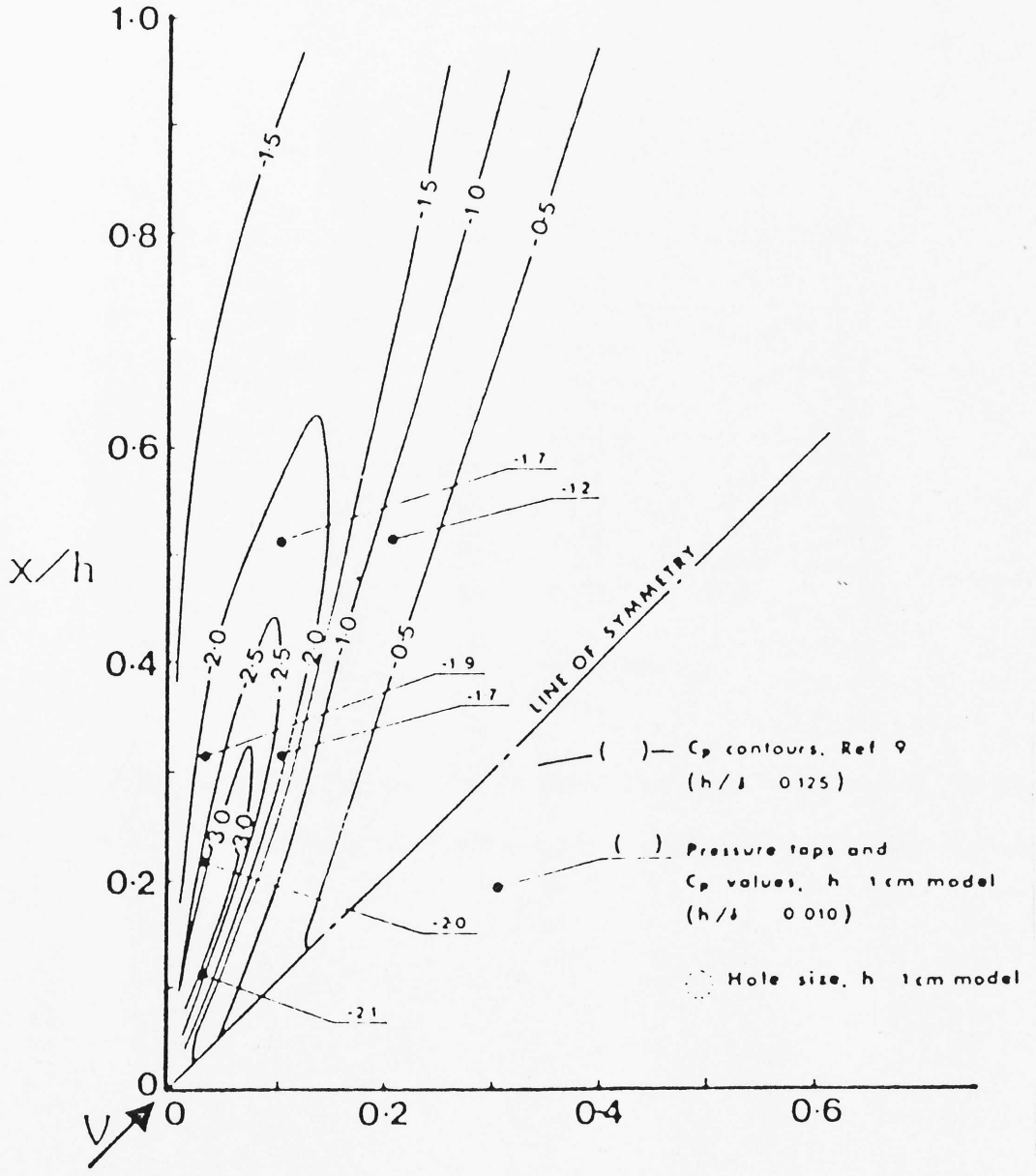


Fig.1.4.1 Contour plot of mean pressure coefficient for flat roof low-rise building, flow yaw angle being forty five degrees, from Kind (1986).

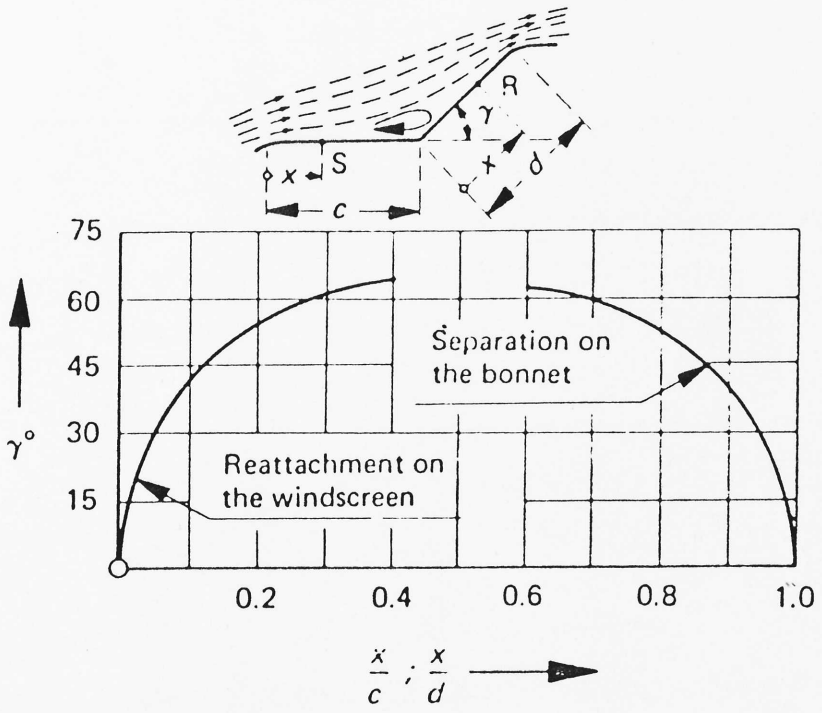


Fig.1.5.1 Flow separation on the bonnet and reattachement on the windscreen as a function of windscreen rake angle γ, from Scibor-Rylski (1984).

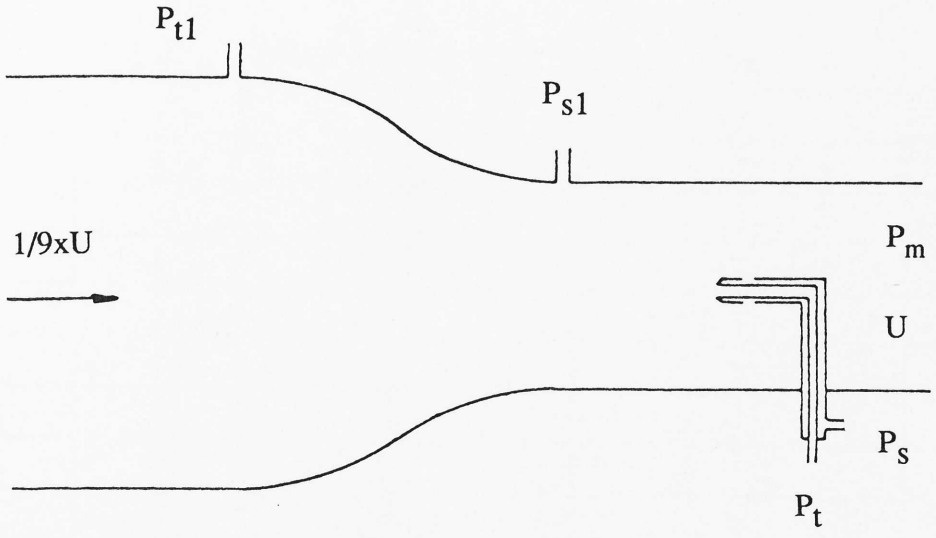


Fig.2.1.3.1 A general sketch of the Wind Tunnel working section and contraction nozzle.

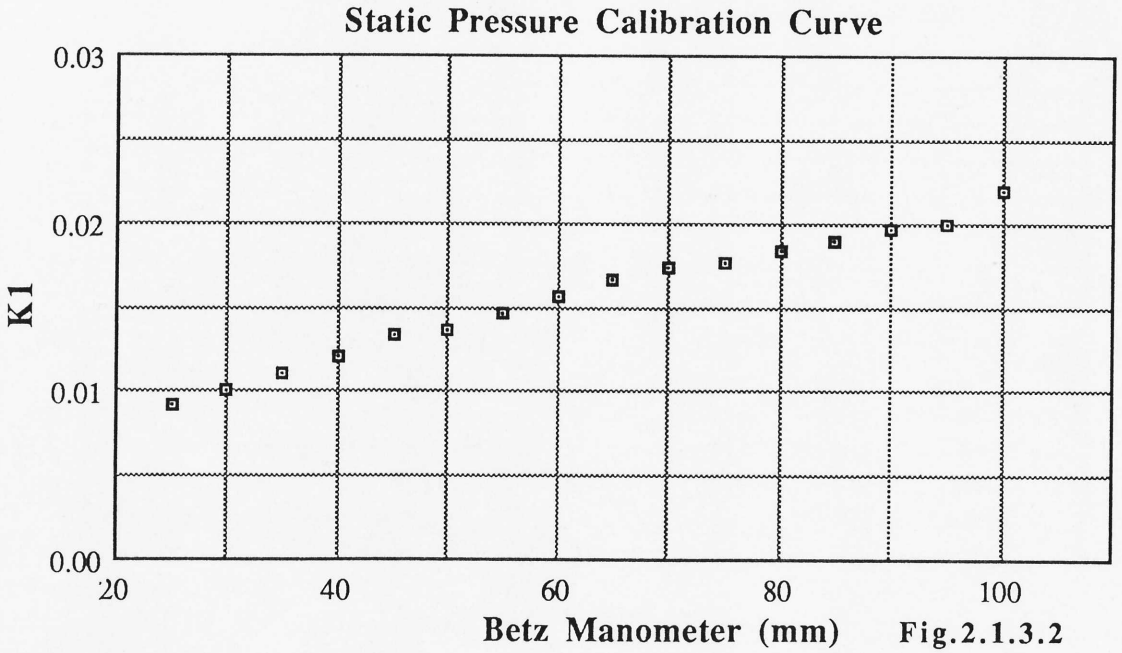


Fig.2.1.3.2

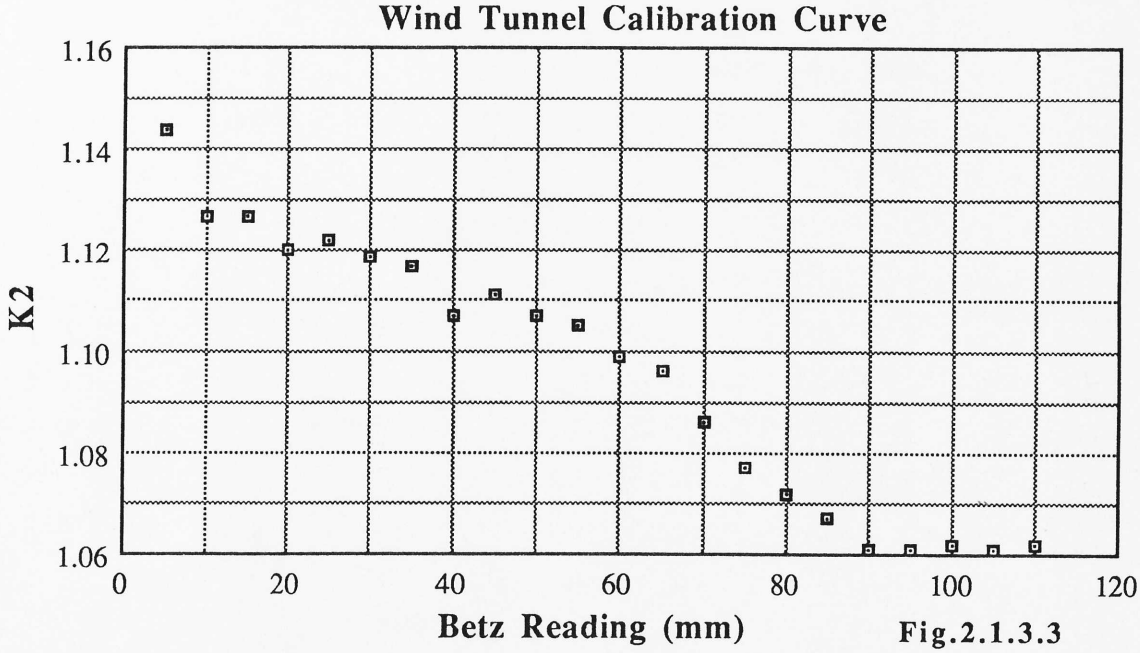


Fig.2.1.3.3

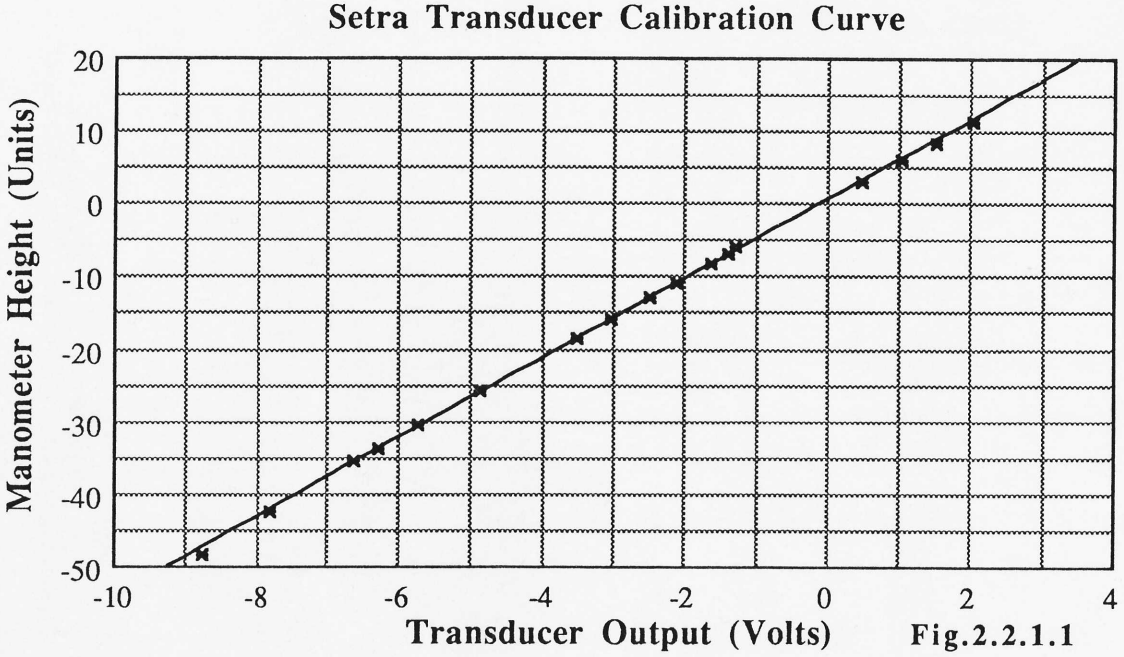


Fig.2.2.1.1

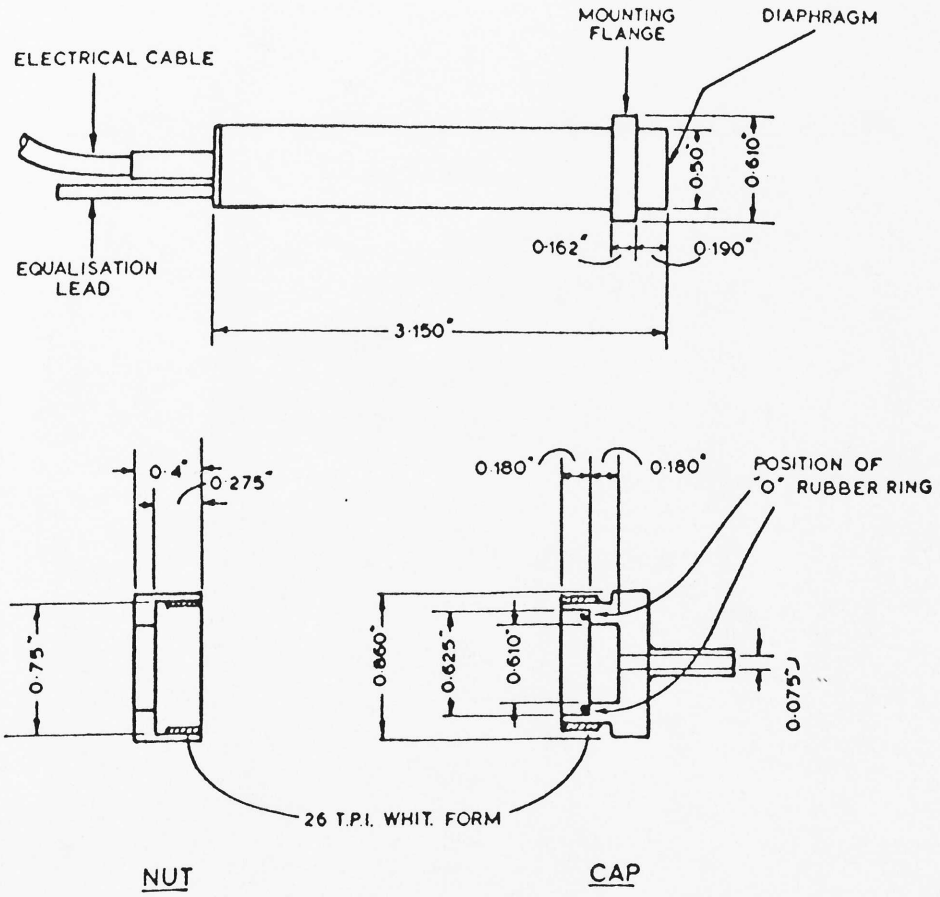


Fig.2.2.1.2 Diagrams of Setra Transducer and cap design.

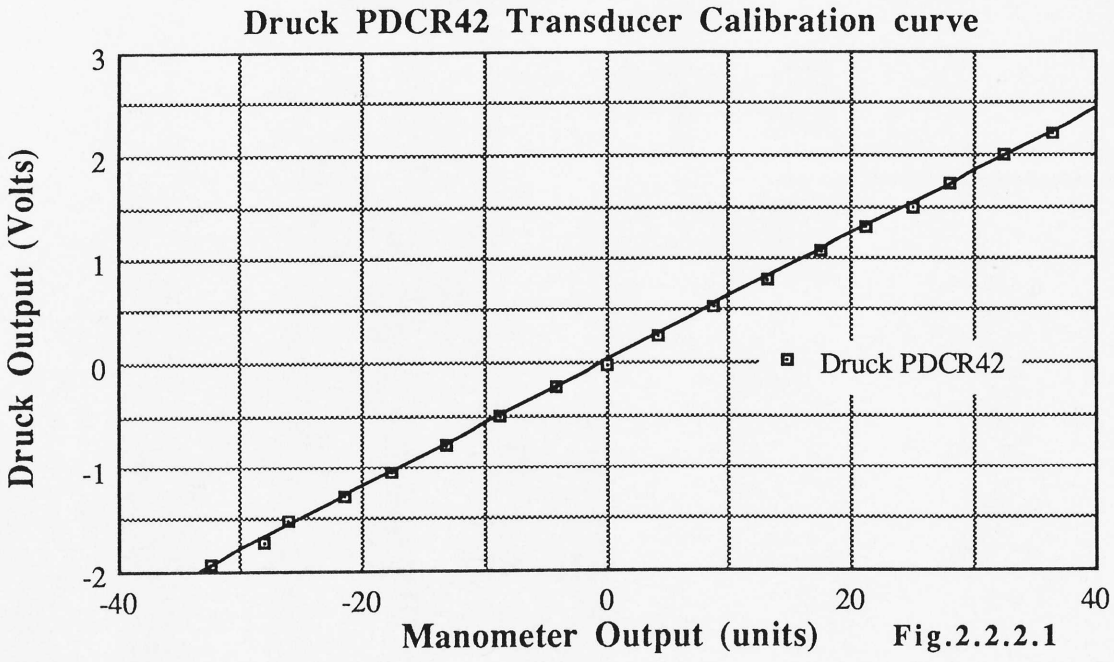
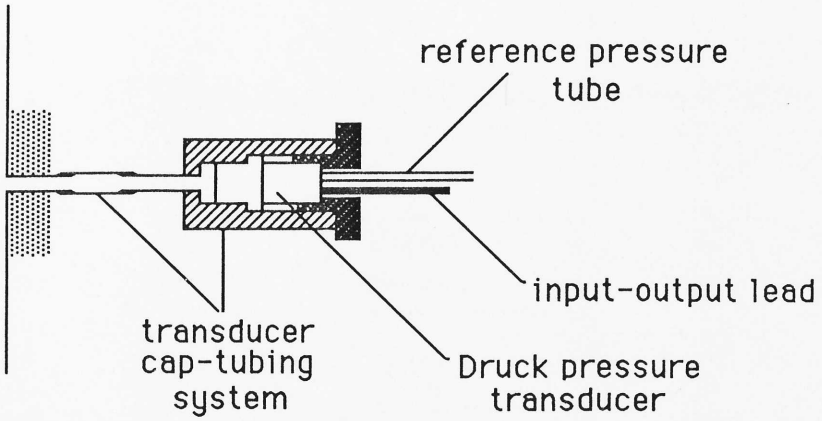


Fig.2.2.2.1

Pressure Transducer setup for measuring Fluctuating Pressure.



Druck PDCR42 Transducer Cap Design

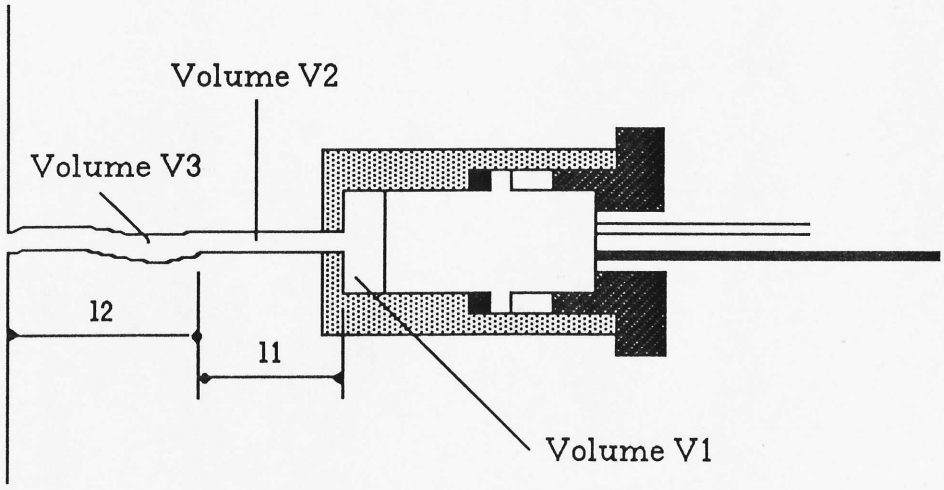


Fig.2.2.2.2

Druck PDCR42 Transducer dynamic Response Setup

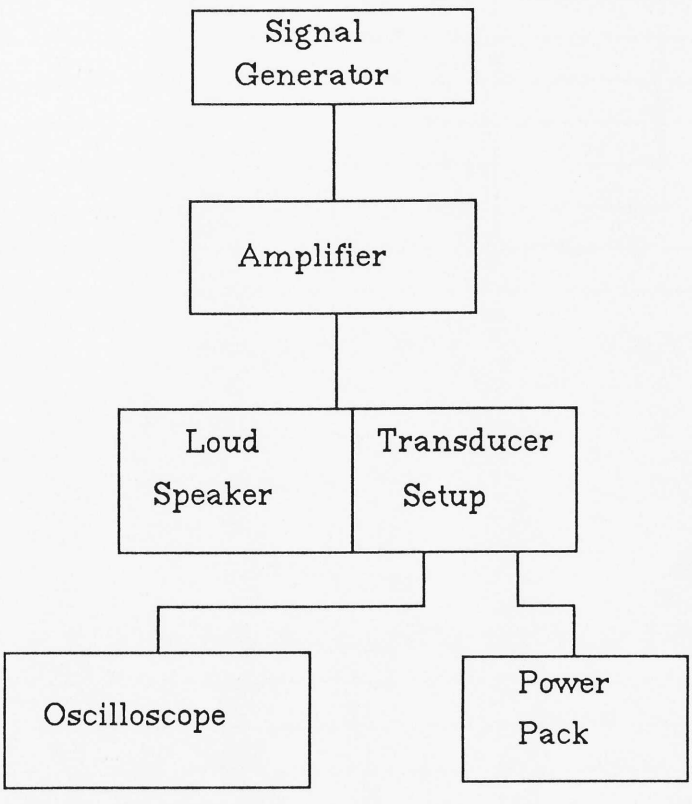


Fig.2.2.2.3

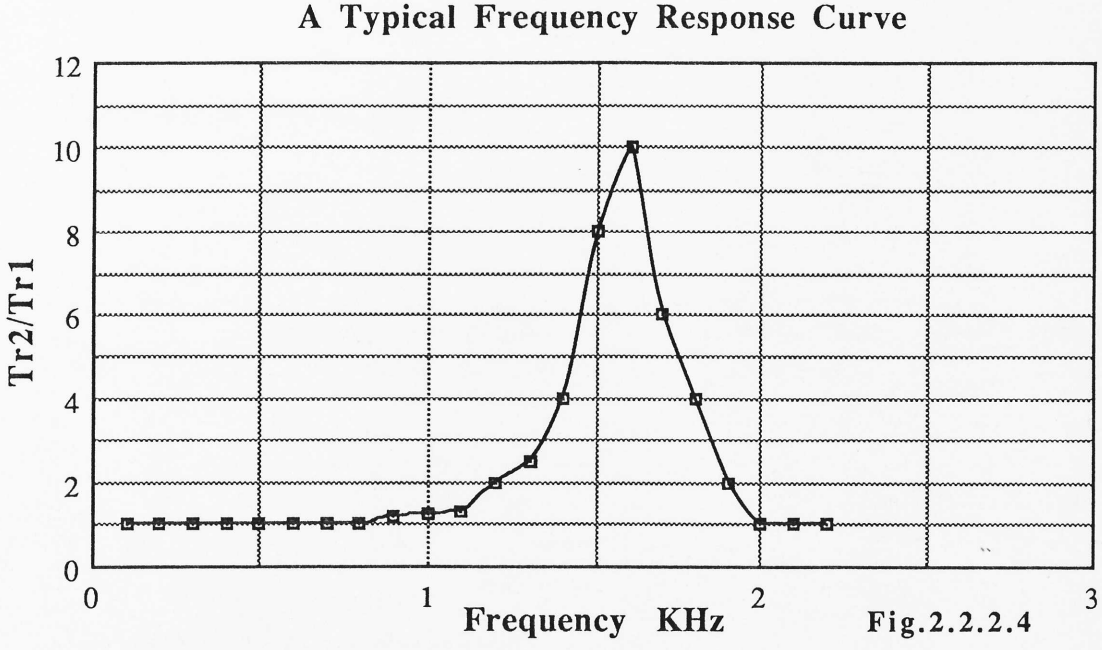


Fig.2.2.2.4

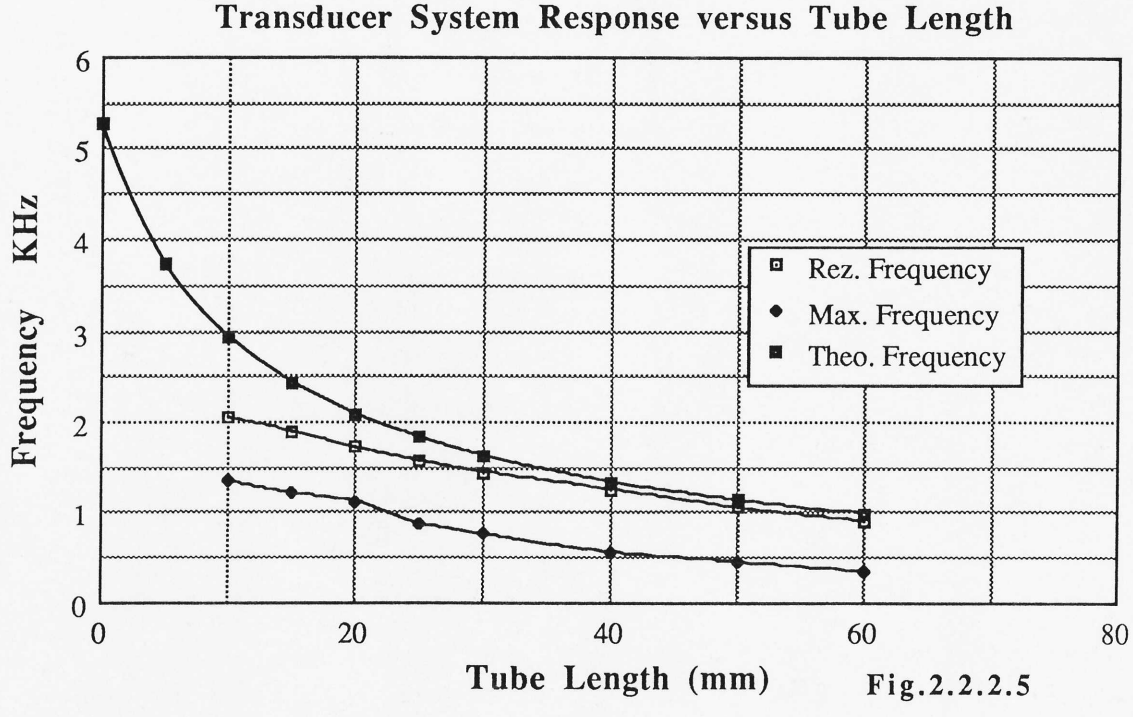


Fig.2.2.2.5

Mean Static Pressure Setup

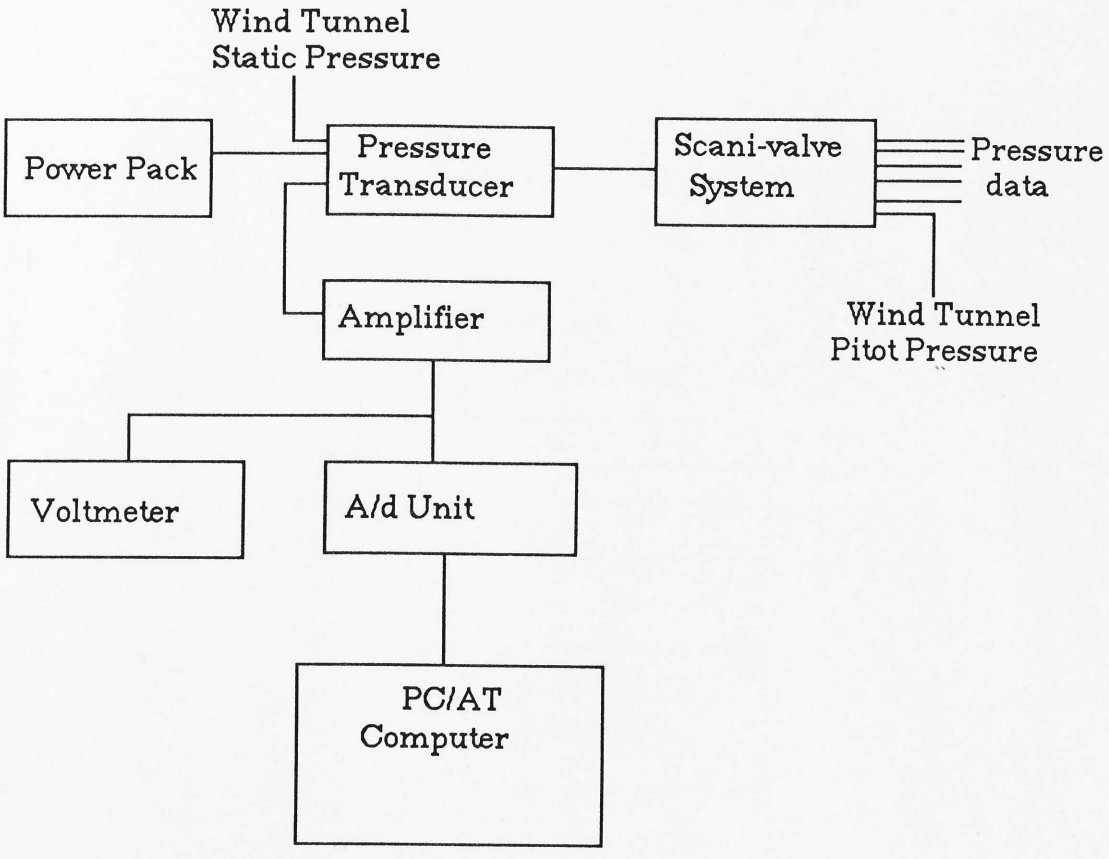


Fig. 2.5.1

Fluctuating Pressure Setup

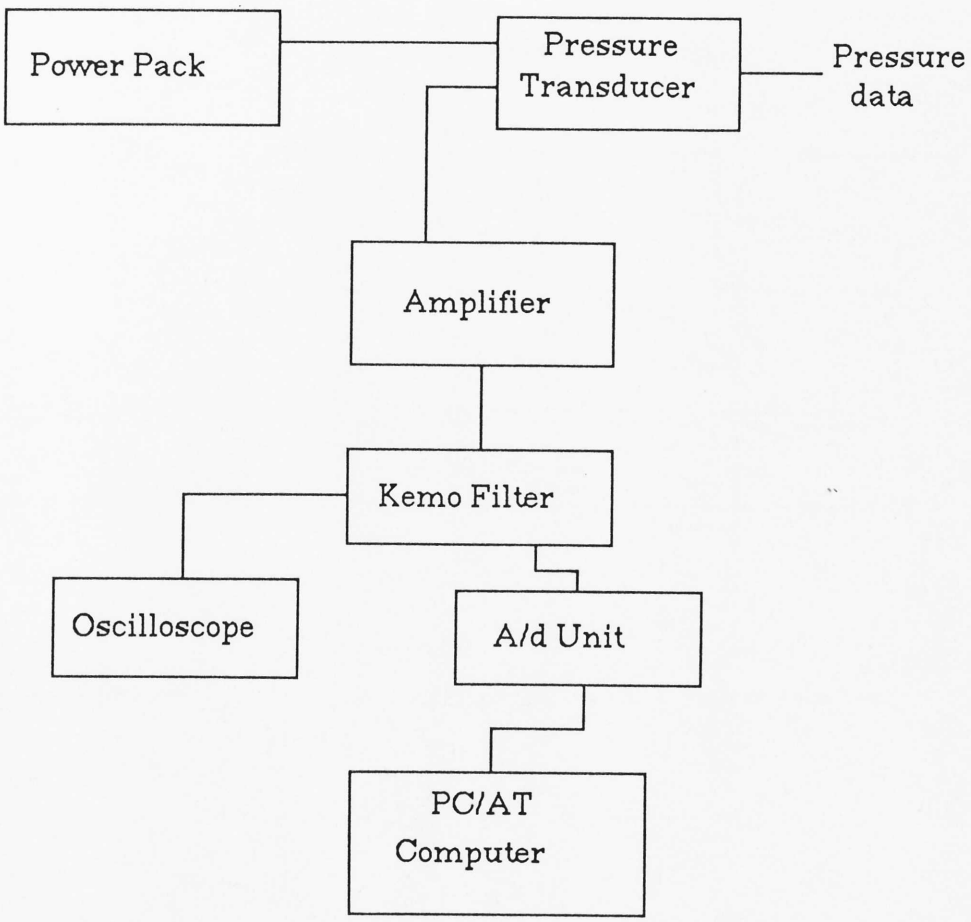


Fig.2.6.1

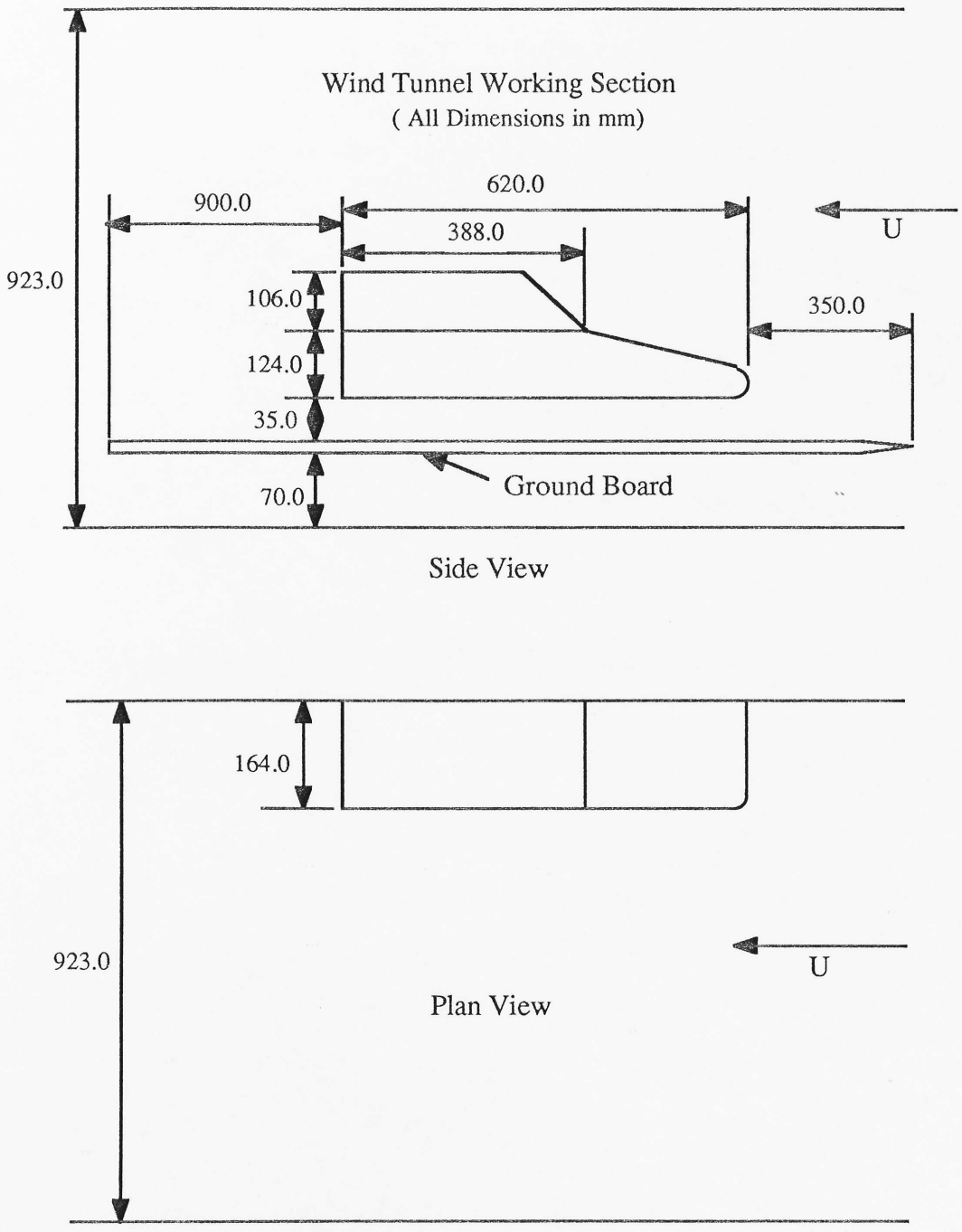
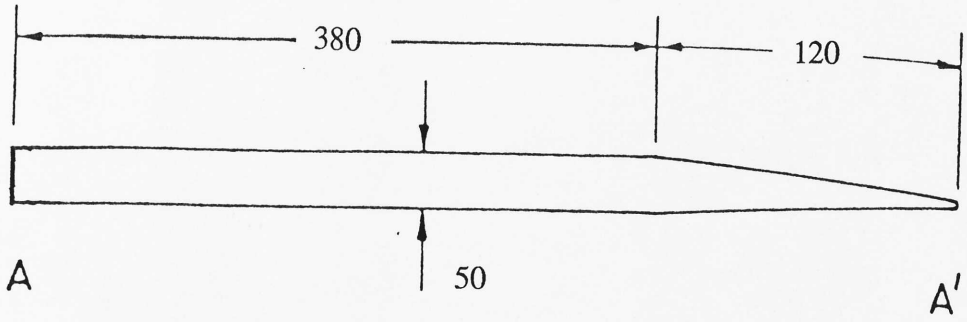


Fig.2.7.1.1 Road Vehicle Set-up in Wind Tunnel



DIMENSIONS ARE IN MILLIMETRES

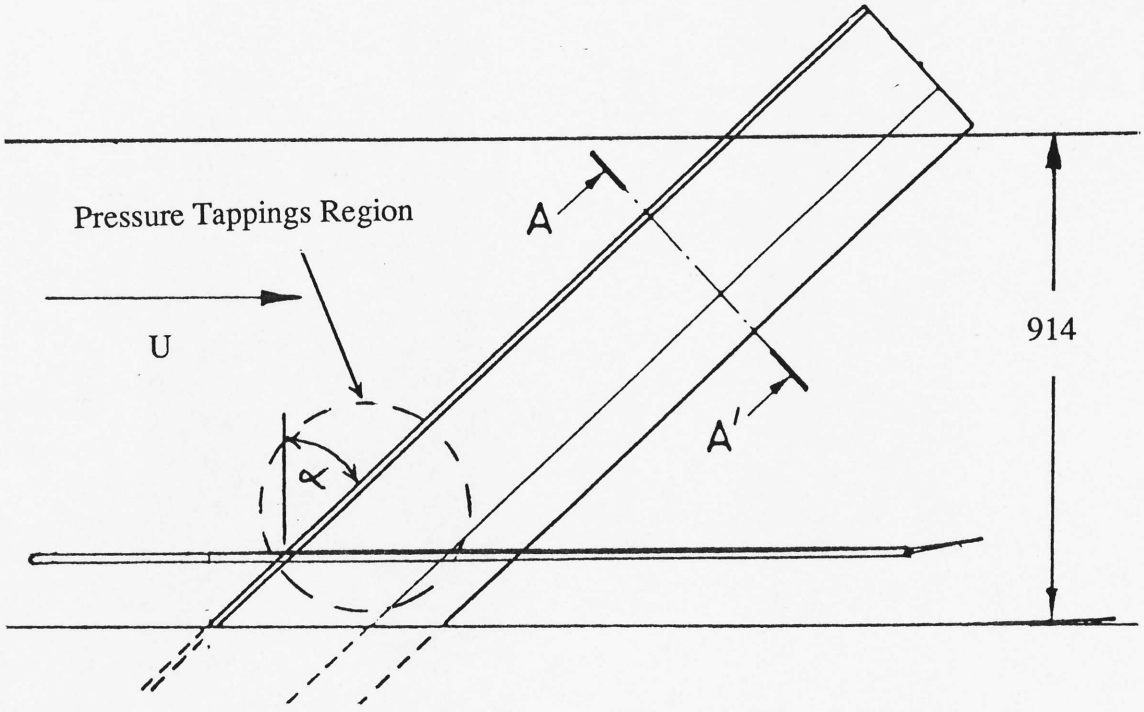
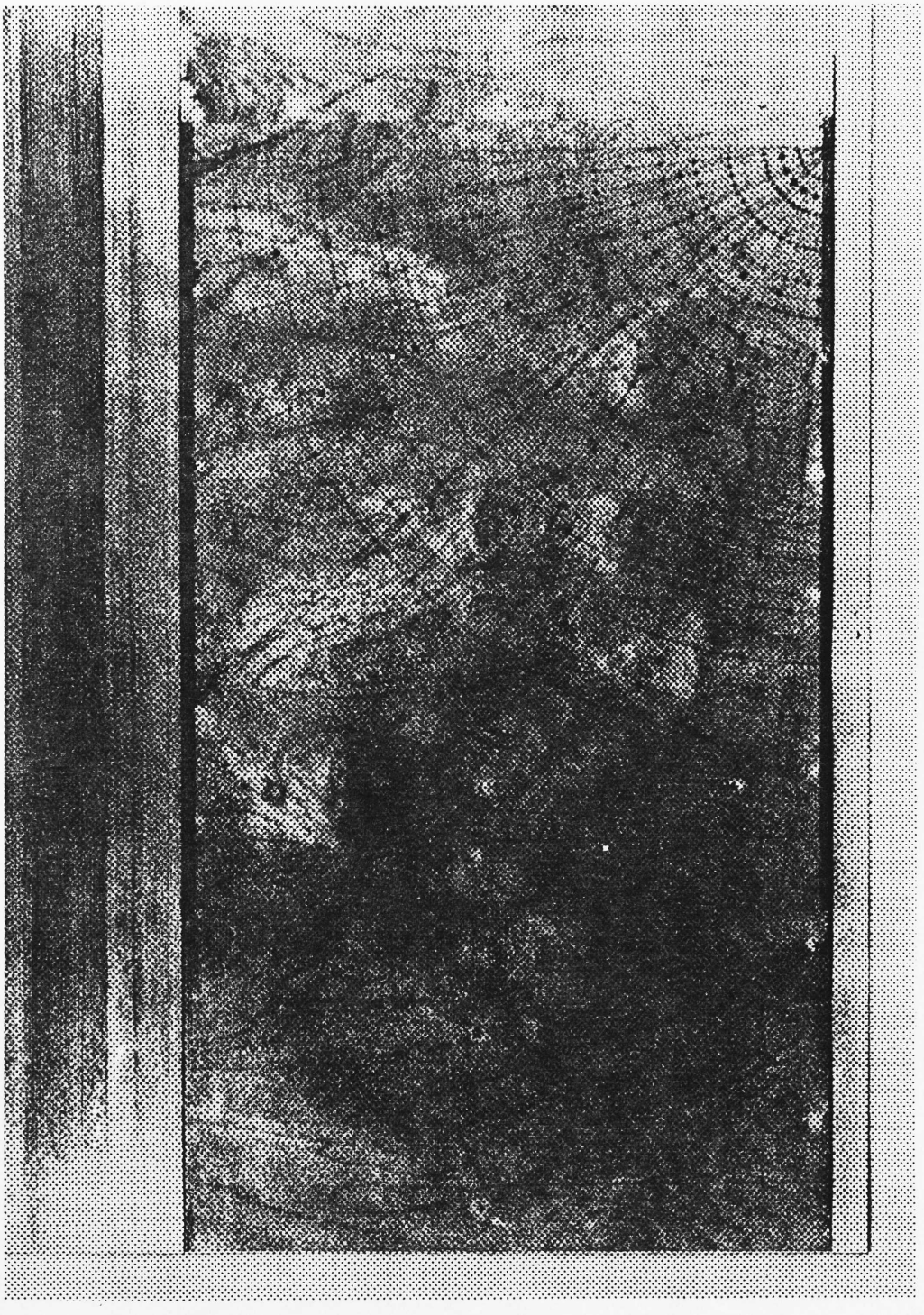
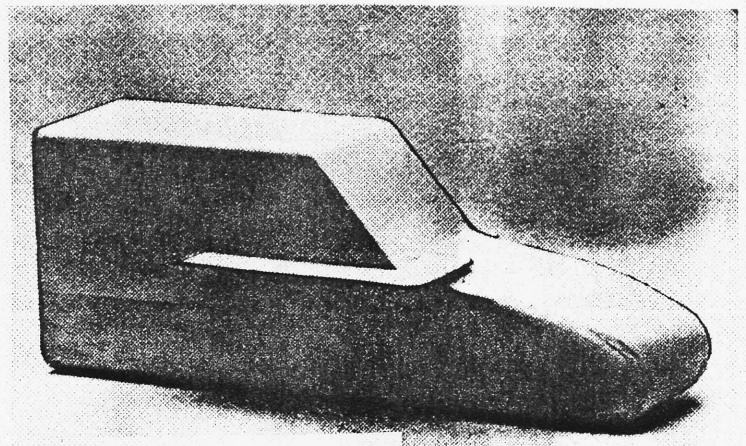


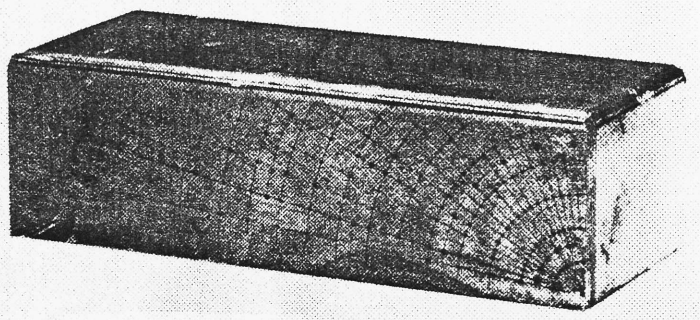
Fig.2.7.2.1 Diagram of Swept Plate model.



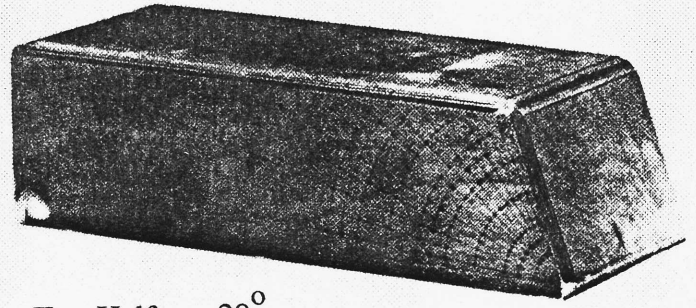
Pl.2.7.2.1 Photograph of the Tapping grids used on the Swept Plate model.



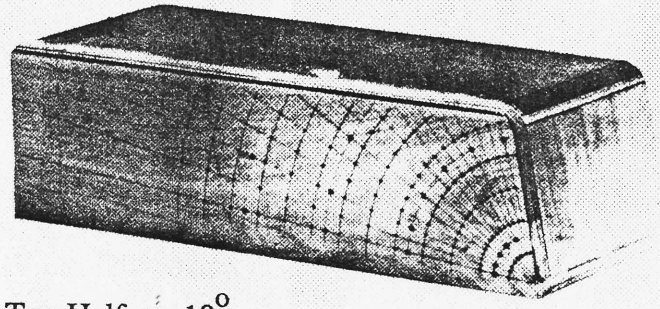
Whole Model with Plate



Top Half, $\gamma = 0^{o}$

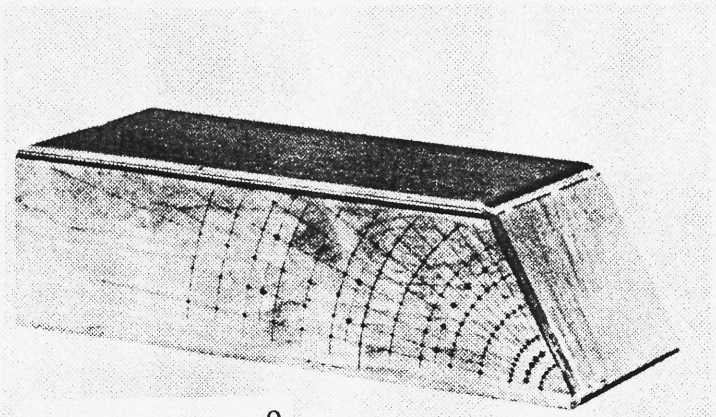


Top Half, $\gamma = 20^{o}$

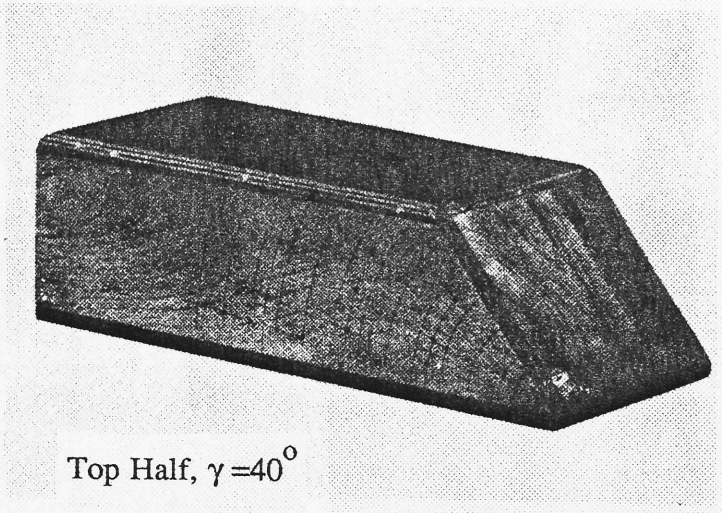


Top Half, $\gamma = 10^{o}$

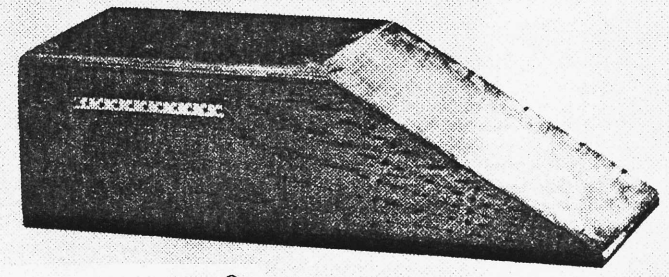
Pl.2.7.1.1 Photographs of the Road Vehicle models.



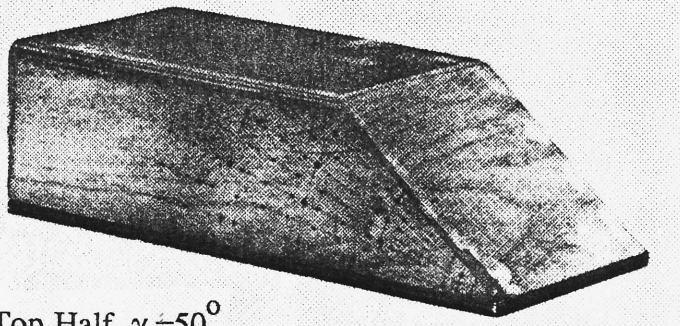
Top Half, $\gamma = 30^{o}$



Top Half, $\gamma = 40^{o}$

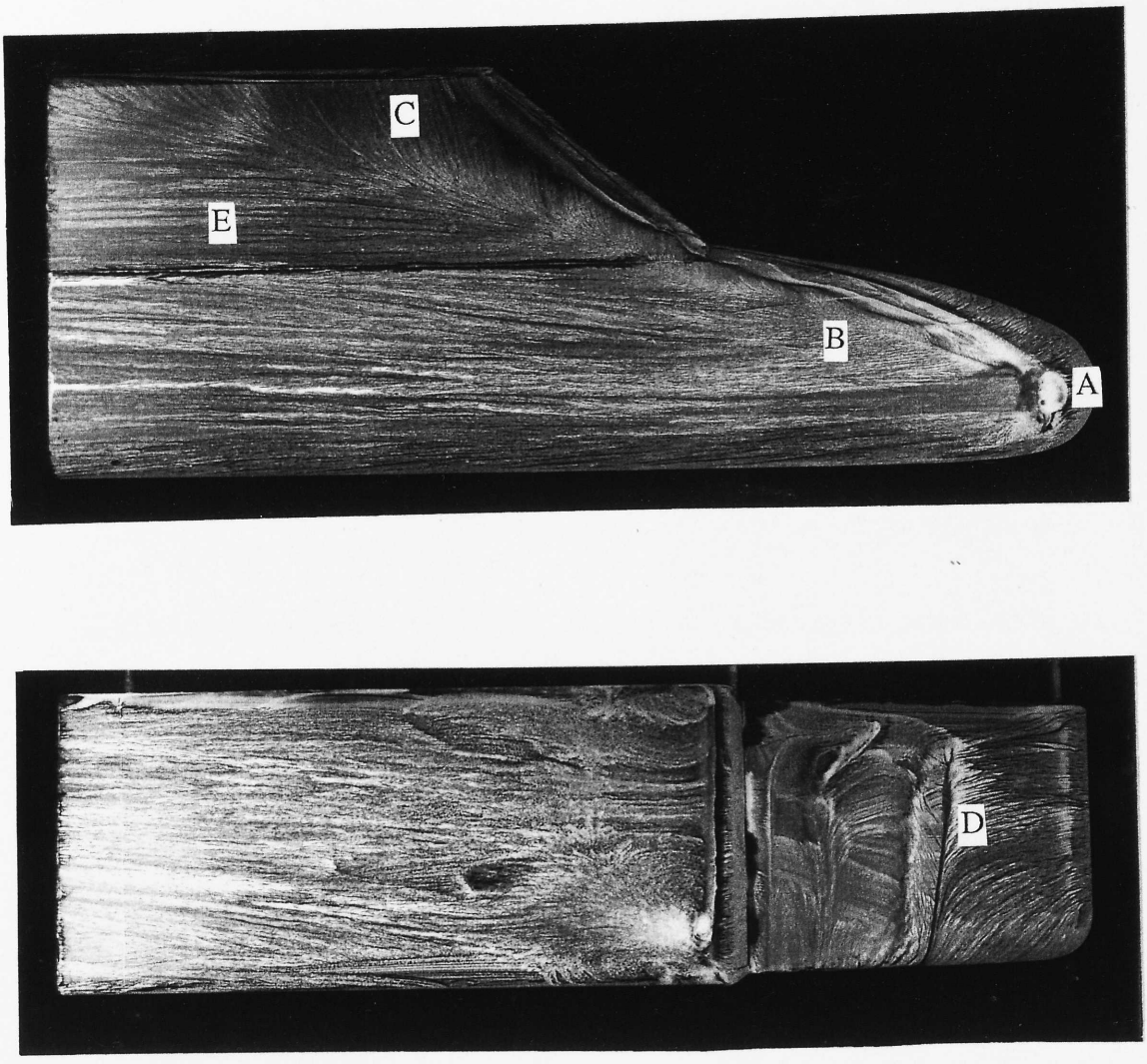


Top Half, $\gamma = 60^{o}$



Top Half, $\gamma = 50^{o}$

Pl.2.7.1.2 Photographs of the Road Vehicle models.



A - Three-Dimensional Separation Bubble

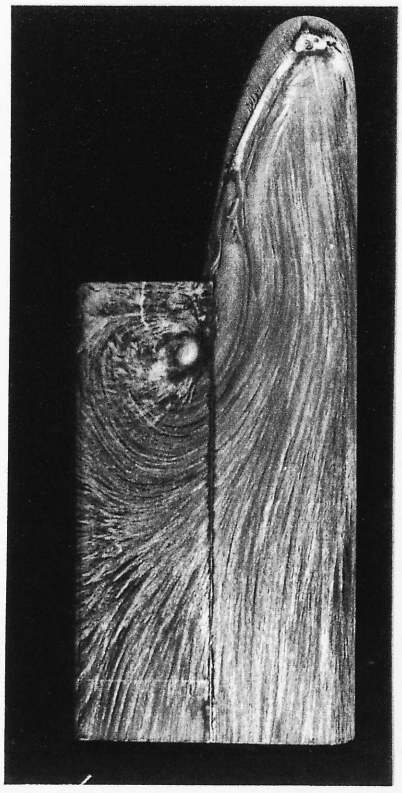
B - Base Vortex

C - A-Pillar Vortex

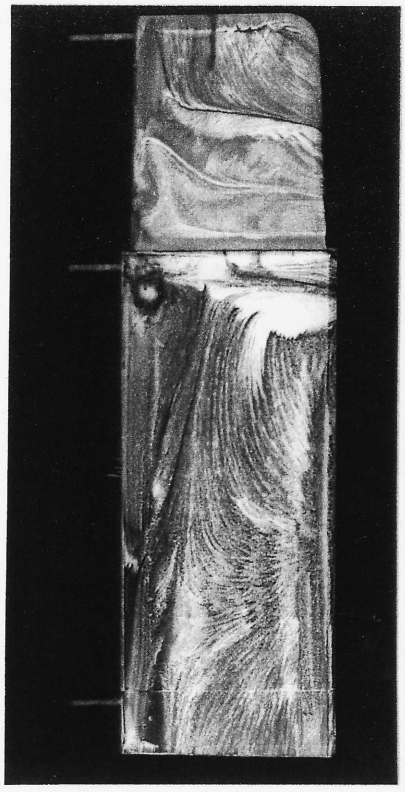
D - Horseshoe Vortex

E - Attached Flow

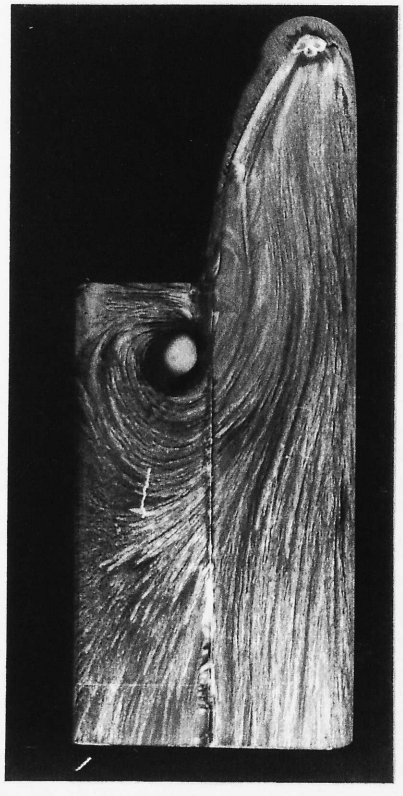
Pl.3.1.1 Typical wind tunnel flow visualization results.



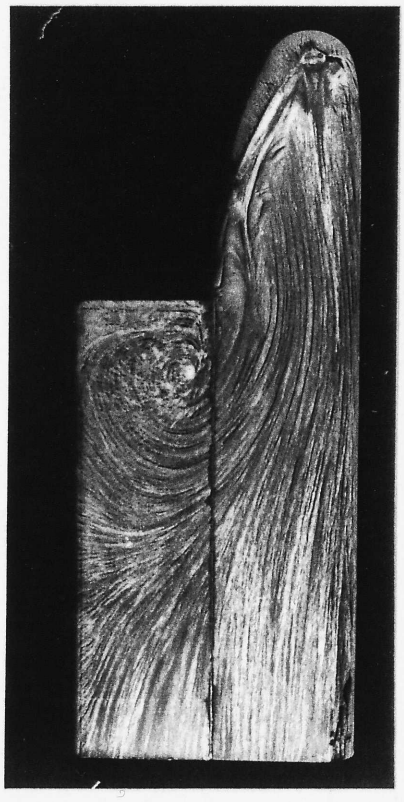
b) Side view, Re No.5.672×10^5



d) Top view, Re No.5.672×10^5

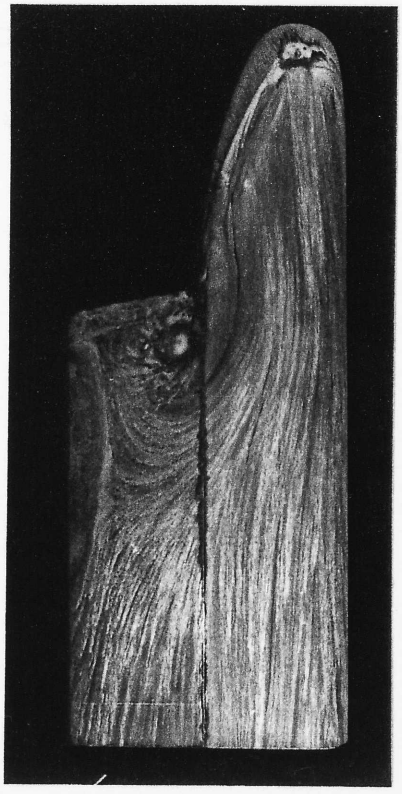


a) Side view, Re No.3.457×10^5

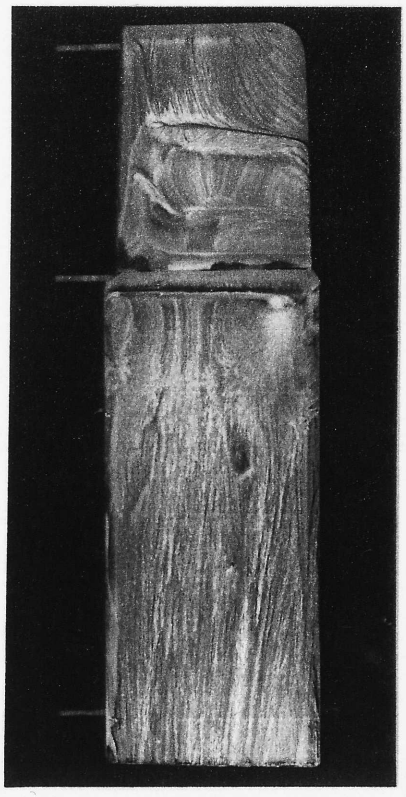


c) Side view, Re No.7.650×10^5

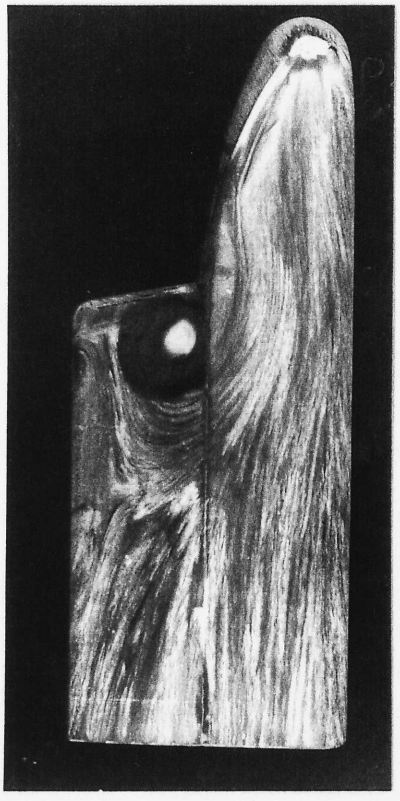
Pl.3.1.1.1a-d Wind Tunnel Flow Visualization of 0° Whole Model at three Reynolds Nos.



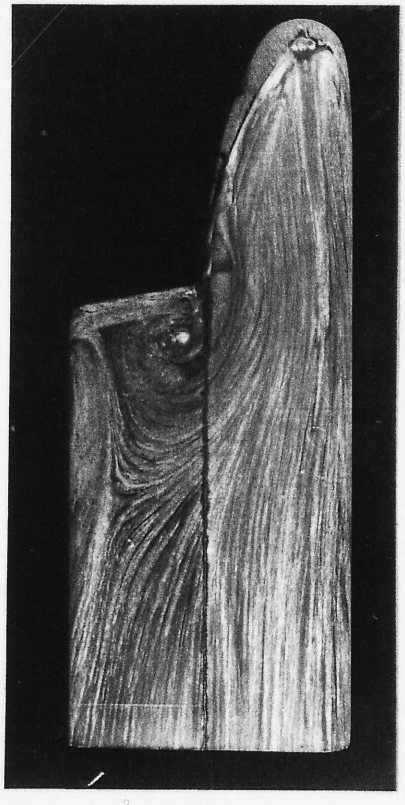
b) Side view, Re No.5.672×10^5



d) Top view, Re No.5.672×10^5

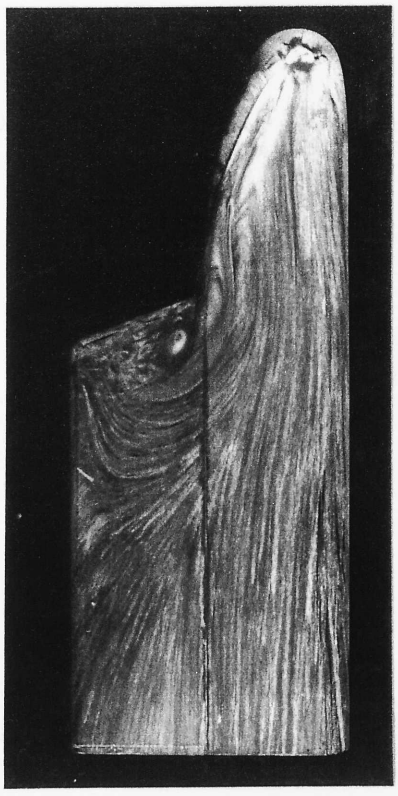


a) Side view, Re No.3.457×10^5

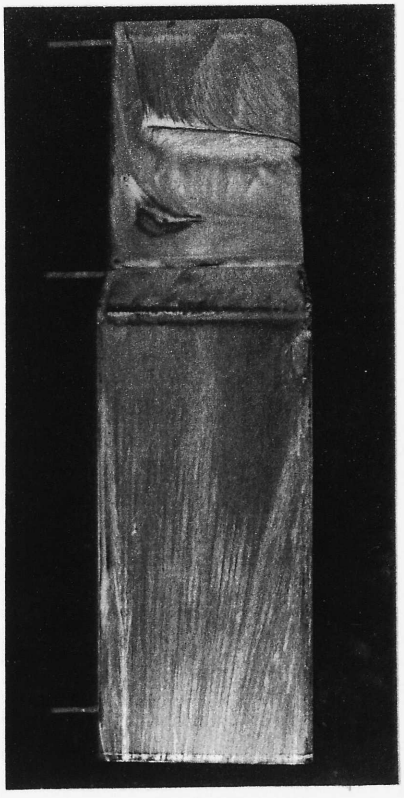


c) Side view, Re No.7.650×10^5

Pl.3.1.1.2a-d Wind Tunnel Flow Visualization of 10° Whole Model at three Reynolds Nos.



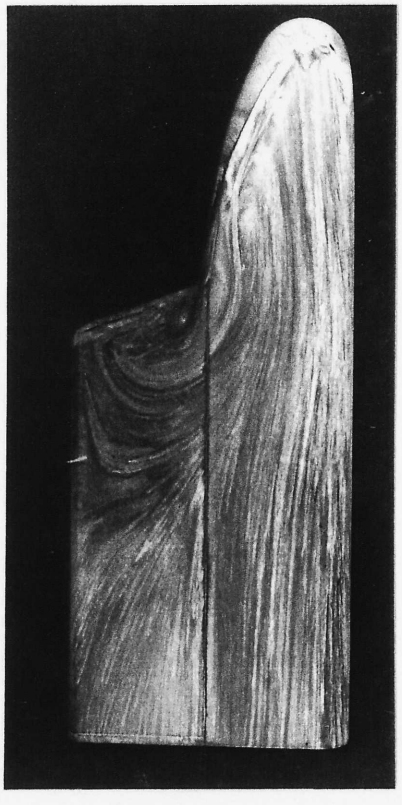
b) Side view, Re No.5.672×10^5



d) Top view, Re No.5.672×10^5



a) Side view, Re No.3.457×10^5

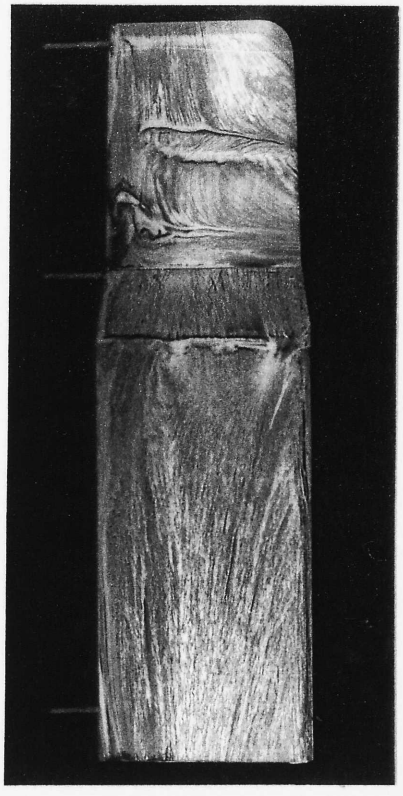


c) Side view, Re No.7.650×10^5

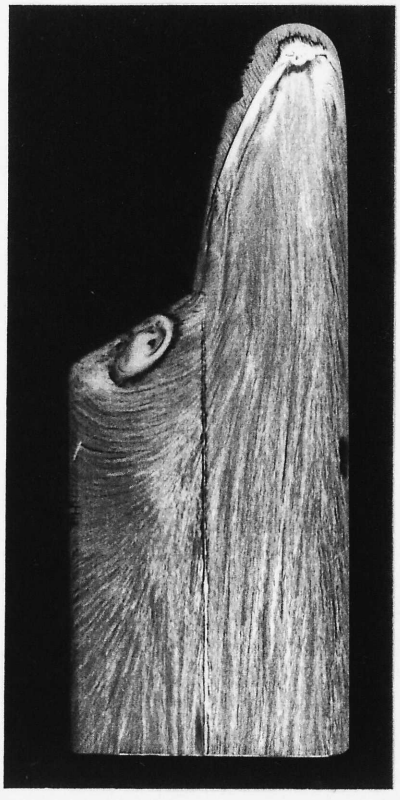
Pl.3.1.1.3a-d Wind Tunnel Flow Visualization of 20° Whole Model at three Reynolds Nos.



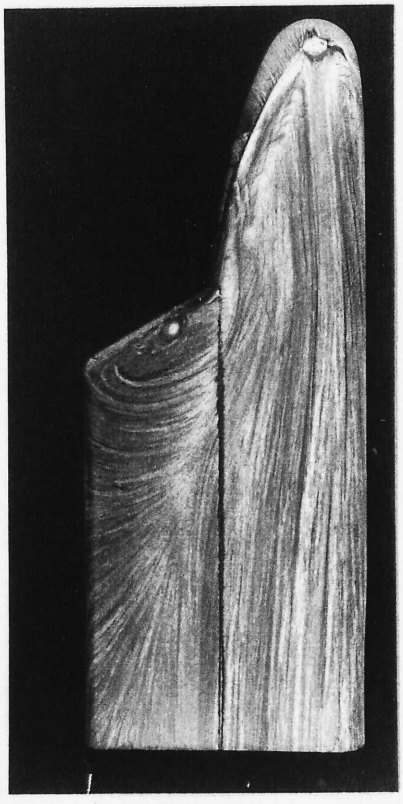
b) Side view, Re No.5.672×10^5



d) Top view, Re No.5.672×10^5

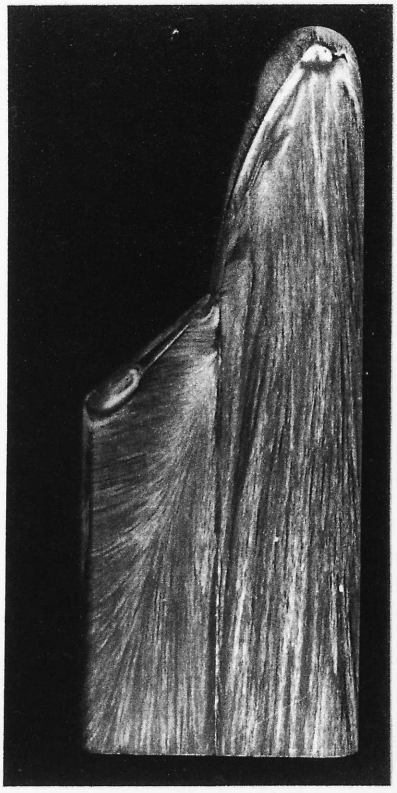


a) Side view, Re No.3.457×10^5

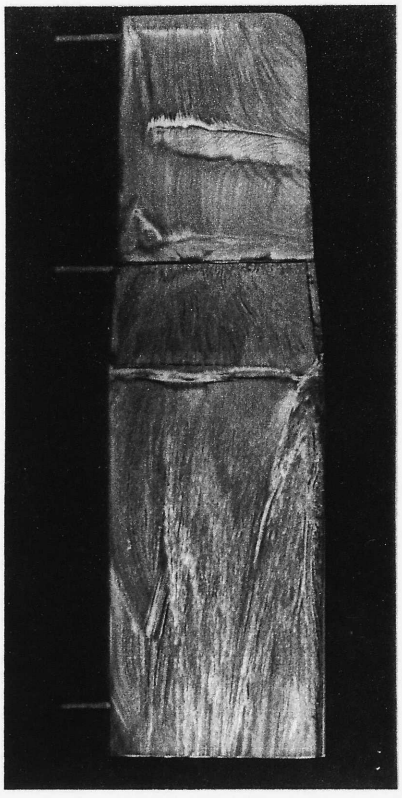


c) Side view, Re No.7.650×10^5

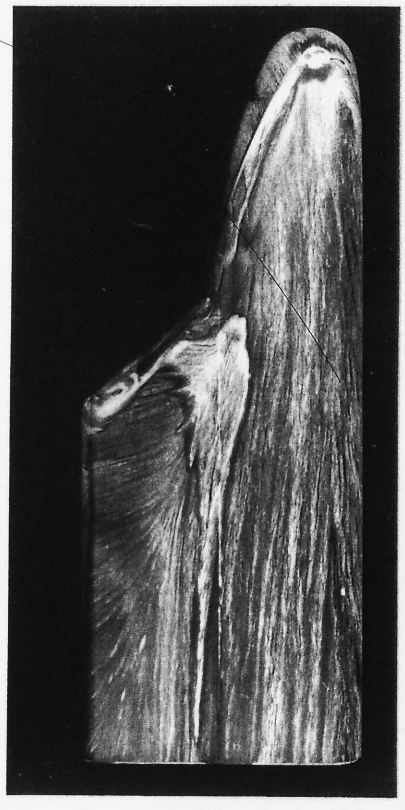
Pl.3.1.1.4a-d Wind Tunnel Flow Visualization of 30° Whole Model at three Reynolds Nos.



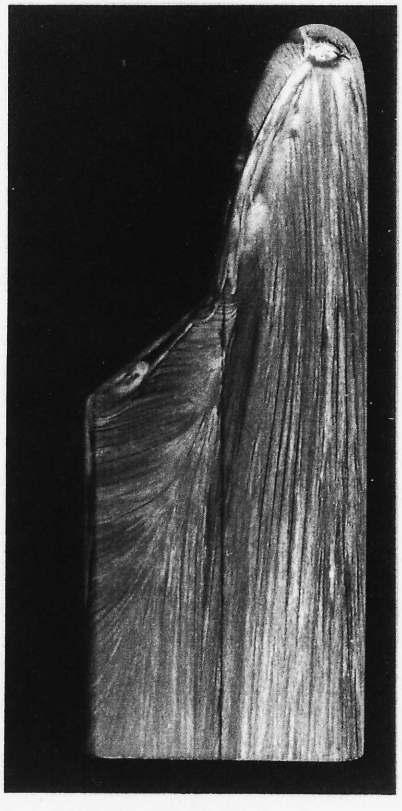
b) Side view, Re No.5.672x10^5



d) Top view, Re No.5.672x10^5

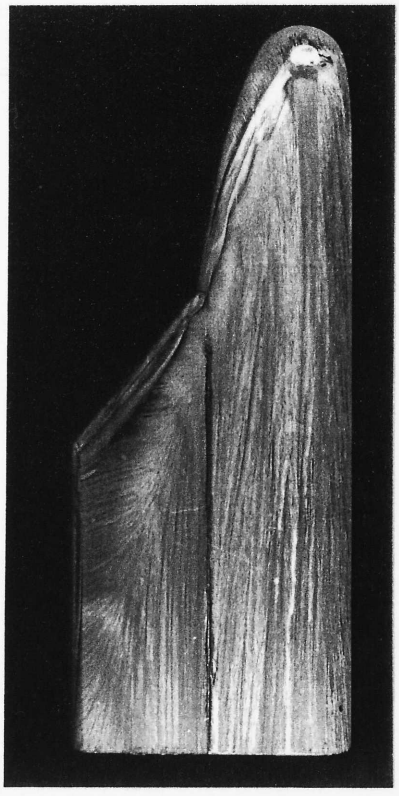


a) Side view, Re No.3.457x10^5

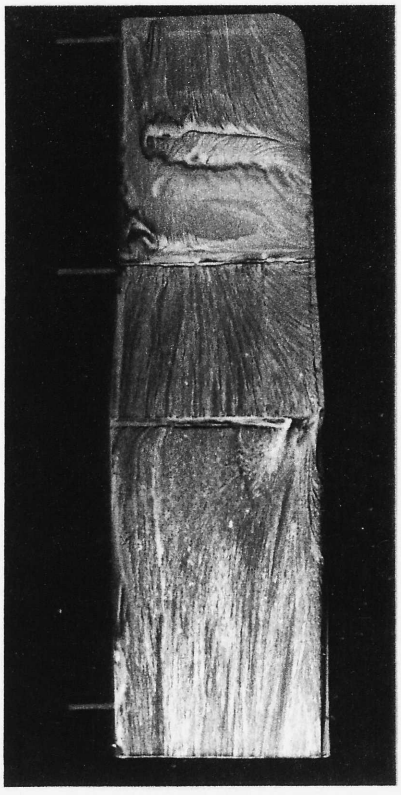


c) Side view, Re No.7.650x10^5

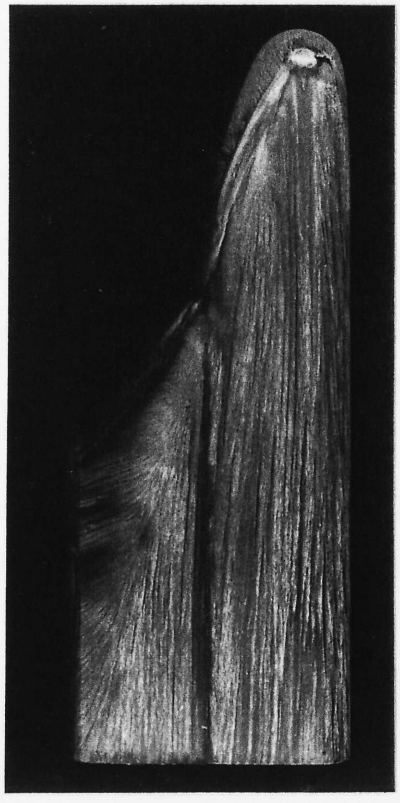
Pl.3.1.1.5a-d Wind Tunnel Flow Visualization of 40° Whole Model at three Reynolds Nos.



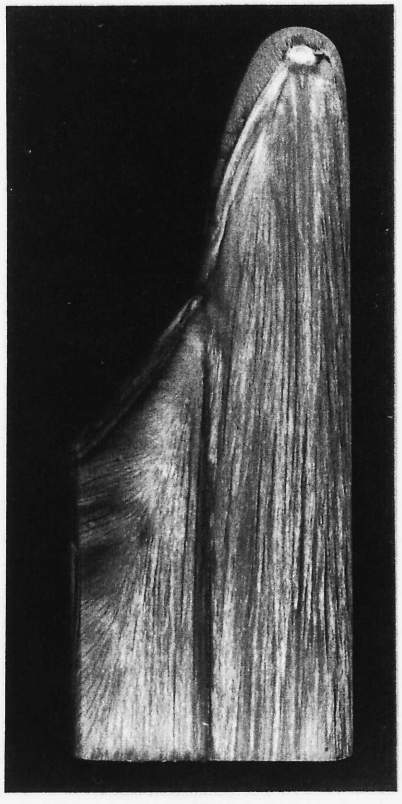
b) Side view, Re No.5.672×10^5



d) Top view, Re No.5.672×10^5



a) Side view, Re No.3.457×10^5

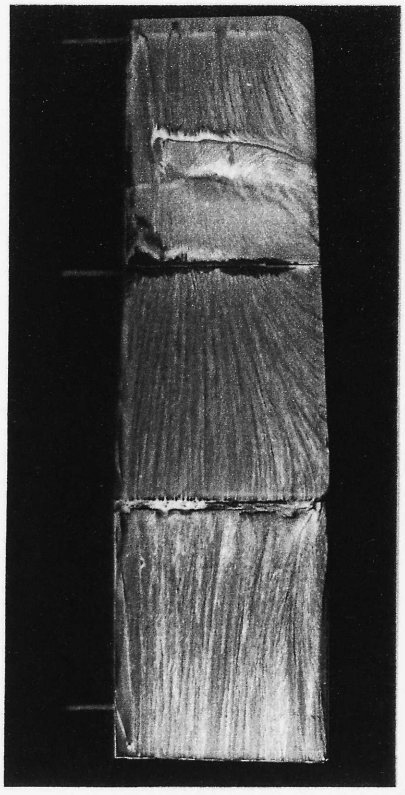


c) Side view, Re No.7.650×10^5

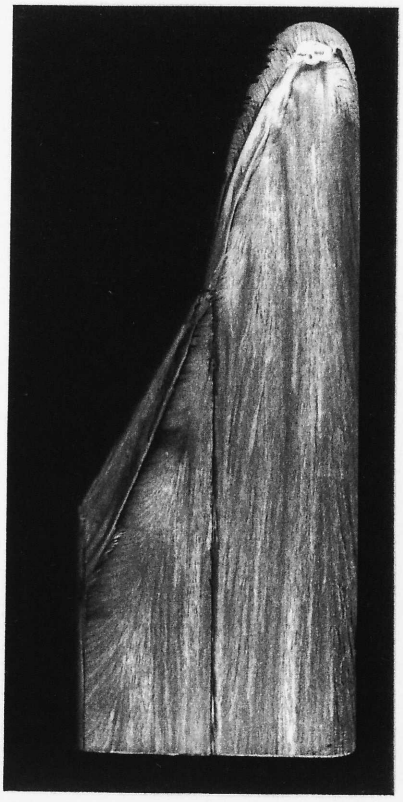
Pl.3.1.1.6a-d Wind Tunnel Flow Visualization of 50° Whole Model at three Reynolds Nos.



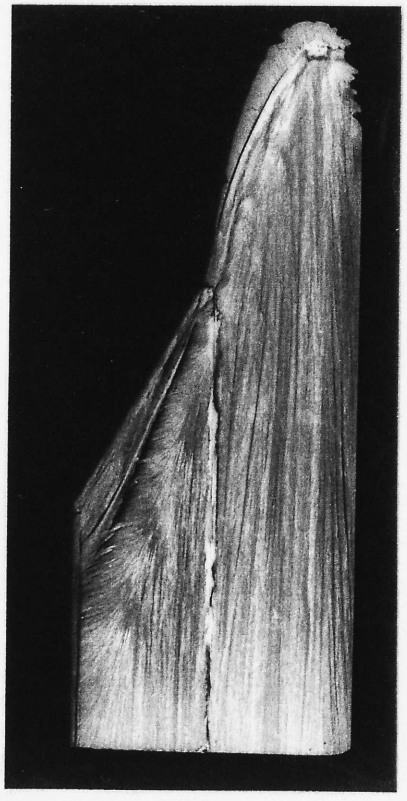
b) Side view, Re No.5.672×10^5



d) Top view, Re No.5.672×10^5

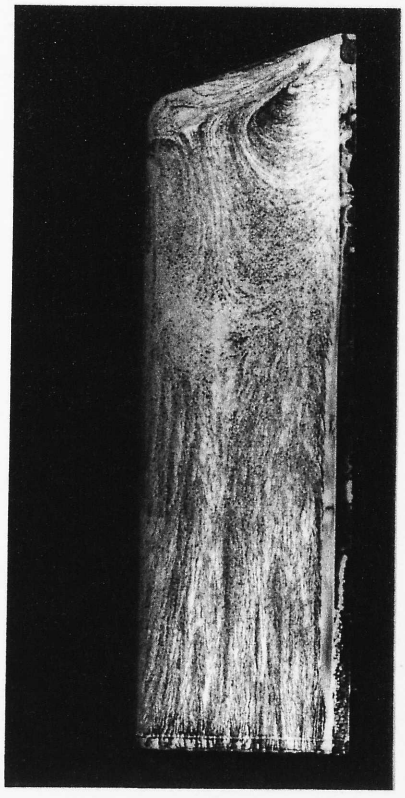


a) Side view, Re No.3.457×10^5

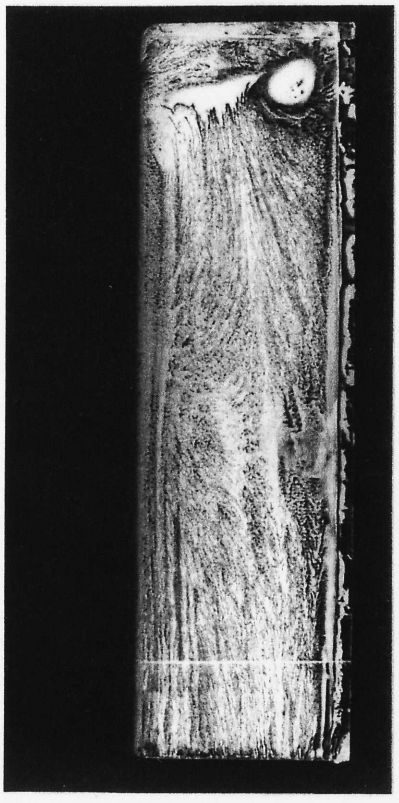


c) Side view, Re No.7.650×10^5

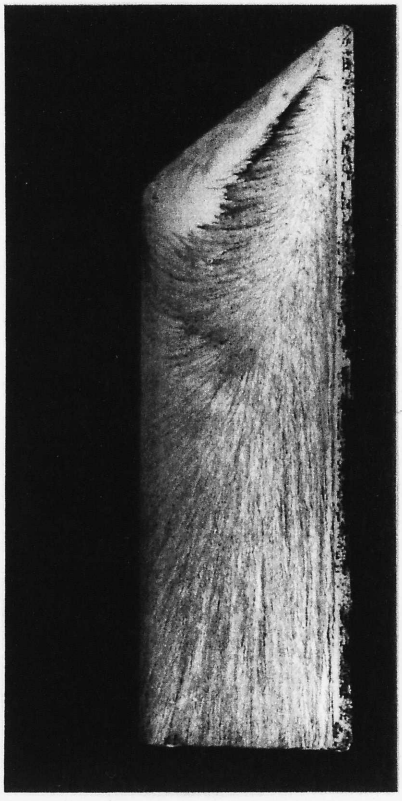
Pl.3.1.1.7a-d Wind Tunnel Flow Visualization of 60° Whole Model at three Reynolds Nos.



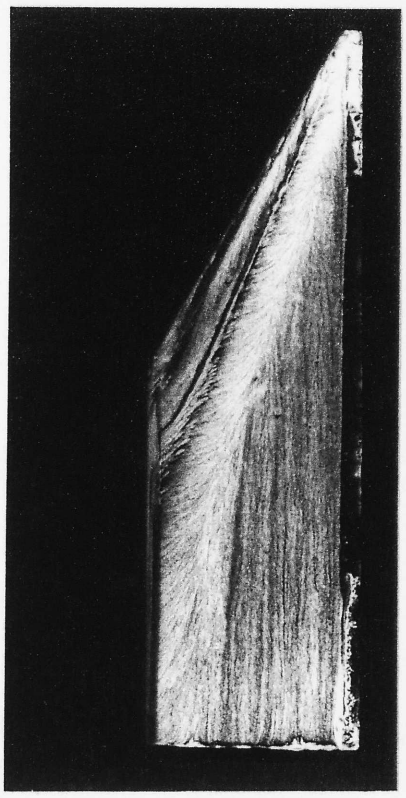
a) $\gamma = 0^{o}$, Re No.7.650×10^{5}



b) $\gamma = 20^{o}$, Re No.7.650×10^{5}

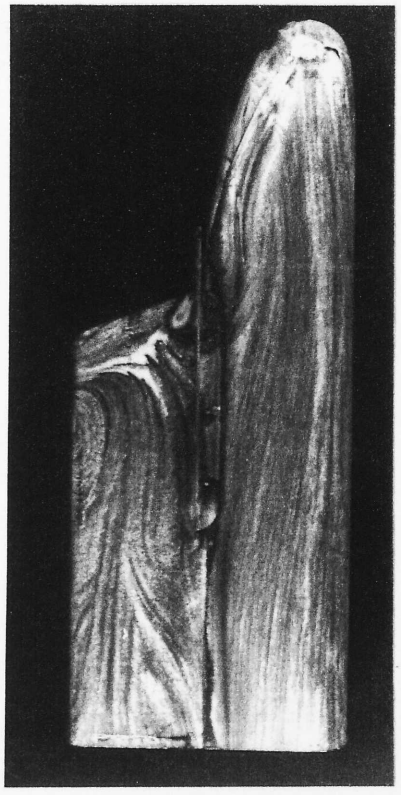


c) $\gamma = 40^{o}$, Re No.7.650×10^{5}



d) $\gamma = 60^{o}$, Re No.5.672×10^{5}

Pl.3.1.2.1 Wind Tunnel Flow Visualization of four Top Half Models ($\gamma = 0^{o}, 20^{o}, 40^{o}, 60^{o}$).



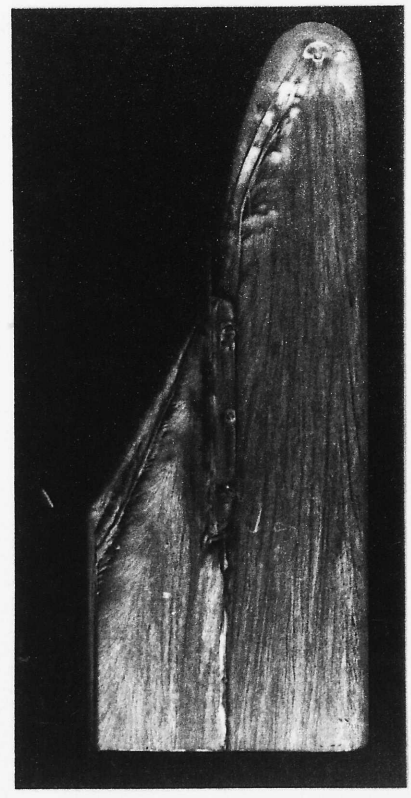
a) $\gamma = 0^{o}$, Re No.7.650×10^{5}



b) $\gamma = 20^{o}$, Re No.7.650×10^{5}

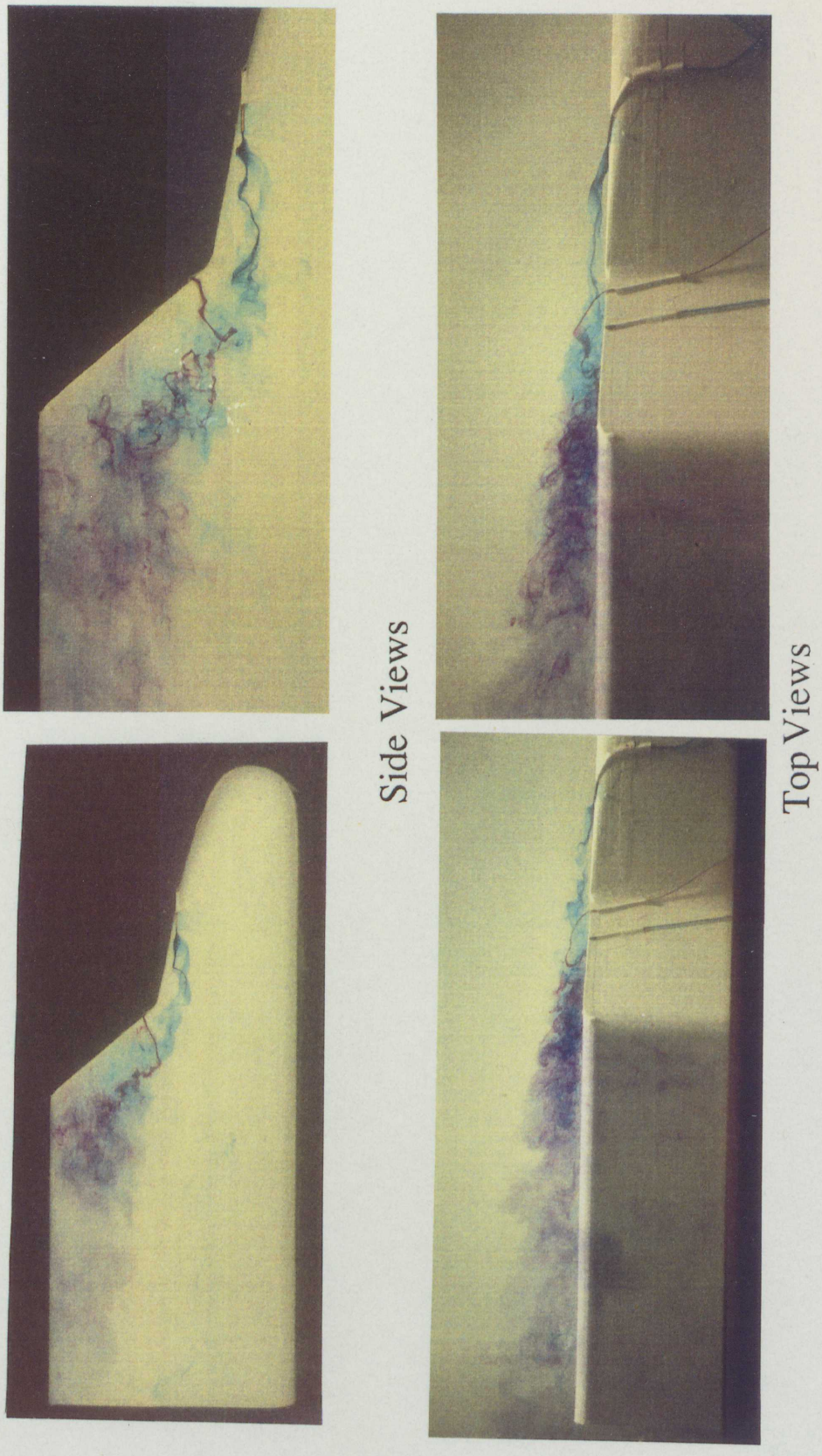


c) $\gamma = 40^{o}$, Re No.3.457×10^{5}

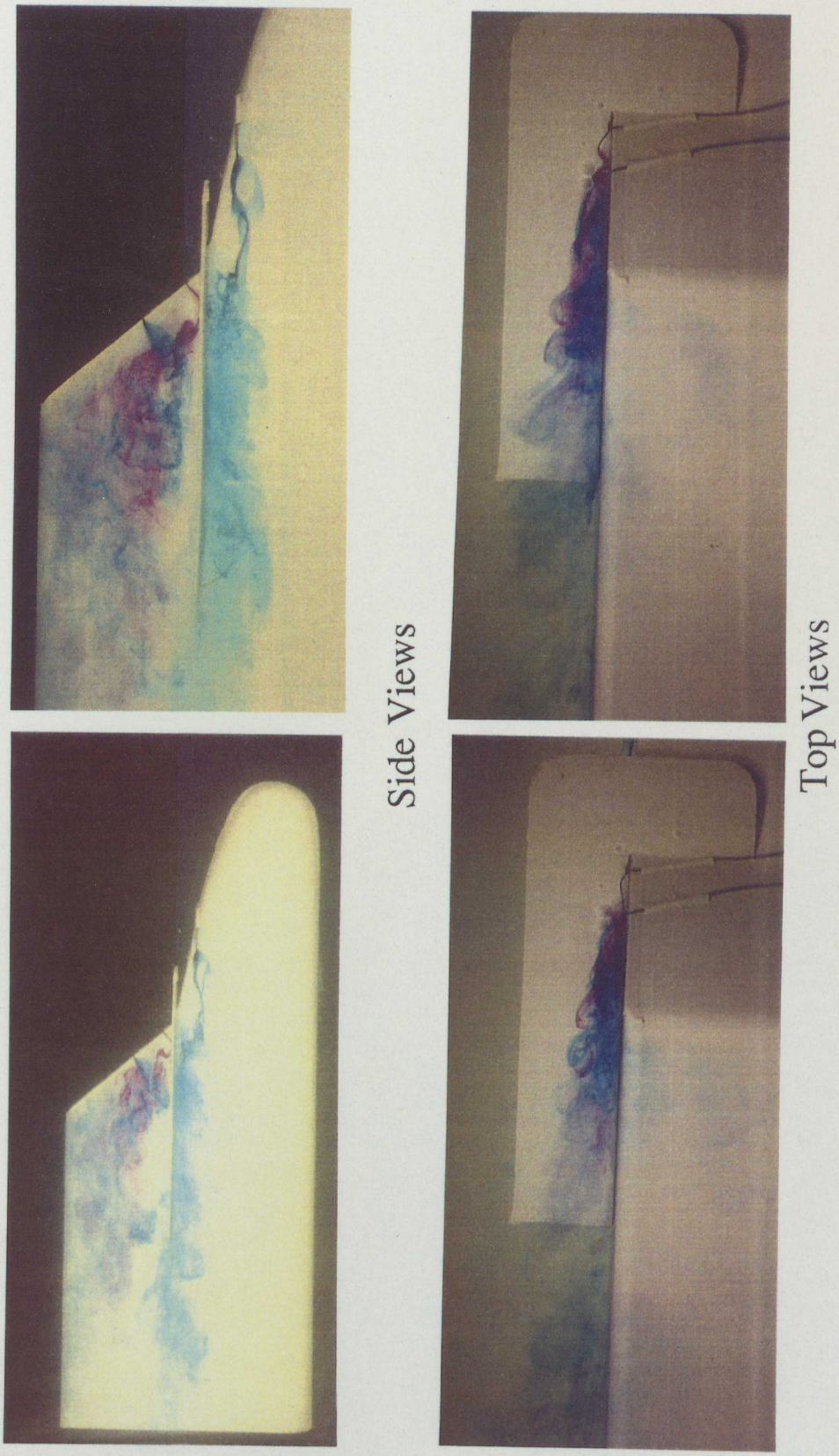


d) $\gamma = 60^{o}$, Re No.5.672×10^{5}

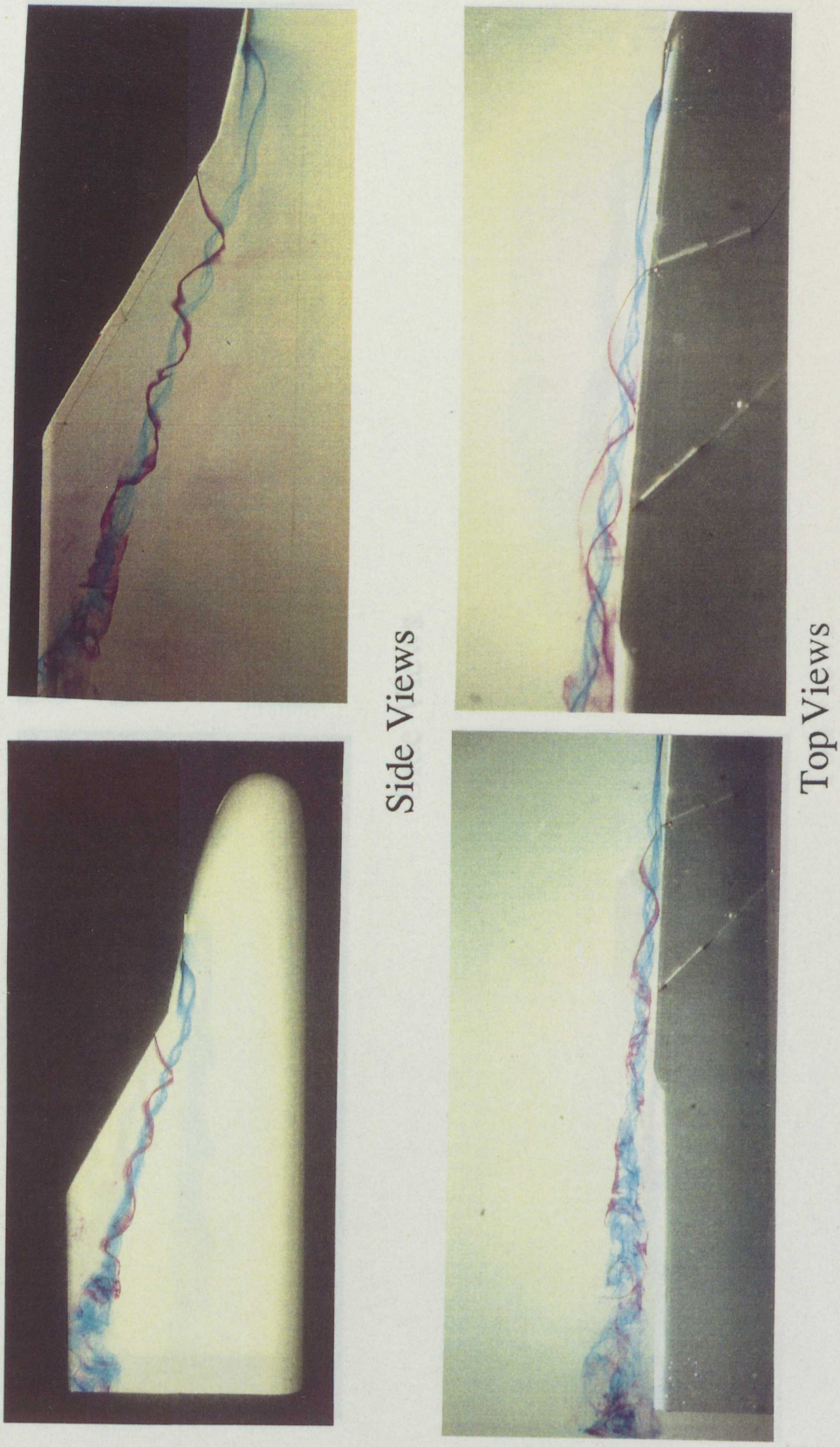
Pl.3.1.3.1 Wind Tunnel Flow Visualization of four Whole Models with Plate ($\gamma = 0^{o}, 20^{o}, 40^{o}, 60^{o}$).



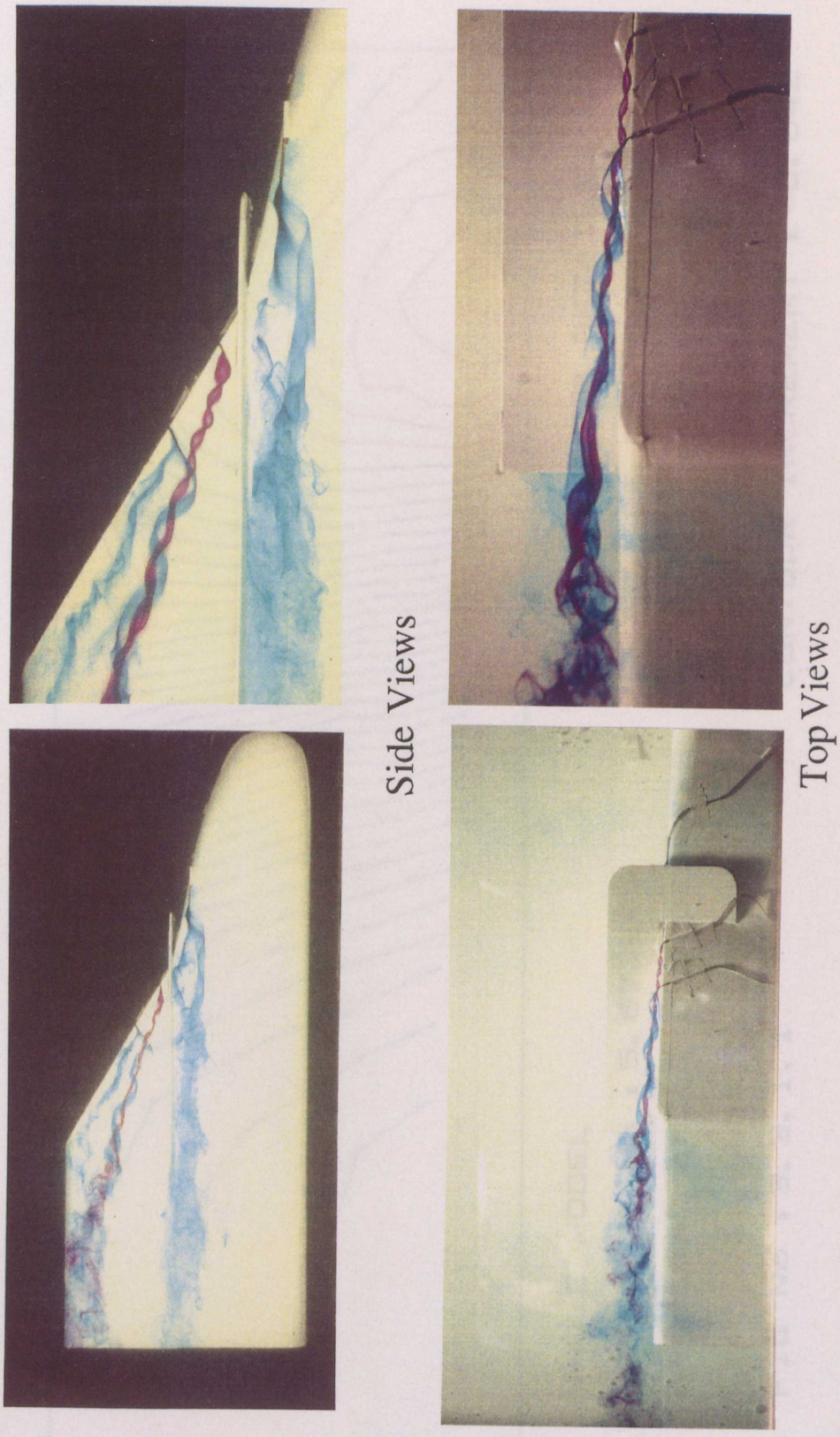
Pl.3.2.1.1 Water Tunnel Flow Visualization of 40^{o} Whole Model at Reynolds No.10^{3}.



Pl.3.2.1.2 Water Tunnel Flow Visualization of 40^{o} Whole Model + Plate at Reynolds No.10^{3}.

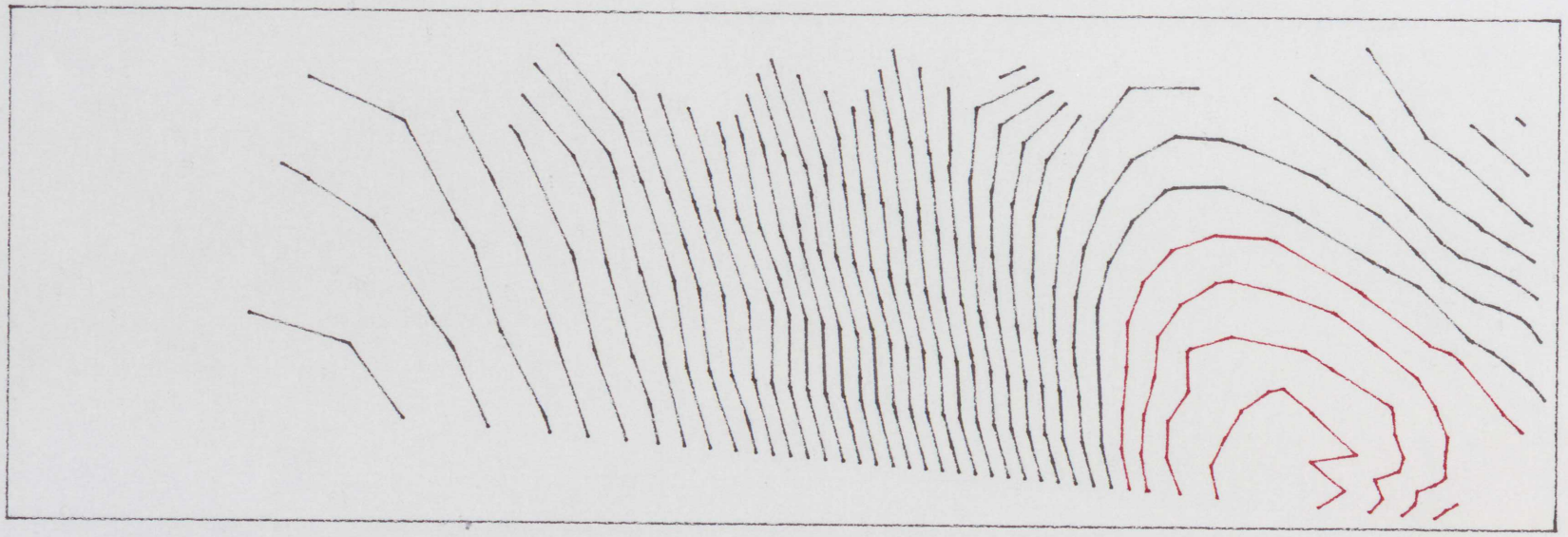


Pl.3.2.2.1 Water Tunnel Flow Visualization of 60^{o} Whole Model at Reynolds No.10^{3}.



Pl.3.2.2.2 Water Tunnel Flow Visualization of 60^{o} Whole Model + Plate at Reynold No.10^{3}.

MEAN Cp DISTRIBUTION IN A-PILLAR REGION



WHOLE MODEL

REYNOLDS No : 5.672E05

A-PILLAR ANGLE : 0 DEGREES

FIG No : 3.3.1.1

Cp CONTOUR DETAILS

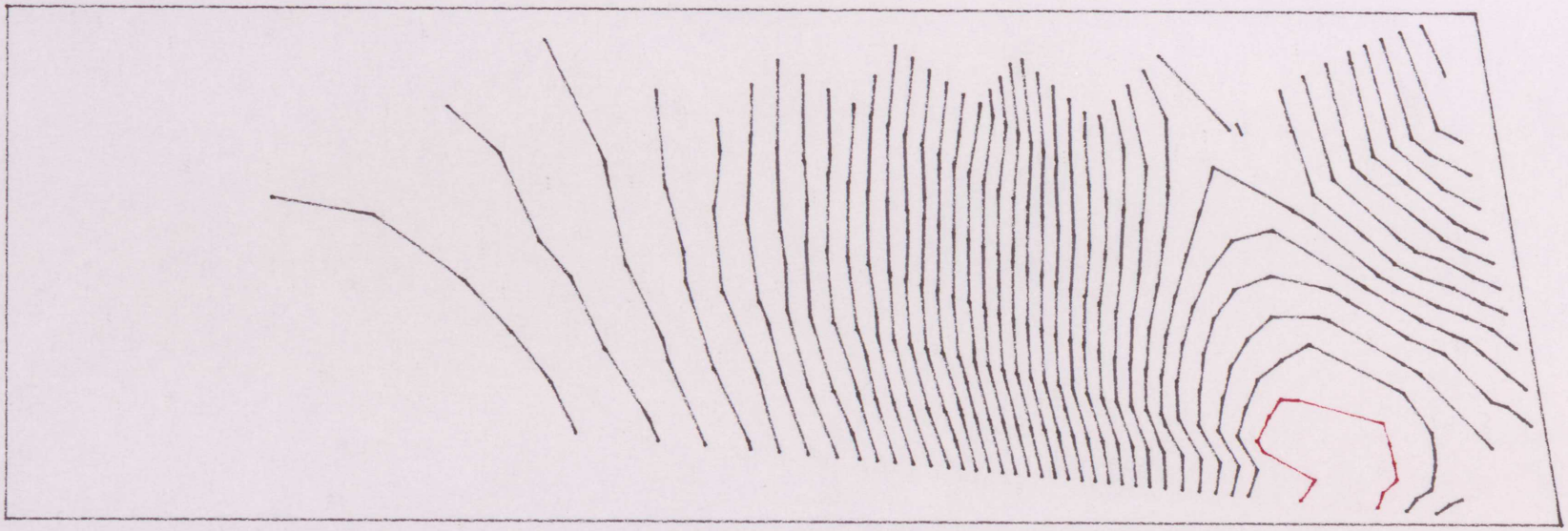
NO. OF CONTOURS : 35

MAX. Cp VALUE : -0.195

MIN. Cp VALUE : -1.671

CONTOUR INCREMENT : -0.042

MEAN Cp DISTRIBUTION IN A-PILLAR REGION



WHOLE MODEL

REYNOLDS No : 5.672E05

A-PILLAR ANGLE : 10 DEGREES

FIG No : 3.3.1.2

Cp CONTOUR DETAILS

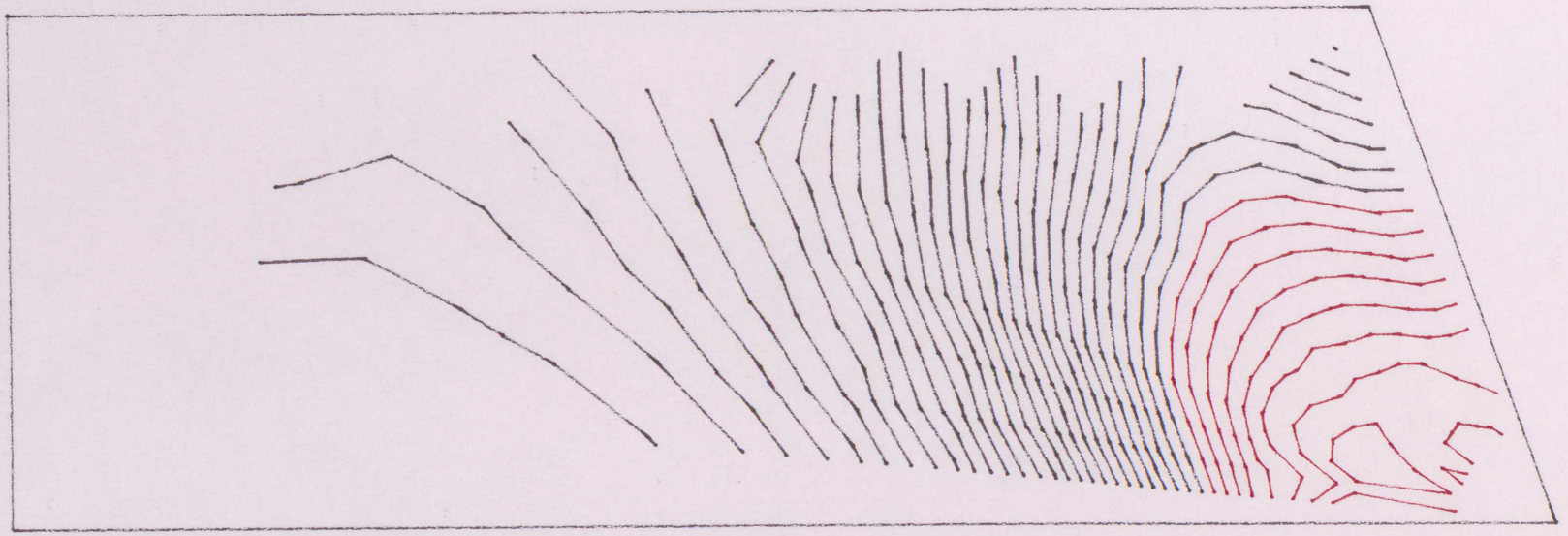
NO. OF CONTOURS : 35

MAX. Cp VALUE : -0.194

MIN. Cp VALUE : -1.545

CONTOUR INCREMENT : -0.039

MEAN Cp DISTRIBUTION IN A-PILLAR REGION



WHOLE MODEL

REYNOLDS No : 5.672E05

A-PILLAR ANGLE : 20 DEGREES

FIG No : 3.3.1.3

Cp CONTOUR DETAILS

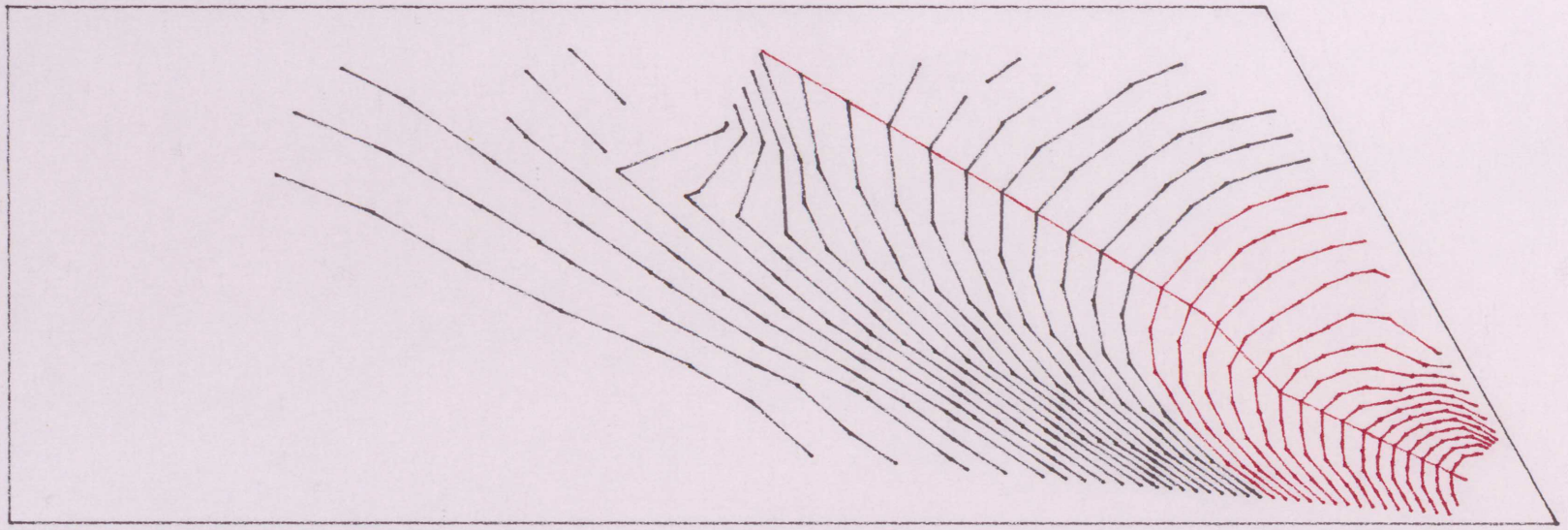
NO. OF CONTOURS : 35

MAX. Cp VALUE : -0.208

MIN. Cp VALUE : -1.912

CONTOUR INCREMENT : -0.049

MEAN Cp DISTRIBUTION IN A-PILLAR REGION



WHOLE MODEL

REYNOLDS No : 5.672E05

A-PILLAR ANGLE : 30 DEGREES

FIG No : 3.3.1.4

Cp CONTOUR DETAILS

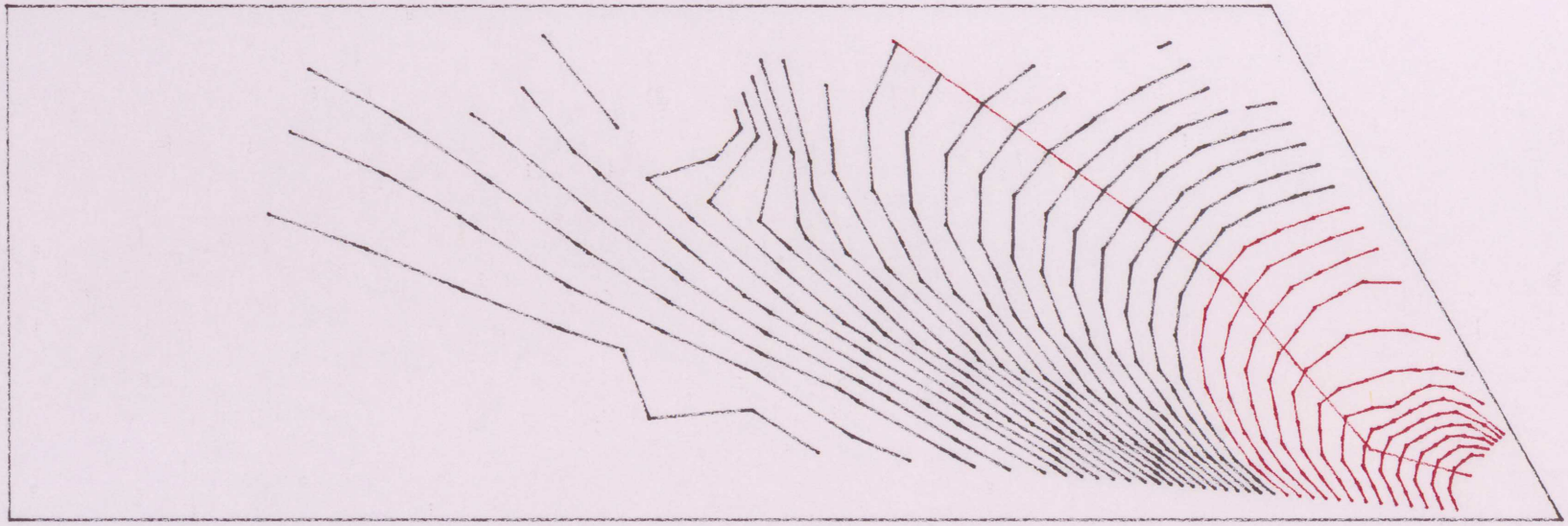
NO. OF CONTOURS : 35

MAX. Cp VALUE : -0.192

MIN. Cp VALUE : -2.563

CONTOUR INCREMENT : -0.068

MEAN Cp DISTRIBUTION IN A-PILLAR REGION



WHOLE MODEL

REYNOLDS No : 7.650E05

A-PILLAR ANGLE : 30 DEGREES

FIG No : 3.3.1.5

Cp CONTOUR DETAILS

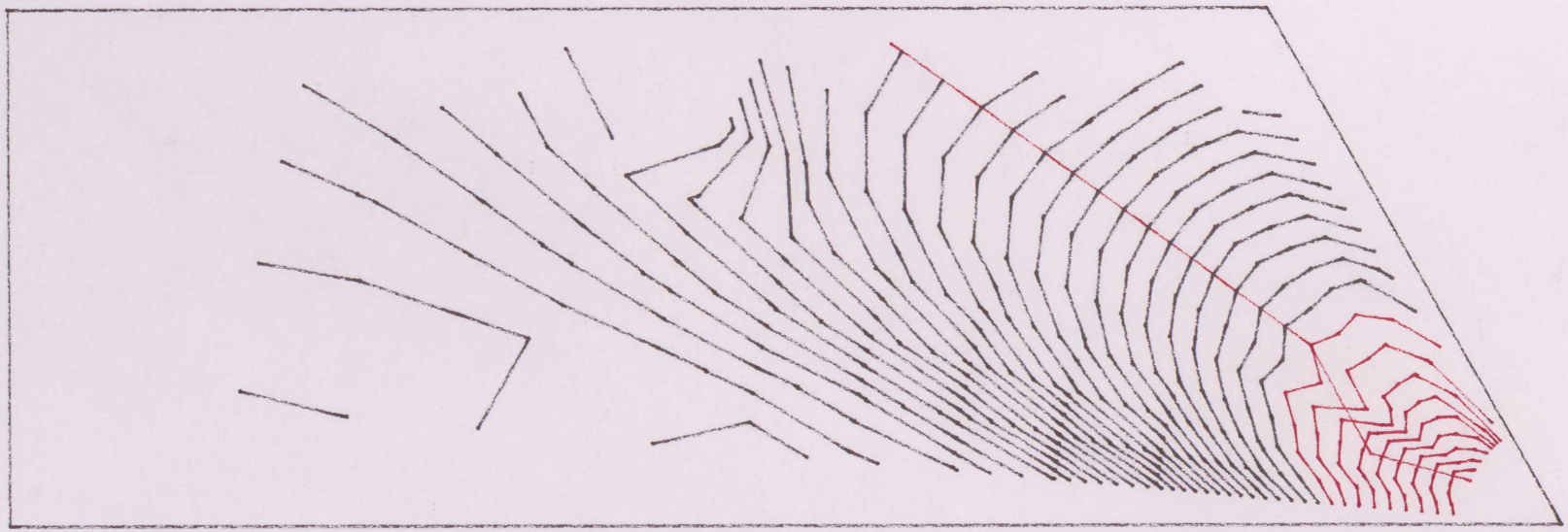
NO. OF CONTOURS : 35

MAX. Cp VALUE : -0.142

MIN. Cp VALUE : -2.303

CONTOUR INCREMENT : -0.062

MEAN Cp DISTRIBUTION IN A-PILLAR REGION



WHOLE MODEL

REYNOLDS No : 9.580E05

A-PILLAR ANGLE : 30 DEGREES

FIG No : 3.3.1.6

Cp CONTOUR DETAILS

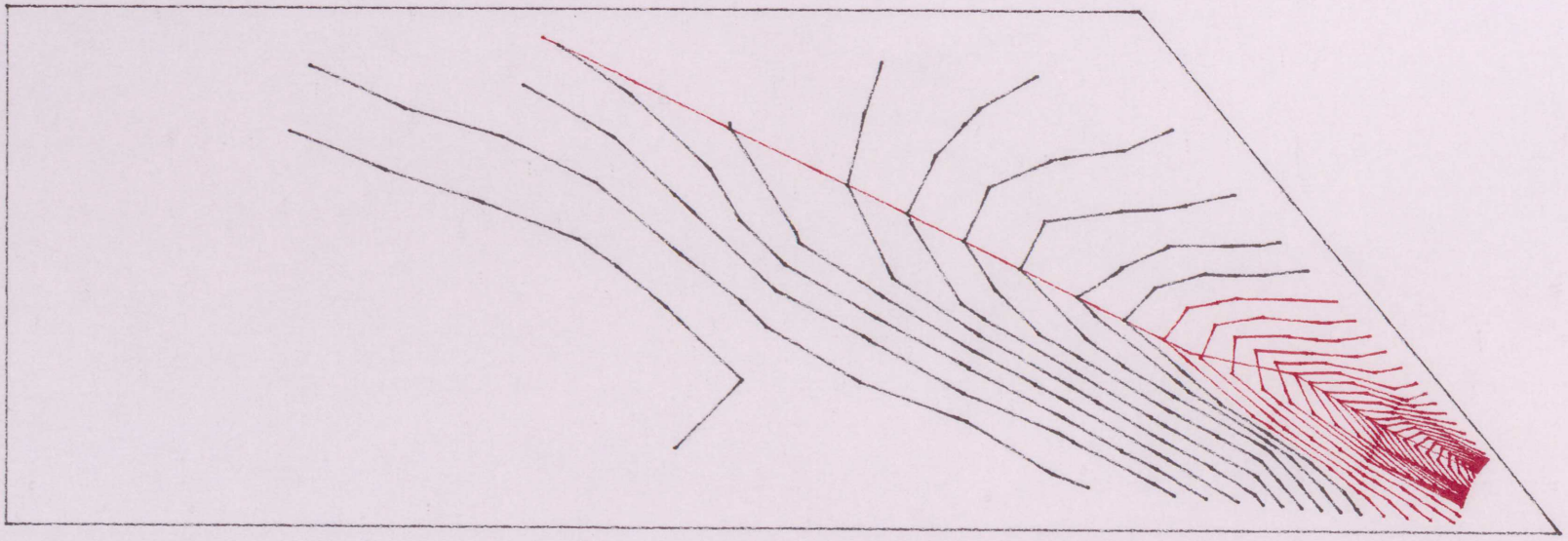
NO. OF CONTOURS : 35

MAX. Cp VALUE : -0.064

MIN. Cp VALUE : -2.013

CONTOUR INCREMENT : -0.056

MEAN Cp DISTRIBUTION IN A-PILLAR REGION



WHOLE MODEL

REYNOLDS No : 9.580E05

A-PILLAR ANGLE : 40 DEGREES

FIG No : 3.3.1.7

Cp CONTOUR DETAILS

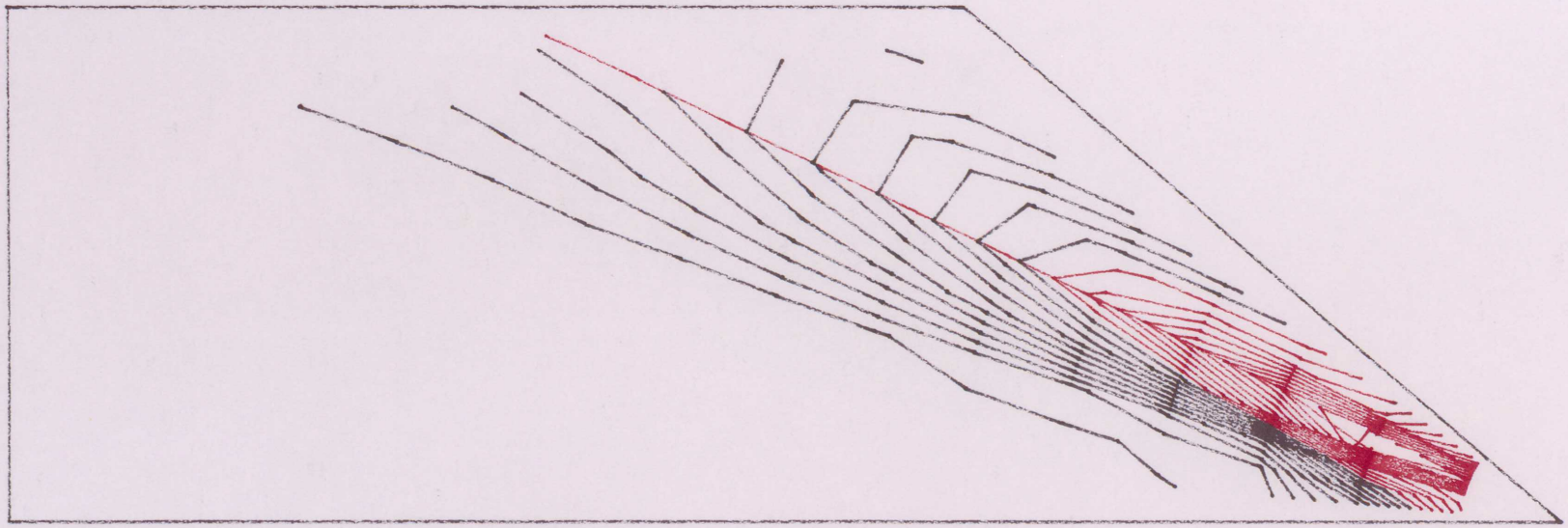
NO. OF CONTOURS : 32

MAX. Cp VALUE : -0.068

MIN. Cp VALUE : -4.118

CONTOUR INCREMENT : -0.127

MEAN Cp DISTRIBUTION IN A-PILLAR REGION



WHOLE MODEL

REYNOLDS No : 9.580E05

A-PILLAR ANGLE : 50 DEGREES

FIG No : 3.3.1.8

Cp CONTOUR DETAILS

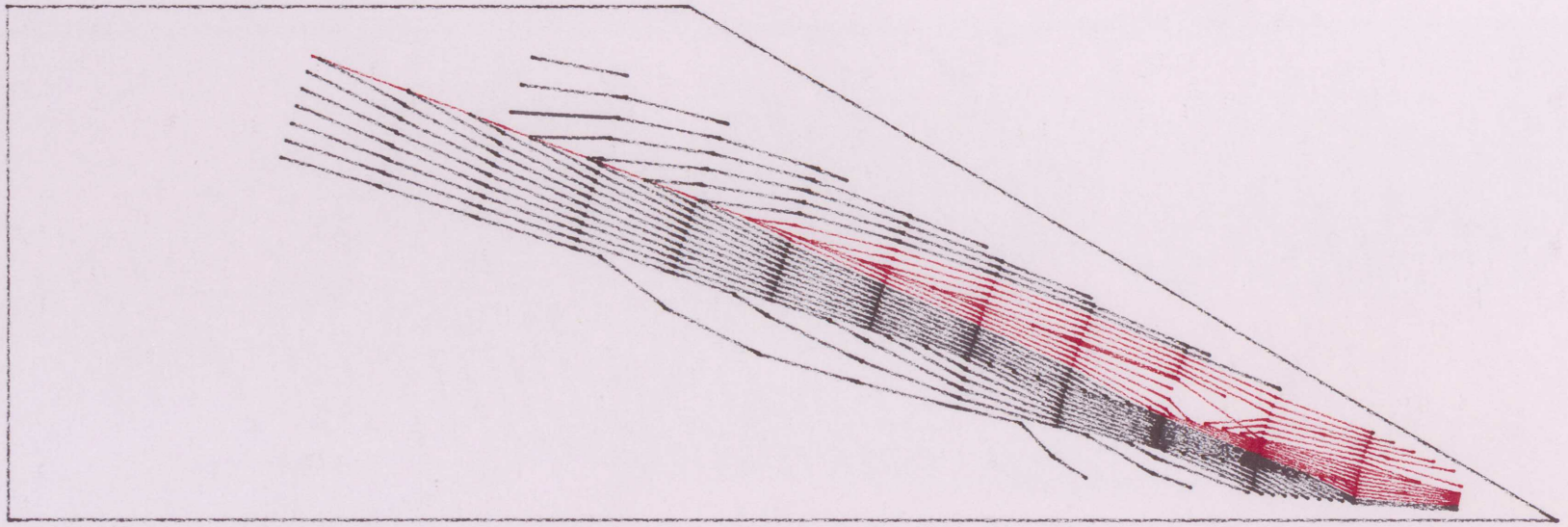
NO. OF CONTOURS : 25

MAX. Cp VALUE : -0.076

MIN. Cp VALUE : -3.288

CONTOUR INCREMENT : -0.128

MEAN Cp DISTRIBUTION IN A-PILLAR REGION



WHOLE MODEL

REYNOLDS No : 5.672E05

A-PILLAR ANGLE : 60 DEGREES

FIG No : 3.3.1.9

Cp CONTOUR DETAILS

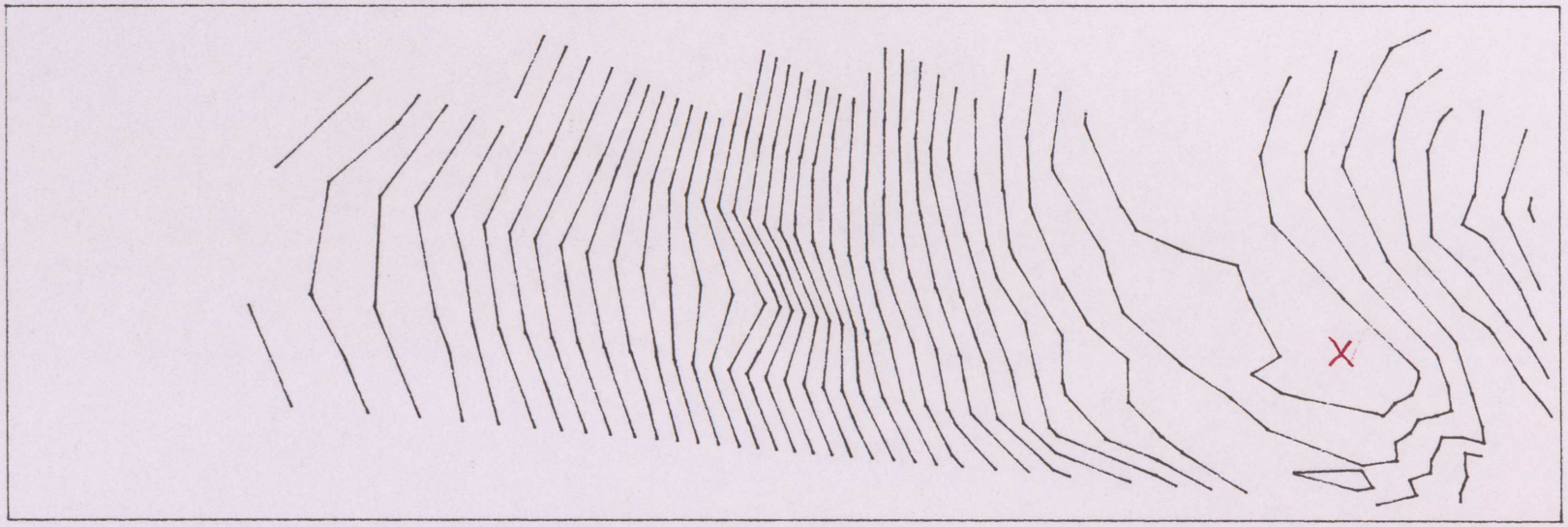
NO. OF CONTOURS : 20

MAX. Cp VALUE : -0.160

MIN. Cp VALUE : -2.302

CONTOUR INCREMENT : -0.107

MEAN Cp DISTRIBUTION IN A-PILLAR REGION



TOP HALF

REYNOLDS No : 7.650E05

A-PILLAR ANGLE : 0 DEGREES

FIG No : 3.3.2.1

Cp CONTOUR DETAILS

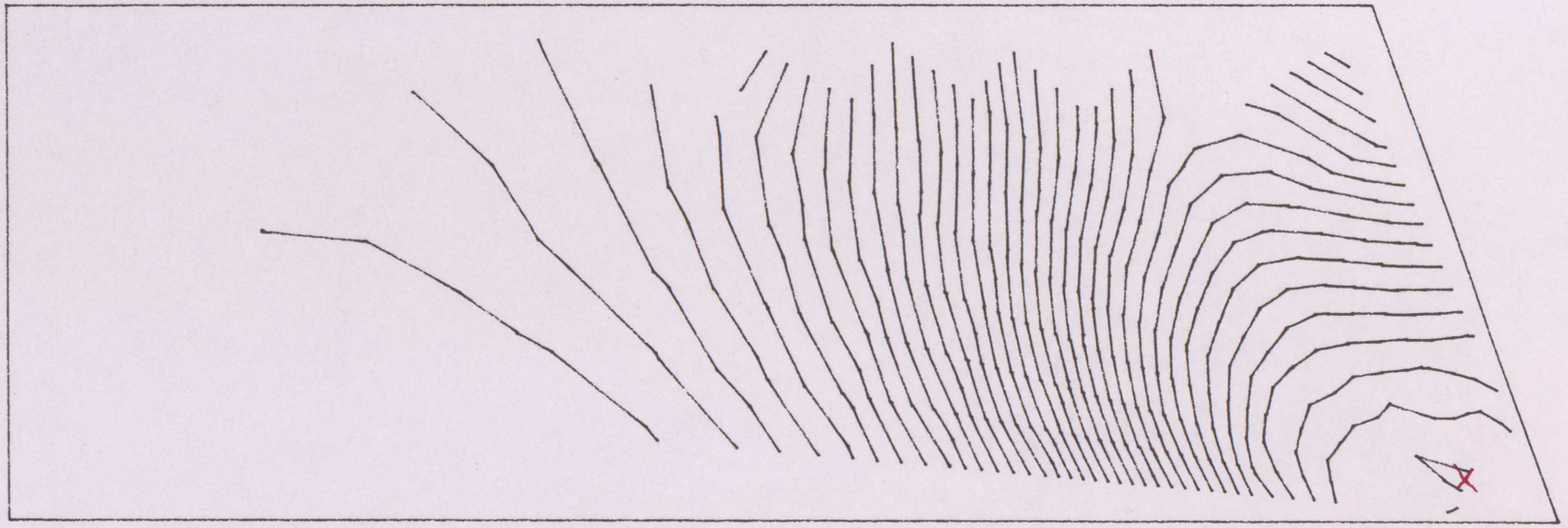
NO. OF CONTOURS : 35

MAX. Cp VALUE : -0.076

MIN. Cp VALUE : -0.987

CONTOUR INCREMENT : -0.026

MEAN Cp DISTRIBUTION IN A-PILLAR REGION



TOP HALF

REYNOLDS No : 9.580E05

A-PILLAR ANGLE : 20 DEGREES

FIG No : 3.3.2.2

Cp CONTOUR DETAILS

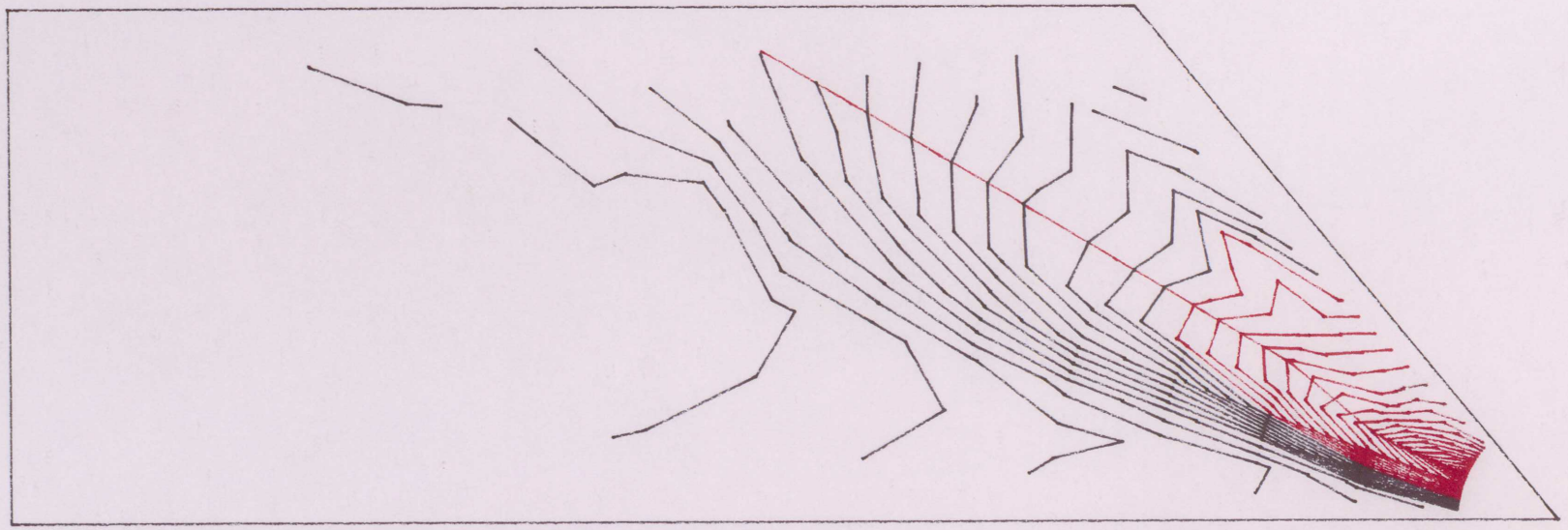
NO. OF CONTOURS : 35

MAX. Cp VALUE : -0.110

MIN. Cp VALUE : -1.466

CONTOUR INCREMENT : -0.039

MEAN Cp DISTRIBUTION IN A-PILLAR REGION



TOP HALF

REYNOLDS No : 5.672E05

A-PILLAR ANGLE : 40 DEGREES

FIG No : 3.3.2.3

Cp CONTOUR DETAILS

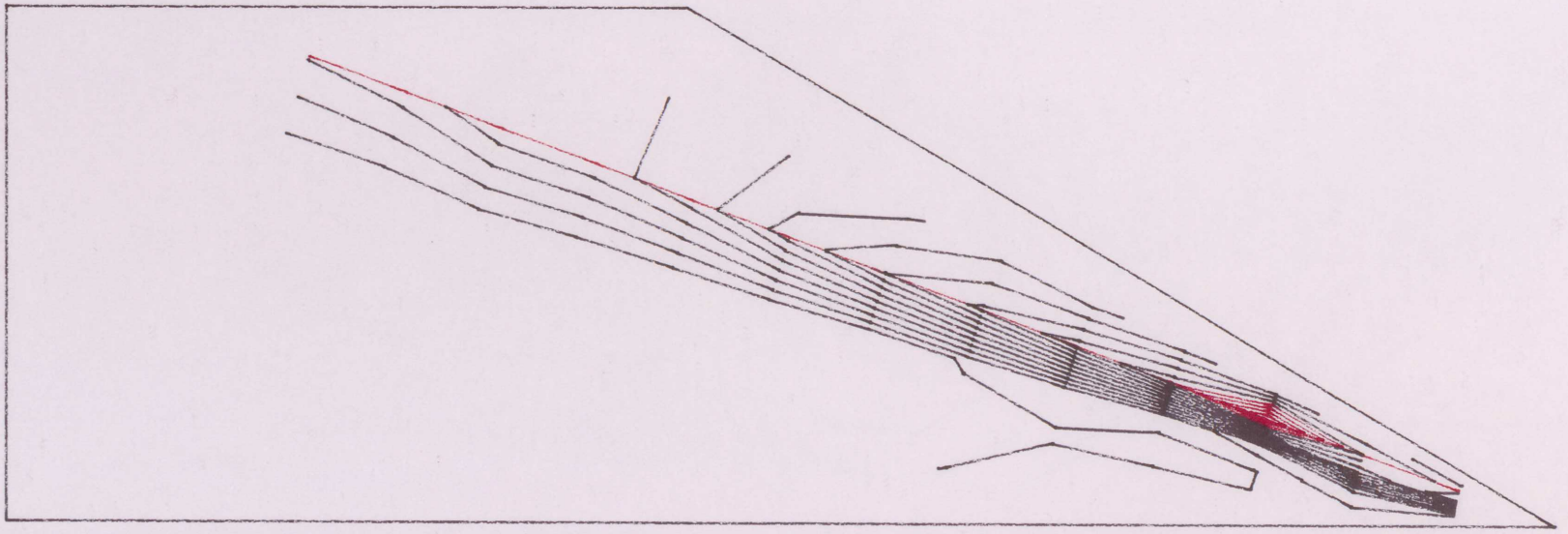
NO. OF CONTOURS : 34

MAX. Cp VALUE : -0.126

MIN. Cp VALUE : -3.544

CONTOUR INCREMENT : -0.101

MEAN Cp DISTRIBUTION IN A-PILLAR REGION



TOP HALF

REYNOLDS No : 9.580E05

A-PILLAR ANGLE : 60 DEGREES

FIG No : 3.3.2.4

Cp CONTOUR DETAILS

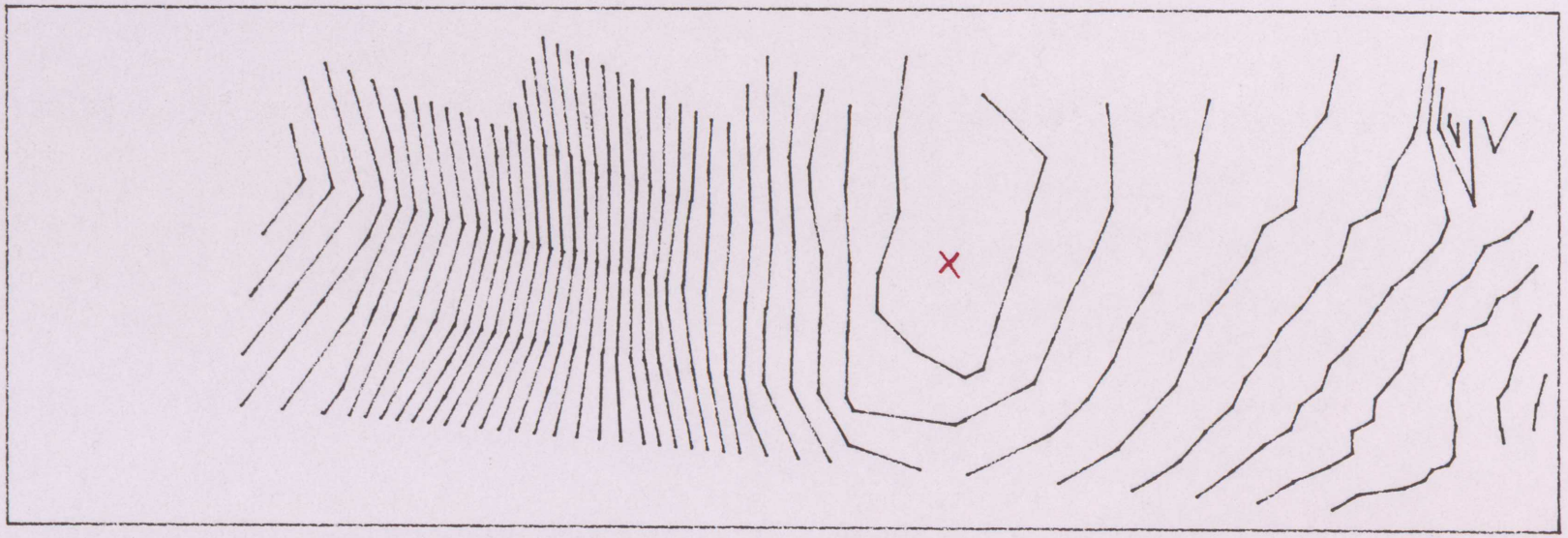
NO. OF CONTOURS : 16

MAX. Cp VALUE : -0.015

MIN. Cp VALUE : -2.107

CONTOUR INCREMENT : -0.131

MEAN Cp DISTRIBUTION IN A-PILLAR REGION

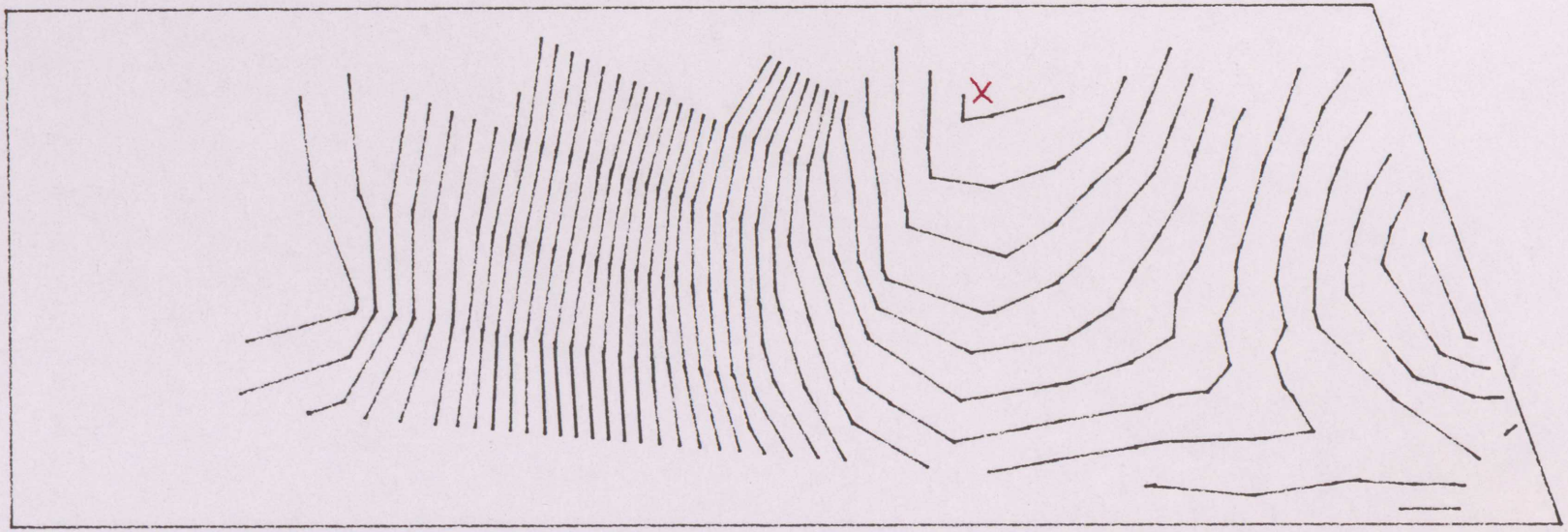


WHOLE MODEL WITH PLATE
REYNOLDS No : 9.580E05
A-PILLAR ANGLE : 0 DEGREES

FIG No : 3.3.3.1

Cp CONTOUR DETAILS
NO. OF CONTOURS : 35
MAX. Cp VALUE : -0.025
MIN. Cp VALUE : -0.793
CONTOUR INCREMENT : -0.022

MEAN Cp DISTRIBUTION IN A-PILLAR REGION



WHOLE MODEL WITH PLATE

REYNOLDS No : 7.650E05

A-PILLAR ANGLE : 20 DEGREES

FIG No : 3.3.3.2

Cp CONTOUR DETAILS

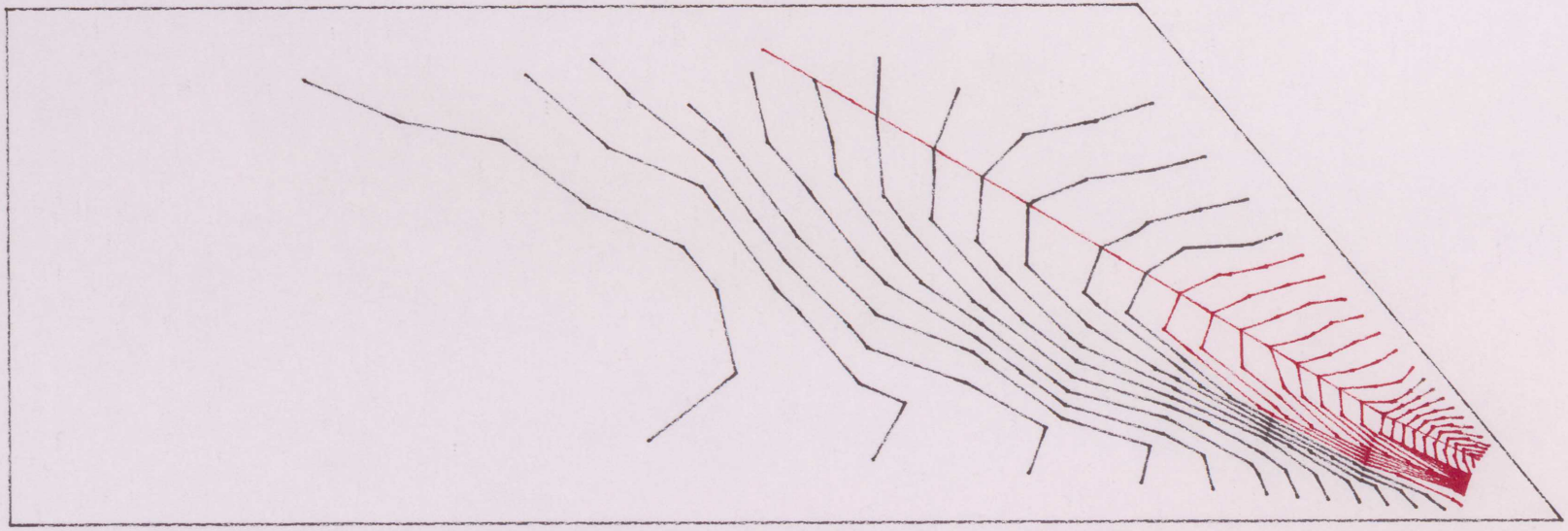
NO. OF CONTOURS : 35

MAX. Cp VALUE : -0.036

MIN. Cp VALUE : -0.920

CONTOUR INCREMENT : -0.025

MEAN Cp DISTRIBUTION IN A-PILLAR REGION



WHOLE MODEL WITH PLATE

REYNOLDS No : 5.672E05

A-PILLAR ANGLE : 40 DEGREES

FIG No : 3.3.3.3

Cp CONTOUR DETAILS

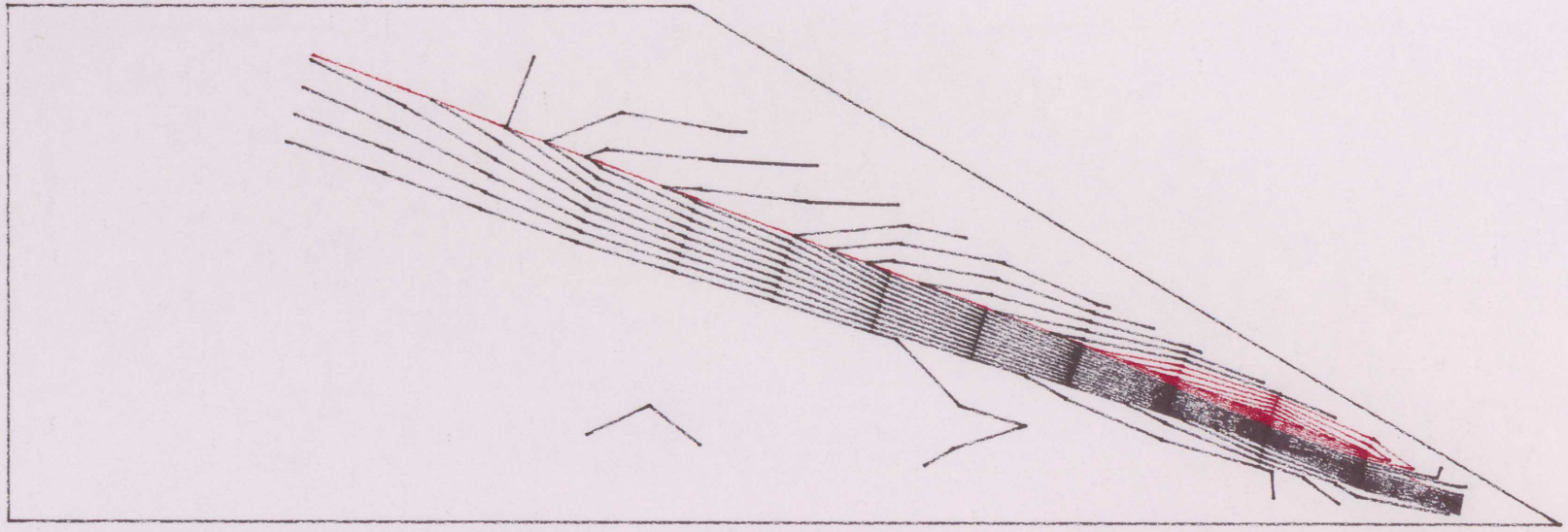
NO. OF CONTOURS : 30

MAX. Cp VALUE : -0.073

MIN. Cp VALUE : -3.477

CONTOUR INCREMENT : -0.113

MEAN Cp DISTRIBUTION IN A-PILLAR REGION



WHOLE MODEL WITH PLATE

REYNOLDS No : 9.580E05

A-PILLAR ANGLE : 60 DEGREES

FIG No : 3.3.3.4

Cp CONTOUR DETAILS

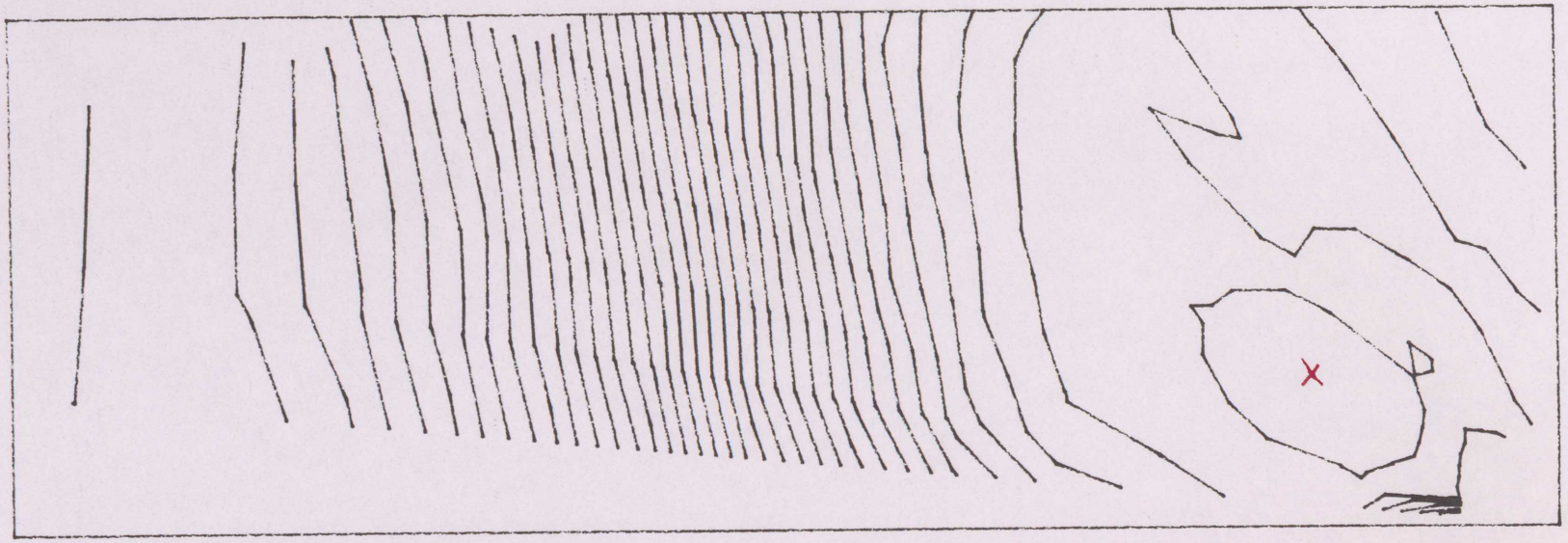
NO. OF CONTOURS : 20

MAX. Cp VALUE : -0.005

MIN. Cp VALUE : -2.017

CONTOUR INCREMENT : -0.101

MEAN Cp DISTRIBUTION IN ROOT REGION ON SWEPT PLATE



REYNOLDS No : 1.166E05

SWEEP ANGLE : 0 DEGREES

FIG No : 3.3.4.1

Cp CONTOUR DETAILS

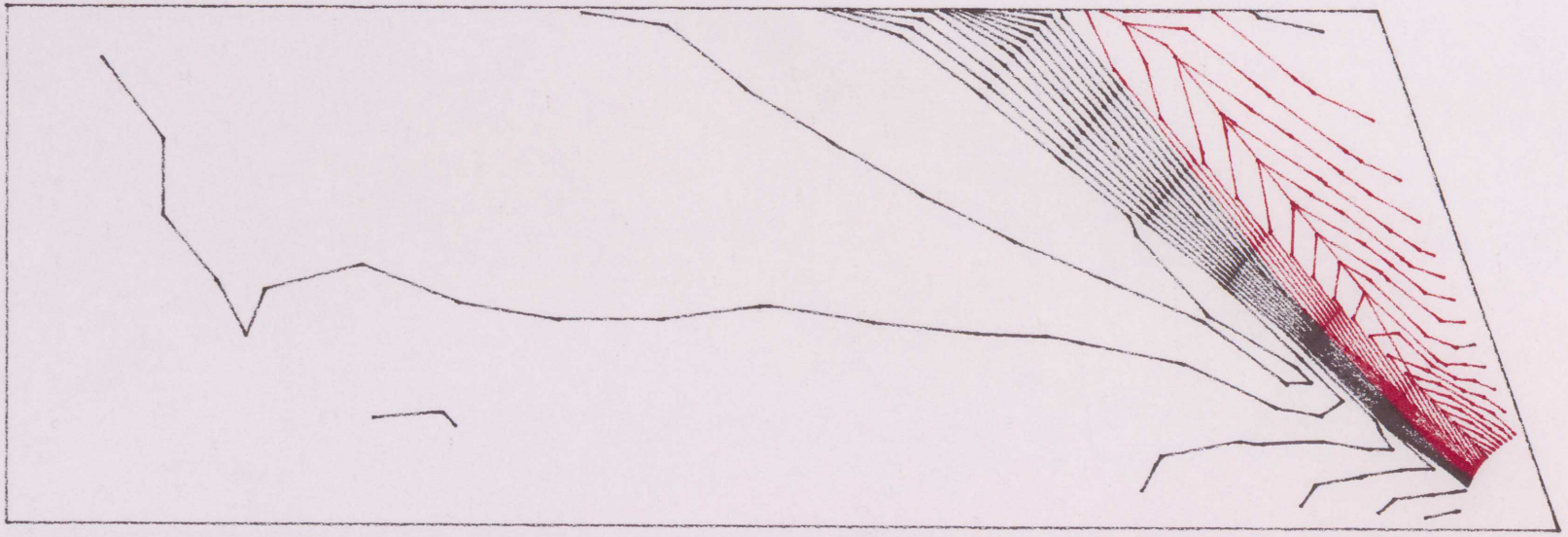
NO. OF CONTOURS : 35

MAX. Cp VALUE : -0.203

MIN. Cp VALUE : -1.060

CONTOUR INCREMENT : -0.025

MEAN Cp DISTRIBUTION IN ROOT REGION ON SWEPT PLATE



REYNOLDS No : 8.652E04

SWEEP ANGLE : 20 DEGREES

FIG No : 3.3.4.2

Cp CONTOUR DETAILS

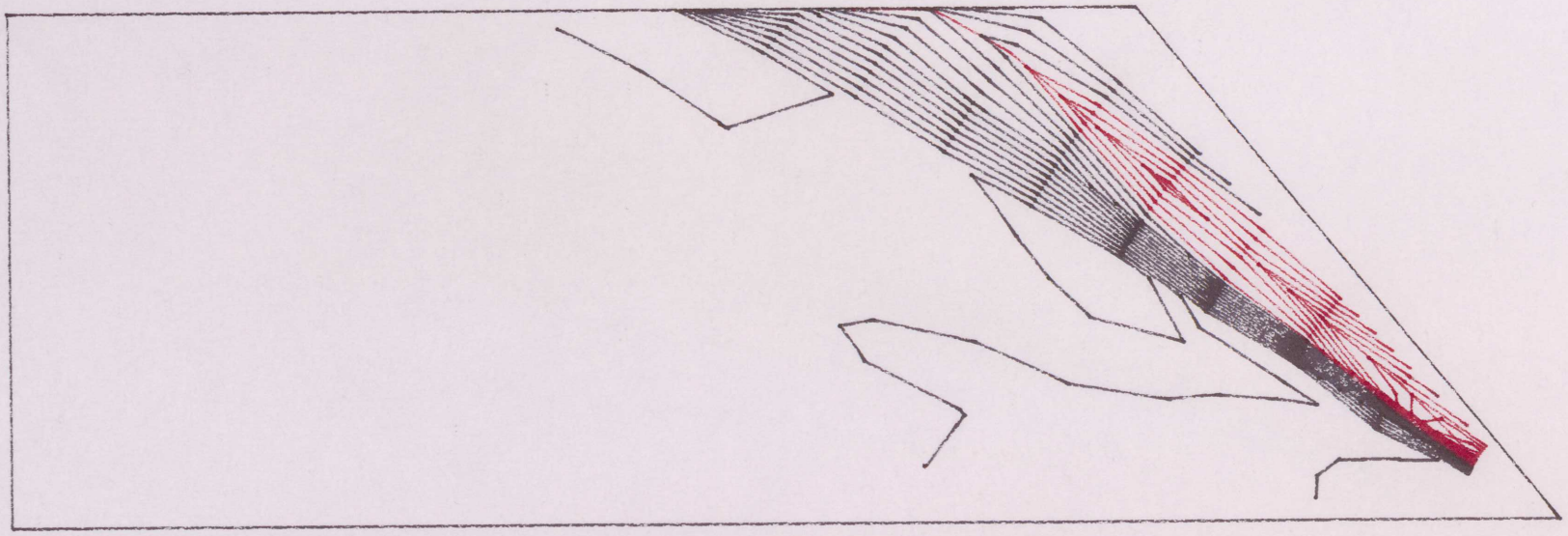
NO. OF CONTOURS : 30

MAX. Cp VALUE : -0.035

MIN. Cp VALUE : -3.668

CONTOUR INCREMENT : -0.121

MEAN Cp DISTRIBUTION IN ROOT REGION ON SWEPT PLATE



206

REYNOLDS No : 8.652E04

SWEEP ANGLE : 40 DEGREES

FIG No : 3.3.4.3

Cp CONTOUR DETAILS

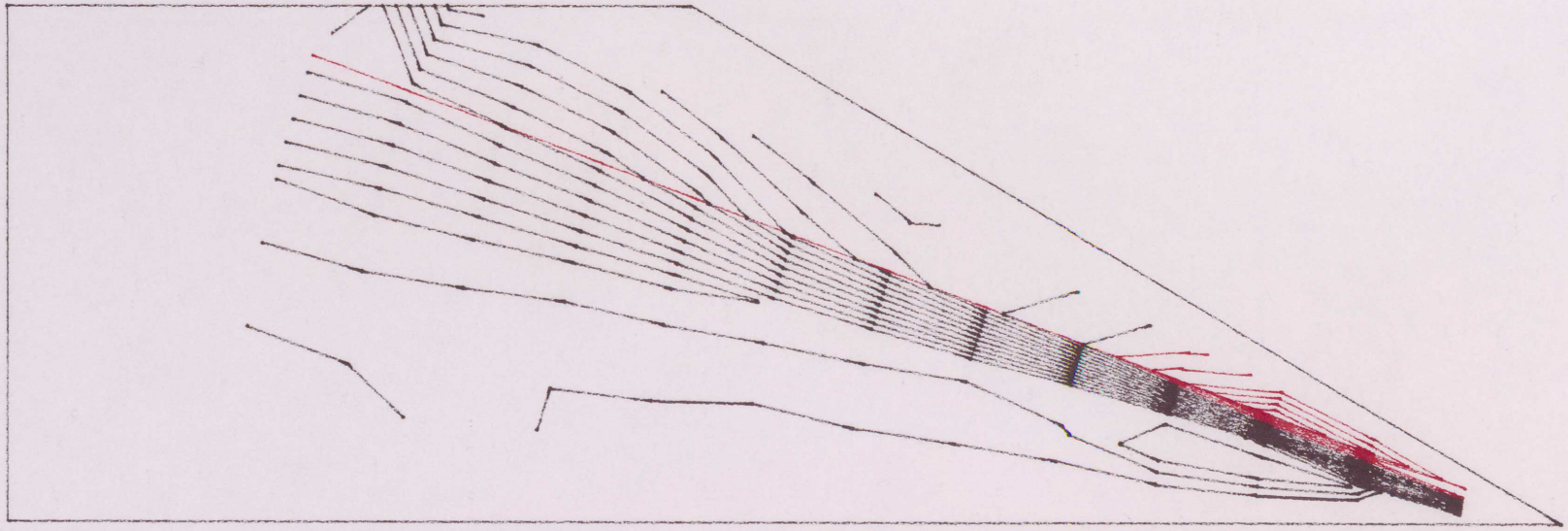
NO. OF CONTOURS : 25

MAX. Cp VALUE : --.024

MIN. Cp VALUE : -2.937

CONTOUR INCREMENT : -0.118

MEAN Cp DISTRIBUTION IN ROOT REGION ON SWEPT PLATE



REYNOLDS No : 8.652E04

SWEEP ANGLE : 60 DEGREES

FIG No : 3.3.4.4

Cp CONTOUR DETAILS

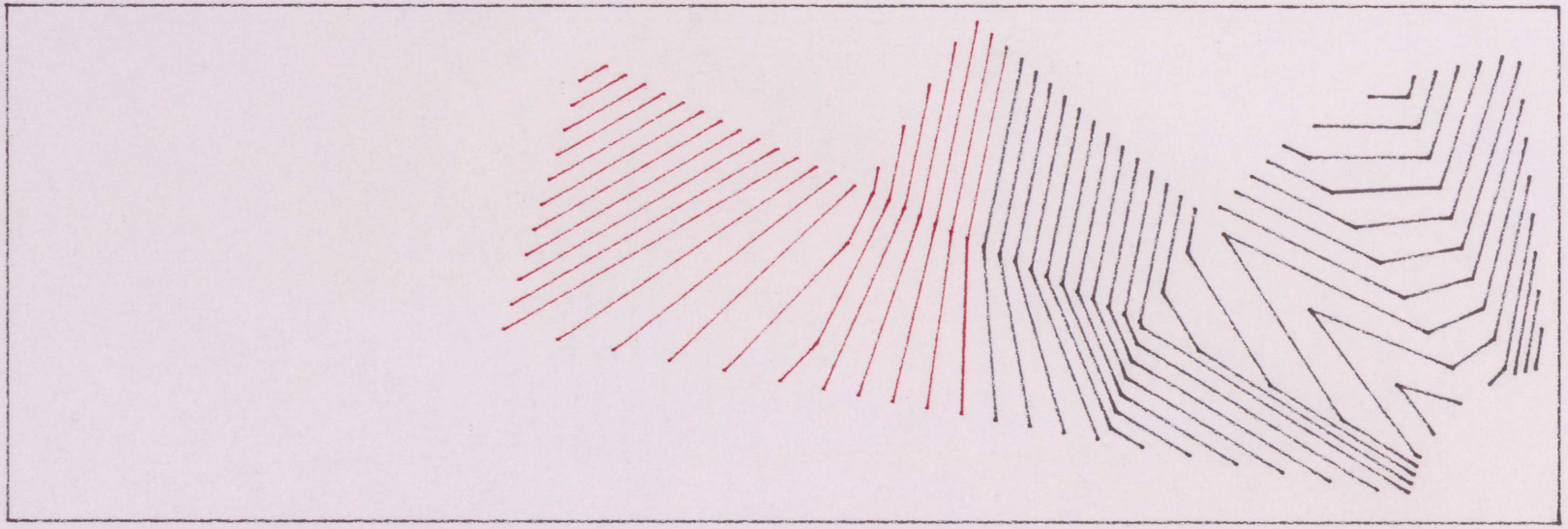
NO. OF CONTOURS : 20

MAX. Cp VALUE : --.099

MIN. Cp VALUE : -2.168

CONTOUR INCREMENT : -0.113

RMS Cp DISTRIBUTION IN A-PILLAR REGION



WHOLE MODEL

REYNOLDS No : 9.580E05

A-PILLAR ANGLE : 0 DEGREES

FIG No : 3.4.1.1

RMS CONTOUR DETAILS

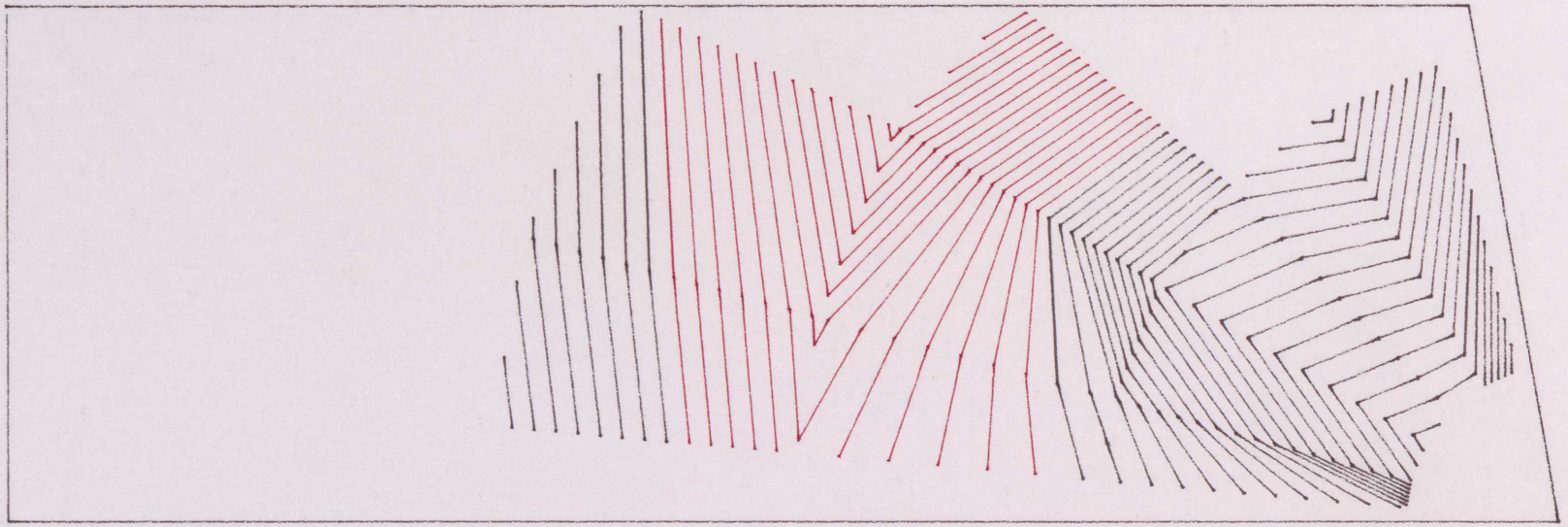
NO. OF CONTOURS : 40

MIN RMS Cp : 0.077

MAX RMS Cp : 0.233

CONTOUR INCREMENT : 0.004

RMS Cp DISTRIBUTION IN A-PILLAR REGION



WHOLE MODEL

REYNOLDS No : 9.580E05

A-PILLAR ANGLE : 10 DEGREES

FIG No : 3.4.1.2

RMS CONTOUR DETAILS

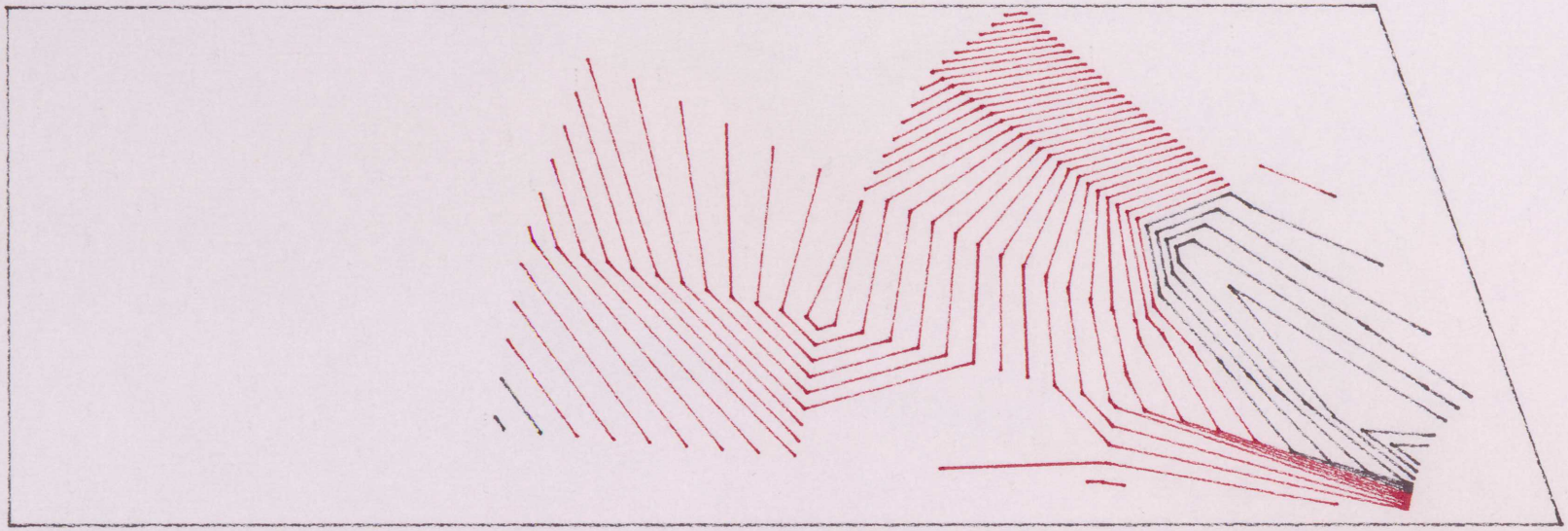
NO. OF CONTOURS : 40

MIN RMS Cp : 0.082

MAX RMS Cp : 0.196

CONTOUR INCREMENT : 0.003

RMS Cp DISTRIBUTION IN A-PILLAR REGION



WHOLE MODEL

REYNOLDS No : 7.650E05

A-PILLAR ANGLE : 20 DEGREES

FIG No : 3.4.1.3

RMS CONTOUR DETAILS

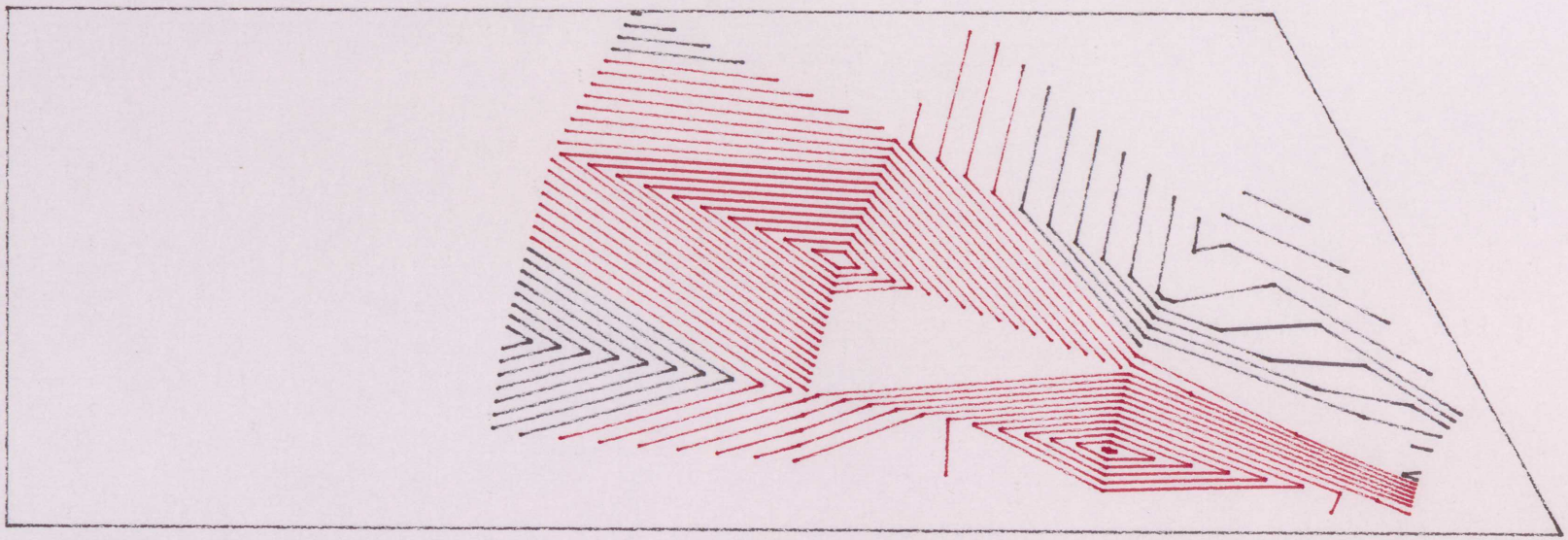
NO. OF CONTOURS : 35

MIN RMS Cp : 0.123

MAX RMS Cp : 0.255

CONTOUR INCREMENT : 0.004

RMS Cp DISTRIBUTION IN A-PILLAR REGION



WHOLE MODEL

REYNOLDS No : 9.580E05

A-PILLAR ANGLE : 30 DEGREES

FIG No : 3.4.1.4

RMS CONTOUR DETAILS

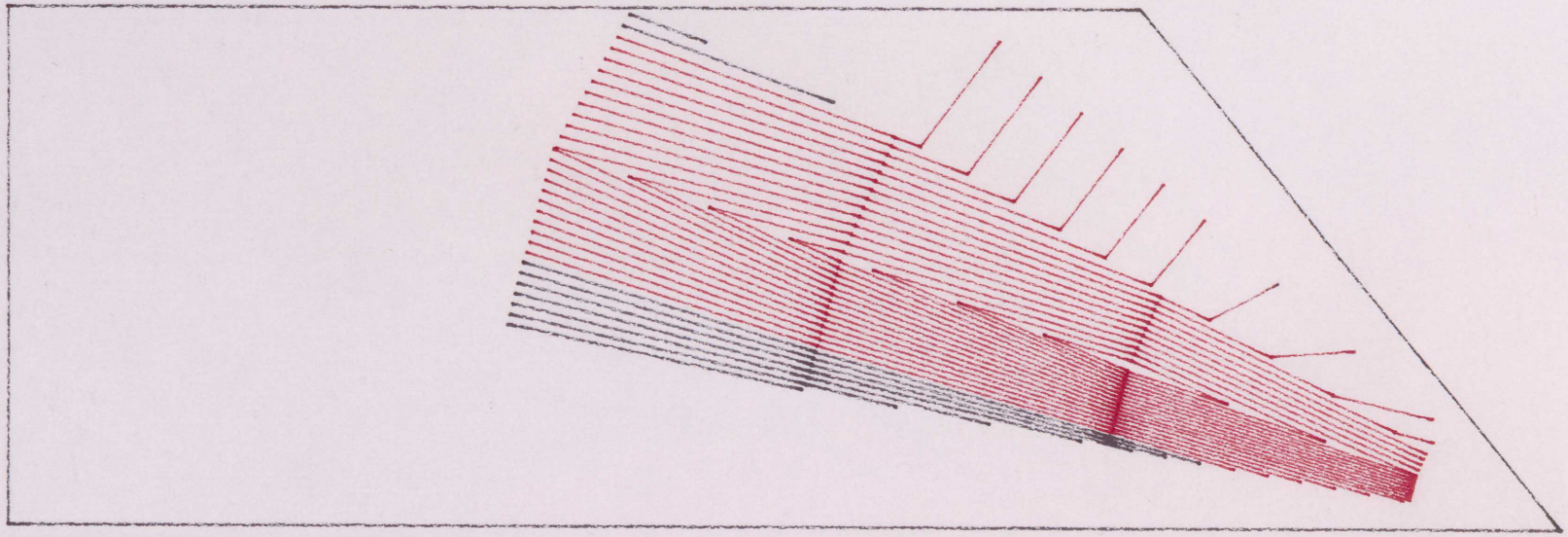
NO. OF CONTOURS : 27

MIN RMS Cp : 0.111

MAX RMS Cp : 0.221

CONTOUR INCREMENT : 0.004

RMS Cp DISTRIBUTION IN A-PILLAR REGION



WHOLE MODEL

REYNOLDS No : 7.650E05

A-PILLAR ANGLE : 40 DEGREES

FIG No : 3.4.1.5

RMS CONTOUR DETAILS

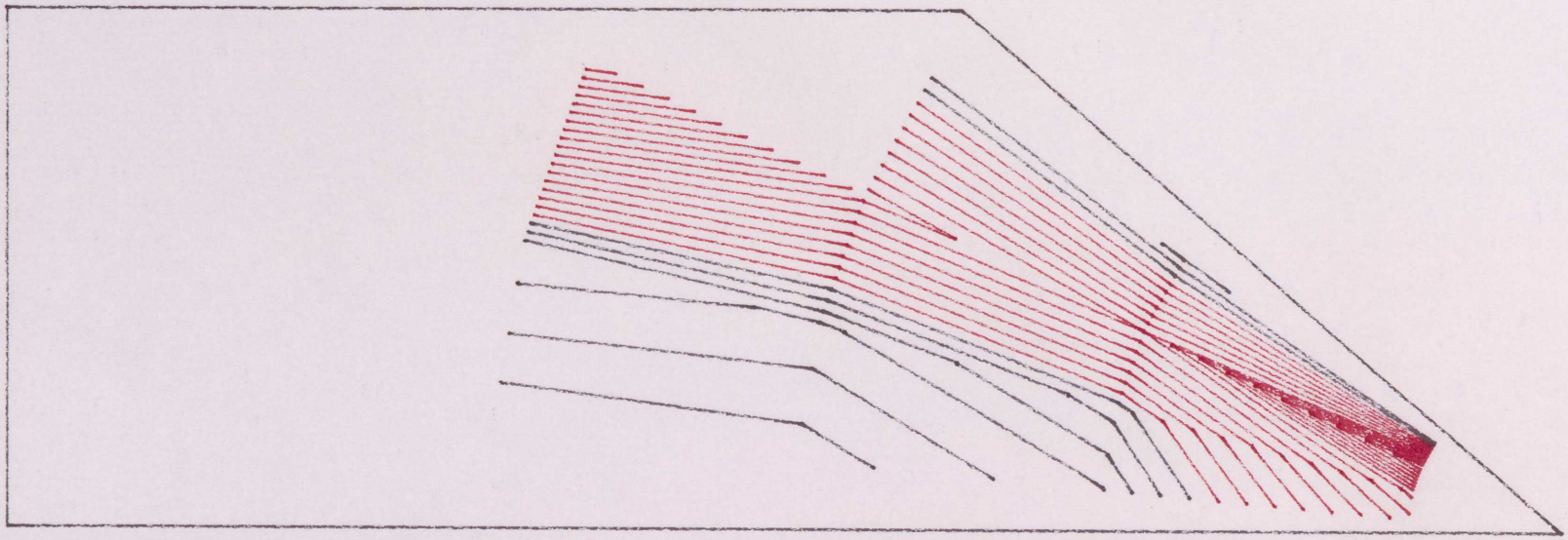
NO. OF CONTOURS : 24

MIN RMS Cp : 0.093

MAX RMS Cp : 0.284

CONTOUR INCREMENT : 0.008

RMS Cp DISTRIBUTION IN A-PILLAR REGION



WHOLE MODEL

REYNOLDS No : 7.650E05

A-PILLAR ANGLE : 50 DEGREES

FIG No : 3.4.1.6

RMS CONTOUR DETAILS

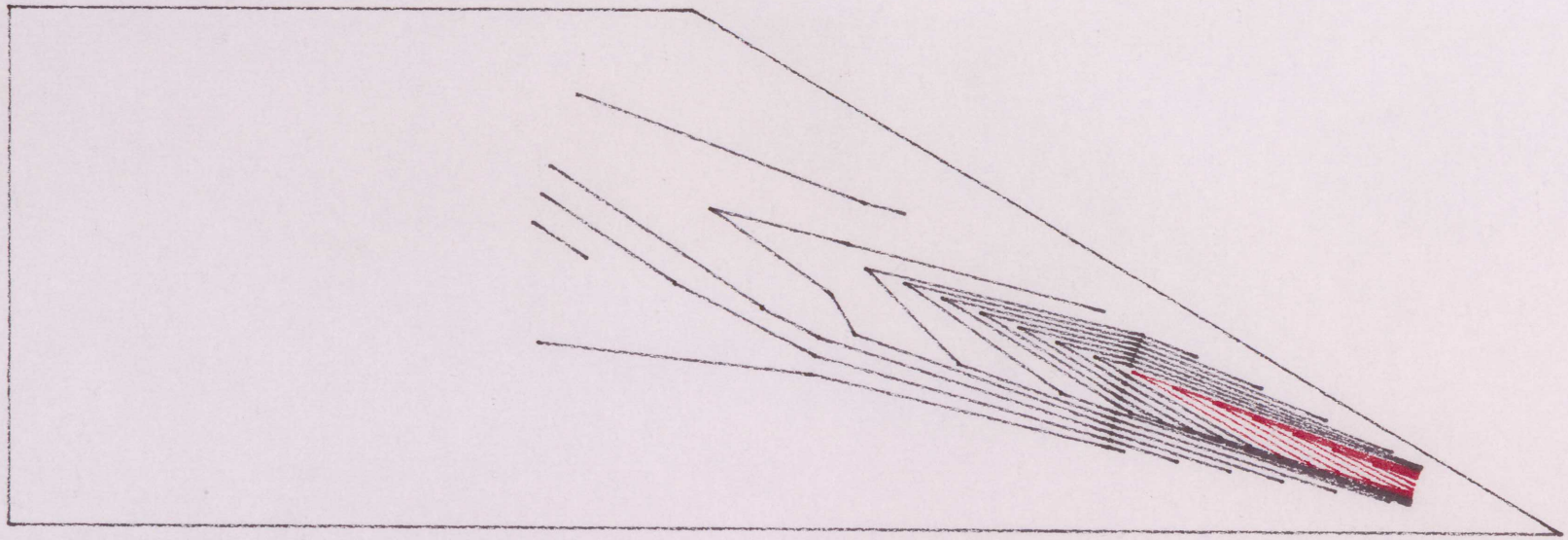
NO. OF CONTOURS : 24

MIN RMS Cp : 0.100

MAX RMS Cp : 0.280

CONTOUR INCREMENT : 0.007

RMS Cp DISTRIBUTION IN A-PILLAR REGION



WHOLE MODEL

REYNOLDS No : 9.580E05

A-PILLAR ANGLE : 60 DEGREES

FIG No : 3.4.1.7

RMS CONTOUR DETAILS

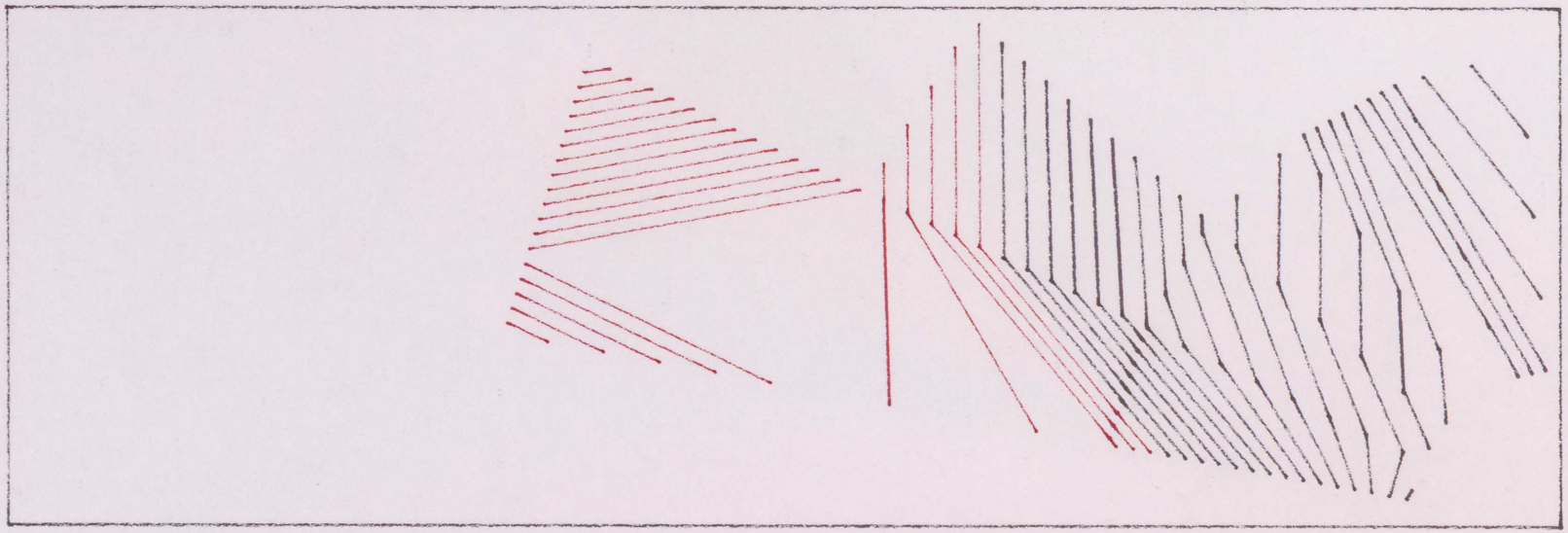
NO. OF CONTOURS : 18

MIN RMS Cp : 0.056

MAX RMS Cp : 0.206

CONTOUR INCREMENT : 0.008

RMS Cp DISTRIBUTION IN A-PILLAR REGION



TOP HALF

REYNOLDS No : 5.672E05

A-PILLAR ANGLE : 0 DEGREES

FIG No : 3.4.2.1

RMS CONTOUR DETAILS

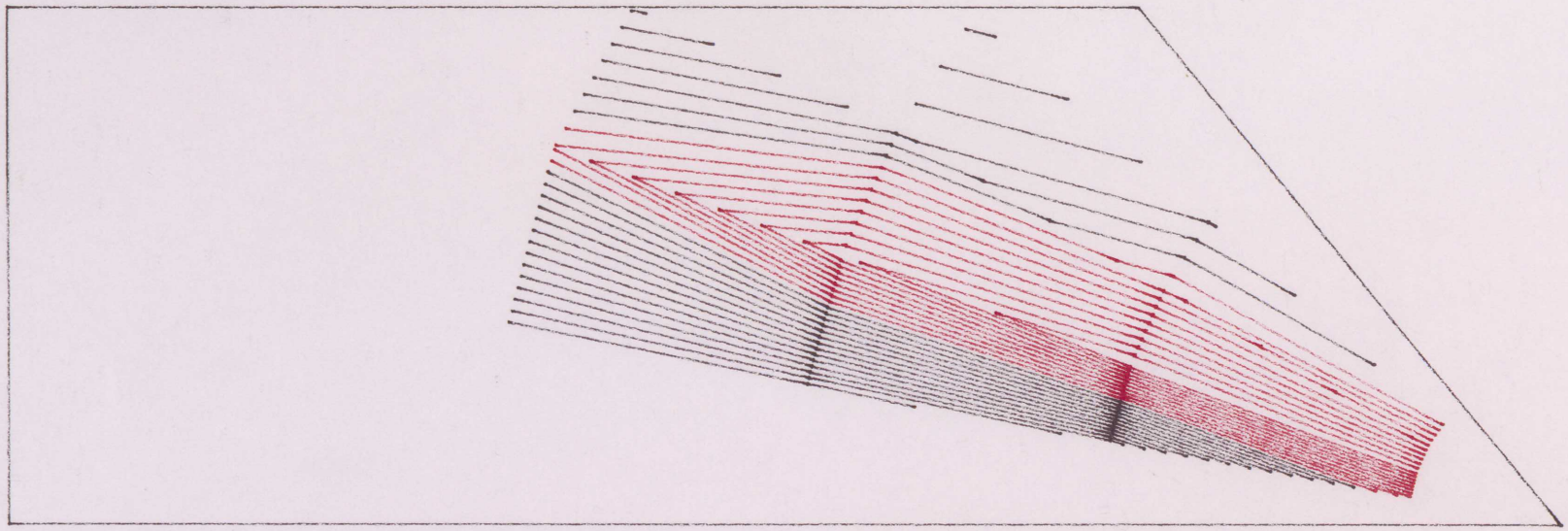
NO. OF CONTOURS : 40

MIN RMS Cp : 0.075

MAX RMS Cp : 0.213

CONTOUR INCREMENT : 0.003

RMS Cp DISTRIBUTION IN A-PILLAR REGION



TOP HALF

REYNOLDS No : 7.650E05

A-PILLAR ANGLE : 40 DEGREES

FIG No : 3.4.2.2

RMS CONTOUR DETAILS

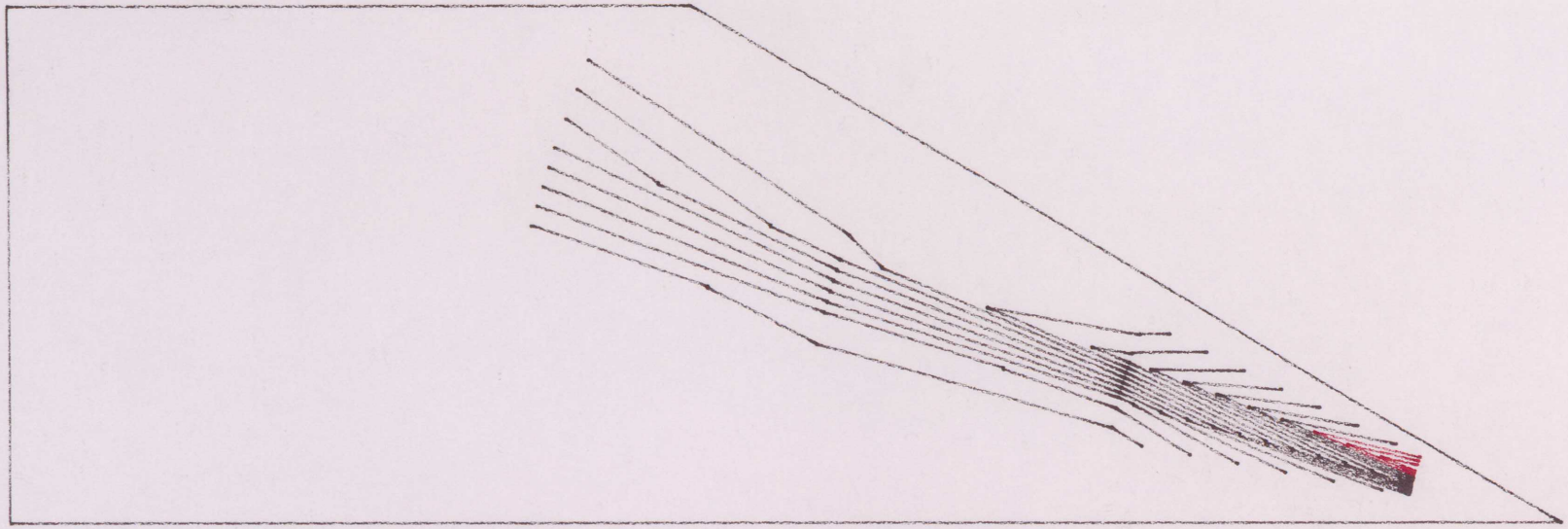
NO. OF CONTOURS : 24

MIN RMS Cp : 0.032

MAX RMS Cp : 0.239

CONTOUR INCREMENT : 0.009

RMS Cp DISTRIBUTION IN A-PILLAR REGION



TOP HALF

REYNOLDS No : 5.672E05

A-PILLAR ANGLE : 60 DEGREES

FIG No : 3.4.2.3

RMS CONTOUR DETAILS

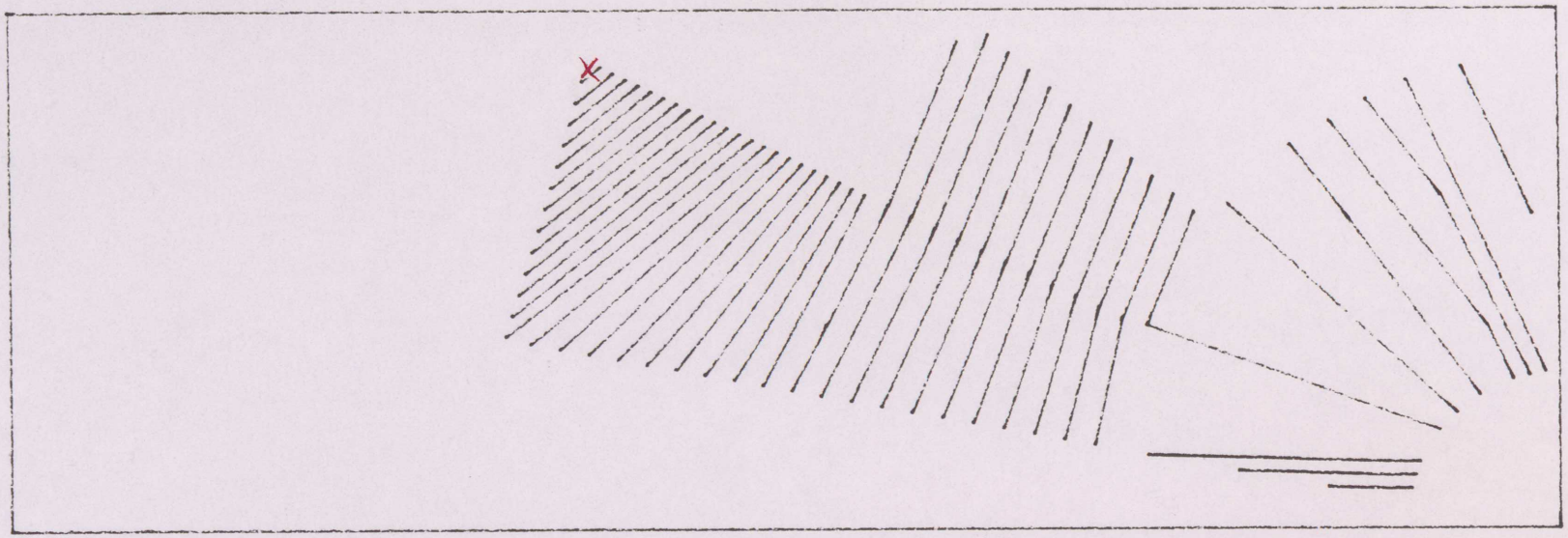
NO. OF CONTOURS : 18

MIN RMS Cp : 0.020

MAX RMS Cp : 0.182

CONTOUR INCREMENT : 0.009

RMS Cp DISTRIBUTION IN A-PILLAR REGION



WHOLE MODEL WITH PLATE

REYNOLDS No : 7.650E05

A-PILLAR ANGLE : 0 DEGREES

FIG No : 3.4.3.1

RMS CONTOUR DETAILS

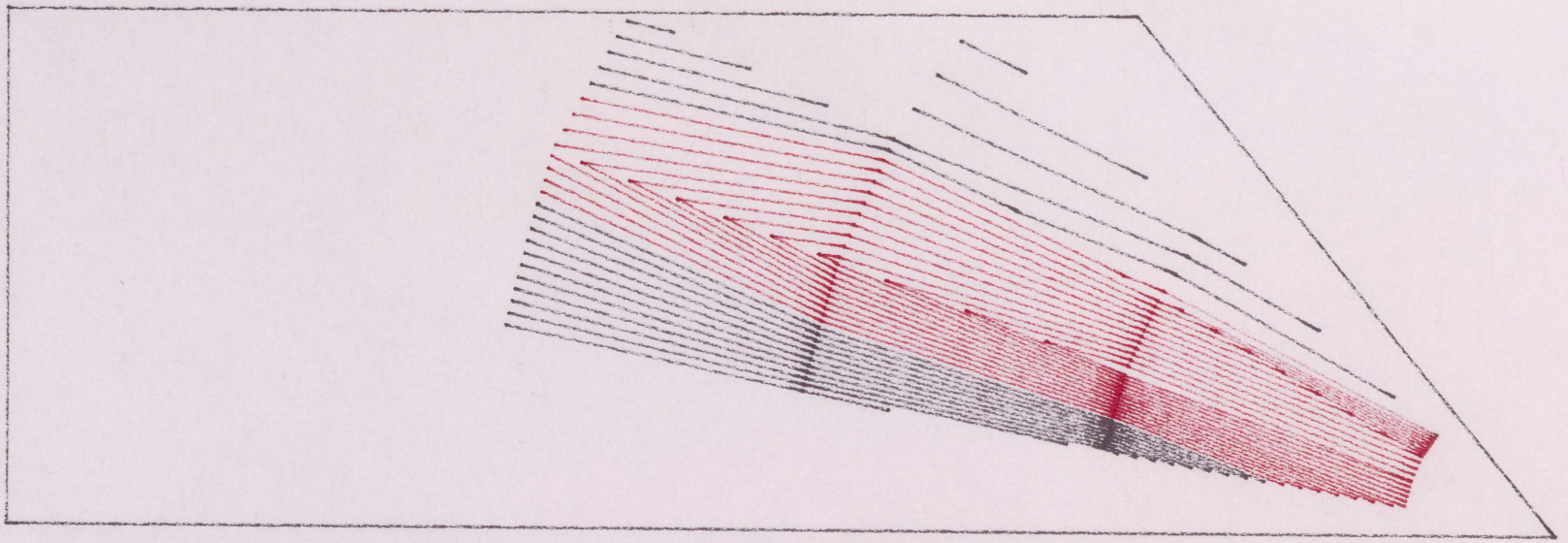
NO. OF CONTOURS : 40

MIN RMS Cp : 0.039

MAX RMS Cp : 0.154

CONTOUR INCREMENT : 0.003

RMS Cp DISTRIBUTION IN A-PILLAR REGION

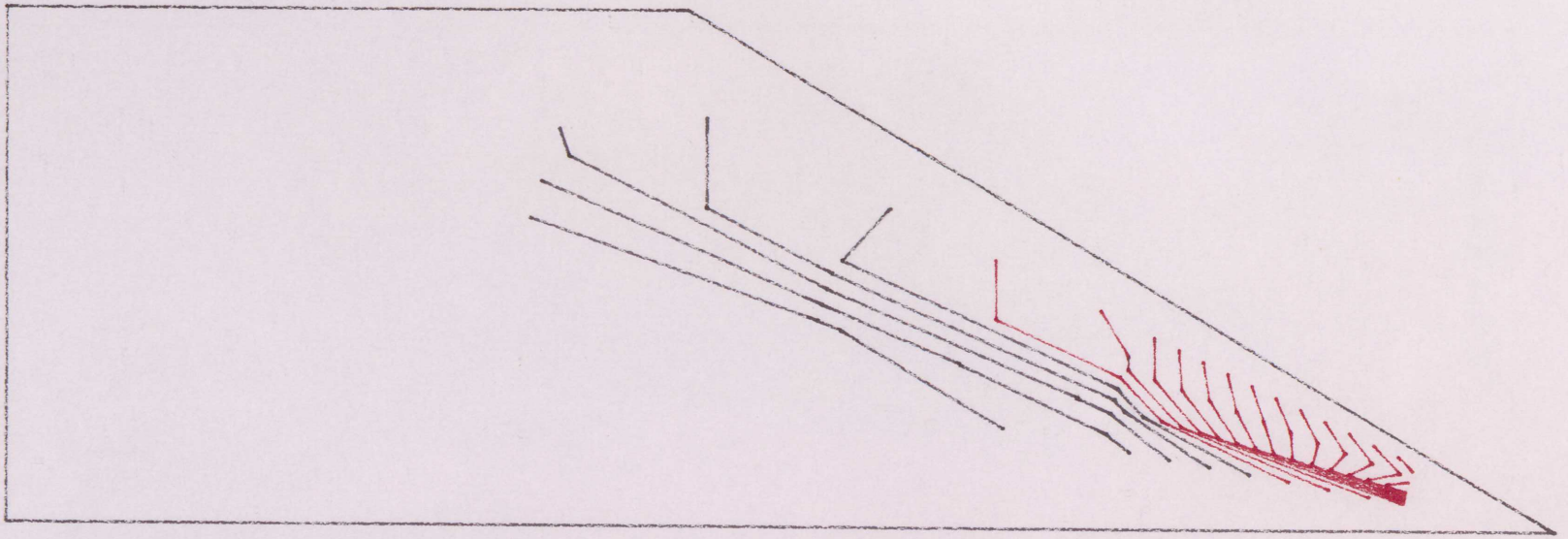


WHOLE MODEL WITH PLATE
REYNOLDS No : 5.672E05
A-PILLAR ANGLE : 40 DEGREES

FIG No : 3.4.3.2

RMS CONTOUR DETAILS
NO. OF CONTOURS : 24
MIN RMS Cp : 0.045
MAX RMS Cp : 0.266
CONTOUR INCREMENT : 0.009

RMS Cp DISTRIBUTION IN A-PILLAR REGION



WHOLE MODEL WITH PLATE

REYNOLDS No : 9.580E05

A-PILLAR ANGLE : 60 DEGREES

FIG No : 3.4.3.3

RMS CONTOUR DETAILS

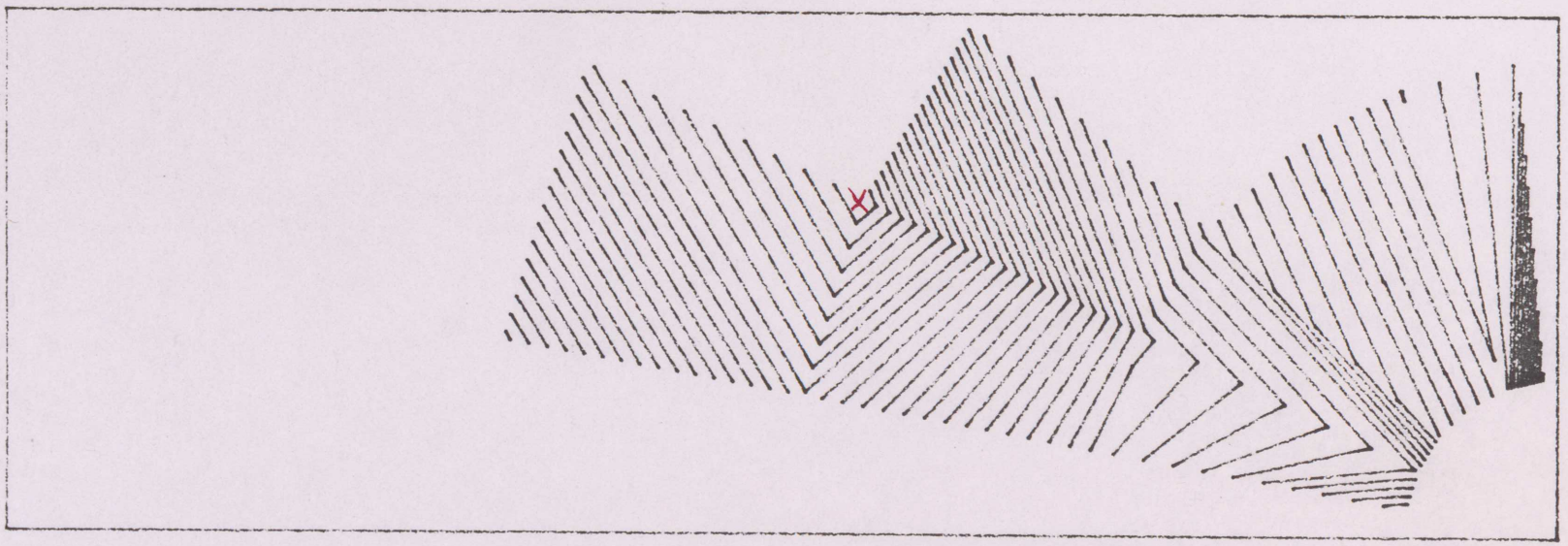
NO. OF CONTOURS : 18

MIN RMS Cp : 0.012

MAX RMS Cp : 0.528

CONTOUR INCREMENT : 0.029

RMS Cp DISTRIBUTION IN ROOT REGION ON SWEPT PLATE



REYNOLDS No : 8.652E04

SWEEP ANGLE : 0 DEGREES

FIG No : 3.4.4.1

RMS CONTOUR DETAILS

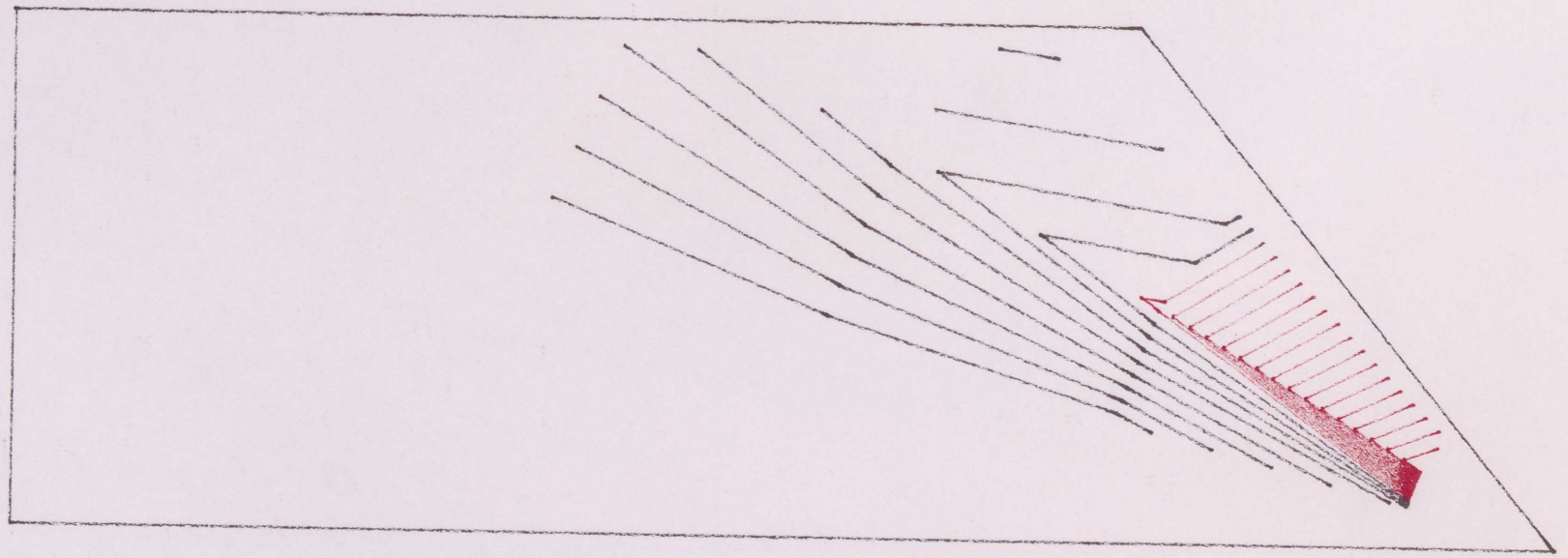
NO. OF CONTOURS : 40

MIN RMS Cp : 0.032

MAX RMS Cp : 0.138

CONTOUR INCREMENT : 0.003

RMS Cp DISTRIBUTION IN ROOT REGION ON SWEPT PLATE



REYNOLDS No : 1.166E05

SWEEP ANGLE : 40 DEGREES

FIG No : 3.4.4.2

RMS CONTOUR DETAILS

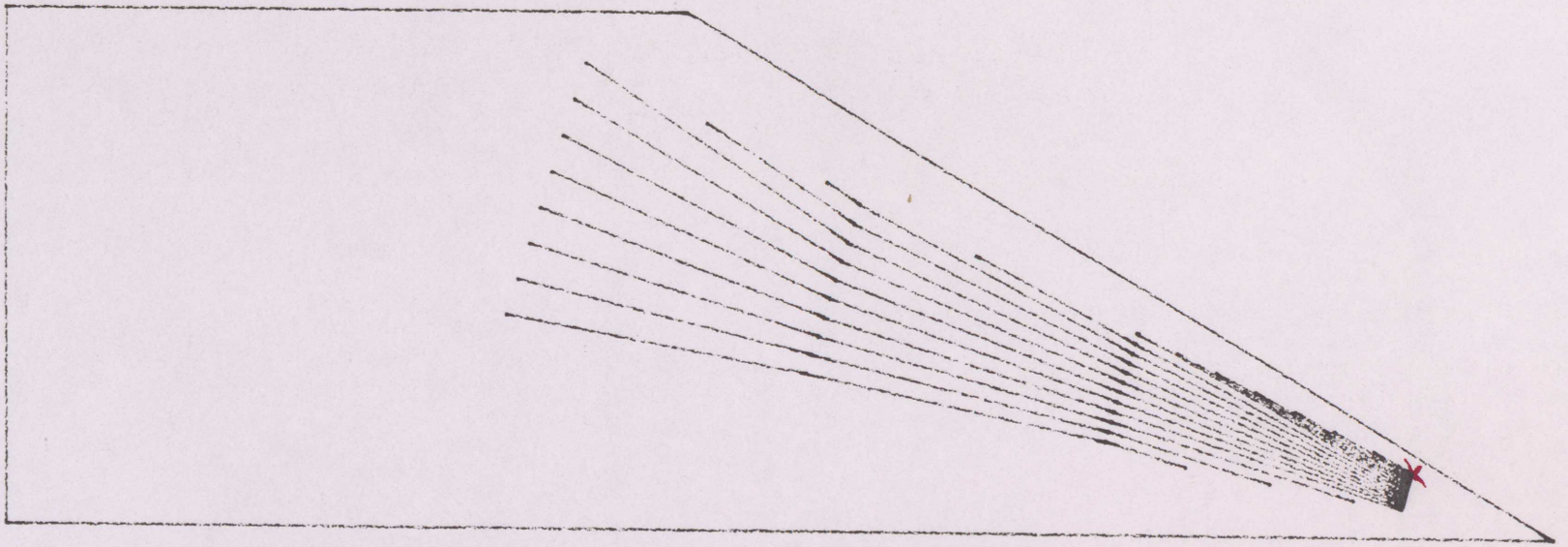
NO. OF CONTOURS : 24

MIN RMS Cp : 0.014

MAX RMS Cp : 0.434

CONTOUR INCREMENT : 0.018

RMS Cp DISTRIBUTION IN ROOT REGION ON SWEPT PLATE



REYNOLDS No : 5.270E04
SWEEP ANGLE : 60 DEGREES

FIG No : 3.4.4.3

RMS CONTOUR DETAILS
NO. OF CONTOURS : 18
MIN RMS Cp : 0.042
MAX RMS Cp : 0.106
CONTOUR INCREMENT : 0.004

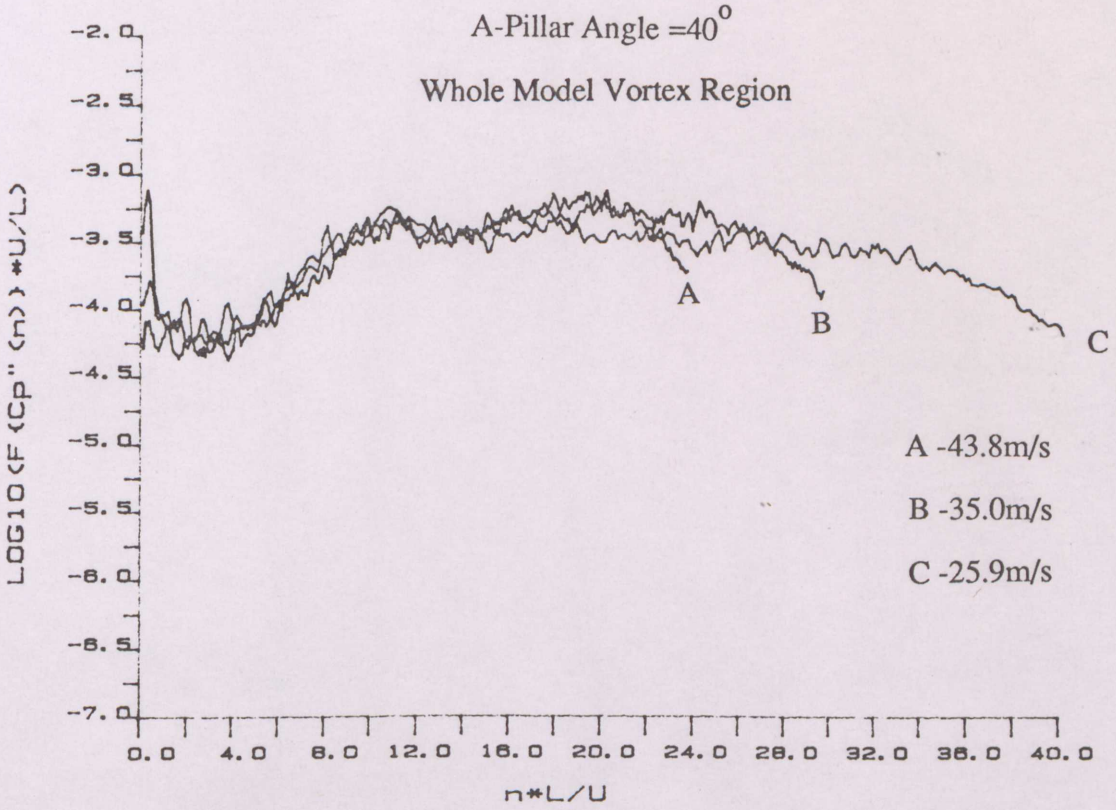


Fig.3.5.1 Power Spectra plot of peak Cp_{rms} Tapping for 40° Whole Model at three speeds (25.9, 35.0, 43.8m/s).

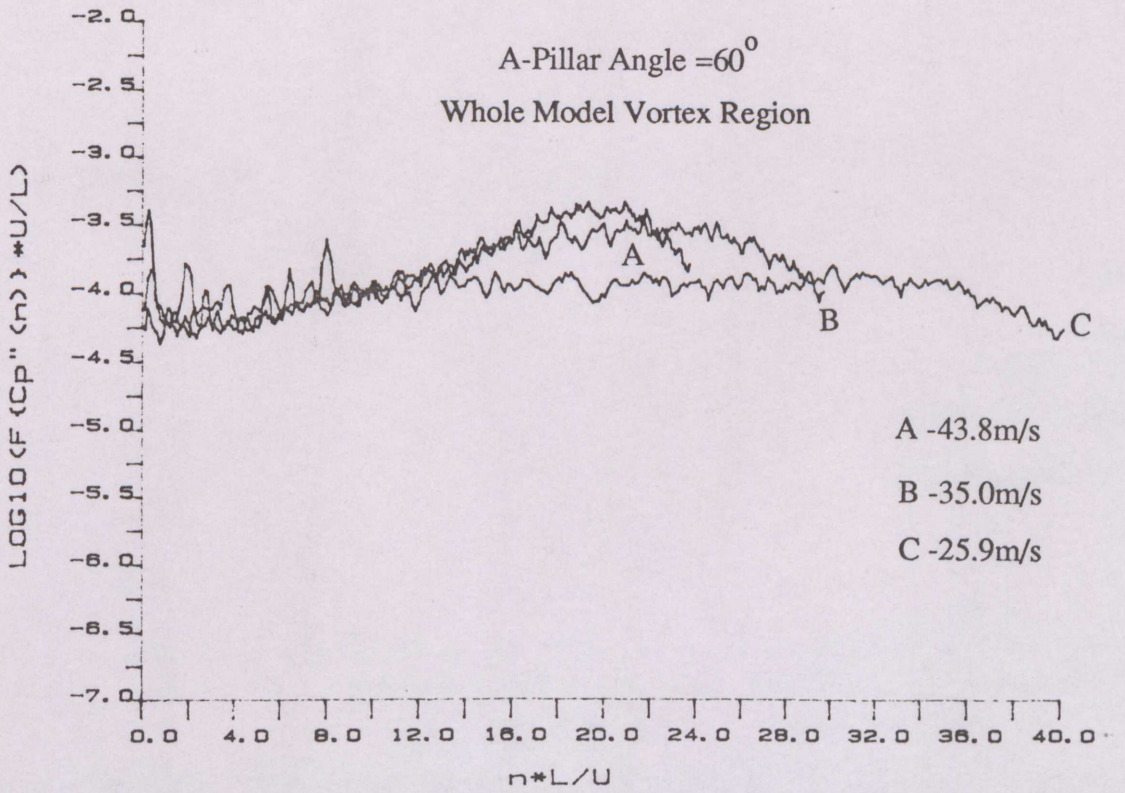


Fig.3.5.2 Power Spectra plot of peak Cp_{rms} Tapping for 60° Whole Model at three speeds (25.9, 35.0, 43.8m/s).

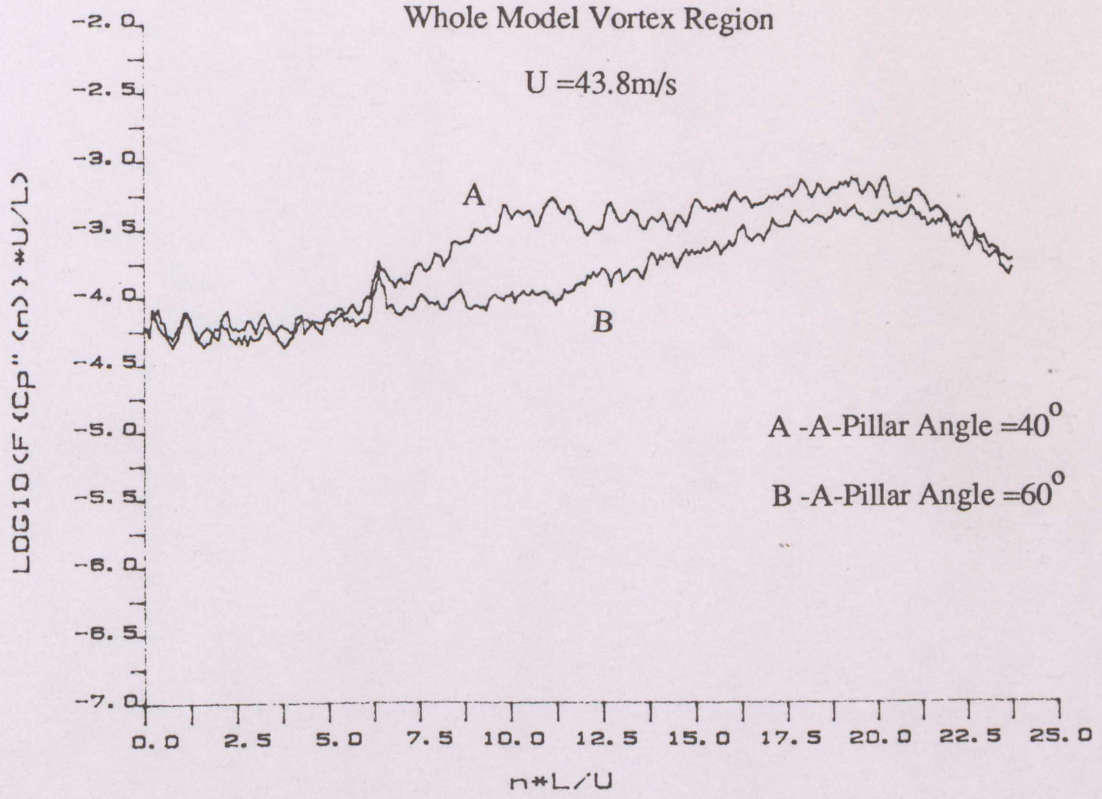


Fig.3.5.3 Comparisons of the Power Spectra curves for the 40° and 60° Whole models (peak Cp_{rms} Tappings) at 43.8m/s.

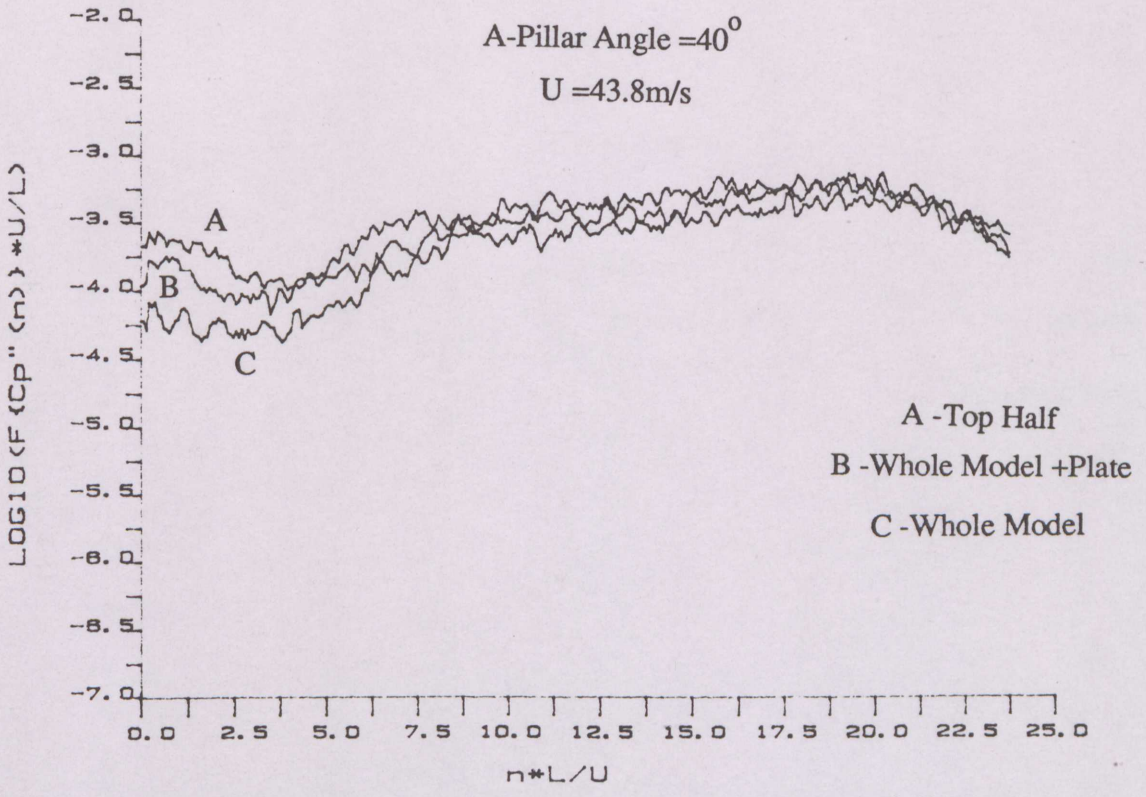


Fig.3.5.4 Power Spectra plot of peak Cp_{rms} Tapping for the three 40° models at 43.8m/s.

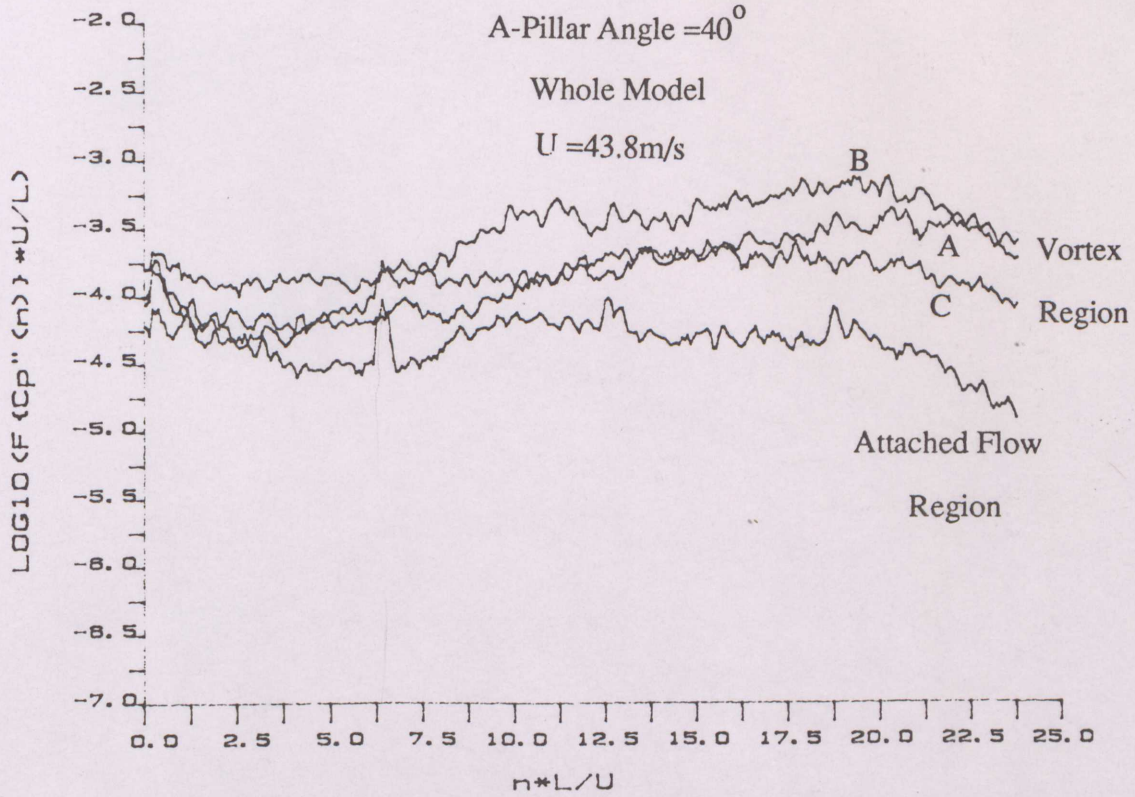


Fig.3.5.5 Power Spectra plot of 4 pressure tappings on the 40° Whole Model at 35.0m/s.

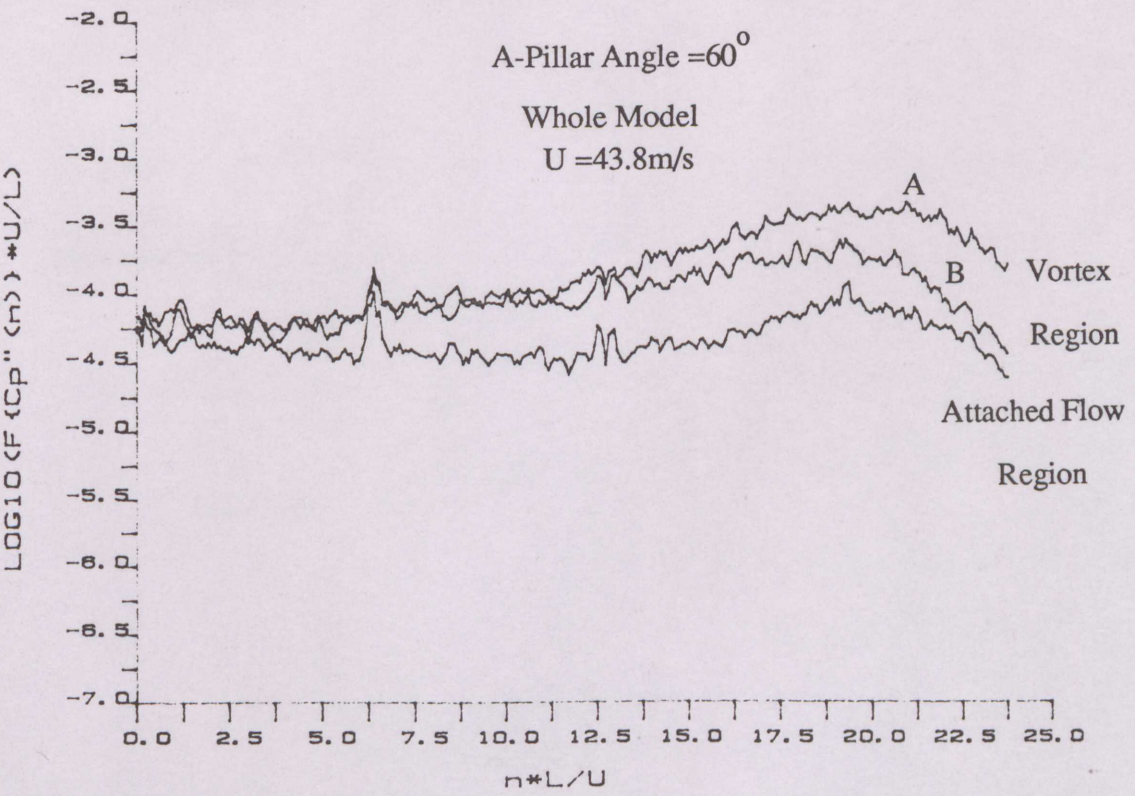


Fig.3.5.6 Power Spectra plot of 3 pressure tappings on the 60° Whole Model at 35.0m/s.

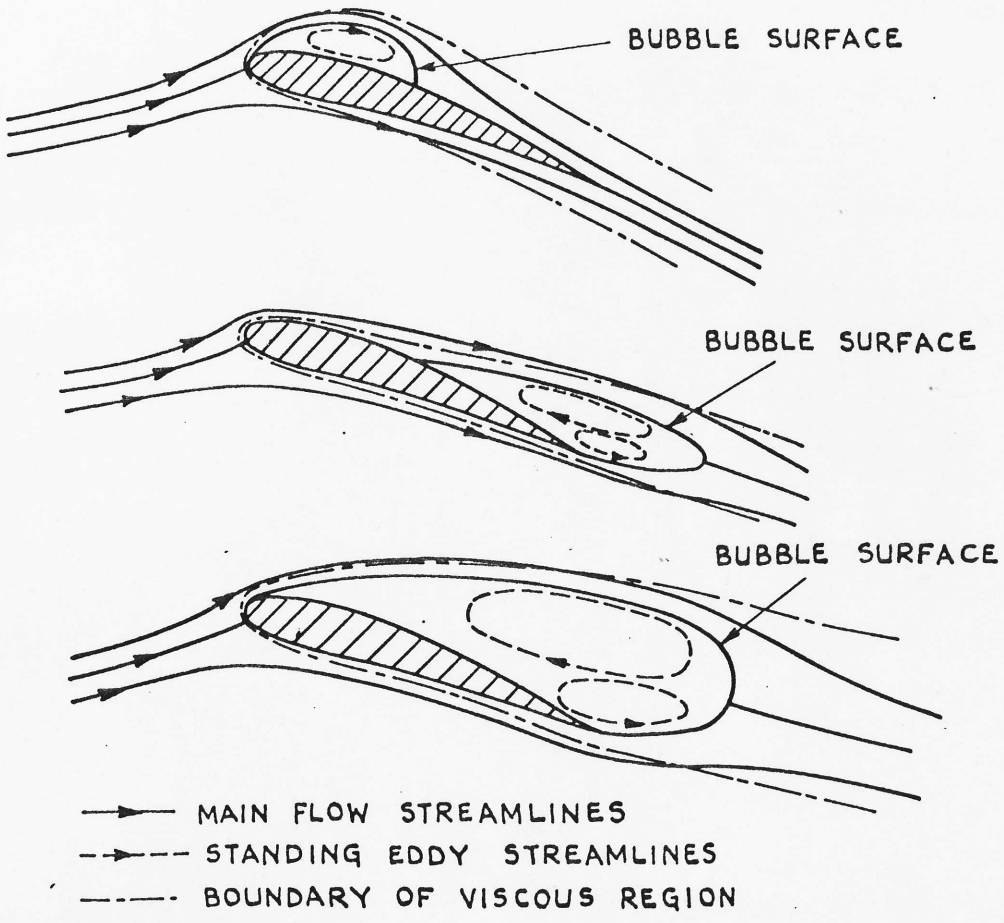


Fig.4.1 Diagram of TYPE I flow - The bubble.

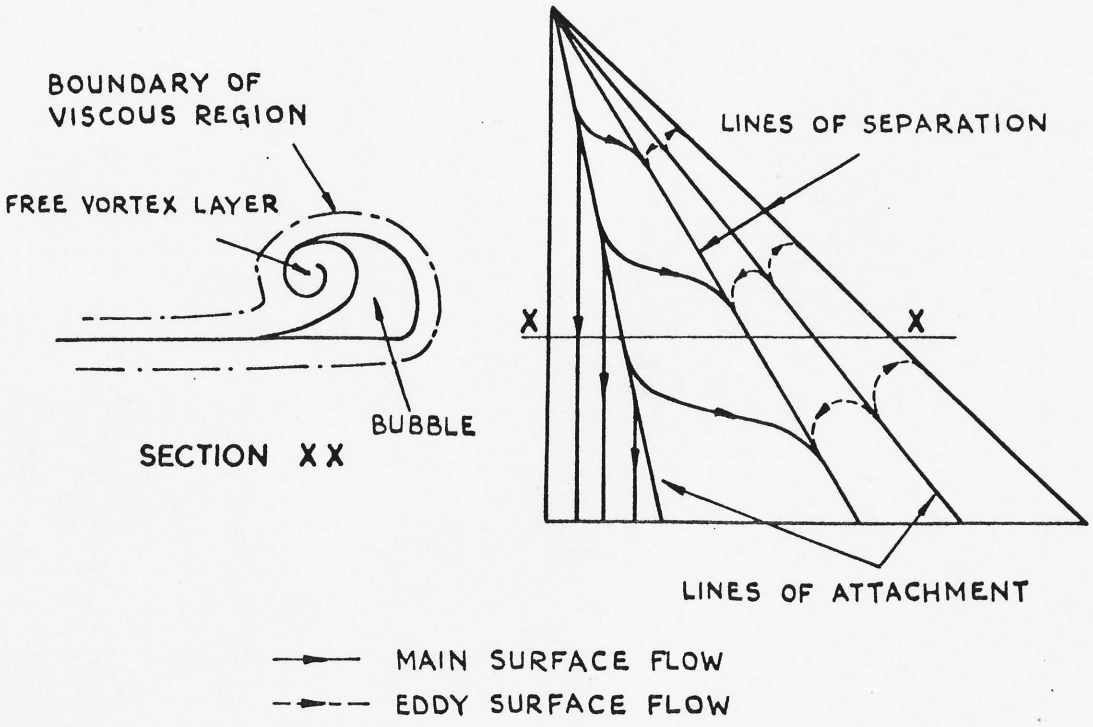


Fig.4.2 Diagram of TYPE II flow - Vortex bubble (mixed flow).

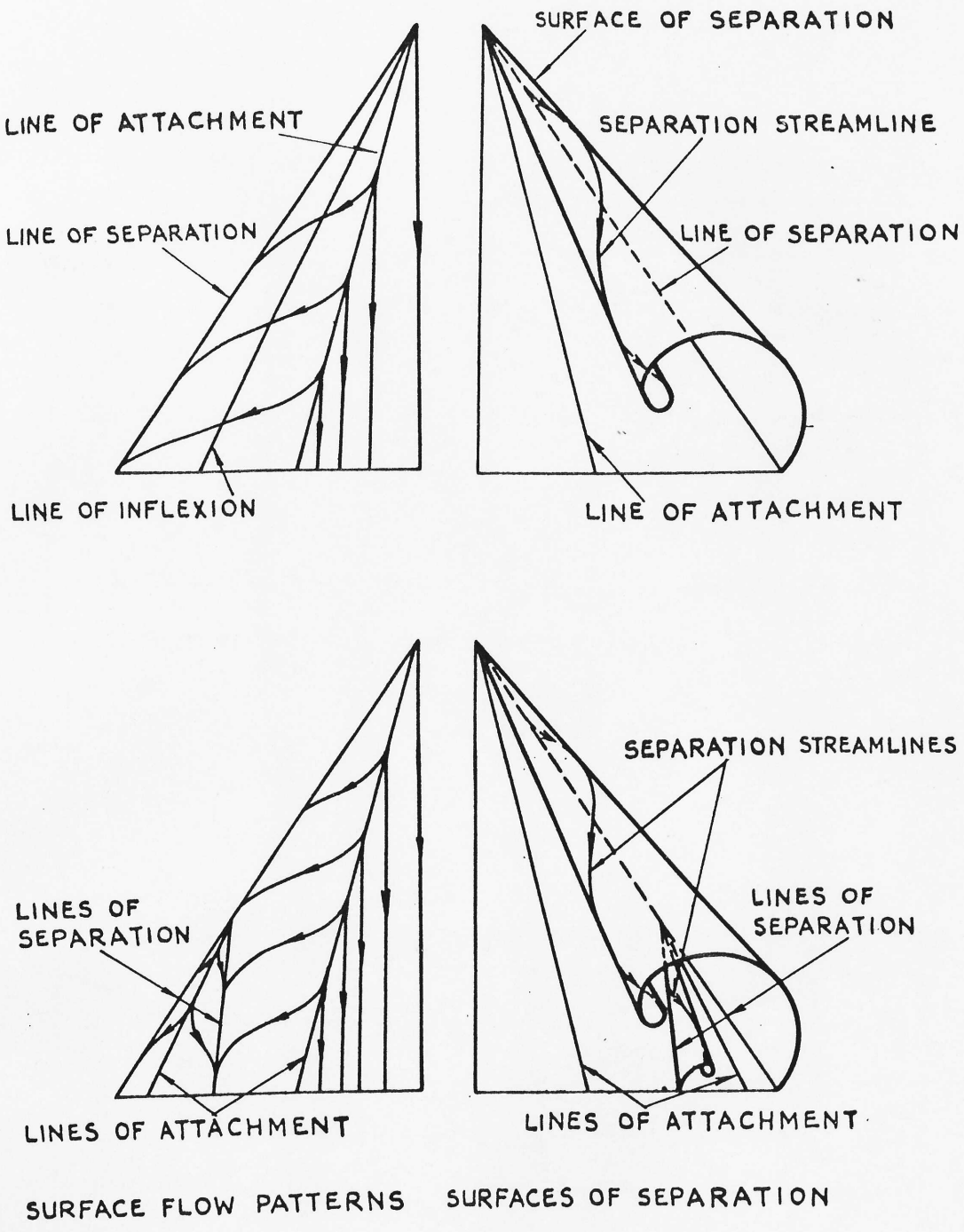


Fig.4.3 Diagram of TYPE III flow - Free vortex layer.

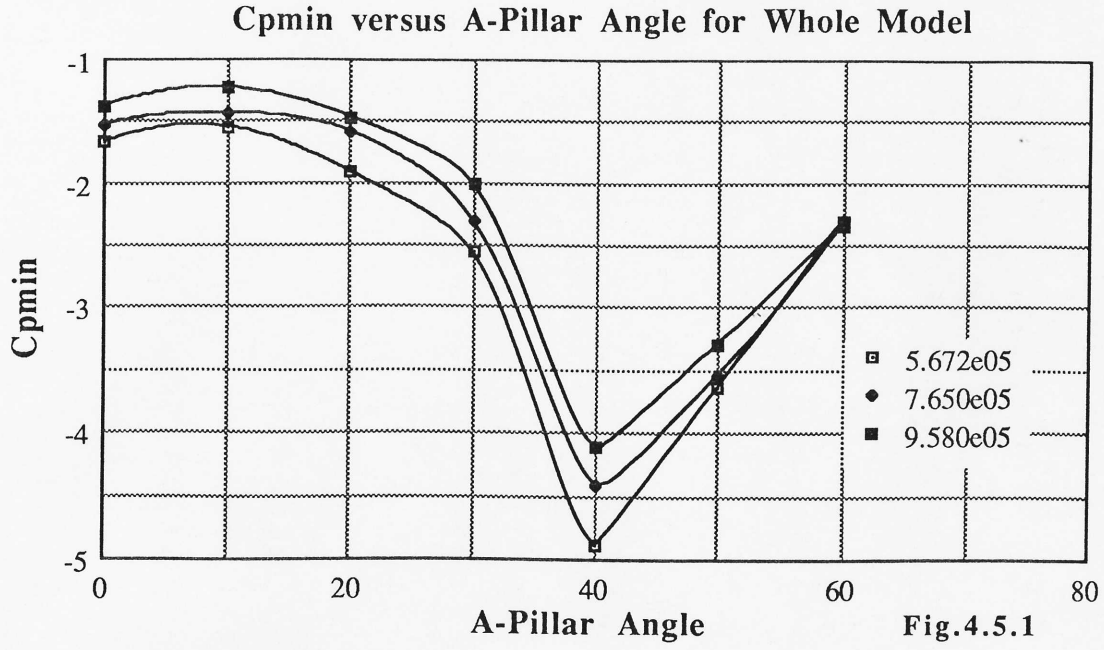


Fig.4.5.1

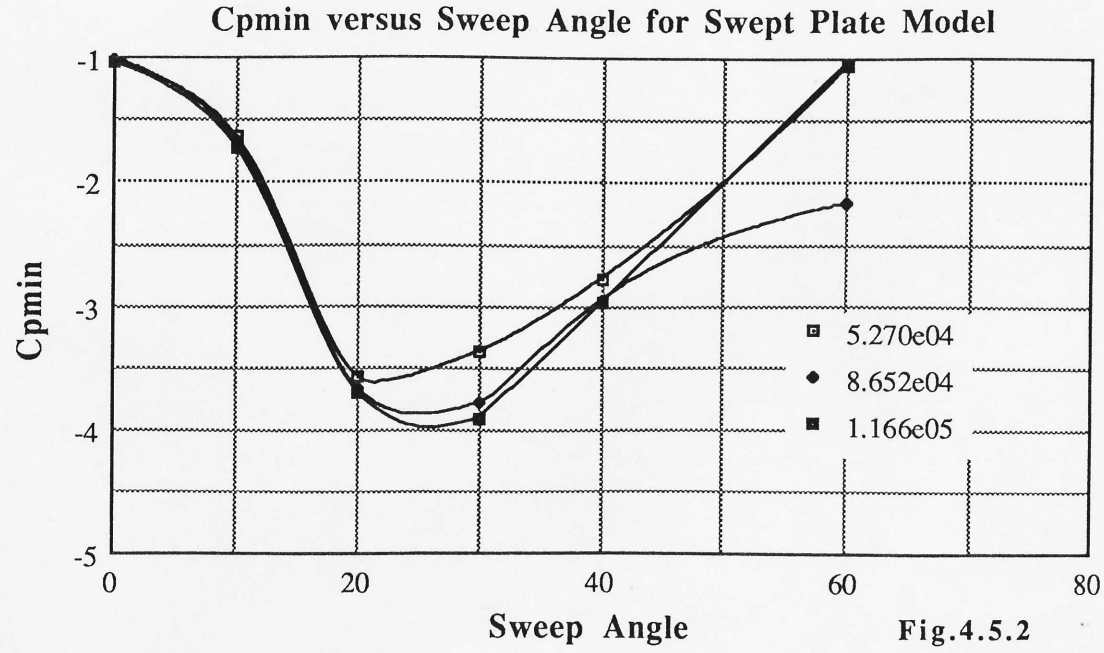


Fig.4.5.2

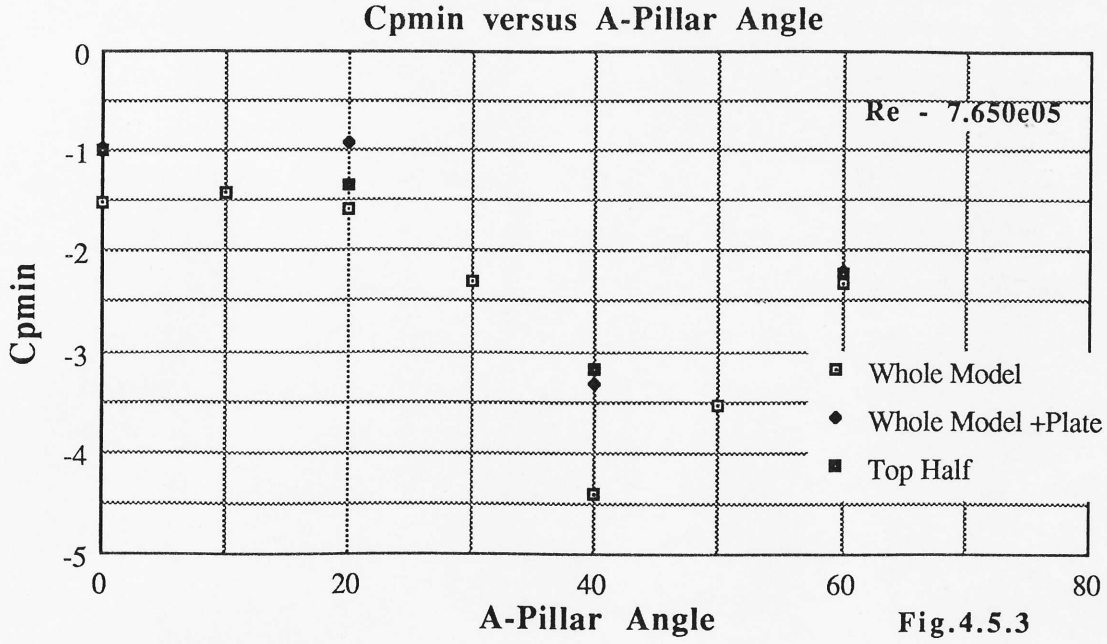


Fig.4.5.3

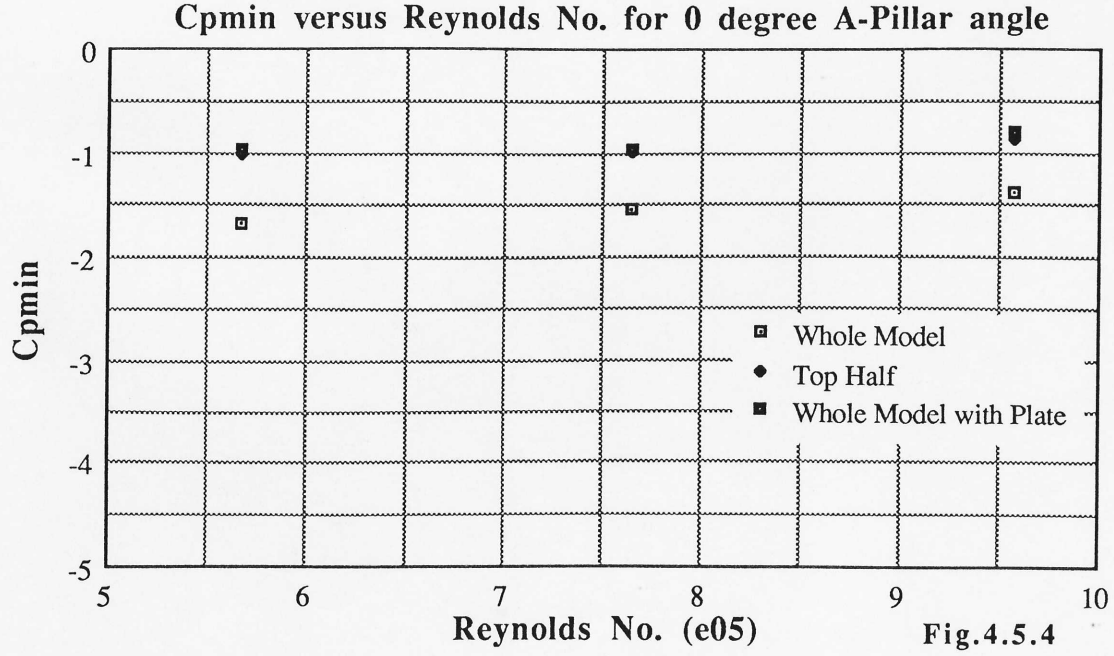


Fig.4.5.4

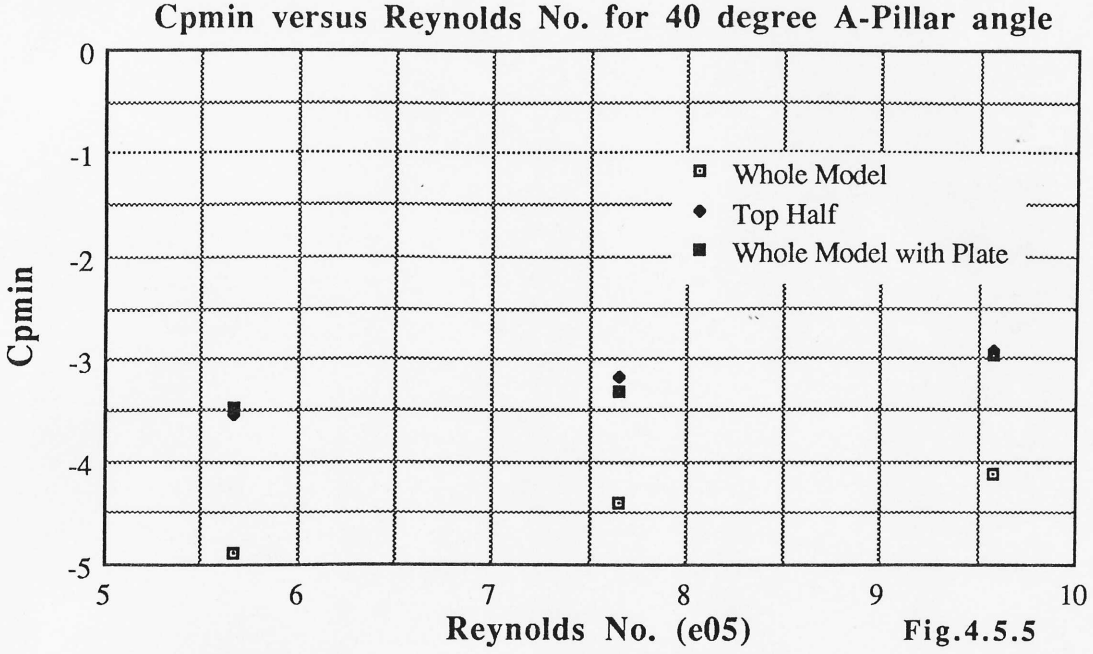


Fig.4.5.5

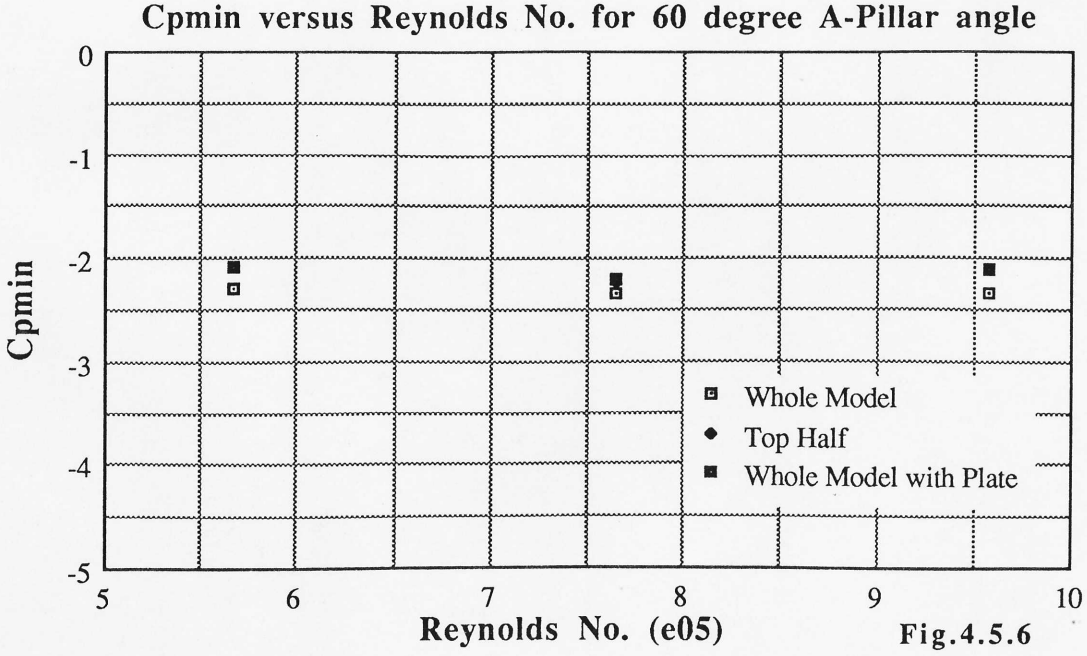


Fig.4.5.6

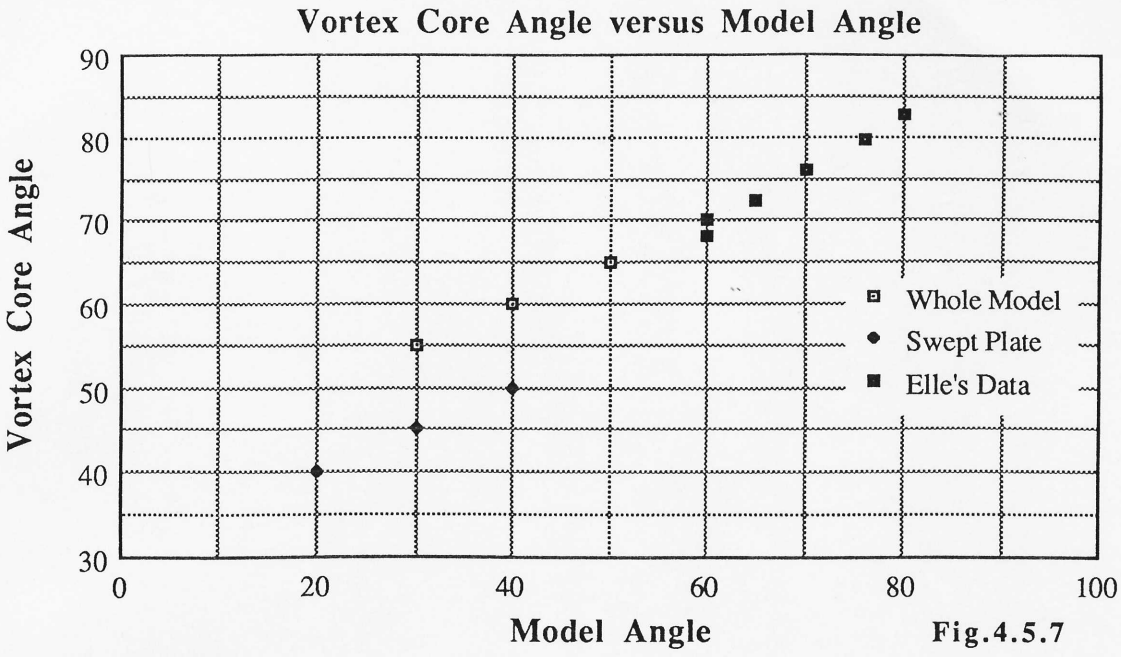
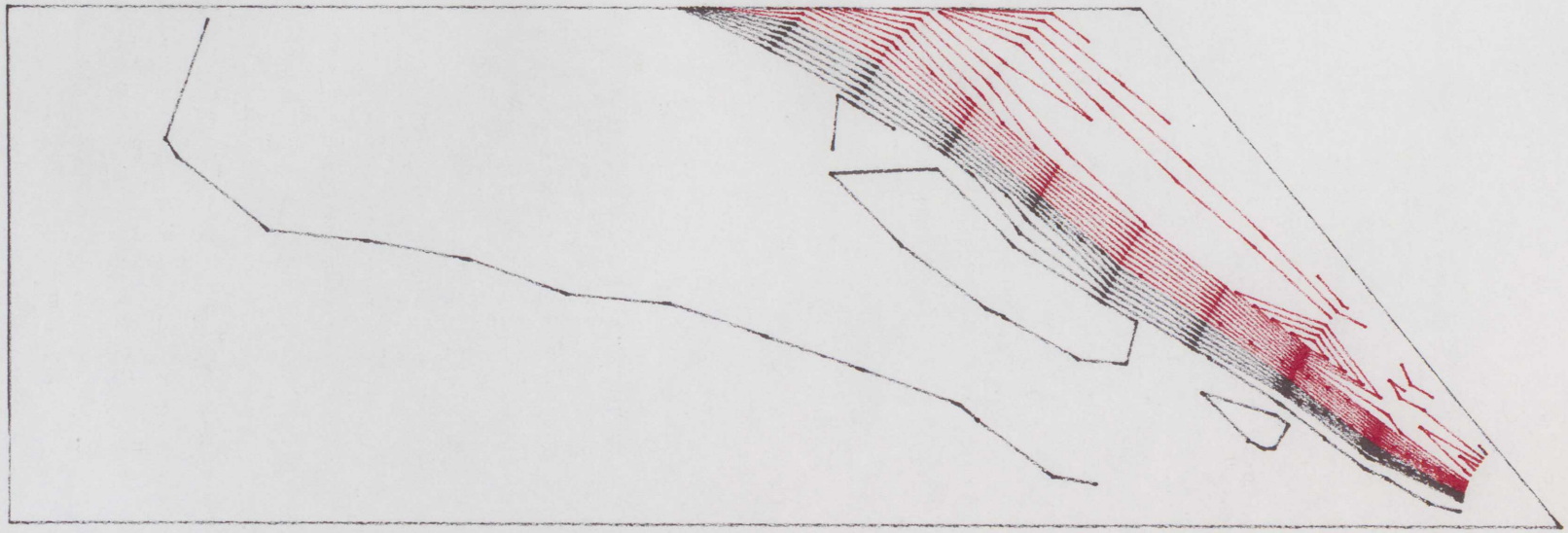

Vortex Core Angle versus Model Angle
Vortex Core Angle
90
80
70
60
50
40
30
0
20
40
60
80
100
Model Angle
Whole Model
Swept Plate
Elle's Data

Fig.4.5.7

MEAN Cp DISTRIBUTION IN ROOT REGION ON SWEPT PLATE



REYNOLDS No : 8.652E04

SWEEP ANGLE : 40 DEGREES

FIG No : 4.5.8

Cp CONTOUR DETAILS

NO. OF CONTOURS : 20

MAX. Cp VALUE : -0.360

MIN. Cp VALUE : -3.724

CONTOUR INCREMENT : -0.168

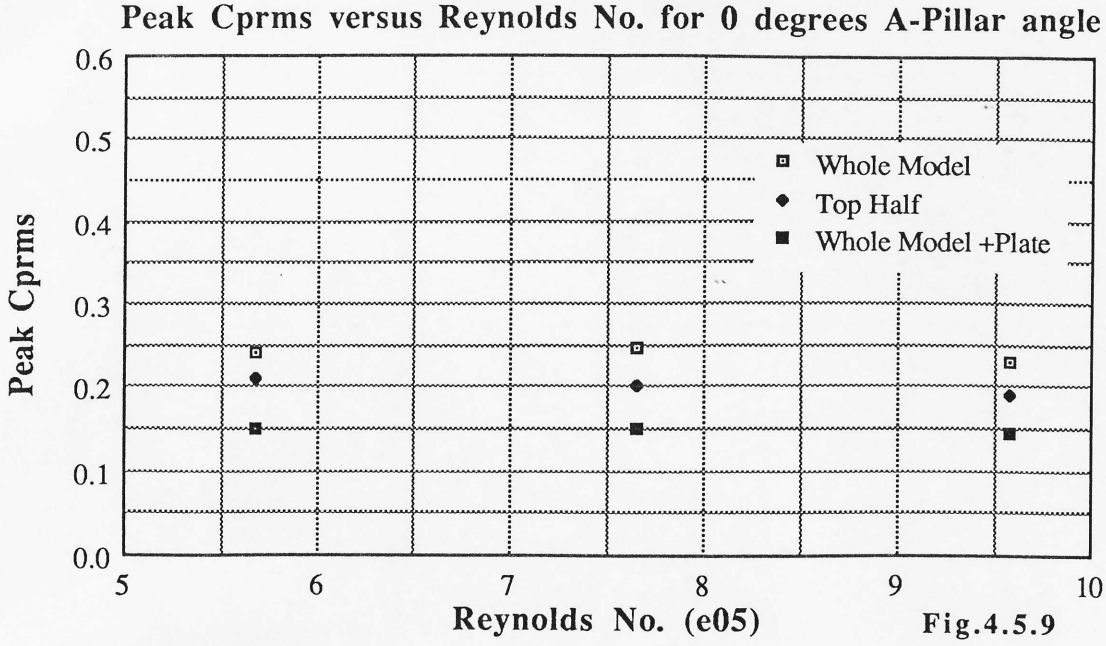


Fig.4.5.9

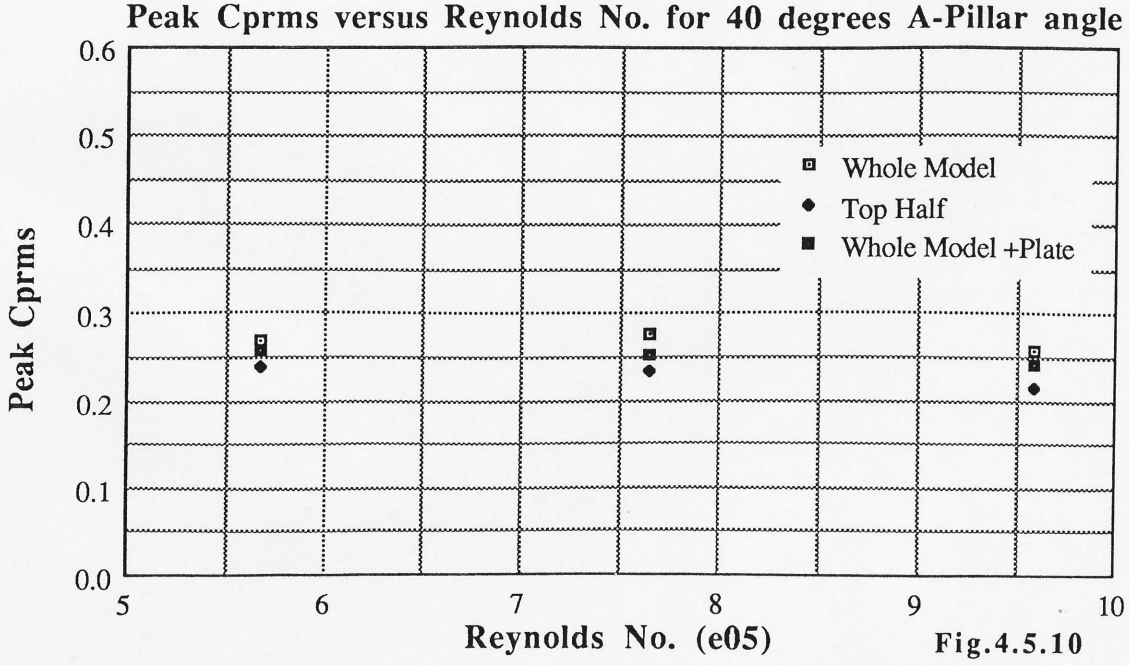


Fig.4.5.10

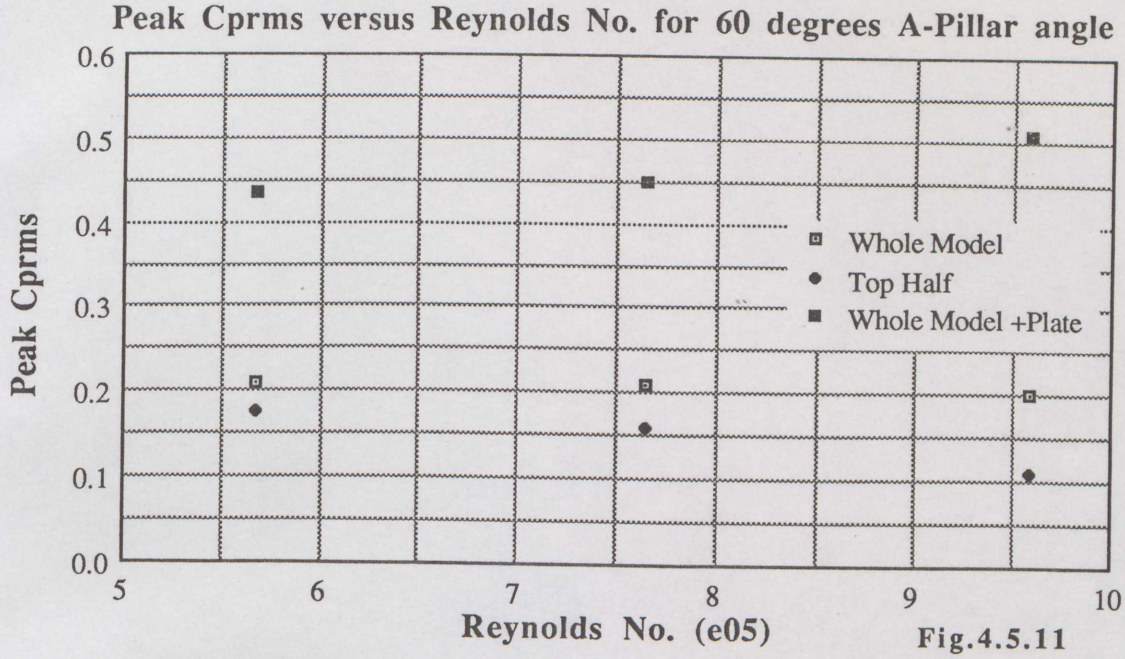


Fig.4.5.11

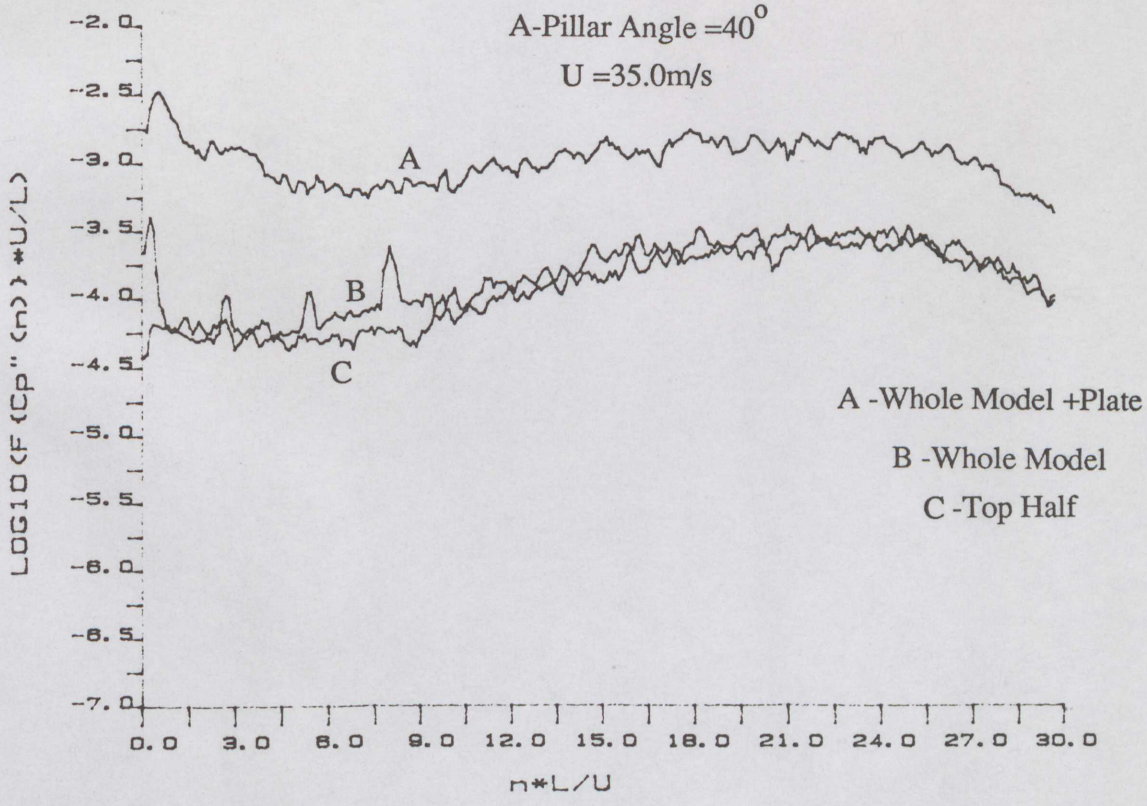


Fig.4.5.12 Power Spectra plot of peak Cp_{rms} Tapping for the three 60° models at 35.0m/s.